The Impact of Donor-Acceptor Polymer Crystal Structure and Mesoscopic Morphology on Opto-Electronic Devices

Von der Fakultät Chemie der Universität Stuttgart zur Erlangung der Würde eines Doktors der Naturwissenschaften (Dr. rer. nat.) genehmigte Abhandlung

Vorgelegt von

Florian S. U. Fischer

aus Marburg, Deutschland

Hauptberichterin:	Prof. Dr. Sabine Ludwigs
Mitberichter:	Prof. Dr. Joris van Slageren
Prüfungsvorsitzender:	Prof. Dr. Frank Gießelmann

Tag der mündlichen Prüfung: 10.07.2015

Institut für Polymerchemie der Universität Stuttgart

IPOC – Functional Polymers

2015

Erklärung über die Eigenständigkeit der Dissertation

Ich versichere, dass ich die vorliegende Arbeit mit dem Titel

The Impact of Donor-Acceptor Polymer Crystal Structure and Mesoscopic Morphology on Opto-Electronic Devices

selbständig verfasst und keine anderen als die angegebenen Quellen und Hilfsmittel benutzt habe; aus fremden Quellen entnommene Passagen und Gedanken sind als solche kenntlich gemacht.

Declaration of Authorship

I hereby certify that the dissertation entitled

The Impact of Donor-Acceptor Polymer Crystal Structure and Mesoscopic Morphology on Opto-Electronic Devices

is entirely my own work except where otherwise indicated. Passages and ideas from other sources have been clearly indicated.

Name/Name: Florian S. U. Fischer

Unterschrift/Signed: _____

Datum/Date: _____

Summary

Organic materials have become more and more important in devices such as light emitting diodes (LEDs), field effect transistors (FETs) and solar cells (OPV) because the demand to build robust, flexible and small electronic devices has increased. Meeting the needs of fast and cheap processing conditions, conjugated polymers have become a real alternative to evaporated small molecules. Moreover, they have the advantage of tunability of their solution processing and optoelectronic properties such as band-gap, charge carrier mobility and photoluminescence via structural changes to the monomers. In recent years high performancing optoelectronic devices have been built using a new type of conjugated copolymers, the so called donor-acceptor copolymers. Such polymers are based on alternating electron-donor and acceptor units and possess typically small band-gaps due to a charge transfer (CT) transition between the alternating backbone units. The small band gap correlates to a shift in the absorption profile to longer wavelengths up to 800 nm and therefore allows coverage of a broad range of the solar spectrum. In the last years, control over film morphology and its effect on the device physics have led to significant progress in improving device performance. Nevertheless up to now little is known about the mesoscopic morphology and crystal structure of such donor-acceptor copolymers, even though the influence on device performance is unquestioned in literature.

In this thesis the high performance donor-acceptor copolymer PCPDTBT (poly[2,6-(4,4-bis-(2-ethylhexyl)-4H-cyclopenta[2,1-b;3,4-b'] dithiophene)-*alt*-4,7-(2,1,3-benzothiadiazole)])[1–3] and its two derivatives Si-PCPDTBT[4] and F-PCPDTBT[5,6] (poly[(4,4'-bis(2-ethylhexyl)dithiene-[3,2-b:2',3'-d]silole)-*alt*-4,7-(2,1,3-benzothiadiazole)]), poly[2,6-(4,4-bis-(2-ethylhexyl)-4H-cyclopenta[2,1-b;3,4-b']dithiophene)-*alt*-4,7-(5-fluoro -2,1,3-benzothiadiazole)]) were investigated. The aim was to establish a general understanding of the mesoscopic morphology and crystal structure obtained by different processing and annealing protocols. Subsequently the influence of the prepared structures on the optical, electrochemical and electronic properties was investigated.

At the beginning of this thesis the basic absorption and photoluminescence (PL) properties of the PCPDTBT polymers in solution and when deposited as thin films, were investigated. In particular the aggregation behavior in solution was characterized by temperature and concentration dependent experiments. It was shown that a strong band at 800 nm was present in solution containing aggregates which are a result of π-stacked interchain interactions. Spano et al.[7–9] introduced a technique to model the absorption and PL spectra for several conjugated homopolymers employing a Frank-Condon analysis.

In this thesis, to the best of my knowledge, this analysis has been transfered for the first time to a donor-acceptor copolymer. It was shown that the spectra of the dissolved, as well as aggregated phases, of PCPDTBT could be perfectly modeled using the same Franck-Condon analysis. [10, Scharsich und Fischer et al. 2015]

The optical and morphological properties of thin films prepared from different processing solvents with and without solvent additives such as 1,8-diiodooctane (DIO) were characterized. [11, Fischer et al. 2013] Different types of processing solvents had a strong impact on the thin film morphology. The prepared structures ranged from amorphous films to micrometer long nanofibers. Employing solvent vapor annealing protocols, F-PCPDTBT and PCPDTBT films of high crystallinity were found contradicting the literature which sometimes describes PCPDTBT as hardly crystallizable. [12, Fischer et al. 2014]

A variety of morphologies and crystal structures were prepared by utilizing different processing solvents and post annealing methods. In the literature, one typically sees reports on conjugated polymers such as poly(3-hexylthiophene) (P3HT) and poly[2-methoxy-5-(2'-ethylhexyloxy)-p-phenylene vinylene] (MEH-PPV), which crystallize in an edge-on fashion, driven by the strong interchain packing of the polmyer backbones. PCPDTBT is also known to pack in a similar way as P3HT when DIO is employed as a solvent additive. Using our optimized solvent vapor annealing procedure, it was possible to identify an additional polymorph and to establish a first tentative crystal structure therefore using TEM/ED and GIWAXS measurements. [12, 13, Fischer et al. 2015] Remarkably the structures gave no evidence for a typical lamellar structure with alternating π-stacking and alkyl chain lamellae. Instead a dimer-like structure was found, similar to the one reported for α-PFO. The ability to control the crystallization and to induce particular polymorphs was used to compare the effect of different morphologies on the operation of optoelectronic devices such as field effect transistors and organic solar cells. [12, Fischer et al. 2015]

The energy levels of the pure polymers and polymer/fullerene blends were investigated employing spectroelectrochemistry. Using cyclic voltammetry the redox potentials and the energy levels of the frontier orbitals could be determined. The coupling of the cyclic voltammetry with in-situ spectroscopy allowed the investigation of the absorption properties of the charged species. In-situ spectroelectrochemistry of polymer/fullerene blends further allowed the assignment of specific redox reactions to either the polymer or fullerene phase. Interestingly, it could be shown that within the polymer/fullerene blends the LUMO energy levels are stabilized. The data obtained from these measurements were used in a collaboration with the physics group of Prof. Neher in Potsdam to investigate

the mechanism of the charge-transfer splitting in Si-PCPDTBT/fullerene organic solar cells. [14, Albrecht and Fischer et al. 2014]

Finally, the ability to obtain thin films consisting of different morphologies was used to investigate the influence of crystal structure and chain orientation on the performance of organic field effect transistors (OFETs) and solar cells. Three different morphologies were compared: i) edge-on structure with long-range π-stacking ii) dimer-like structure with an in-plane orientation of the polymer backbones and iii) a film with predominantly amorphous domains. The OFETs of the long-range π-stacking structure revealed a hole mobility which was one order of magnitude higher compared to the dimer-like and amorphous structures. In analogy to P3HT [15, 16, Crossland and Fischer et al. 2011/2012] it was suggested that the edge-on morphology provides a good in-plane 2D charge transport. On the other hand in the dimer-like structure the charge transport is reduced in the direction perpendiuclar to the polymer chains by the alkyl side chains between the dimers. Only a 2D charge transport allows the charges to find pathways of the least resistance over macroscopic distances as probed in OFETs. This leads to an overall increased charge carrier mobility in the samples comprising a long-range π-stacked morphology.

Bilayer solar cells were built from the same, above mentioned, three morphologies and characterized by J-V-curve, external quantum efficiencies (EQE) and time delayed collection field (TDCF) measurements. [12, Fischer et al. 2015] Surprisingly the higher charge carrier mobility in the π-stacked morphology did not lead to an increased performance or reduced recombination rate. In contrary all investigated morphologies revealed overall very similar efficiencies which can be explained by an imbalance in the hole and electron mobility of PCPDTBT and C_{60}.

Overall this thesis presents a systematic study of the representative donor-acceptor copolymers PCPDTBT, Si-PCPDTBT and F-PCPDTBT regarding the influence of the crystal structure and mesoscopic morphology on opto-electronic device properties. The correlation between the absorption and different crystal structures was shown and the spectra were modeled using a Frank-Condon analysis. By employing solvent vapor annealing, highly crystalline samples were prepared and a first tentative crystal structure was presented. The energy levels of pure polymer films and polymer/fullerene blends as used in organic solar cells were investigated. Finally, the fabrication and testing of OFETs and organic solar cells revealed how the thin film structure influences the performance of opto-electronic devices.

Zusammenfassung

Mit immer neuen Anforderungen an elektronische Geräte wie Flexibilität, geringes Gewicht und günstige Produktionskosten ist die organische Elektronik in den Fokus von Wissenschaft und Industrie gerückt. In den letzten Jahren konnte beobachtet werden, wie vermehrt organische Elektronik in Form von organischen Feldeffekttransistoren (OFET), Leuchtdioden (LED) oder Solarzellen (OPV) Einzug in unser alltägliches Leben fanden. Der Vorteil dieser Bauteile liegt in der einfachen, meist schnellen und kostengünstigen Prozessierbarkeit aus Polymerlösungen oder durch Verdampfung kleiner Moleküle. Des Weiteren lassen sich im Vergleich zu anorganischen Materialien durch relativ kleine Veränderungen an den Monomerbausteinen die optischen und elektronischen Eigenschaften an die jeweiligen Anforderungen anpassen.

In den letzten Jahren wurde in organischen Solarzellen vermehrt eine neue Klasse von Polymeren, die sogenannten Donor-Akzeptor-Copolymere, verwendet. Die Wiederholungseinheiten solcher Polymere bestehen aus alternierenden Donor–Akzeptor Bausteinen, wodurch ein Ladungstransfer zwischen Donor und Akzeptor begünstigt wird. Dies führt zu einer Verkleinerung der Bandlücke und damit zu einer Rotverschiebung des Absorptionsspektrums im Vergleich zu klassischen konjugierten Polymeren, wie z.B. P3HT. Insbesondere die Rotverschiebung erlaubt es, mehr Photonen des Sonnenspektrums zu absorbieren und dadurch die Effizienz von organischen Solarzellen zu steigern.

Durch Optimierungen im Bereich der Morphologie konnte die Leistung von polymerbasierter Elektronik gesteigert werden. Trotz allem ist bis heute nur sehr wenig über die Struktur-Eigenschaftsbeziehungen von Donor-Akzeptor-Copolymeren und deren Einfluss auf organische Bauteile bekannt und das, obwohl die Möglichkeit der Leistungssteigerung durch Strukturoptimierung unbestritten ist.

Das Ziel dieser Arbeit war es, ein grundsätzliches Verständnis der Wechselwirkungen zwischen der Struktur und den elektrischen, optischen und elektrochemischen Eigenschaften der Donor-Akzeptor-Copolymere zu erarbeiten. Dafür wurde das oft zitierte und leistungsstarke Donor-Akzeptor-Copolymer Poly[2,6-(4,4-bis-(2-ethylhexyl)-4H-cyclopenta [2,1-b;3,4-b'] dithiophen)-*alt*-4,7-(2,1,3-benzothiadiazol)][1–3] (PCPDTBT) zusammen mit seinen zwei Derivaten F-PCPDTBT (Poly[2,6-(4,4-bis-(2-ethylhexyl)-4H-cyclopenta[2,1-b;3,4-b']dithiophen)-*alt*-4,7-(5-fluoro-2,1,3-benzothiadiazol)])[5,6] und Si-PCPDTBT (Poly [(4,4'-bis(2-ethylhexyl)dithien-[3,2-b:2',3'-d]silol)-*alt*-4,7- (2,1,3-benzothiadiazol)])[4] untersucht. Durch den Vergleich der drei Polymere wurde es möglich, den Einfluss typischer

Polymerrückgrat-Modifikationen, wie das Fluorieren oder das Ersetzen eines Kohlenstoffatoms durch Silizium, zu untersuchen.

Zu Beginn dieser Arbeit wurde das Absorptions- und Photolumineszenzverhalten in Lösung untersucht. Ein besonderes Augenmerk lag dabei auf der Aggregation und ihrem Einfluss auf die optischen Eigenschaften. Zur Untersuchung wurden temperatur- und konzentrationsabhängige Experimente mit in-situ Absorptions- und Photolumineszenz- (PL) Messungen durchgeführt. Es konnte gezeigt werden, dass zeitgleich mit der Aggregation eine Bande bei 800 nm in der Absorption entsteht. Diese ist auf π-Orbital-Wechselwirkungen zwischen planar zueinander angeordneten Polymerketten zurückzuführen.[17] Die Absorption und PL von klassischen konjugierten Polymeren, wie P3HT oder MEH-PPV, wurde schon früher von Spano et al.[7–9] mithilfe des Franck-Condon-Prinzips beschrieben. In dieser Arbeit wurde das Franck-Condon-Prinzip, soweit mir bekannt, zum ersten Mal auf ein konjugiertes Donor-Akzeptor-Copolymer angewendet. Es konnte gezeigt werden, dass die in Lösung und während der Aggregation gemessenen Absorptions- und PL-Spektren sehr gut von diesem Modell beschrieben werden können. Im Vergleich zu konjugierten Polymeren ohne Donor-Akzeptor-Einheiten musste keine zusätzliche H- oder J-Aggregation bei der Beschreibung der Spektren beachtet werden. [10, Scharsich und Fischer et al. 2015]

Von den Arbeiten in Lösung ausgehend wurden dünne Polmyerfilme durch Schleuderbeschichtung aus verschiedenen Lösungsmitteln mit und ohne Zusatz des Additivs 1,8-Diiodooktan hergestellt und deren optische und morphologische Eigenschaften untersucht. [11, Fischer et al. 2013] Einen starken Einfluss auf die Filmbildung hatte die Siedetemperatur des Lösungsmittels. So konnten aus tief siedenden Lösungsmitteln, wie z.B. CS_2, überwiegend amorphe Filme hergestellt werden, wohingegen mit steigendem Siedepunkt Aggregate von ca. 40 nm Durchmesser im AFM und TEM beobachtet wurden. Für das Lösungsmittel mit dem höchsten Siedepunkt, 1-Chlornaphthalin, wurde eine Überstruktur mit mikrometerlangen Fibrillen beobachtet. Diese schienen, wie aus AFM-Bildern erkennbar, aus den oben genannten 40 nm-Aggregaten aufgebaut zu sein.

Anschließend wurde Lösungsmitteldampftempern verwendet, um amorphe Filme zu rekristallisieren und Sphärolithe von bis zu 40 µm Durchmesser herzustellen. DSC-Messungen zeigten für diese Proben einen Schmelzpunkt bei ca. 280 °C und bestätigten damit die deutlich höhere Kristallinität im Vergleich zu den durch Schleuderbeschichtung hergestellten Filmen. [12, Fischer et al. 2015]

Einen Vorschlag für eine erste vorläufige Kristallstruktur wurde aus TEM/ED- und GIWAXS-Daten der in Lösungsmitteldampf getemperten Proben entwickelt. Überraschenderweise wurde anstelle einer für konjugierte Polymere typischen lamellaren Struktur eine

Dimer-Struktur gefunden. In dieser lagern sich jeweils zwei Polymerketten planar zu einem Dimer zusammen. Zwei solche Dimere bilden jeweils eine orthorhombische Einheitszelle, wobei sich die Dimere quasi-hexagonal anordnen. [12, 13, Fischer et al. 2015] Des Weiteren konnten durch Schleuderbeschichtung aus Lösungen mit zwei Prozent DIO Filme mit einer für konjugierte Polymere typischen lamellaren Struktur hergestellt werden. In dieser finden sich im Gegensatz zur Dimer-Struktur weitreichende π–π-Wechselwirkungen zwischen parallel gestapelten Ketten.

Die Energien der Grenzorbitale sowohl von den reinen Polymeren als auch von Mischungen (Blends) aus Si-PCPDTBT und Fullerenen wurden mittels Elektrochemie bestimmt. Durch die Kopplung von in-situ UV/Vis-Spektroskopie mit Cyclovoltammetrie (CV) war es nicht nur möglich die Redoxpotentiale der einzelnen Materialien und der Mischungen zu bestimmen, sondern auch die einzelnen Redoxreaktionen bestimmten Materialphasen in den Mischungen zuzuordnen. Auffällig bei diesen Messungen war, dass eine Stabilisierung der LUMOs in den Mischungen stattfand. In Zusammenarbeit mit S. Albrecht aus der Gruppe von Prof. Neher (Potsdam) wurden die Elektrochemie-Daten dazu verwendet am Beispiel von Si-PCPDTBT/Fulleren-Blends den Mechanismus der auffällig effizienten Ladungsträgerseparation an der Polymer/Fulleren-Grenzfläche zu untersuchen. [14, Albrecht und Fischer et al. 2014]

Die Möglichkeit, zwei verschiedene Strukturen mit und ohne weitreichende π-Orbital-Wechselwirkungen in dünnen Filmen herzustellen, wurde anschließend dazu verwendet, ihren Einfluss auf OFET und Doppelschicht-Solarzellen zu untersuchen. [12, 14, Fischer und Albrecht et al. 2014] In den OFET wurde eine um ca. eine Zehnerpotenz höhere Ladungsträgermobilität in der Struktur mit weitreichenden π-Orbital-Wechselwirkungen im Vergleich zur Dimerstruktur festgestellt. In Analogie zu P3HT wurde vermutet, dass in den Filmen mit den π-Orbital-Wechselwirkungen ein zweidimensionaler Ladungstransport entlang der Polymerketten und den π-Orbitalen stattfindet. Bezüglich der Dimerstruktur hingegen kann vermutet werden, dass der schnelle Ladungstransport ausschließlich entlang der Polymerketten erfolgt. Der Transport senkrecht dazu wird durch die Alkylketten zwischen den Dimern verhindert bzw. verlangsamt. Von P3HT ist aber bekannt, dass ein zweidimensionaler Ladungstransport für eine hohe Ladungsträgermobilität über makroskopische Distanzen notwendig ist. [15, 16, Fischer und Crossland et al. 2011/2012]

In organischen Doppelschicht-Solarzellen wurden dieselben Morphologien wie in den OFET verglichen. Überraschenderweise wurde keine erhöhte Effizienz in den Zellen mit den höheren Ladungsträgermobilitäten festgestellt. Stattdessen zeigten alle Experimente (Strom-Spannungs-Kurven, EQE und TDCF) keine bemerkenswerten Unterschiede zwisch-

en den Solarzellen mit den unterschiedlichen Morphologien. Es wurde vermutet, dass der Grund hierfür bei den aufgedampften C_{60}-Akzeptorschichten liegt. Diese sind so gute Elektronenleiter, dass von allen generierten freien Ladungen die Elektronen schnell zur entsprechenden Elektrode abgeführt werden können. Es kann vermutet werden, dass dadurch die unterschiedlichen Ladungsträgermobilitäten in der Polymerschicht ohne Einfluss auf die Rekombinationswahrscheinlichkeit bleiben.

Diese Arbeit zeigt zusammenfassend eine systematische Untersuchung der Struktur-Eigenschaftsbeziehungen von Donor-Akzeptor-Copolymeren anhand dreier representativer Polymere: PCPDTBT, F-PCPDTBT, Si-PCPDTBT. Es konnte eine direkte Korrelation zwischen den optischen Eigenschaften und der Bildung von Aggregaten hergestellt und die Änderung der Absorptions- und PL-Spektren während der Aggregation mithilfe des Franck-Condon-Prinzips modelliert werden. Durch die Optimierung verschiedener Prozessierungs- und Tempermethoden, wie z.B. des Lösungsmitteldampftemperns, wurden verschiedene Polymorphe hergestellt. Anhand TEM/ED- und GIWAXS-Daten wurde eine erste Kristallstruktur vorgeschlagen. Die Möglichkeit, verschiedene Polymorphe in dünnen Filmen gezielt herzustellen, wurde abschließend verwendet um den Einfluss der unterschiedlichen Strukturen auf die Ladungsträgermobiltät und die Leistung von Solarzellen zu untersuchen.

Publications

In Preparation:

- F. S. U. Fischer, G. L. Schulz, D. Trefz, A. Melnyk, M. Brinkmann, D. Andrienko, S. Ludwigs *A family of PCPDTBT derivatives: correlations between polymer morphology and transport properties in organic field-effect transistors*, **2015**, submitted.

Scientific Papers:

- F. S. U. Fischer, N. Kayunkid, D. Trefz, S. Ludwigs, M. Brinkmann, *Structural models of PCPDTBT and F-PCPDTBT with branched side chains: impact of a single fluorine atom on the crystal structure of a conjugated polymer*, Macromolecules **2015**, 48, 3974.
- F. S. U. Fischer, D. Trefz, J. Back, N. Kayunkid, B. Tornow, S. Albrecht, K. Yager, G. Singh, A. Karim, D. Neher, M. Brinkmann, S. Ludwigs, *Highly Crystalline Films of PCPDTBT with Branched Side Chains by Solvent Vapor Crystallization: Influence on Opto-Electronic Properties*, Adv. Mater. **2015**, 27, 1223.
- C. Scharsich, F S. U. Fischer, K. Wilma, R. Hildner, S. Ludwigs, A. Köhler, *Revealing structure formation in PCPDTBT by optical spectroscopy*, Polymer Physics B **2015**, 53, 1416.
- D. Di Nuzzo, D. Viola, F. S. U. Fischer, Giulio Cerullo S. Ludwigs, E. Da Como, *Enhanced photo-generation of polaron pairs in neat semicrystalline donor-acceptor copolymer films via direct excitation of interchain aggregates*, J. Phys. Chem. Lett. **2015**, 6, 1196.
- S. Albrecht, K. Vandewal, J. R. Tumbleston, F. S. U. Fischer, J. D. Douglas, J. M. J. Fréchet, S. Ludwigs, H. Ade, A. Salleo, D. Neher, *On the efficiency of charge transfer state splitting in polymer:fullerene solar cells*, Adv. Mater. **2014**, 26, 2533.
- K. Tremel, F. S. U. Fischer, N. Kayunkid, R. Di Pietro, R. Tkachov, A. Kiriy, D. Neher, S. Ludwigs, M. Brinkmann, *Charge Transport Anisotropy in Highly Oriented Thin Films of the Acceptor Polymer P(NDI2OD-T2)*, Adv. Energy Mater. **2014**, 4, 1301659.
- F. S. U. Fischer, K. Tremel, A.-K. Saur, S. Link, N. Kayunkid, M. Brinkmann, D. Herrero-Carvajal, J. T. L. Navarrete, M. C. R. Delgado, S. Ludwigs, *Influence of*

Processing Solvents on Optical Properties and Morphology of a Semicrystalline Low Bandgap Polymer in the Neutral and Charged States, Macromolecules **2013**, 46, 4924.

- E. J. W. Crossland, K. Tremel, F. S. U. Fischer, K. Rahimi, G. Reiter, U. Steiner, S. Ludwigs, *Anisotropic charge transport in spherulitic poly(3-hexylthiophene) films*, Adv. Mater. **2012**, 24, 839.

- F. S. U. Fischer, K. Tremel, M. Sommer, E. J. W. Crossland, S. Ludwigs, *Directed crystallization of poly(3-hexylthiophene) in micrometre channels under confinement and in electric fields*, Nanoscale **2012**, 4, 2138.

Oral Presentations:

- F. S. U. Fischer, K. Tremel, M. Brinkmann, E. J. C. Crossland and S. Ludwigs, *Induced in-plane orientation of poly(3-hexylthiophene) chains by controlled crystallization, 24th International Liquid Crystal Conference*, **2012**, Mainz.

- F. S. U. Fischer, S. Ludwigs, *Influence of processing solvents and additives on PCPDTBT morphology and optical properties in the neutral and charged states, MRS Fall Meeting*, **2013**, Boston.

- F. S. U. Fischer, M. Brinkmann, S. Ludwigs, *Large scale orientation by crystallizing PCPDTBT under confinement*, MRS Spring Meeting, **2014**, San Francisco.

Poster Presentations

- F. U. S. Fischer, K. Tremel, E. J. W. Crossland, S. Ludwigs, *Controlled crystallization and alignment of polythiophenes*, SPP-1355 PhD-Workshop, **2012**, Würzburg.

- F. U. S. Fischer, K. Tremel, C. R. Delgado, M. Brinkmann, S. Ludwigs, *Influence of processing solvents on PCPDTBT morphology and optical properties in the neutral and charged state.* E-MRS Spring Meeting, **2013**, Strasbourg.

- F. S. U. Fischer, K. Tremel, A.-K. Saur, M. Plachetta, M. Brinkmann, J.T. López Navarrete M.C. Ruiz Delgado, S. Ludwigs, *Controlled crystallization and alignment of conjugated polymers*, SPP-1355 Spring School, **2013**, Dresden. - SPP1355 Spring School Poster Prize 2013.

- F. S. U. Fischer, B. Tornow, S. Albrecht, N. Kayunkid, D. Neher, M. Brinkmann, and S. Ludwigs, *Highly Crystalline Films of PCPDTBT by Solvent Vapor Crystallization*, SPP-1355 Meeting, **2015**, Bad Honnef.
- F. S. U. Fischer, B. Tornow, S. Albrecht, N. Kayunkid, D. Neher, M. Brinkmann, and S. Ludwigs, *Highly Crystalline Films of PCPDTBT by Solvent Vapor Crystallization*, 42$^{\text{nd}}$ German Liquid Crystal Conference, **2015**, Stuttgart.

Danksagung

Diese Arbeit entstand an der Universität Stuttgart am Institut für Polymerchemie im Zeitraum von 2011 bis 2015. Insbesondere fachliche Diskussionen und wissenschaftliche Kooperationen mit einer Vielzahl von Personen haben wesentlich zum Gelingen dieser Arbeit beigetragen. Ich möchte mich daher bei allen Personen, welche zum Entstehen dieser Arbeit in der ein oder anderen Art und Weise beigetragen haben, bedanken.

Prof. Dr. Sabine Ludwigs danke ich ganz besonders für die Aufnahme in den Arbeitskreis und die Bereitstellung des spannenden Themas meiner Promotion. Mit ihrer eigenen Begeisterung für das Thema motivierte sie mich, in den Bereich der konjugierten Polymere einzusteigen und ließ mich frei und selbstständig arbeiten. Ich möchte mich auch für die unzähligen Diskussionen, guten Arbeitsbedingungen und insbesondere für die Möglichkeit einer so interdisziplinären Arbeit mit vielen verschiedenen Kooperationspartnern bedanken.

Prof. Dr. Joris van Slageren danke ich für die freundliche Übernahme des Mitberichtes.

Bei *Prof. Dr. Frank Gießelmann* bedanke ich mich für die Übernahme des Prüfungsvorsitzes und für die Möglichkeit, das Nanostar für WAXS-Messungen nutzen zu dürfen.

Dr. Martin Brinkmann und *Dr. Navaphun Kayunkid* möchte ich für die spannende Kooperation und für die gute Betreuung während meiner Aufenthalte in Straßburg danken. Ich danke beiden auch für die vielen fachlichen Diskussionen, die mich immer wieder inspirierten, die unzähligen TEM/ED-Messungen und für die unermüdliche Hilfe bei der Auswertung der TEM/ED-Daten.

Prof. Dr. Dieter Neher danke ich für die gute Zusammenarbeit innerhalb der zwei Solarzellen-Projekte und für die fachlichen Diskussionen. Ich danke auch *Dr. Steve Albrecht* und *Benjamin Tornow* für die Hilfe bei den Solarzellen-Messungen, für die fachlichen Diskussionen und für die angenehme Atmosphäre während meines Aufenthalts in Potsdam.

Prof. Dr. Alamgir Karim und *Dr. Gurpreet Singh* danke ich für die gute Zusammenarbeit bei den GIWAXS-Messungen. Ganz besonders möchte ich hierbei auch *Dr. Kevin G. Yager* für die Messungen an der Beamline und für die Hilfe bei der Auswertung der Daten danken.

Prof. Dr. Anna Köhler danke ich für die Zusammenarbeit bei der temperaturabhängigen Spektroskopie. Ich danke auch *Christina Scharsich* für die Absorptions- und PL-Messungen, die langen fachlichen Diskussionen und für die angenehme Zusammenarbeit während meiner beiden Aufenthalte in Bayreuth.

Bei den Theoretikern vom MPI in Mainz *Dr. Denis Andrienko*, *Dr. Björn Baumeier*, *Anton Melnyk* und *Jens Wehner* möchte ich mich für die gute Zusammenarbeit, für fachlichen Diskussionen und viele theoretische Berechnungen bedanken.

Dr. Carmen Ruiz Delgado danke ich für die DFT-Rechnungen und für die fachlichen Diskussionen während ihrer Besuche in Stuttgart.

Frau *Dr. habil. Silvia Janietz* danke ich für die Bereitstellung des F-PCPDTBT-Polymers.

Bei *Prof. Dr. Harald Giessen* möchte ich mich dafür bedanken, dass ich regelmäßig das Rasterelektronenmikroskop verwenden durfte.

Ganz besonders danke ich meinem Forschungspraktikanten, späteren Masterstudenten und jetzigen Kollegen *Daniel Trefz* für eine sehr produktive, immer engagierte Zusammenarbeit und für die vielen fachliche Diskussionen. Daniels Unterstützung im Labor war von großem Wert für diese Arbeit.

Ich danke *Dr. Adrian Ruff* für die gute Zusammenarbeit und für die vielen Hilfestellungen in der Elektrochemie. Seine guten Ratschläge und seine Unterstützung motivierten mich auch, das langwierige Projekt der Elektrochemie erfolgreich abzuschließen.

Schon während meiner Diplomarbeit in Freiburg durfte ich mit *Dr. Ed Crossland* und *Dr. Kim Tremel* zusammenarbeiten. Ich danke beiden für die vielen Einführungen, Ratschläge und für die immer sehr gute Atmosphäre. Kim danke ich auch für die sehr gute, nie langweilige Zusammenarbeit in Stuttgart.

Danken möchte ich auch *Dr. Christoph Braun* und *Dr. Steffen Link*, die mich von meinem Forschungspraktikum bis hin zur Promotion mit Rat und Tat und viel guter Laune unterstützten und mich für die Arbeit mit konjugierten Polymeren begeisterten. Mein besondere Dank gilt auch *Martin Scheuble* für viele Diskussionen, Hilfen im Labor und ganz besonders für die sehr gute Atmosphäre und die Zusammenarbeit über die gesamten letzten Jahre. *Miriam Goll* und *Justus Back* danke ich für unzählige fachliche Diskussionen und für die gute Atmospähre im Arbeitskreis.

Ich danke *Dr. Klaus Dirnberger* für die vielen fachlichen Anregungen und Diskussionen und für die Unterstützung bei allen organisatorischen Hürden.

Beatrice Omiecienski danke ich für die großartige Unterstützung im Labor und insbesondere für die unermütliche Hilfe beim Aufbau neuer Laborgeräte und für die vielen Gänge in die Werkstatt.

Corinne Rost-Schmidt und *David Freytag* danke ich für die unzähligen kleinen Hilfen im Labor.

Ganz besonders danke ich auch den Master-Studenten *Martin Plachetta, Matthias Jasch* und *Daniel Trefz*, der Bachelor-Studentin *Heike Strumberger* und der Forschungspraktikantin *Clarissa Dietrich* für die gute Zusammenarbeit.

Den beiden wissenschaftlichen Hilfskräften *Simon Tannert* und *Sebastian Jobst* danke ich für die unzähligen Stunden am Computer, in denen sie Skripte verbesserten oder gleich ganz neu erfanden.

Mein besonderer Dank gilt auch der *Werkstatt des Instituts für Physikalische Chemie*, insbesondere *Thomas Fischer*, für die Anfertigung zahlreicher Aufbauten.

Anke Schrogl danke ich für die organisatorische Hilfe bei Formularen aller Art und ihrer immer gute Laune.

Ich danke auch allen aktuellen und ehemaligen Mitgliedern des Arbeitskreises und den vielen Menschen, die ich im Rahmen meiner Kooperationen und Konferenzbesuche getroffen habe und die mich durch fachliche Diskussionen inspiriert haben. Die gute Atmosphäre und große Hilfsbereitschaft des Arbeitskreises motivierten mich immer wieder. Insbesondere bei meinen ehemaligen Bürogenossen *Alexander Zoller, Angela Holst, Dr. Anna Sophia Schenk, Dr. Christoph Braun, Christian Rothe, Daniel Trefz, Erna Muks*, *Justus Back*, *Martin Scheuble* und *Sebastian Jobst* möchte ich mich für ein immer gutes Büroklima bedanken.

Meiner Familie, insbesondere meinen Eltern, möchte ich dafür danken, dass sie mir das Chemiestudium ermöglichten und mich immer und in jeder Hinsicht unterstützen.

Ganz besonders möchte ich meiner Freundin Lena Baron für das Korrekturlesen zahlreicher Texte, der Hilfe bei mathematischen Problemen und der Unterstützung während des gesamten Studiums und der Promotion danken.

Nomenclature

ϵ	polarity
μ	field effect mobility
1-CN	1-chloronaphthalene
6T	α-sexithiophene
$TBAPF_6$	tetrabutylammonium hexafluorophosphate
$THAPF_6$	tetrahexylammonium hexafluorophosphate
AFM	atomic force microscopy
AM 1.5G	air mass coefficient 1.5 global
BF	bright field
bp.	boiling point
BT	benzothiadiazole
C12-pBTTT	poly(2,5-bis(3-dodecyl-2-yl)-thieno[3,2-b]thiophene)
CB	chlorobenzene
CNRS	Centre national de la recherche scientifique
CPDT	cyclopentadithiophene
CT	charge transfer
DCB	1,2-dichlorobenzene
DFT	density functional theory
DI	deionized
DIO	1,8-diiodooctane
DPSQ	2,4-bis[4-(N,N-diphenylamino)-2,6-dihydroxy-phenyl] squaraine
DSC	differential scanning calorimetry
ECE	energy conversion efficiency
ED	electron diffraction
EQE	external quantum efficiency
F-PCPDTBT	poly[2,6-(4,4-bis-(2-ethylhexyl)-4H-cyclopenta[2,1-b;3,4-b']dithiophene)-*alt*-4,7-(5-fluoro-2,1,3-benzothiadiazole)]
FC	Franck-Condon
Fc	ferrocen
FF	fill factor
GIWAXS	gracing incidence wide angle X-ray scattering
HOMO	highest occupied molecular orbital
HT	head-to-tail

HT-GPC ..... high temperature gel permeation chromatography
ICBA ..... indene-C_{60} bisadduct
ICMA ..... indene-C_{60} monoadduct
ICS ..... Institut Charles Sadron
ICTA ..... indene-C_{60} trisadduct
IMPS ..... Frauenhofer Institut for Photonic Microsystems
IPOC ..... Institut für Polymer Chemie
ITO ..... indium tin oxide
J-V-curve ..... current-voltage-curve
L ..... channel length
LUMO ..... highest unoccupied molecular orbital
M_n ..... number average molecular weight
M_w ..... weight average molecular weight
MeCN ..... acetonitrile
MEH-PPV ..... poly[2-methoxy-5-(2'-ethylhexyloxy)-p-phenylene vinylene]
MTHF 2-methyltetrahydrofuran
NDI ..... naphthalene diimid
NEXAFS ..... near edge X-ray absorption fine structure
NIR ..... near infrared
OC ..... open circuit
ODT 1,8-octanedithiol
OFET ..... organic field effect transistors
OLED ..... organic light emitting diode
P(NDI2OD-T2) poly[N,N'-bis(2-octyldodecyl)-1,4,5,8-naphthalene-dicarboximide-2,6-diyl]-*alt*-5,5'-(2,2'-bithiophene)
P-SoXs ..... resonant polarized soft X-ray scattering
P3AT ..... poly(3-alkylthiophene)
P3HT ..... poly(3-hexylthiophene)
PA ..... polyacetylene
PCBM ..... [6,6]-phenyl-C_{61}-butyric acid methyl ester
PCE ..... power conversion efficiency
PCM ..... polarizable continuum model
PCPDTBT ..... poly[2,6-(4,4-bis-(2-ethylhexyl)-4H-cyclopenta [2,1-b;3,4-b'] dithiophene)-*alt*-4,7-(2,1,3-benzothiadiazole)]
PDI ..... polydispersity

PDS ..... sensitive photo thermal deflection spectroscopy
PEDOT ..... poly(3,4-ethylenedioxythiophene)
PFO ..... polyfluorenes
PMMA ..... poly(methyl methacrylate)
POM ..... polarized optical microscope
PPP ..... poly(*p*-phenylene)
PPV ..... poly(*p*-phenylene vinylene)
PSS ..... polystyrene sulfonate
PTFE ..... polytetrafluoroethylene
RT ..... room temperature
SAED ..... selected area electron diffraction
SC ..... short circuit
Si-PCPDTBT .. poly[(4,4'-bis(2-ethylhexyl)dithiene-[3,2-b:2',3'-d]silole)-*alt*-4,7- (2,1,3-benzothiadiazole)]
Si-wafer ..... silicon wafer
SiO_x ..... silicon oxide
T2 ..... bithiophene
TCB 1,2,4-trichlorobenzene
TDCF ..... time delayed collection field
TDDFT ..... time-dependent density functional theory
TEM ..... transmission electron microscopy
TGA ..... thermal gravimetric analysis
THF ..... tetrahydrofuran
TM ..... unregistered trade mark
UV/Vis ..... ultraviolet/visible
VB ..... valance band
W ..... channel width
w% ..... weight percent

1 Introduction

The discovery of semi-conducting polymers has started with polyacetylene and the work of Shirakawa, Heeger and MacDiarmid,[18–20] which was acknowledged by a Nobel Price in 2000.[21–23] Since then new and more complex conjugated polymers have been synthesized mainly for the use in organic electronics devices such as organic solar cells, organic field effectors (OFETs), organic light emitting diodes (OLED) or thermoelectric generators.

The fast development of new chemical structures was mainly motivated by the goal to increase the performance of optoelectronic devices making them competitive to inorganic ones. New structures going from polyacetylene to aromatic and further to thiophene based systems improved the energy levels and absorption properties. A key factor for this development was the feedback from fundamental studies investigating the structure-function relationships and device performance of conjugated polymers. The electronic, optical and structural properties were investigated employing mainly spectroscopic, electrochemical and microscopic techniques.[24] From the perspective of the device optimization further feedback was given and beside the pure synthetic approach also the optimization of the morphology was considered. The inter- and intrachain interactions of the polymer backbones which influence not only the absorption properties but also the charge carrier mobility became a key role in the device engineering.[7,8,15,16,25,26]

For many years now poly(3-hexylthiophene) (P3HT) has been considered as the work-horse of the organic solar cell community and is probably the best known and investigated conjugated polymer. It was used to make many principle statements regarding structure-function relationships and will be introduced in more detail in chapter 1.2. In the recent years the synthetic effort to increase the performance of conjugated polymers led to a new generation of so called donor-acceptor or low band gap copolymers. These polymers show very promising efficiencies in organic solar cells mainly due to their small band gaps and good charge separation efficiencies in organic solar cells with fullerenes or n-type polymers as acceptor phase.[14,27,28] The small band gap leads to a red shift of the absorption and thereby better coverage of the solar spectrum and increased light harvesting. Today donor-acceptor copolymers are the state of the art materials used in high performance polymer based organic solar cells.

In this thesis the basic optoelectronic properties of donor-acceptor copolymers were studied on the example of the prominent and high performance donor-acceptor copolymer PCPDTBT (poly[2,6-(4,4-bis-(2-ethylhexyl)-4H-cyclopenta [2,1-b;3,4-b']dithiophene)-*alt*-4,7(2,1,3-benzothiadiazole)]) and its derivatives, figure 1.1. PCPDTBT was first introduced

by Brabec et. al[2] in 2006 and up to today more than 500 publications regarding this polymer and its derivatives have been published. Most publications focused on the PCPDTBT/fullerene blends neglecting the pure polymer. Therefore little is known about its crystal structure and mesoscopic morphology and how they influence the optoelectronic properties. Si-PCPDTBT and F-PCPDTBT, compare figure 1.1, are two well known derivatives and will be discussed and compared together with PCPDTBT throughout this thesis.

This thesis starts with the investigation of the very basic properties as absorption spectra in solution and thin film formation which is followed by a detailed crystal structure and electrochemical analysis. Finally the fabrication of organic field effect transistors and solar cells is described and the earlier gained knowledge on the optical and structural properties is used to correlate and understand the influence of the morphology on the device performance.

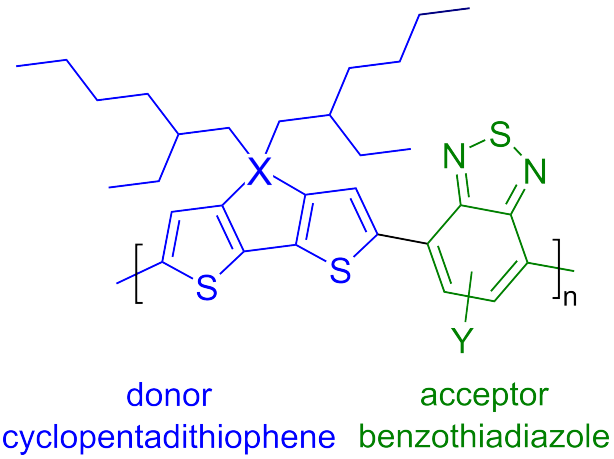

Fig. 1.1: Chemical structure of the donor-acceptor copolymer PCPDTBT (X = C, Y = H) and its derivatives Si-PCPDTBT (X = Si, Y = H) and F-PCPDTBT (X = C, Y = F).

1.1 Fundamentals of Conjugated Polymers

Before we consider the class of donor-acceptor polymers a basic understanding on how the conductivity in aromatic conjugated polymers is achieved and why conjugated polymers can be used today as materials for organic solar cells, organic field effect transistors (OFETs), organic light emitting devices (OLEDs) or thermoelectric generators. The main reason therefore lies in their electronic structure. An overview over some selected chemical structures in the order of their development is shown in figure 1.2. It starts with the first known conjugated polymer polyacetylene (PA) and the shortly afterwards prepared

aromatic structures such as poly(*p*-phenylene) (PPP) and poly(*p*-phenylene vinylene) (PPV). The last four structures show the next generation of conjugated polymers with thiophene based backbones such as poly(3-hexylthiophen-2,5-diyl) (P3HT) or poly(3,4-ethylenedioxythiophene) (PEDOT) and the state of the art donor-acceptor copolymers such as poly[N,N'-bis(2-octyldodecyl)-1,4,5,8-naphthalene-dicarboximide-2,6-diyl]-*alt*-5,5'-(2,2'-bithiophene) (P(NDI2OD-T2)) and PCPDTBT.

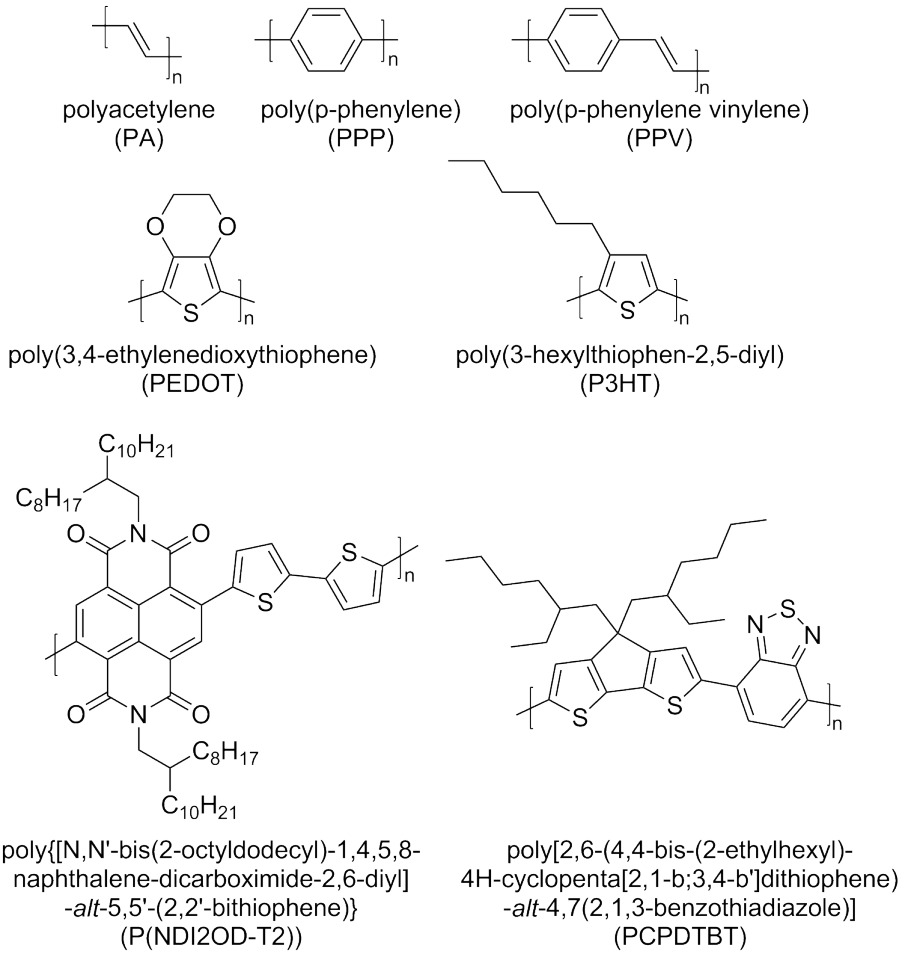

Fig. 1.2: A small selection of typical conjugated polymers as they were developed over the last decades.

The orbitals of the conjugated monomers in an organic polymer backbone can, similar as in a crystal, interact with their next neighbors forming new electron bands as shown schematically on the left in figure 1.3A.[29] In an all conjugated polymer chain the highest occupied molecular orbital (HOMO) and the lowest unoccupied molecular orbital (LUMO) form the so called valence band (VB) and conducting band (CB), respectively, figure 1.3A. The gap between the HOMO and LUMO is an intrinsic property of a material and is called electronic band gap (E_g). If the band gap range is between 0 and 3 eV the material

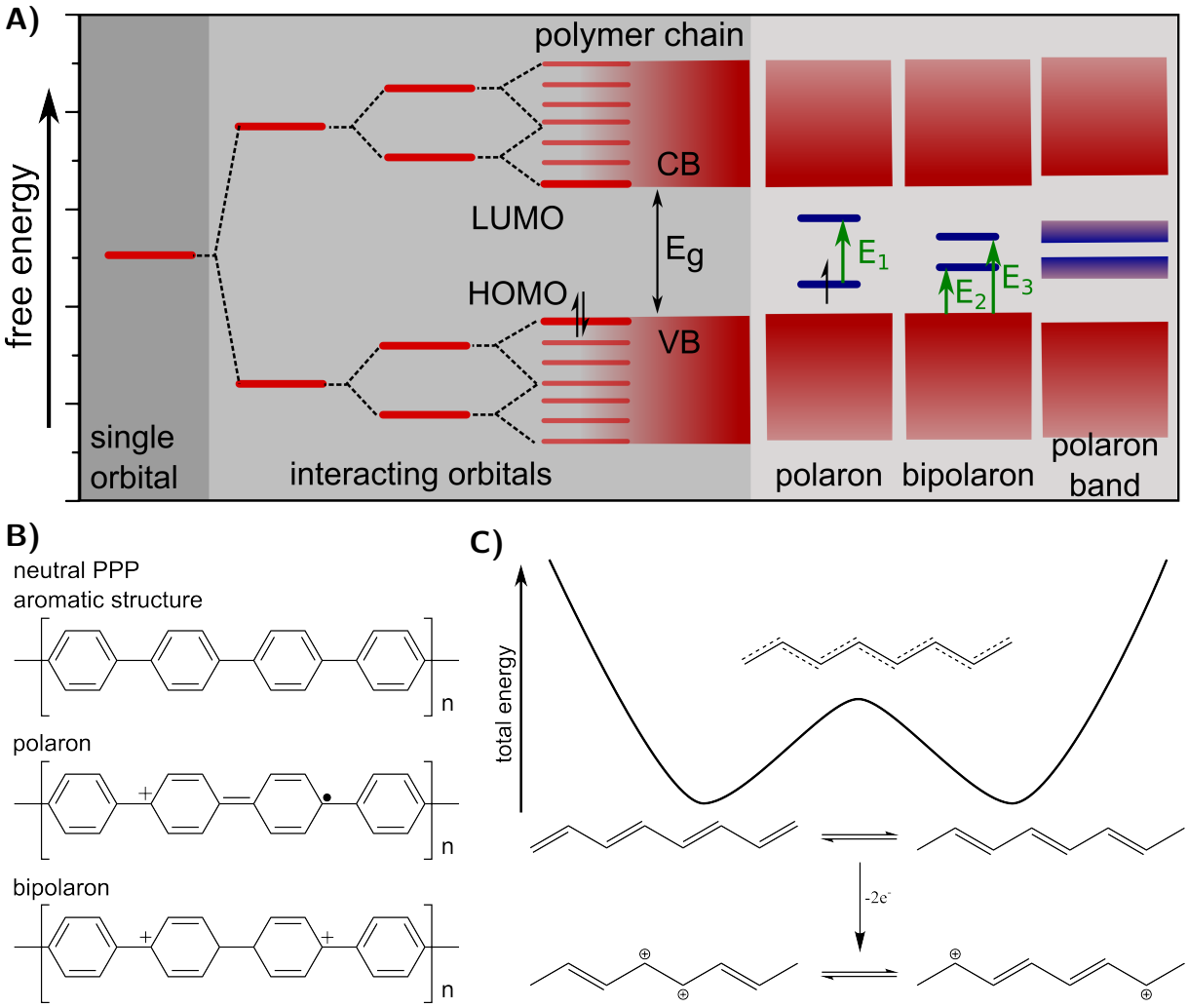

Fig. 1.3: A) Schematic of the electronic structure in conjugated polymers going from a single orbital (left) to an electronically coupled polymer chain forming a valence (VB) and a conducting (CB) band. The right side shows the formation of a polaron band starting with a single polaron, adapted from [29, Rehahn 2003]. **B)** Chemical structure of the neutral, polaron and bipolaron of poly(*p*-phenylene vinylene) (PPV) relaxed in a localized quinoid structure formed by oxidation. **C)** Energy curve for an infinite *trans*-polyacetylene showing the two possible geometrical structures. After oxidation, removing two electrons, two solitons are formed which can move independently along the polymer chain without changing the overall energy.

is considered a semiconductor, as it is the case for most conjugated polymers. This means that only if enough energy is added for an electron to transfer from the VB into the CB, by e.g. temperature or irradiation, the material becomes conductive.[29]

Typically conductivity in conjugated polymers is induced by p- (n-) type doping, meaning an oxidation (reduction) of the polymer by chemical or electrochemical doping. In the case of aromatic conjugated polymers the first oxidation (reduction) leads to a polaron formation. The charge is localized on the polymer chain due to a relaxation into a quinoid-like structure, figure 1.3B, and a single occupied molecular orbital (SOMO) is formed,

polaron figure 1.3A. When a second electron is taken out from the chain a bipolaron with an even more quinoid-like structure is formed, bipolaron figure 1.3B. Comparing the formation of two polarons against one bipolaron it was shown that a bipolaron is energetically favored because the polymer chain around the quinoid structure can relax into its aromatic form. In the orbital picture the bipolaron bands are moved closer together and thereby further away from the VB and CB edges, figure 1.3A. For high doping levels polaron bands as shown on the right in figure 1.3A are formed and lead to conduction along the polymer chains.[30]

A closer look at the new orbital structure of the doped polymer chain reveals that additional optical transitions occur, figure 1.3A (green arrows). In a positively charged polaron or bipolaron (p-type) three new transitions are possible: between the two polaron bands (E_1) and from the VB to the lower (E_2) and higher (E_3) bipolaron level.

After high conductivities of up to 10^5 S/cm and band gaps of around 1.5 eV had been found in *trans*-polyacetylene (PA) high performance organic electronics had been expected to be introduced within years.[31] New promising conjugated polymers with an aromatic structure such as poly(p-phenylene) (PPP) or poly(p-phenylene vinylene) (PPV) were synthesized. Surprisingly, large band gaps of around 3 eV were measured and it became clear that the high mobility and low band gap of *trans*-polyacetylene is due to its unique electronic structure.[31] The Peierls distortion allows *trans*-PA to form two geometric structures with a single/double bond alternation. Both correspond to exactly the same total energy as schematically shown in figure 1.3C. Therefore all conjugated bonds in *trans*-PA are indistinguishable and when PA is twice oxidized the two charges on the polymer backbone can move freely along the polymer chain (soliton). In contrast to the above discussed aromatic conjugated polymers no localized bipolaron with a quinoid-like structure is formed.[30]

With this in mind the lower mobility in aromatic conjugated polymers can be understood. Comparing the quinoid with the aromatic structure it is obvious that the aromatic one is more stable which leads to a localization of the charges on the polymer chain. The charged polymer chain relaxes therefore and resumes its aromatic geometry around the quinoid structure, figure 1.3B. This leads to a reduced charge transport since the charges can not, as in PA, move freely along the polymer chain. This further explains the larger band gap in the aromatic conjugated polymers since the formation of a polaron (oxidation) requires a less stable quinoid structure.

1.2 P3HT – the Working-Horse of the Solar Cell Community

The observation that the high aromaticity in the phenylene based polymers increases the band gap led to the first synthetic improvement of the chemical structure. The phenylene rings were substituted by less aromatic thiophenes, figure 1.2. The smaller energetic difference to the quinoid structure results in a smaller band gap and increases the charge carrier mobilities. Further the 5-ring allows a smaller torsional angle than a phenylene ring which leads to a more planar structure with a better conjugation and therefore a further decreased band gap.[24]

1.2.1 Synthetic Approaches

The first polythiophenes were synthesized by the groups of Yamamoto,[32] Dudek[33] and others[34–36] adopting the Kumada cross-coupling reaction[37,38] and resulted in small molecular weights. From those only the smallest molecular weight fractions were soluble and it was impossible to perform any deeper studies of the energy levels or to build electrical devices. In 1983 Yamamoto et al.[39] discovered that they could improve the solubility of polythiophenes by adding methyl-side chains at the β-position. This was followed by the synthesis of a series of poly(3-alkylthiophenes) (P3ATs) with varying alkyl side chain lengths and led to the new class of highly soluble and stable P3ATs.[40–42] Even though these P3ATs were highly soluble and stable they still showed a relatively large band gap and low charge carrier mobilities.[43,44] The next optimization was introduced again by a synthetic approach. P3ATs of high regioregularity with pure head-to-tail (HT) linkages between the 3-alkylthiophene units were synthesized, figure 1.4. This was necessary since in irregular P3ATs the steric hindrance between neighboring alkyl chains increased the torsional angle between the thiophene units and minimized the planarization and conjugation lengths.[45] Further it was shown that the tendency to form aggregates and to crystallize is much higher for regioregular (HT) compared to regioirregular P3ATs.[44]

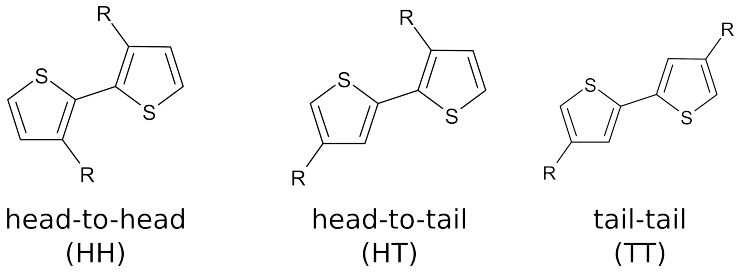

Fig. 1.4: Possible linkages between thiophene units in P3ATs (R = alkyl chain).

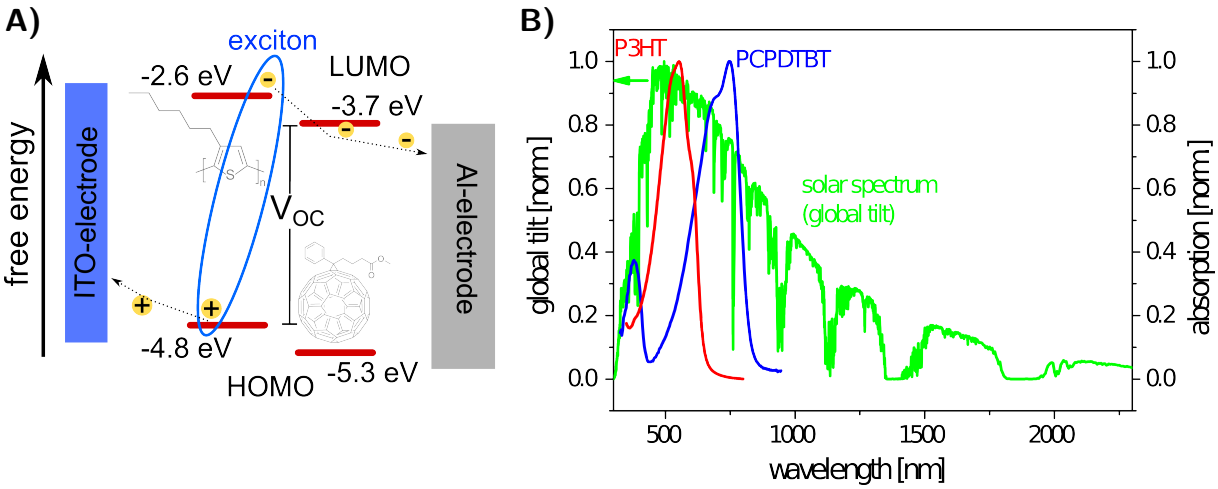

Fig. 1.5: A) Schematic of a basic energy diagram of a P3HT/fullerene solar cell, with the P3HT HOMO/LUMO values measured in our group (figure 1.7) and published in [50, p. 44]. The [6,6]-phenyl-C_{61}-butyric acid methyl ester (PCBM) energy values were measured during this thesis, chapter 5.1. **B)** Comparison between the solar spectrum (AM 1.5G spectra at global tilt from the American Society for Testing and Materials)[51] and the absorption of the conjugated polymer P3HT and the donor-acceptor copolymer, PCPDTBT.

The increased crystallinity additionally improved the performance in organic solar cells and OFETs and will be discussed in more detail in the next chapter.

The two best known thiophene based polymers which resulted from these findings are poly(3-hexylthiophene) (P3HT) and poly(3,4-ethylenedioxythiophene) (PEDOT), figure 1.2. Compared to the phenylene ring based polymers they showed increased conductivity of up to 10^3 S/cm and reduced band gaps of around 2 to 2.5 eV.[31]

1.2.2 Organic Solar Cells

In 1986 Tang et al.[46] first showed that excitons can be split into free charges by using a bilayer device of an electron-rich (donor) and an electron-poor (acceptor) material. Even though at this time efficiencies of only around 1 % were reported a new field of research was established. In 1995 it was discovered that using fullerenes as acceptor material in organic solar cells leads to very good charge separation.[47] In the following years many groups started to investigate organic solar cells using as donor material the often called "working horse polymer" P3HT and fullerenes as acceptor materials. Today the highest efficiencies found for P3HT/fullerene solar cells are around 5 %[48] which is an increase in efficiency by a factor of almost 5 compared to the beginning of organic photovoltaics. This extraordinary improvement was mainly based on material, morphology and device optimization. It should be pointed out that currently efficiencies of up to 12 % can be reached with donor-acceptor copolymers.[49]

Figure 1.5A. shows a very basic energy diagram which explains why P3HT/fullerene solar cells perform that well. After irradiation with light, which is mainly absorbed by the P3HT, excitons are formed (electron/hole pairs bound by coulombic forces). The excitons diffuse to the P3HT/fullerene interface and the energy difference between the LUMO of the P3HT and the fullerene acts as driving force to separate the excitons. Free charges are formed and transported to their respective electrodes. Hereby the maximum gained voltage of the solar cell (V_{OC}) is defined by the difference between the HOMO and LUMO of the donor and the acceptor, respectively. This simple picture already reveals the key factors which have to be optimized in an organic solar cell:

i) For good charge separation and a high V_{OC} the difference between HOMO/LUMO energies of the donor and acceptor materials has to be as large as possible. At the same time the offset between the two LUMOs must be large enough to still induce charge separation.

ii) After the exciton separation the free charges have to be transported to the respective electrodes before they can recombine. This is only possible if a high charge carrier mobility within the respective layers exists in the direction of the electrodes.

iii) A third important factor becomes evident from the solar spectrum in figure 1.5B. The solar spectrum has its main intensity between 400 to 1200 nm with a maximum around 700 nm. Comparing this with the absorption spectrum of P3HT (red) it is obvious that only a small portion of the possibly usable solar spectrum is absorbed. An optimized polymer should provide a smaller band gap and an absorption in a broader region of the solar spectrum such that as much photons as possible can be harvested. The decrease of the band gap should be obtained by decreasing the HOMO energy of the polymer, since a high LUMO is needed for a good charge separation due to the condition in i).

Influence of the Device Configuration

Independent of the pure phases the interfacial area between the donor and the acceptor materials must be optimized to allow an efficient charge separation for all generated excitons.[52,53] In a theoretically optimized active layer geometry there would be standing cylinders of one phase embedded in a matrix of the second (interdigitated structure). The domain spacings should be in the region of the exciton diffusion length which is typically around 10 nm for conventional conjugated polymers such as P3HT and below 10 nm for low band gap polymers, figure 1.6A.[54–56] Additionally, each electrode must be covered with the respective material sandwiching the cylindrical structure to avoid short circuits. Such a configuration is typically referred to as the perfect active layer morphology because

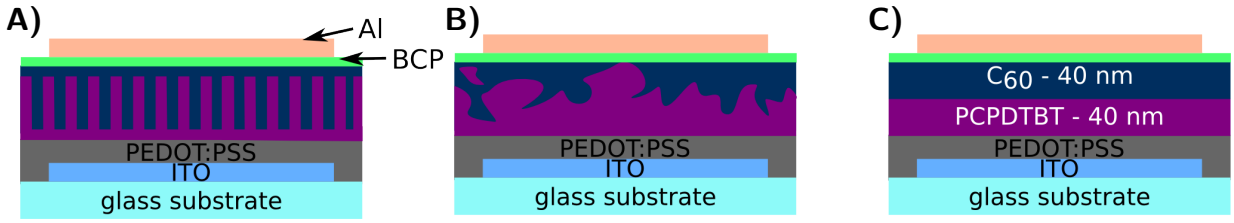

Fig. 1.6: Typical active layer configurations in organic solar cells. **A)** Standing cylinders embedded in a matrix of the other phase present a maximized interface area (interdigitated structure). **B)** Bulk heterojunction prepared by processing from a donor/acceptor mixture and often optimized by post annealing or solvent additives. **C)** Bilayer configuration as often used for academic studies of organic solar cells.

of the large interfacial area and the optimized domain sizes both allowing an optimum exciton harvesting.[52,53] Building such nanostructured devices with length scales of around 10 nm is still a challenge and up to today no devices of high efficiencies were reported with such configuration.

The most frequently used configuration is a bulk heterojunction of the donor and acceptor materials due to its easy preparation and high efficiencies, figure 1.6B.[57] Here the donor and acceptor materials are processed from a mixed solution forming a thin film of intermixed phases. The degree of intermixing and the domain sizes are typically controlled by either the processing solvents with and without solvent additives[58,59] or post-annealing protocols.[60–63] Optimized processing conditions lead to thin films with domain sizes around the exciton diffusion length and a large interface area. Additionally the individual phases must have continuous pathways to the respective electrodes to avoid short circuits and enclosed islands which could trap generated charges and lead to non-geminal recombination.

The simplest configuration is the bilayer solar cell with the donor and acceptor layers on top of each other, figure 1.6C. The first layer can be prepared by solution processing. The second layer is subsequently added by either thermal evaporation or spin coating using an orthogonal solvent. Since charge separation occurs at the donor/acceptor interface, which is quite small in this configuration, bilayer solar cells never obtain high efficiencies and are mainly used for academic purposes.[64,65] The advantage of the bilayer structure is that the individual phases can be investigated and annealed separately and that the preparation methods allows high control over the donor and acceptor interface.

1.2.3 Energy Levels and Spectroelectrochemistry of P3HT

The HOMO/LUMO energy levels of conjugated polymers play an important role in the device physics. For example, in organic solar cells the charge separation efficiency and the open circuit voltage (V_{OC}) are directly correlated to the LUMO and HOMO values,

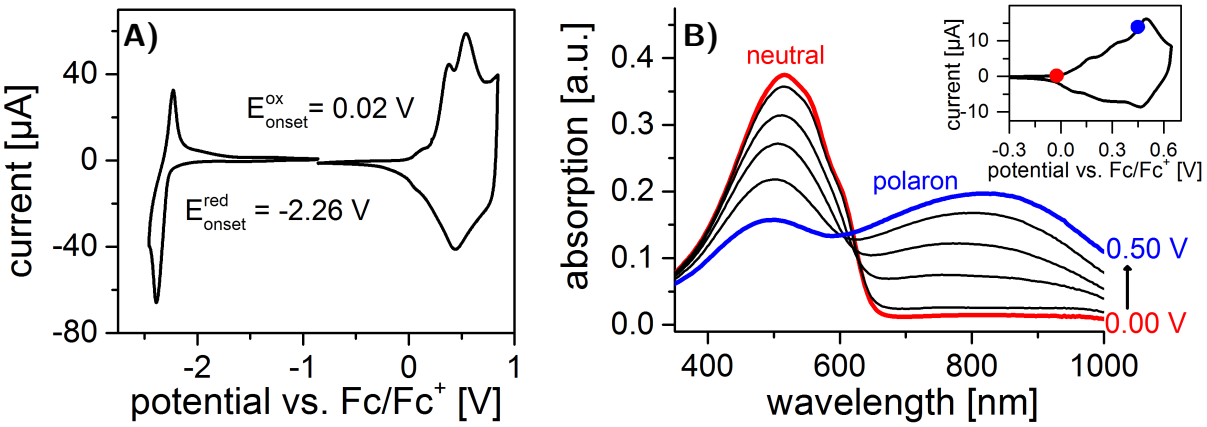

Fig. 1.7: Electrochemistry measurements of P3HT films measured in 0.1 M $TBAPF_6$/MeCN, 20mV/s. **A)** Cyclic voltammogram of the oxidation and reduction from a P3HT film cast on a Pt working electrode (measured by M. Goll and Dr. A. Ruff). **B)** Spectroelectrochemistry measurement of a P3HT film spin coated on an ITO-substrate. The in-situ UV/Vis-spectra of the oxidation cycle with the corresponding cyclic voltammogram (inset) show the development of the absorption signature going from the neutral (red) to the oxidized/polaron (blue) state (measured by K. Bruchlos).

respectively (chapter 1.2.2).[27] Also in organic field effect transistors the alignment of the energy levels between the active materials and electrodes is highly important for a good charge injection and transistor performance.[66]

The determination of energy levels is typically performed by electrochemistry. A cyclic voltammogram (CV) of a P3HT film is shown in figure 1.7A with the oxidation and reduction measured in separate cycles. In contrast to small molecules the redox signals of conjugated polymers are broad due to the conjugation length distribution and do often not allow to determine half wave potentials. It is assumed that at the onset potential the longest π-conjugated system is oxidized/reduced and therefore typically the onset potential is used to calculate the respective energy levels.

The redox potentials in figure 1.7A were determined to 0.02 V and −2.26 V against the internal redox standard ferrocene/ferrocenium (Fc/Fc^+).[67] Assuming an energy level of Fc/Fc^+ at −4.8 eV under the vacuum level the HOMO/LUMO values of the P3HT film were calculated to −4.82 eV and −2.55 eV, respectively, employing the following equations:[68]

$$E^{HOMO} = -E^{ox}_{1/2} - 4.8eV \tag{1}$$

$$E^{LUMO} = -E^{red}_{1/2} - 4.8eV \tag{2}$$

Employing spectroelectrochemistry the evolution of the absorption during the electrochemical oxidation/reduction can be followed. This is shown for the oxidation of P3HT in

figure 1.7B and reveals characteristic signatures of the neutral and the charged species. The spectra show how the neutral absorption from the HOMO/LUMO transition (red) disappears and a new red-shifted polaron band (blue) of the doped polymer appears upon doping, compare figure 1.3.

1.2.4 Mesoscopic Morphology and Crystal Structure

In the last chapters some examples were given on how the chemical structure can be modified to enhance device efficiencies by, for example, lowering the band gap or optimizing the frontier orbital levels. Besides the chemical structure it is well known for conjugated polymers that morphology has a significant impact on the device performance.[15,69–72] Understanding and controlling the morphology in the active layers on the nanometer to micrometer length scale is therefore of similar importance as optimizing the chemical structure itself.

Since conjugated polymers often form complex semi-crystalline microstructures comprising amorphous and crystalline domains is is a great challenge to understand their crystallization behavior and to determine a crystal structure.[73,74] The control over nucleation and crystallization is therefore a key factor to investigate the crystal structure and to understand the relationship between mesoscopic morphology and functional properties.

It should be pointed out that a crystal structure analysis of conjugated polymers is much more difficult than in the case of small molecules which form single crystals and can be characterized by a single crystal analysis. Particularly for the class of donor-acceptor copolymers very little is known about their crystal structure and its influence on the functional properties such as absorption or charge carrier mobility. In the following P3HT is used to give a short overview on how crystallization of a functional semi-crystalline polymer can be controlled and how morphology affects its functional properties.

Crystal structure and mesoscopic morphology investigations of conjugated semi-crystalline polymers are typically performed on thin films processed from solutions by spin-coating, blade-coating or dip-coating.[75] Depending on the boiling point of the processing solvent amorphous or ordered films can be prepared. The different evaporation rates influence the drying time during film formation and thereby give the polymer chains more or less time to reorganize in ordered structures.[76] P3HT exhibits a representative morphology for many conjugated polymers and can be taken as a typical example. Its morphology is schematically summarized in figure 1.8.

The semi-crystalline character is given by the alternation of π-stacked crystalline domains (green squares) and amorphous regions (red). Similar structures are also found for many

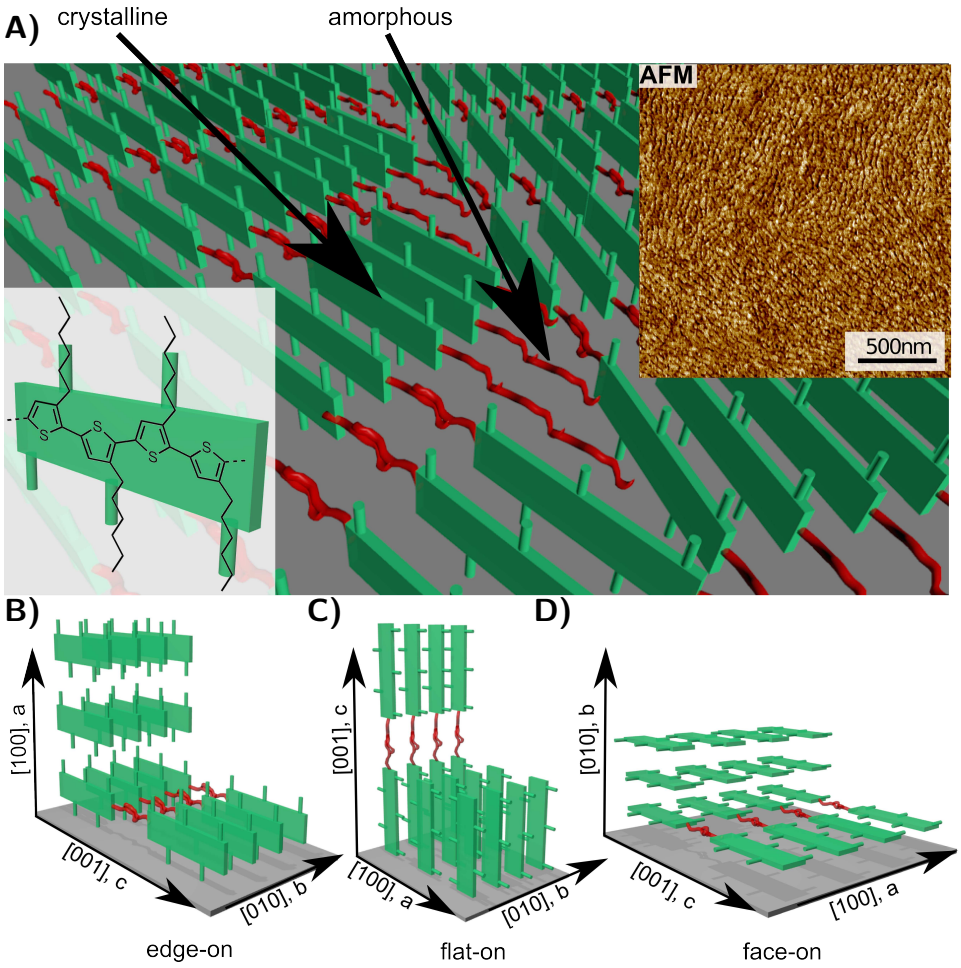

Fig. 1.8: A) Sketch of a semi-crystalline conjugated P3HT film with alternating crystalline (green) and amorphous (red) regions. Inset: AFM phase image of a highly crystalline P3HT film with a typical lamellar texture which reassembles the alternating crystalline and amorphous regions ($M_W = 59\,kg/mol$, PDI $= 1.9$), measured by Dr. E. Crossland. **B-D)** Different polymer chain orientations of crystallized P3HT on substrates: edge-on (B), flat-on (C) and face-on (D).

flexible, non-conjugated standard polymers as e.g polyethylene or polypropylene.[73,74] The amorphous parts consist mainly of folds and chain ends which do not crystallize. The crystalline phases on the other hand are composed of parallel backbones stacked by interchain coupling of the conjugated π-systems. This π-stacking of backbones is typical for conjugated polymers and determines strongly their crystallization behavior. Since the π-stacking is the driving force of the crystallization often long fibers with the π-stacking along the fiber axis and parallel to the substrate are formed. Depending on the molecular weight either single fibers are formed ($\lesssim 10\,kg/mol$) or the fibers are interconnected by the amorphous regions forming a lamellar structure ($\gtrsim 10\,kg/mol$) of alternating amorphous and crystalline domains.[77] The inset of figure 1.8A shows a characteristic AFM phase image of a high molecular weight ($M_W = 59\,kg/mol$, PDI $= 1.9$) P3HT film with a typical

lamellar morphology which reflects the alternating crystalline/amorphous structure.[78] This kind of texture is called edge-on morphology since the polymer chains stand on their long edges, figure 1.8B.

Besides this edge-on morphology two other polymer chain orientations are known for P3HT: flat-on and face-on, shown in figure 1.8C and D. In the face-on orientation the polymer chains lie flat on the substrate with the alkyl side chains parallel to the substrates. This orientation can for example be induced by mechanical rubbing which aligns the polymer backbone by shearing forces.[80] Little is reported in literature regarding the flat-on orientation in which the polymer chains are standing on the substrate and no general method to induce this morphology is known up to now.[81,82]

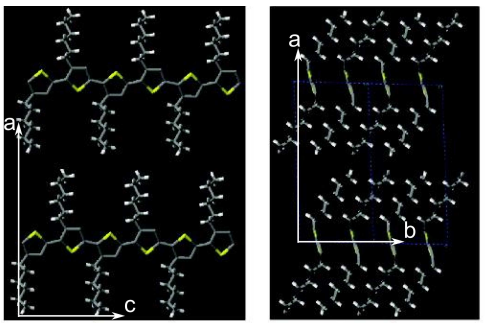

Fig. 1.9: Crystal structure of P3HT seen along the b- (left) and c-axis (right). Reprinted (adapted) with permission from [79, Brinkmann et al. 2009]. Copyright (2009) American Chemical Society.

The most reported and probably thermodynamically stable structure is the edge-on morphology. Typical distances for the crystal structure of P3HT are around 3.8 Å between the π-stacked backbones (b-axis, [020]) and around 15 Å (a-axis, [010]) in the direction of the alkyl side chain stacking, figure 1.9.[50] Especially the value of 3.8 Å is characteristic for π-stacked polymer backbones and can be found in many conjugated polymers.

1.2.5 How Absorption is Influenced by Morphology

A well known phenomenon for conjugated polymers is that the absorption spectra are red shifted and reveal an additional fine structure in the aggregated state compared to the solution. Figure 1.10A shows the evolution of the P3HT absorption going from a solution-like state with a maximum at 460 nm (red) to a highly crystalline film (blue). The absorption of the film reveals a fine structure with two main maxima around 550 and 610 nm, labeled as $A_{0\text{-}1}$ and $A_{0\text{-}0}$, respectively.

Spano et al.[7–9,84,85] investigated this change in absorption for P3HT employing mainly the Franck-Condon principle. They found that the red shift is caused by an increased conjugation due to a planarization of the backbones during the aggregation. The fine structure on the other hand is caused by different transitions ($A_{0\text{-}0}$, $A_{0\text{-}1}$, ...) of the first electronic transition between the HOMO and LUMO. Interestingly the ratio between the $A_{0\text{-}1}$ and $A_{0\text{-}0}$ absorption can be correlated to the degree of *inter*chain and *intra*chain

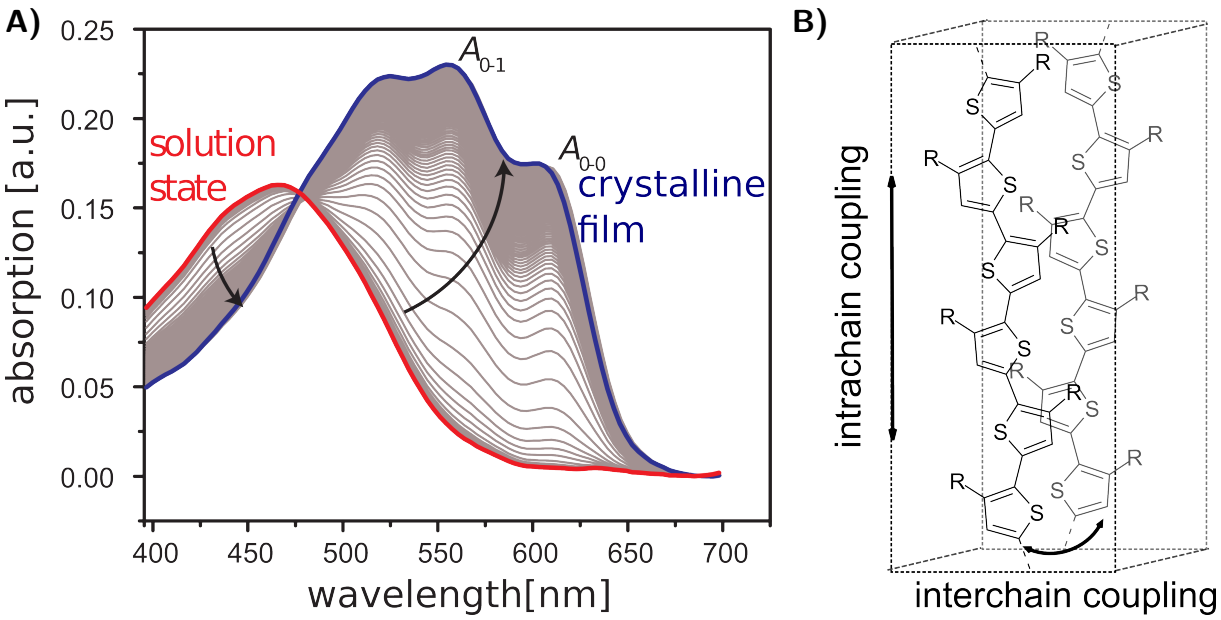

Fig. 1.10: A) In-situ absorption spectra of a thin P3HT film during recrystallization in CS_2 vapor, measured by Dr. Ed Crossland (adapted from[83]). **B)** Two π-stacked P3HT backbones highlighting the *intra*- and *inter*chain coupling between the polymer backbones and monomer units, respectively.

coupling (figure 1.10B) of the polymer backbones and monomer units in the solid state, respectively.[7,86,87]

Franck–Condon Analysis

The Franck-Condon principle is based on the publication of J. Franck and E. Condon from 1926.[88,89] The principle describes the electronic excitation and relaxation in molecules as electron transitions between electronic states without change of the nuclei position. It can be described by the Jablonski diagram including the transitions, figure 1.11. The IUPAC gives a good definition of the Franck-Condon principle:

> Classically, the Franck-Condon principle is the approximation that an electronic transition is most likely to occur without changes in the positions of the nuclei in the molecular entity and its environment. The resulting state is called a Franck-Condon state, and the transition involved, a vertical transition. The quantum mechanical formulation of this principle is that the intensity of a vibronic transition is proportional to the square of the overlap integral between the vibrational wavefunctions of the two states that are involved in the transition.
>
> IUPAC Compendium of Chemical Terminology, 2nd Edition (1997)

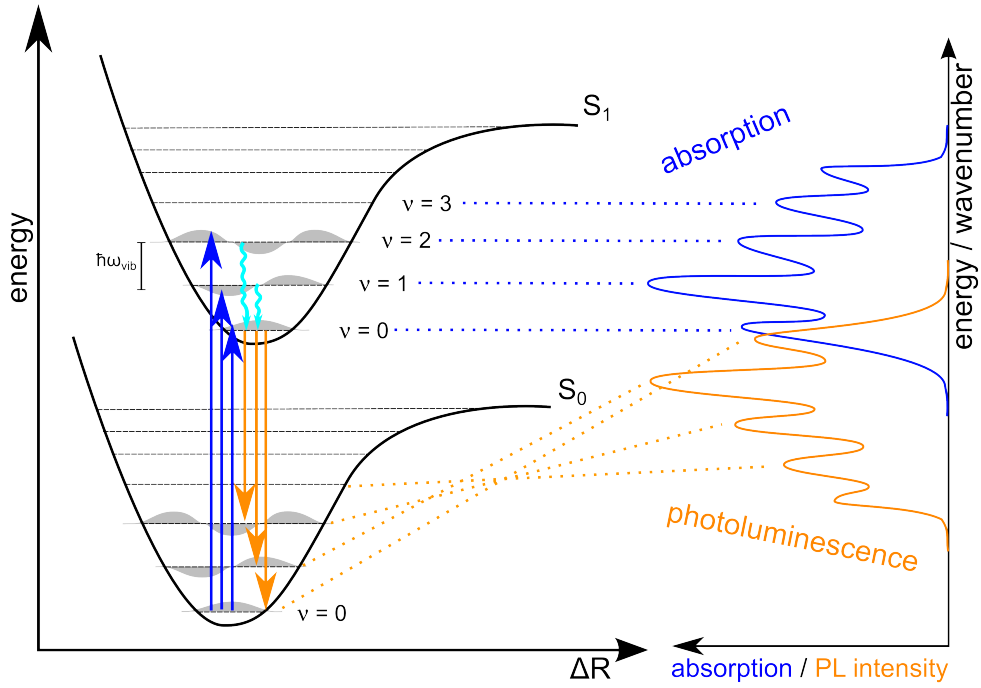

Fig. 1.11: The Jablonski diagram is shown on the left and an idealized spectrum on the right. Arrows indicate the electron transitions of the absorption (blue) and photoluminescence (orange) between the ground (S_0) and the first excited state (S_1). Additionally the non radiative vibrational relaxations (cyan) between the vibrational modes (ν) are shown. On the right side the absorption and photoluminescence spectra belonging to the indicated electron transitions are plotted.

Employing a Franck-Condon analysis to investigate the absorption spectra of conjugated polymers was first introduced by Friend et al.[26] in 2001. The authors investigated the temperature dependent evolution of the vibronic band intensities in the absorption and PL spectra of poly(p-phenylenevinylene) (PPV). Interestingly, a strong decrease of the 0-0 transition was found upon cooling. Employing the Franck-Condon analysis the authors were able to model the spectral signatures as described in the following:

For a single electronic transition the emission spectra (PL($\hbar\omega$)) can be fitted by the sum of all the vibronic transitions with the quantum numbers $m_i = 0,1,2,...$ of one oscillator i with the frequency ω_i:[26]

$$PL(\hbar\omega) \propto \sum_{m_i} I_{0\to m_i} \cdot \Gamma\delta\left[\hbar\omega - (\hbar\omega_0 - m_i\hbar\omega_i)\right] \tag{3}$$

where $\hbar\omega_0$ is the 0-0 transition energy, δ is the Kronecker delta, and Γ is the Lorentzian-Gaussian line shape operator. The intensity of a vibronic transition ($I_{0\rightarrow m_i}$) is given by the product of the density of states and the Franck-Condon factor:[26]

$$I_{0\rightarrow m_i} \propto n_f^3(\hbar\omega)^3 \frac{S_i^{m_i} exp(-S_i)}{m_i!} \tag{4}$$

with n_f^3 as the real part of the refractive index and S_i the Huang-Rhys factor of the oscillator i.[90]

The authors found that to explain all changes in the PPV spectra not only one dominant oscillator but two (here labeled as i=1 and i=2) must be considered. Equation 3 was therefore generalized for the case of two or more oscillators:

$$PL(\hbar\omega) \propto \sum_{m_i} \prod_i \left[\frac{S_i^{m_i} exp(-S_i)}{m_i!}\right] \cdot \Gamma\delta \left[\hbar\omega - \left(\hbar\omega_0 - \sum_i m_i\hbar\omega_i\right)\right] \tag{5}$$

The authors found evidence that two competing electronic transitions dominate the spectral signatures of PPV: one belonging to an isolated molecule and the other to an interchain coupled aggregate. Friend et al. used therefore two electronic transitions to describe the evolution of the spectral signature going from the dissolved to the aggregated state.

In 2005, building up on the work of Friend et al., Spano et al.[9] fitted the absorption and PL spectra of P3HT in the dissolved and aggregated phase. In contrast to Friend et al. they used the H- and J-aggregation model in addition to the Franck-Condon principle. This allowed them to explain the fine structure in the absorption signature employing only a single electronic transition.

Originally the H-/J-aggregation model was developed by Kasha et al.[86,87] to understand the absorption and photoluminescence in aggregates of small molecules. Spano et al. transferred this concept to P3HT and could thereby explain the evolution of the fine structure caused by aggregation, figure 1.10A. The authors considered each monomer unit as a single chromophore which stack along the polymer backbone. It was shown that the oscillator strength of vibronic transitions change because of either *intra-* or *inter*chain dominant couplings between the monomers, figure 1.10B.

The *intra-* and *inter*chain aggregates were called J- and H-aggregates, respectively, and were defined as described in the following: J-aggregation is assumed if a strong *intra*chain coupling between the monomer units along the polymer backbone occurs. This typically

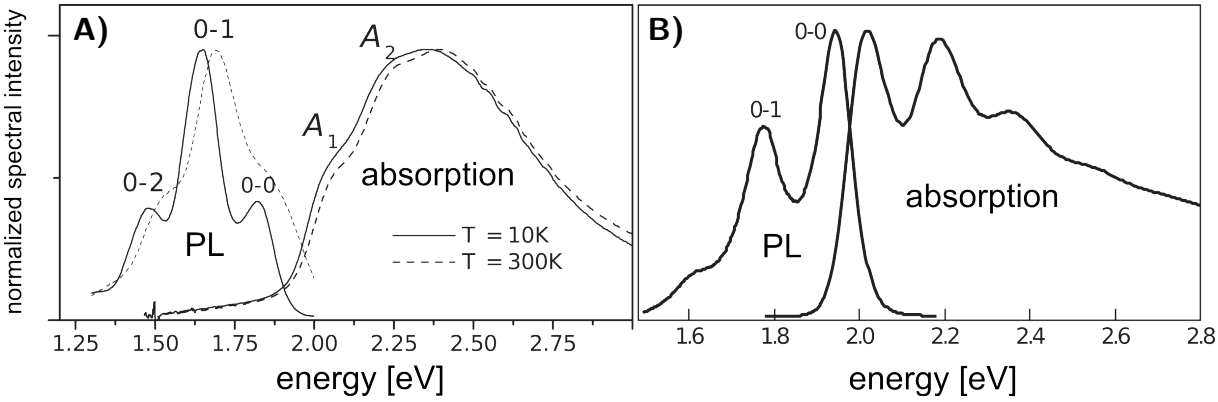

Fig. 1.12: A) Absorption and photoluminescence (PL) spectra of a P3HT film spin coated from a chloroform solution showing a reduced 0-0 transition due to strong H-aggregation. Adapted with permission from [91, Spano et al. 2009]. Copyright (2009) AIP Publishing LLC. **B)** Absorption and PL spectra of P3HT nanofibers grown in toluene showing a strong 0-0 transition due to a strong J-aggregation. Adapted with permission from [85, Spano et al. 2012]. Copyright (2012) American Chemical Society.

leads to a red shift compared to a pure monomer absorption and a strong transition between the vibrational ground states (0-0 transition).

On the other hand H-aggregation was described as an *inter*chain coupling caused by a side-by-side orientation of several monomer units due to e.g. π-stacking between polymer backbones. H-aggregation generally leads to a blue shift of the absorption and a suppressed 0-0 transition in P3HT.

It should be noted that energetic red or blue shifts of the spectra can also be caused by a planarization of the polymer backbone. They are therefore no sufficient indications for an H- or J-aggregate behavior in P3HT.[7]

In later studies[7–9,91,92] the same model was also employed to explain the spectral signatures of different P3HT morphologies. Depending on the preparation method a more J- or H-aggregate like behavior in P3HT films was found. It was shown that a rather amorphous P3HT film behaves more like an H-aggregate with a suppressed 0-0 peak, figure 1.12A. This is probably because of the short conjugation length and strong *inter*chain interaction between the polymer chains.[91] On the other hand highly ordered P3HT nanofibers grown in toluene show almost pure J-aggregate like spectra with strong 0-0 peak intensities, figure 1.12B, probably due to the long conjugation length and thereby enhanced *intra*chain coupling between the monomer units along the backbones.[85] In the recent years this model was successfully refined and transfered to other homopolymers such as poly[2-methoxy-5-(2'-ethylhexyloxy)-p-phenylene vinylene] (MEH-PPV),[93] PPV[94] or PFO.[95] To the best of my knowledge the manuscript[10] submitted from us together

with the group of Prof. Köhler is the first which used the Franck-Condon principle on donor-acceptor copolymers.

1.2.6 How Charge Mobility is Affected by Morphology

A high charge carrier mobility in conjugated polymers is desirable for organic field effect transistors (OFETs) as well as organic solar cells in which a fast charge extraction is required to prevent recombination.

Studies from Kowalewski et al.[81] with P3HT samples of different molecular weights have shown that with increasing molecular weight up to around 10 kg/mol (M_W) the

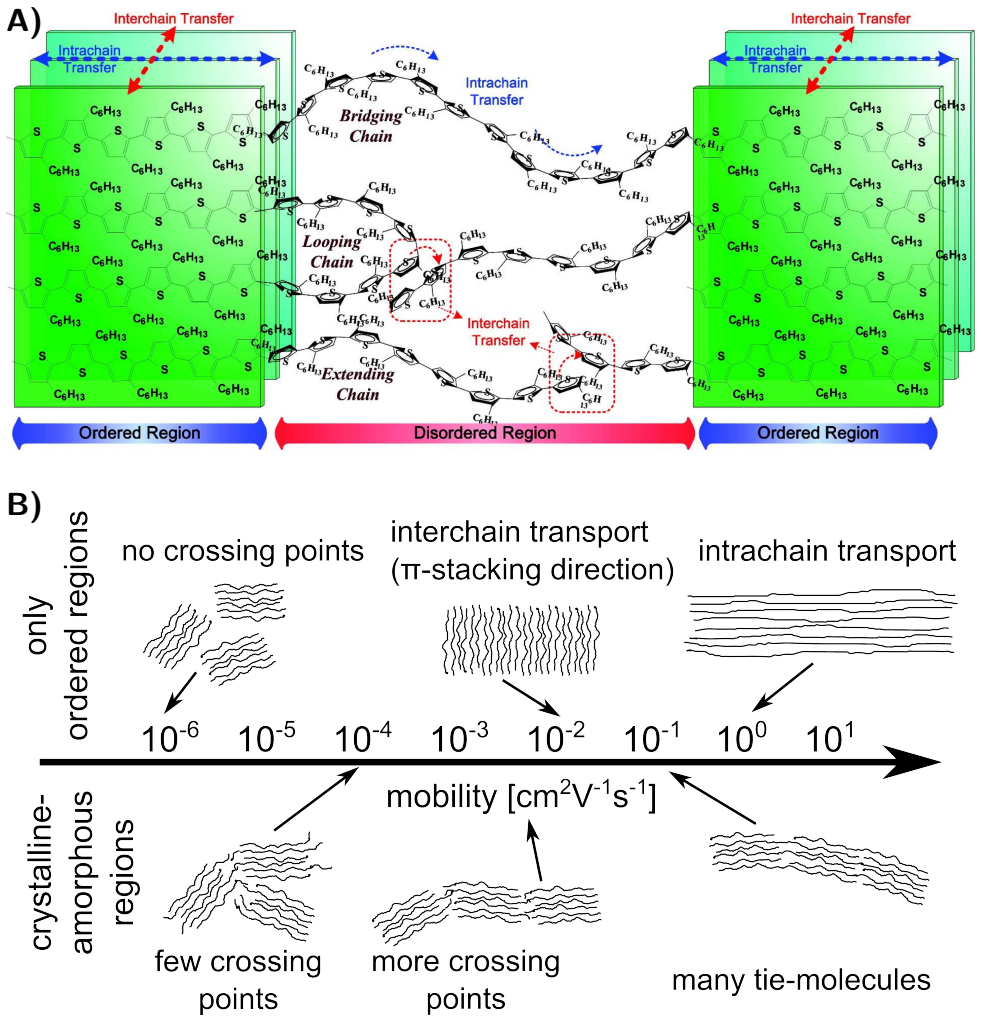

Fig. 1.13: A) Schematic of a ordered-disordered-ordered region in a P3HT film. Within the ordered regions (green) the inter- and intrachain charge transport is indicated. The disordered regions show different chain types: bridging-, looping- and extended chains. **B)** Possible correlation between P3HT morphology and charge carrier mobilities suggested by Lan et al.[96] Reprinted (adapted) with permission from [96, Lan et al. 2009]. Copyright (2009) American Chemical Society.

width of the crystalline domains increases. Coinciding the hole mobility was found to also increase from 10^{-5} to $10^{-2}\,cm^2/Vs$. Above 10 kg/mol a saturation of the crystalline domain width and the charge carrier mobility was reported. These results already indicate that the morphology and molecular weight have a great influence on the charge transport in conjugated polymers and that the charge transport is favored in crystalline domains.

As described in chapter 1.2.4 there are typically three main crystallographic directions in conjugated polymers: the polymer chain (c-axis), the π-stacking (b-axis) and the alkyl side chain (a-axis) direction. It is well established that the slowest transport is along the alkyl side chain direction due to the non-conjugated side chain barriers between the conjugated backbones.[69] In the following the focus will therefore be on the difference in charge transport along the π-stacking and polymer backbone direction over macroscopic length scales as found in real devices.

In general two mechanisms for the charge transport have to be considered: The transport along the polymer chain where the charges travel along the conjugated backbones. At the end of each backbone the charges have to transfer to an other polymer chain by a hopping process. In the direction of the π-stacking on the other hand a constant hopping process from one backbone to the next determines the charge carrier mobility.

Theoretical calculations from Lan et al.[45,96] suggest that within crystalline domains with optimized relative orientation of the polymer backbones the charge transport is 2-3 decades slower along the π-stacking direction compared to the chain direction. This is probably due to the many hopping steps in the π-stacking direction. However over macroscopic distances the amorphous regions separating the crystalline domains may interrupt and limit the charge transport in the direction of the polymer backbone, figure 1.13A. Therefore Lan et al.[96] calculated the mobility over several crystalline/amorphous domains taking the amorphous barriers into account. They predicted a correlation between the charge carrier mobility and the number of crossing points and bridging polymer chains (tie-molecules) inside the disordered region and between the crystalline domains, respectively, figure 1.13.

Our group experimentally studied the direction dependence of charge transport over macroscopic distances for P3HT by growing large spherulites [15, Crossland and Fischer et al. 2012] and using crystallization in confined geometries [16, Fischer et al. 2012]. Both studies showed that for P3HT with a molecular weight of 60 kg/mol (M_W) the charge carrier mobility was significantly higher in the direction of the polymer backbone compared to the π-stacking direction. During my diploma thesis it was shown that for P3HT of low molecular weight and narrow PDI (M_W = 31 kg/mol, PDI = 1.2) an isotropic charge transport along both directions occurs. The charge transport along the polymer backbone

direction is limited by the amorphous domains between adjacent crystalline lamellae. It is therefore likely that only in the high molecular weight polymer tie-molecules bridge the amorphous regions and act as charge transport channels, figure 1.13A. For the lower molecular weight samples such tie-molecules are less likely. Therefore, in the amorphous regions the mobility is probably limited to similar mobilities along the π-stacking and polymer chain direction. Our experimental studies confirmed therefore the model of Lan et al. Figure 1.13B displays an overview from Lan et al. on the proposed charge carrier mobilities for different morphologies and chain lengths.

1.3 Chemical Modifications towards Donor-Acceptor Copolymers

P3HT has used to be the most promising conjugated polymer for the use in organic solar cells for a long time. The main drawback of P3HT is a relatively large band gap which leads to an absorption covering only a small portion of the solar spectrum, figure 1.5B. Therefore new synthetic strategies to further reduce the band gap and increase the charge carrier mobility had to be developed.

One chemical approach was to fuse two adjacent thiophene rings by a bridging atom. This eliminates an otherwise possible tilt between the two rings and thereby increases the conjugation along the polymer chain by planarization. This approach was used when synthesizing poly(cyclopentadithiophene) with different alkyl-side chains attached to the bridging atom for solubility reasons. Electrochemistry and absorption spectroscopy confirmed the decrease of the band gap showing a red shift of the absorption up to 630 nm for this polymer.[97]

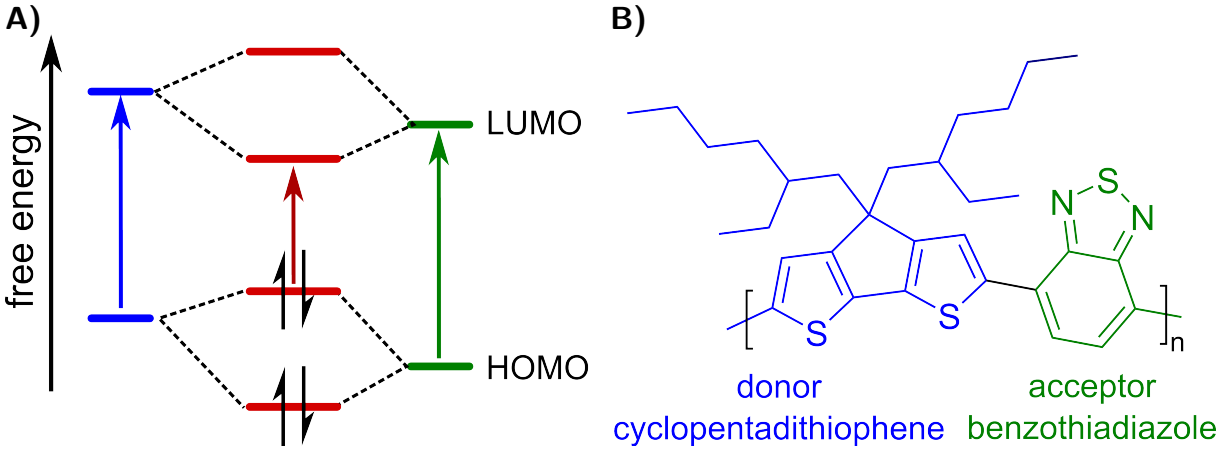

Fig. 1.14: A) Molecular orbital scheme of the hybridization between donor and acceptor units in a conjugated copolymer leading to a reduced band gap. **B)** Chemical structure of PCPDTBT (poly[2,6-(4,4-bis-(2-ethylhexyl)-4H-cyclopenta [2,1-b;3,4-b']dithiophene)-*alt*-4,7(2,1,3-benzothiadiazole)]) with the donor and acceptor unit highlighted in the same color as the corresponding molecular orbitals in A).

The second possibility to reduce the band gap even further is to increase the quinoidal character of the polymer chain since the quinoidal form has a higher ground state energy (HOMO) than the aromatic form. An additional advantage of this method is the increased charge carrier mobility due to the reduced energy difference between the quinoid and aromatic structures similar as in PA, chapter 1.1. One very effective method to enhance the quinoidal character is to design alternating copolymers from electron-rich (donor, D) and electron-poor (acceptor, A) monomer units. The strong push and pull driving force leads to an easier switching between the mesomeric structures (D–A $\rightarrow$ D^+–A^-) and therefore to a decrease of the energy difference between the two resonance structures. A molecular orbital picture is shown in figure 1.14. The molecular orbital hybridization occurs through an intramolecular charge transfer between the two comonomers which form new HOMO and LUMO orbitals with a reduced band gap.

The very promising acceptor monomer unit benzothiadiazole (BT) was first introduced by Janssen et al.[98] Together with an electron-rich 2,5-bis(2-thienyl)-N-dodecyl pyrrole (PPT) donor an alternating copolymer was synthesized. The optical band gap of the new polymer was reported to be around 1.4 to 1.6 eV, which is around 0.4 eV smaller than what was found for P3HT. Based on this concept a wide variety of donor-acceptor copolymers were synthesized, among them PCPDTBT containing the earlier mentioned cyclopentadithiophene (CPDT) as donor unit.

1.3.1 PCPDTBT and its Derivatives Si-PCPDTBT and F-PCPDTBT

In 2006 Brabec et al.[99] first introduced poly[2,6-(4,4-bis-(2-ethylhexyl)-4H-cyclopenta[2,1--b;3,4-b']dithiophene)-*alt*-4,7(2,1,3-benzothiadiazole)] (PCPDTBT) with an alternating cyclopentaditiophene (donor) and benzothiadiazole (acceptor) structure. For solubility reasons ethylhexyl side chains were attached to the bridging carbon between the two thiophenes. Brabec et al. could show that PCPDTBT contained many of the desired properties required for high performance organic solar cells. Its structural planarity allowed an extended conjugation and together with its donor-acceptor structure led to a small optical band gap of around 1.4 eV (890 nm), figure 1.5B (blue).

In literature[2] its HOMO/LUMO values were determined by electrochemistry to 5.3 and 3.5 eV, respectively. A more detailed study regarding the energy levels is shown in chapter 5.1. Heeger et al.[3] reported that in organic solar cells using PCPDTBT as donor and [6,6]-phenyl-C_{61}-butyric acid methyl ester (PCBM) as acceptor material ultrafast charge separation (t<200 fs) and efficiencies of up to 3.6 % were observed. It was suggested that a short-living charge-transfer state limits the efficiency of the recombination and that

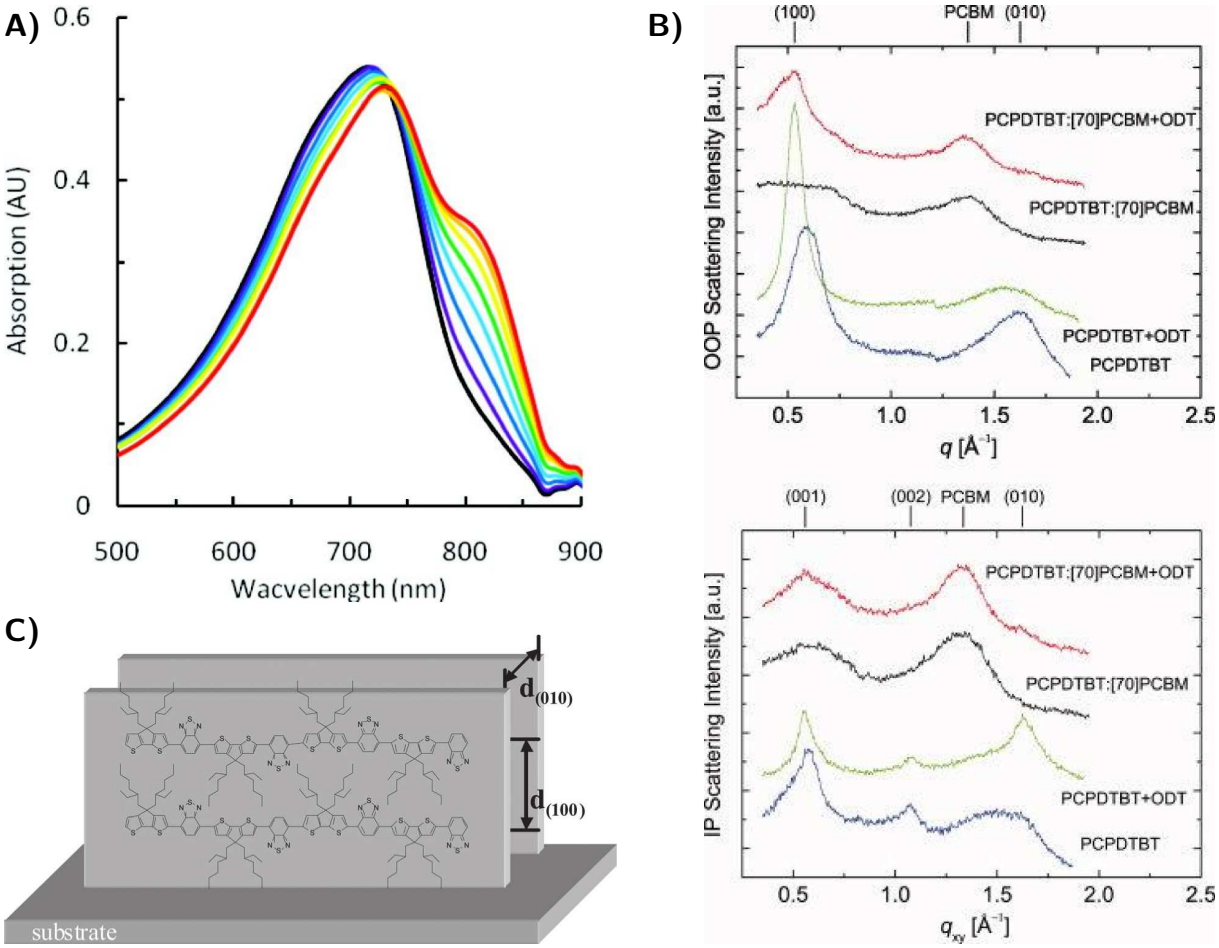

Fig. 1.15: A) Absorption spectra of PCPDTBT dissolved in pure DIO at 80 °C (black), 70 °C (purple), 60 °C (dark blue), 50 °C (light blue), 40 °C (green), 30 °C (yellow), 20 °C (orange), and 15 °C (red). Reprinted with permission from [17, Bazan et al. 2008]. Copyright (2008) American Chemical Society. **B)** GIXRD out-of-plane (OOP) (top) and in-plane (IP) profiles (bottom) for PCPDTBT processed with and without ODT. Reprinted with permission from [102, Nelson et al. 2011]. Copyright (2011) John Wiley and Sons. **C)** Edge-on structure of PCPDTBT as proposed by Russell et al. based on GIWAXS data. Reprinted with permission from [58, Russell et al. 2012]. Copyright (2012) John Wiley and Sons.

with an optimized micro-structure and blend morphology efficiencies of up to 7 % should be possible.

Previously thermal annealing had been often used to optimize the morphology of conjugated polymer/fullerene blend. In 2007 Peet and Bazan et al.[1] showed that in the case of PCPDTBT/PCBM it is not possible to optimize the blend morphology by classical thermal annealing.[100,101] Instead the authors achieved the proposed morphology optimization by using solvent additives such as 1,8-octanedithiol (DIO) or 1,8-octanedithiol (ODT) for the blend preparation and reported solar cell efficiencies of up to 5.5 %.

A year later the same authors presented a study[17] explaining that such solvent additives improve the blend morphology mainly by inducing aggregation of PCPDTBT during the blend formation. Temperature dependent absorption experiments in DIO showed that the aggregates reveal a red-shifted absorption around 800 nm, figure 1.15A. The authors suggested that the origin of the 800 nm band lies either in planarization of the polymer backbone or an increased interchain coupling due to π-stacking similar as it had been discussed before for P3HT.[17,102] Surprisingly, thermal annealing of this structure did not further increase the aggregation but rather blue shifted the absorption. This observation was interpreted as a destruction of the aggregates and suggests that these aggregates form a thermodynamically unstable structure.

J. Nelson et al.[102] and T. Russell[58] et al. further investigated thin films prepared with and without solvent additives such as DIO and ODT employing GIWAXS measurements, figure 1.15B. All films prepared using solvent additives revealed a strong 800 nm band and increased reflection intensities in the XRD experiments compared to films prepared without solvent additive. In all diffraction patterns two main reflections were found: An in-plane (IP) π-stacking reflection (0 1 0) around 3.8 Å (q = 1.6 $Å^{-1}$) and an out-of-plane (OOP) reflection (1 0 0) around 11 Å. From these measurements the authors suggested an edge-on morphology similar to P3HT, figure 1.15C.[58,102] Overall the found reflections were rather weak and no melting point was reported. PCPDTBT was therefore referred to as hardly crystallizable in the literature.

In the following years until 2011 less than 40 publications each year regarding PCPDTBT were published and no major efficiency increase was reported. Bazan et al.[103] further optimized the synthesis of PCPDTBT by a streamlined microwave-assisted preparation method. It was shown that by replacing the ethylhexyl side chains by linear C_{12}-chains the crystallinity slightly increased, but no crystal structure or efficiency increase was reported.

In 2011 Müllen et al.[104,105] reported that hole mobilities of up to 3.3 cm^2/Vs in thin films and up to 5.5 cm^2/Vs in fibers of PCPDTBT are possible when employing linear C_{16} alkyl side chains instead of branched ethylhexyl side chains. It was further shown that the hole mobility is directly correlated to the molecular weight and increases by more than a factor of ten when going from 11 to 35 kg/mol (M_W). This can probably be attributed to tie-molecules similar as discussed for P3HT in the previous chapter 1.2.6. X-ray diffraction and solid state NMR were further utilized to investigate the morphology. A π-stacking of the chains with a segregated stacking, in which donor and acceptor units form separated columns, was proposed. A theoretical investigation of the morphology also supported

this model and suggested three different polymorphs all with a similar π-stacking of the backbones.[106]

In the following years the number of publications regarding PCPDTBT raised to around 100 each year but no further increase of the organic solar cell efficiencies, hole mobilities or a crystal structure was reported. Most publications studied either the effect of solvent additives[58,61,107,108] or the charge separation mechanism[5,55,109] but only few investigated the morphology[58,102,108,110] of PCPDTBT.

F-PCPDTBT and Si-PCPDTBT

In an attempt to further optimize the chemical structure of the PCPDTBT backbone two important modifications were made over the years:

In 2008 Yang et al.[4] replaced the bridging carbon atom in the CPDT unit by a silicon atom gaining a new polymer called poly[(4,4'-bis(2-ethylhexyl)dithiene-[3,2-b:2',3'-d]silole)-*alt*-4,7-(2,1,3-benzothiadiazole)] (Si-PCPDTBT or PSBTBT, figure 1.16). Literature had shown that replacing the bridging carbon of the fluorene in poly[(9,9-dialkylfluorene)-2,7-diyl-*alt*-(4, 7-bis(2-thienyl)-2,1,3-benzothiadiazole)-5,5'-diyl] (PFDTBT) increases the photovoltaic properties significantly. Yang et al.[111] therefore hoped to find a similar effect in PCPDTBT. Measurements revealed that Si-PCPDTBT showed similar properties as PCPDTBT regarding orbital energy levels and absorption but achieved higher efficiencies of up to 5.1 % without the need of solvent additives. More detailed studies of the Si-bridged PCPDTBT showed that this is mainly due to an increased π-stacking of the polymer backbones. The longer C-Si bonds reduce the steric hindrance of the bulky alkyl side chains and thereby induce the increased aggregation.[103,112,113]

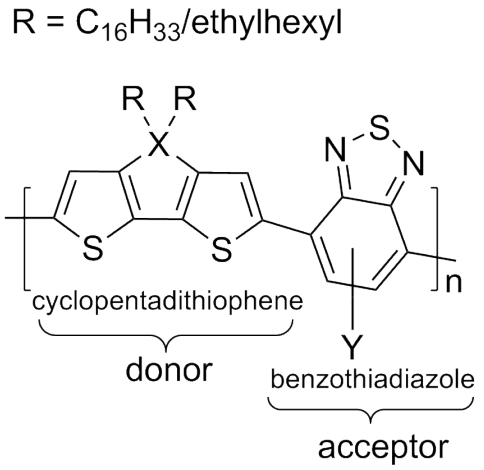

Fig. 1.16: Chemical structure of PCPDTBT (X = C, Y = H), Si-PCPDTBT (X = Si, Y = H) and F-PCPDTBT (X = C, Y = F).

In 2012 another structural modification was introduced by the groups of Neher et al.[5] and Jen et al.[6] They replaced one of the hydrogen atoms at the benzothiadiazole monomer by a fluorine, figure 1.16. Two main reasons were given for this modification: First to increase the V_{OC} in the organic solar cells by lowering the HOMO energy level. Second to increase the interchain coupling of the polymer backbones. Both groups reported that

the new polymer poly[2,6-(4,4-bis-(2-ethylhexyl)-4H-cyclopenta[2,1-b;3,4-b']dithiophene)-*alt*-4,7-(5-fluoro-2,1,3-benzothiadiazole)] called F-PCPDTBT or PCPDTFBT showed an increased aggregation tendency compared to PCPDTBT and solar cell efficiencies of up to 6 %. At this time 6 % was one of the highest ever reported values for donor-acceptor copolymer/PCBM heterojunction solar cells. Cyclic voltammetry[6] showed a decrease of the HOMO value from −5.02 eV for PCPDTBT to −5.15 eV for F-PCPDTBT after fluorination. External quantum efficiency (EQE) measurements revealed an increase of up to 50 % in the EQE value. Both explain the higher solar cell efficiencies of F-PCPDTBT.

Jen et al.[114] published a second paper comparing different alkyl side chains and double versus single fluorinated BT acceptor units. The authors showed that the ethylhexyl side chain with the single fluorine on the BT unit gave the best solar cell efficiencies for F-PCPDTBT.

In summary little is known about the pure PCPDTBT and its derivatives. Most literature has been concentrating on the optimization of the active layer blend morphology even though the past showed that understanding the pure phases is essential for the optimization and understanding of optoelectronic devices. The following thesis is therefore a thorough investigation of PCPDTBT and its derivatives Si-PCPDTBT and F-PCPDTBT. The basic properties of the pure polymers are investigated and used to understand how they influence the device performance of optoelectronic devices.

2 Techniques and Theory for Characterization

2.1 Structural Characterization: Microscopy and Scattering Methods

2.1.1 Polarized Visible-Light Microscopy - POM

The visible-light microscope Axio Imager.A1 from *Zeiss* was the fastest and easiest method to investigate thin films and often used during this thesis to check if certain annealing protocols led to the expected results. The Axio Imager.A1 is equipped with lenses of 2.5 x, 10 x, 20 x, 50 x and 100 x magnification which all could be used either in reflection or transmission mode. In both modi two linear polarizers (analyzer and polarizer) could be inserted separately into the optical path and be freely rotated with respect to each other. The images shown in this study were taken with an attached camera (AxioCam IC 1, *Zeiss*) and processed with the associated program AxioVison40 V4.8.2.0. In all microscopy images which were taken with one or both polarizers inserted into the optical path (POM images) the orientations of the polarizers are indicated by small arrows. The solvent vapor annealing chamber as well as the hot stage could be mounted onto the microscope stage when operated in reflection mode allowing in-situ observations during the annealing processes.

2.1.2 Atomic Force Microscopy - AFM

In this study an atomic force microscope (AFM) was used to investigate the top surface of thin polymer films. The advantage of AFM lies in the simple sample preparation and the possibility to measure thin films on all kinds of substrates. This allows a simple access to the surface morphology of the polymer films with a resolution of a few nanometer. The draw back is that only the top surface can be investigated and no information about the bulk morphology is gathered.

The AFM was always operated in the tapping mode, illustrated in figure 2.1, utilizing a Dimension Icon from *Bruker Nano Surface* (Karlsruhe) with silicon cantilevers (TESPA, force constant: 50 N/m) purchased from *Bruker*. The tapping mode was preferred over the contact mode because the surface is less stressed and altered when a cantilever is tapped over the sample. Further the tapping mode provides an additional phase information which is calculated from the change of the resonance frequency and the oscillation amplitude when tapping over areas of different hardness ($\Delta f = f_0 - f_{0'}$). The phase images allow

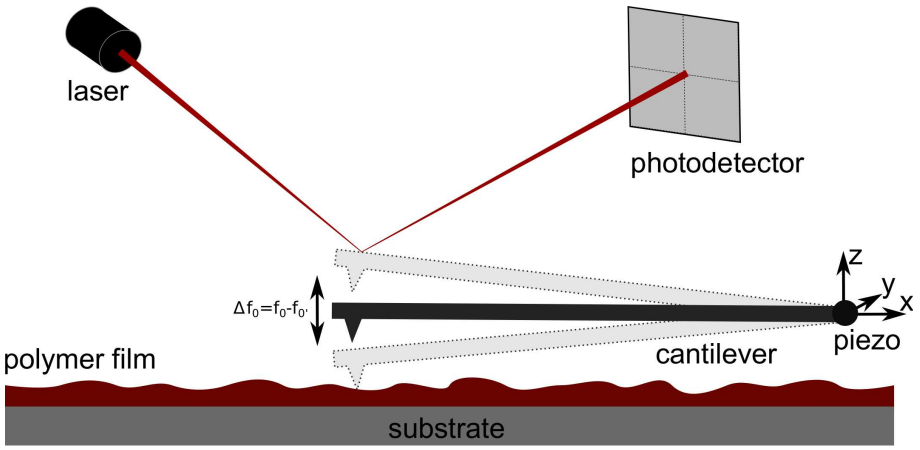

Fig. 2.1: Schematic illustrating the tapping mode using an atomic force microscope (AFM). The cantilever is tapped with its resonance frequency (f_0) over the substrate. Using a laser and a photodetector the height differences (Δz) and the changes in frequency ($\Delta f = f_0 - f_{0'}$) can be measured resulting in a height and phase image, respectively.

to distinguish between areas of different mechanical properties such as crystalline and amorphous phases and is therefore well suited to display the semi-crystalline nature of conjugated polymers.

Besides top surface morphology investigations the AFM was used to determine film thicknesses. The films were prepared on hard substrates such as Si-wafers or glass slides and scratched with a needle at several places. The film thickness was determined by extracting a height profile at several points from an AFM image taken along a scratch in the film. All film thicknesses and their errors given in this study were always determined from at least three scratches.

The images were obtained with the software *Nanoscope Analysis* from *Bruker* and subsequently flatted and evaluated employing the free software *Gwyddion*.[115]

2.1.3 Scanning Electron Microscopy - SEM

Scanning electron microscopy (SEM) was rarely used in this study since conjugated polymers are early degraded by the electron beam during the measurement and conductive substrates (n-doped Si-wafer or gold wafer) are necessary. The advantage of SEM compared to AFM is that large areas of a sample can be rapidly scanned and zooms into interesting areas can easily be performed. Similar to AFM only the top layer of the film (ca. 10 nm depth depending on the detector) and not the bulk can be investigated. All images shown in this study were obtained at the S-4800 from *Hitachi* located in the group of Prof. Gießen, Physics Department, University of Stuttgart. The experimental conditions and used substrates are stated in the captions of the respective figures.

2.1.4 Transmission Electron Microscopy and Diffraction - TEM/ED

Transmission electron microscopy combines microscopic imaging (bright field mode) and electron diffraction (ED, diffraction mode) making this method very valuable for thin film investigations of semicrystalline polymers. The advantage of TEM compared to the microscopy methods described above is that not only the surface but the bulk is investigated and that additionally electron diffraction patterns of areas pre-selected in the bright field mode can be obtained. This opens experimental access to the correlation between bulk morphology and diffraction patterns and further provides information about the crystal structure and the orientation of the unit cell and polymer chains relative to the substrate. The drawback of TEM/ED measurements is the time consuming sample

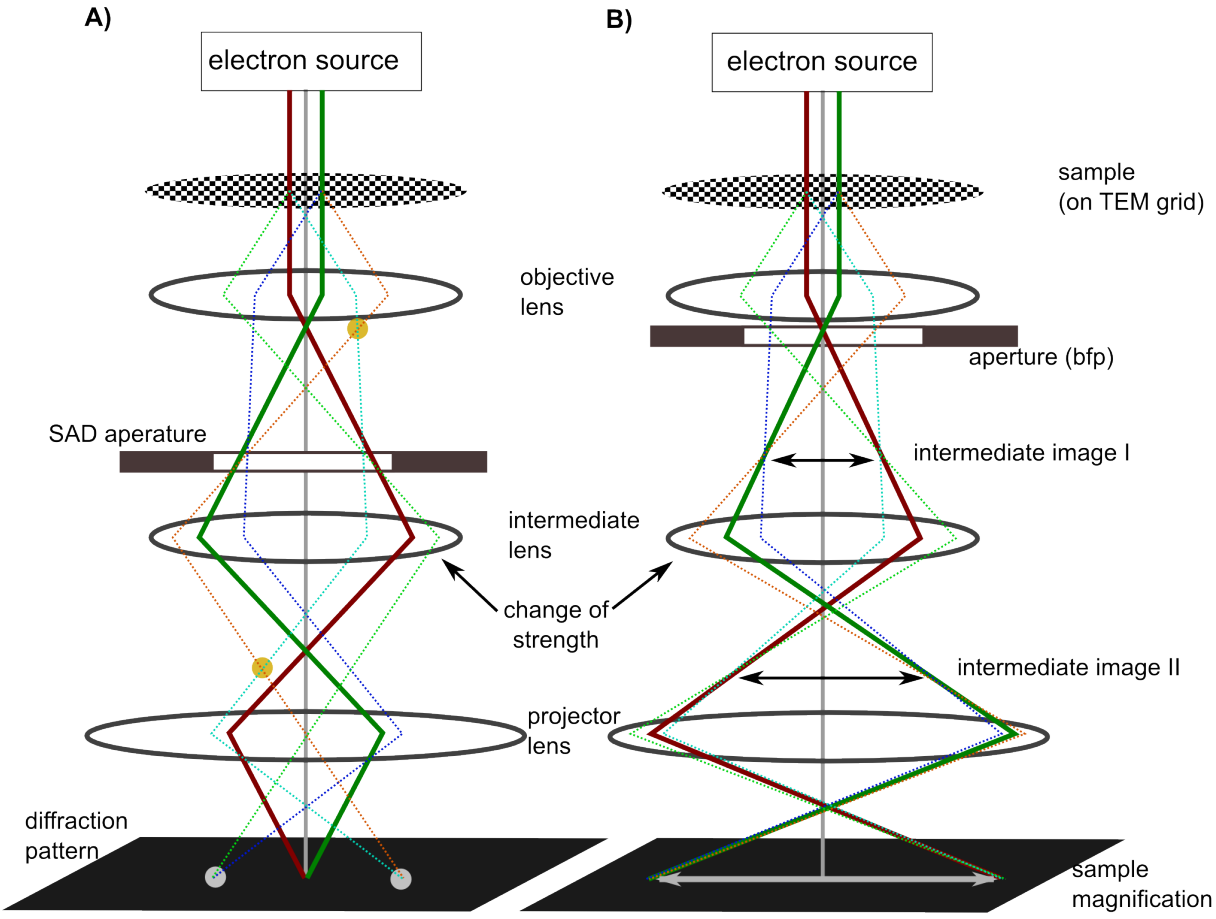

Fig. 2.2: Schematic sketch of the transmission electron microscope (TEM) illustrating the bright field **(B)** and the diffraction mode **(A)**. To switch between diffraction and bright field mode the intermediate lens can be changed in strength selecting either the back focal plane (bfp, A) or the image plane (B), respectively. This is a simplified picture of the complex lens systems inside modern TEMs adapted from "Transmission Electron Microscopy" by D. B. Williams and C. B. Carter.[116]

preparation including transfer of the thin film from a SiO_x-wafer onto a copper TEM grid, as described in detail in chapter 3.2.2.

Figure 2.2 illustrates the two TEM modi used in this study: electron diffraction and bright field imaging. A lanthanum hexaboride (LaB_6) electron source was used, the electrons parallelized (not shown) and directed onto the sample via electromagnetic lenses. Passing through the sample the electrons get scattered by interacting with both the nucleus and the electrons from the scattering material through Coulomb forces. Depending on the strength of the intermediate lens either the diffraction pattern (A) or a magnification of the sample (B) is projected onto the viewing screen/CCD (charge-coupled device). Knowing the wavelength and the distance between detector and viewing screen the distances (d) between lattice planes can be calculated from the diffraction pattern using the Bragg equation

$$2dsin(\Theta) = n\lambda \tag{6}$$

with the distance d, the angle of scattering Θ, n as any integer and the wavelength λ of the electrons.[116]

Transmission electron microscopy and electron diffraction (TEM/ED) was performed at the *Institut Charles Sadron* together with Dr. M. Brinkmann and Dr. N. Kayunkid using a CM12 Philips microscope equipped with a MVIII (Soft Imaging System) charge-coupled device camera. The measurements were done by Dr. M. Brinkmann and Dr. N. Kayunkid.

2.1.5 Gracing Incidence Wide Angle X-Ray Scattering - GIWAXS

X-ray diffraction measurements were in a complementary way used to the electron diffraction described above. The advantages of electron scattering (TEM/ED) is that electrons scatter stronger than X-ray beams leading to diffraction patterns of higher orders and allow nm-size crystal analysis of organic thin films. The disadvantage of TEM/ED on the other side is that only information along one crystallographic plane (or a few when tilting the sample) are retrieved and that it is limited to small areas of a few micrometers. GIWAXS was therefore employed to gain informations along all crystallographic directions and to average over large areas (around $1\,cm^2$) of the sample.

Figure 2.3 illustrates a simplified GIWAXS setup. X-rays from a synchrotron beamline are directed with a small incident angle (7 to 12°) onto the substrate. The X-ray beam is scattered in the polymer film and directed to a CCD-detector. Two main plane directions from which the beam is scattered are distinguished: planes parallel and perpendicular to the substrate typically referred to as out-of-plane (OOP) and in-plane (IP) direction,

respectively. Knowing the distance between film and detector the length of the reciprocal lattice vector (q, equation 7) can be calculated. Using the Bragg's law (equation 6) the distances (d) between lattice planes can be determined:

$$q = \frac{4\pi}{\lambda} sin(\Theta) \tag{7}$$

$$d = \frac{2\pi}{q} \tag{8}$$

with the X-ray wavelength λ and the scattering angle Θ.

Gracing incidence wide angle X-ray scattering was performed at the X9 undulator-based beamline at the National Synchrotron Light Source by the beam scientist Dr. Kevin Yager, using a X-ray beam of 13.5 keV (wavelength = 0.0918 nm). The samples were prepared on Si-wafers and shipped to the beamline under a nitrogen atmosphere. The data were collected under vacuum using a fiber-coupled CCD detector, at a distance of 235 mm from the sample. The interpretation of the data was done utilizing the program View.gtk in Stuttgart.

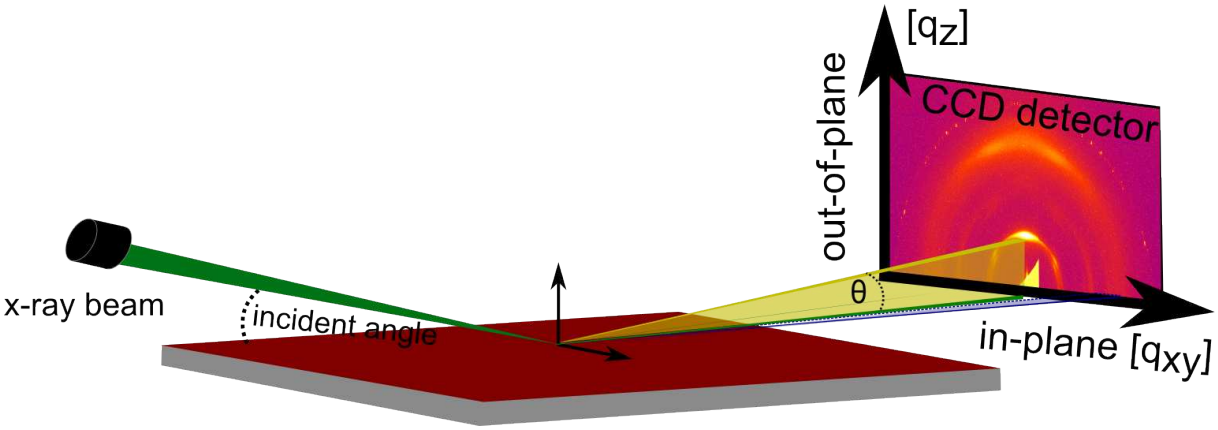

Fig. 2.3: Sketch of a GIWAXS experiment. An X-ray beam generated from a beamline is directed onto a thin polymer film prepared on a Si-wafer with a certain incident angle (7 to 12°). The X-rays are scattered from the thin polymer film and captured by a CCD-detector. It can be distinguished between two main scattering directions: out-of-plane (yellow) and in-plane (blue) linked to the crystallographic planes parallel and perpendicular to the substrate, respectively.

2.2 Spectroscopy

The optical properties including electron and vibrational transitions were investigated by UV/Vis-absorption, photoluminescence (PL) and Raman spectroscopy. Using these methods the aggregation behavior was investigated employing temperature dependent

measurements by which specific electronic transitions can be correlated to aggregated or dissolved phases or even different crystal structures. Applying a Franck-Condon-Analysis to the absorption and photoluminescence data, including the known vibrational modes from the Raman spectroscopy, it was further possible to identify different kinds of aggregates within solution and thin films and to gain a deeper understanding of the absorption and PL band and their fine structure.

2.2.1 UV–Vis–NIR Spectroscopy

UV–Vis–NIR-absorption spectroscopy probes the electron transitions between vibrational modes of the ground and excited states as shown in figure 1.11. The absorption (A) after light irradiation is usually plotted as either function of the wavelength (nm) or the energy (eV) and can be described as material property by the Lambert-Beer law for diluted solutions:

$$A = -log(\frac{I}{I_0}) = -\epsilon cl \tag{9}$$

with the intensities I and I_0 after and before passing through the sample, the molar extinction coefficient ϵ, the concentration c and the thickness of the sample l. Each electronic transition gives an absorption band in the spectrum which reveals an additional fine structure. This fine structure within an absorption band (e.g. S_0 to S_1) is caused by transitions from the ground state into different vibrational states (ν) of the excited electronic state as shown in figure 1.11.

The absorption spectra in this study were all obtained with one of the two diode array spectrometers of the *Zeiss MCS 600* series from *Carl Zeiss MicroImaging GmbH* which were equipped with a halogen lamp CLH600 (380 to 2500 nm) or CLH600F - (340 to 2500 nm). Two different detectors were used MCS611 2.2 (910 to 2200 nm) and MCS621VIS-II (310 to 1050 nm) and thereby in total a range between 340 to 2200 nm covered. Both spectrometers could be connected by fiber optics either in transmission or reflection mode to a variety of setups: hot-stage, temperature controlled cuvette holder or the electrochemistry setups.

2.2.2 Photoluminescence Spectroscopy

The photoluminescence (PL) spectroscopy probes the emission of electronic transitions from an excited state (typically S_1) to the ground state (S_0), compare figure 1.11. Typically the PL is obtained in wavelengths (nm) which can be converted into an energy scale (eV) and plotted against the intensity. When converting from a wavelength to an energy

scale the intensity has to be corrected by dividing through the square energy (E) for each wavelength according to

$$PL(E) = PL(\lambda)\frac{d\lambda}{dE} \tag{10}$$

and

$$\lambda = \frac{hc}{E} \tag{11}$$

with PL as photoluminescence intensity as function of the energy (E) or the wavelength (λ), the Planck constant h and the speed of light c.

For probing the PL the material is illuminated by a specific wavelength inducing an excited state ($S_0 \rightarrow S_1$) which non-radiatively relaxes into the vibrational ground state ($\nu = 0$). The measured emission is then caused by a radiative relaxation from the vibrational ground state of the electronic excited state (e.g. S_1) into the electronic ground state (S_0). Similar to the absorption spectra a fine structure is found within the PL band caused by the relaxation into different vibrational states (ν = 0,1,2..) of the ground state (S_0). Comparing the PL spectra to the absorption they are typically red shifted due to the loss of energy from the non-radiative relaxation and mirror the fine structure of the absorption spectra.

For the PL measurements of PCPDTBT a setup with a detection range up to the NIR region (ca. 1000 nm) was necessary. The measurement was therefore performed at a self-built setup in the group of Prof. A. Köhler with the help of C. Scharsich. The setup allowed besides the NIR detection also in-situ absorption measurements and cooling down to a temperature of a few Kelvin. The self-built setup consisted of a monochromator (*CVI Instruments Digikrom 240*) with Si-photodiode (by *Thorlabs*) and a lock-in technique (*Standford Research System, Model SR830 DSP lock-In Amplifier*) for the signal detection. The absorption measurements were performed with a Xe-lamp (LAX 1530 by *Müller GmbH Elektronik - Optik*) equipped with a monochromator (LTI by *Amko Light Technology Instruments*) and for fluorescence excitation a Compass continuous wave 405 nm diode laser from *Coherent* was used.

For low temperature measurements the samples (quartz substrate or quartz cuvette of 1 mm) were placed into a continuous helium flow cryostat and the temperature was controlled by a ITC503 Oxford instrument controller.

2.2.3 Raman Spectroscopy

Raman spectroscopy was performed on thin films utilizing a HORIBA Jobin Yvon HR-800 confocal Raman schematically shown in figure 2.4. The spectrometer was equipped with a 500:1 polarized He-Ne-laser with a wavelength of 632.82 nm (20 W) and a CCD-detector. A $\lambda/2$ plate and a polarizer could be inserted into the optical path to measure polarization dependent.

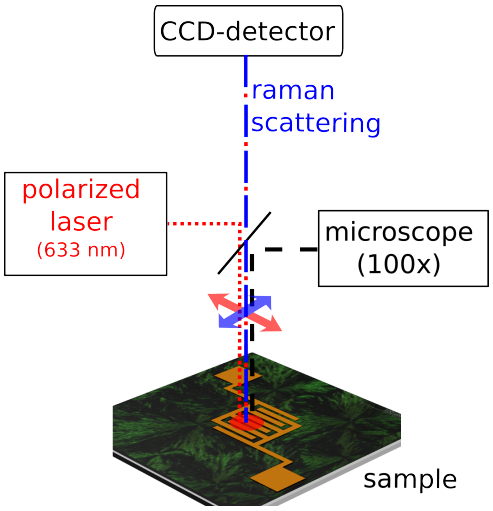

Fig. 2.4: Schematic of the confocal Raman optical pathway used in this study.

2.3 Energy Level Characterization

The electrochemical characterization in this thesis was performed by cyclic voltammetry (CV) to determine the redox potentials and energy levels. The CV was further coupled to the absorption spectrometers to observe the changes of the absorption during the charging and discharging of the polymers in-situ. This technique is called in-situ spectroelectrochemistry. For each experiment the internal redox standard Fc/Fc^+[67] was measured to reference the redox potentials. The HOMO/LUMO values were calculated assuming an energy level of Fc/Fc^+ at $-4.8\,eV$ under the vacuum level.[68]

The in-situ coupling with absorption spectroscopy provided further information about the redox processes within the materials and additionally helped to determine redox potentials. In addition to the conventional cyclic voltammogram the evolution of the absorption was plotted against the applied potential for characteristic wavelengths. These plots allow to determine the potentials at which certain absorption bands start to change in intensity (absorption onset potentials) which is typically correlated to specific redox reactions. The absorption onset potentials can therefore be compared to the half-wave and onset potentials from the cyclic voltammograms and were additionally used to determine redox potentials. Especially for the broad and often non-reversible polymer peaks in the CV this method is well suited to be used as additional technique to determine energy levels.

Spectroelectrochemistry was further employed to identify in polymer/fullerene blends the active material (phase) responsible for certain redox processes. This is of great interest

since in organic solar cells bulk heterojunctions (blends of donor and acceptor materials) are typically used as active layers. Often the two phases are separately characterized and subsequently the band gap of the blend is calculated from the HOMO of the polymer and the LUMO of the fullerene. The coupling of the CV with in-situ absorption spectroscopy opens the possibility to not only determine the real bulk heterojunction band gap, but also to identify the species oxidized or reduced at certain potentials.

Last but not least spectroelectrochemistry was used to capture the absorption signatures of the charged species and to identify e.g. typical polaron or bipolaron absorption signatures.

2.3.1 Cyclic Voltammetry - CV

The classical cyclic voltammetry (CV) was used in first experiments to obtain cyclic voltammograms since it is easier and faster to perform than spectroelectrochemistry due to the simpler setup. CV was performed in a self built glass cell with a platinum counter electrode. As working electrode a Au-substrate was used either blank or covered with a thin polymer film for solution or thin film measurements, respectively. As solvent typically methylene chloride (CH_2Cl_2, stored over active Al_2O_3 - basic:neutral 1:1) with the supporting electrolyte $TBAPF_6$ (0.1 M) was used and deaerated by argon bubbling for at least 5 min before each measurement. Further a Ag/AgCl pseudo reference electrode which consisted of a silver wire in a 0.01 M $AgNO_3$ solution connected via a 0.1 M NBu_4PF_6/acetonitrile salt bridge to a 0.1 M $TBAPF_6$/acetonitrile solution was used. The exact measurement conditions are given during the discussion of the respective samples.

The HOMO and LUMO values were calculated from the oxidation and reduction potentials referenced to the formal potential of the internal redox standard Fc/Fc^+[67] assuming an energy level of Fc/Fc^+ at -4.8 eV under the vacuum level.[68] The redox potentials were obtained from the half-wave or the onset potentials (E) for fullerenes and polymers, respectively using the equations 1 and equation 2 (p. 10).

2.3.2 In-Situ Spectroelectrochemistry

In-situ spectroelectrochemistry means the coupling between the typical cyclic voltammetry, as described above and absorption spectroscopy (see figure 2.5). To calculate the frontier orbitals the redox potentials were referenced to the formal potential of the internal redox standard Fc/Fc^+[67] assuming an energy level of Fc/Fc^+ at -4.8 eV under the vacuum level.[68] The solution or thin film measurements were performed in one of the two setups shown in figure 2.5:

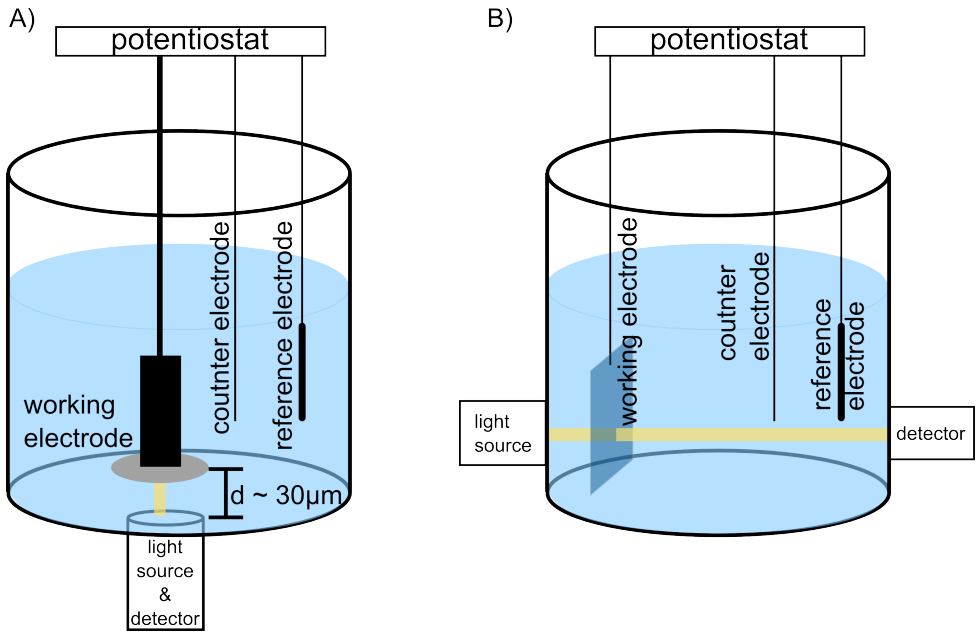

Fig. 2.5: In-situ spectroelectrochemistry setups for solution (A) and thin film (B) measurements. In both a platinum counter electrode and a silver wire coated with AgCl as pseudo reference electrode was used. **A)** The thin layer cell setup used for measurements in solution under thin film conditions. A working electrode of polished platinum was used as mirror to measure the absorption in a reflection configuration. The distance between glass bottom and Pt-working electrode could be adjusted by micrometer screws. **B)** Spectroelectrochemistry setup for the measurement of thin films prepared on ITO-substrates (indium tin oxide) which functioned as working electrode. The absorption was measured in a transmission configuration with a diode array spectrometer connected via fiber optics to the cell (not shown).

The thin layer cell setup was used for measurements in solution and was adapted from the setup described by C. Geskes et al.[117] Figure 2.5A shows the configuration with platinum working and counter electrodes and a AgCl coated Ag wire as pseudo reference electrode. The working electrode consisted of a polished platinum disk which was mounted only a few micrometer above the quartz glass bottom of the cell and was adjustable in height by a micrometer screw. The absorption was captured during the measurement utilizing a diode array spectrometer in reflection mode using the working electrode as mirror (see chapter 2.2.1). The solutions were prepared typically in CH_2Cl_2 with 0.1 M $TBAPF_6$ and deaerated before the measurement by argon bubbling.

Thin film in-situ spectroelectrochemistry was performed in a different configuration than the thin layer cell setup, figure 2.5B. Again a platinum counter electrode and a AgCl coated Ag wire was employed as reference electrode. The investigated films were typically prepared via spin coating on O_2-plasma cleaned ITO-substrates. Using transparent substrates allowed transmission absorption measurements utilizing one of the

two diode array spectrometer depending on the wavelength range of interest (see chapter 2.2.1).

2.4 Device Characterization

To understand the impact of different morphologies on the device performance, organic solar cells as well as organic field effect transistors (OFETs) were built. For each material several processing and post annealing methods were used to induce different chain orientations and crystal structures within the devices.

2.4.1 Organic Field Effect Transistors - OFETs

Field effect transistors (FETs) are used in a wide range of electronic devices such as displays and microprocessors. Even though nowadays still primarily field effect transistors based on single crystalline silicon are used OFETs have become more and more important over the last years.

OFETs are further a well known fundamental method in literature to determine hole and electron mobilities in semi-conducting polymers.[15,16,25,105,118,119] In this thesis OFETs were prepared to investigate the influence of the morphology on the mobility which is is of great interest for organic solar cells. The device performance in organic solar cells strongly depends on a fast charge transport away from the donor-acceptor interface since it prevents a non-geminal recombination of free charges (a bimolecular recombination of two charges generated during different absorption processes).[27,120]

To focus on the morphology influence we chose a top-gate, bottom-contact transistor configuration as shown in the inset of figure 2.6B. In this configuration the polymer layer is sandwiched between the source-/drain-electrodes located on the substrate and the dielectric poly(methyl methacrylate) (PMMA) layer on top. The advantage of this configuration is that the top surface of the polymer film, along which the charge transport occurs,[121] can be investigated by optical- and atomic force microscopy before the PMMA layer is applied. N-butyl acetate which is an orthogonal solvent for the investigated polymers was used as processing solvent for PMMA. The use of an orthogonal solvent is important here since changes in the morphology during the application of the PMMA layer must be avoided to be able to correlate the measured mobilities with the different morphologies afterwards. Finalizing the device an aluminum top electrode was evaporated on top of the PMMA layer.

The inset in figure 2.6B shows a top-gate, bottom-contact OFET with the circuit diagram as used in this thesis (for preparation details see chapter 3.2.5). Generally a voltage between

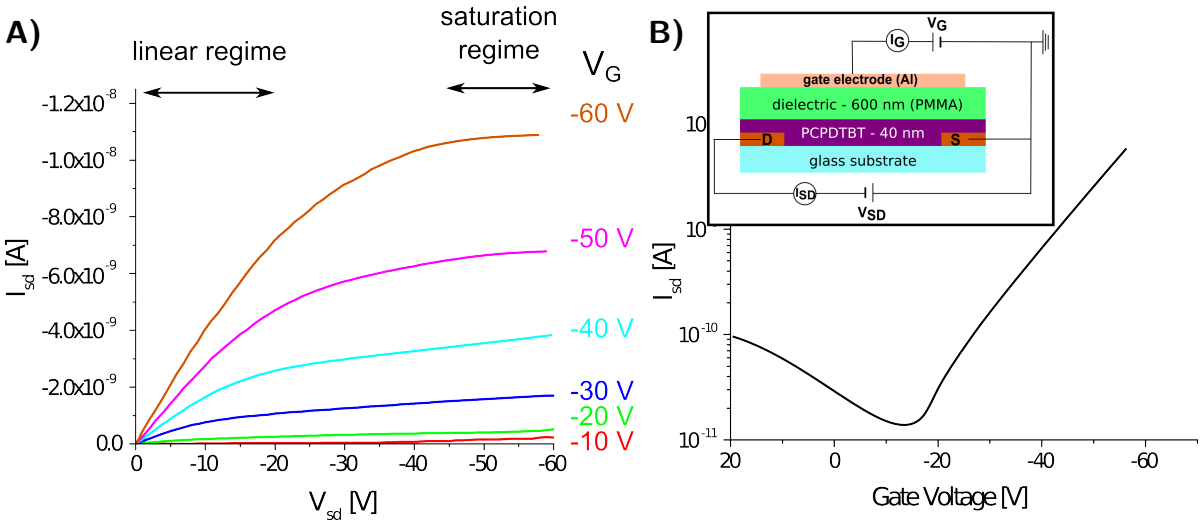

Fig. 2.6: Schematic Output- (**A**) and Transfer-Characteristics (**B**) for an organic field effect transistor. **A)** Set of output curves with the source-drain-current (I_{SD}) plotted against the source-drain-voltage (V_{SD}) for different gate voltages (V_G). Output curves can be divided into two regimes: the linear- (small V_{SD}) and the saturation regime (large V_{SD}). **B)** A typical transfer curve with the gate voltage swept from 20 to -60 V. Inset: Side view of a bottom-contact (source (S) and drain (D) gold electrodes), top-gate (30 nm thick Al-layer) transistor with the circuit diagram as used in this study.

source- and drain-electrodes (V_{SD}) results in a current (I_{SD}) which strength depends on the gate voltage (V_G) applied to the gate electrode. Applying a voltage to the gate electrode accumulates charges at the interface between dielectric (PMMA) and polymer layer and thereby controls the number of charge carriers within the transistor channel between the source- and drain-electrode. Since the accumulation is limited to the polymer/dielectric interface the charge transport is also limited to the top few nm of the polymer layer.[121] Typically two different measurements were performed to determine the quality of the transistors and the charge carrier mobility: Output- and Transfer-Characteristics.

All OFETs were measured in a top-gate, bottom-contact configuration under nitrogen atmosphere utilizing a micromanipulator probestation (EP6, *SUSS MicroTec Test Systems*, Germany) and a *Keithley SourceMeter* (Model 2636, Dual channel).

The **Output-Characteristics** were measured by applying seven different gate voltages (V_G) and sweeping the source/drain-voltage (V_{SD}) from 0 V to -60 V for each V_G. The respective output curves, schematically shown in figure 2.6A, were obtained by plotting the source-drain-current (I_{SD}) against the source-drain-voltage (V_{SD}) for each gate-voltage. The Output-Characteristics are divided into the linear and the saturated regime. The linear regime is defined at small V_{SD} where the current (I_{SD}) increases linearly with V_{SD}. At higher V_{SD} the current (I_{SD}) saturates into a plateau called the saturation regime.[122]

The Output-Characteristics were used to check the quality and to determine leakage currents or short circuits in the devices. Such fault currents are typically indicated by negative currents at $V_{SD} = 0$ or the lack of a field dependency with the gate voltage.

In addition the Output-Characteristics can be used to determine the threshold voltage (V_{th}). V_{th} is defined as the minimum voltage difference between the gate and the source electrode that is need to obtain a charge flow inside the transistor channel.

The Transfer-Characteristics were used to determine the charge carrier mobility μ_{FET}, from here on just referred to as µ. For the measurement a fixed source-drain voltage (V_{SD}) in the saturation regime ($|V_{SD}| > |V_G|$ - $|V_{th}|$) was applied at −60 V and the gate voltage (V_G) was swept from 20 to −60 V. Plotting the source drain current (I_{SD}) as function of the gate-voltage (V_G) leads then to the Transfer-Characteristics as schematically plotted in figure 2.6B. The charge carrier mobility (µ) can be extracted using the following equation:[123]

$$I_{SD} = \frac{W}{2L}\mu \cdot C_i \left(V_G - V_{th}\right)^2 \tag{12}$$

were C_i is the capacitance per unit area of the dielectric layer and L and W define the channel length and width, respectively (see figure A.1). The capacity was calculated from the dielectric thickness (d), measured by AFM, and the relative (ϵ_r) and vacuum (ϵ) permittivity using the equation:

$$C_i = \frac{\epsilon \cdot \epsilon_r}{d}. \tag{13}$$

Further the threshold voltage (V_{th}) can be determined, which is defined by the minimum gate voltage needed to generate a measurable current (I_{SD}) and can be typically taken from the minimum of the transfer curves.

The charge carrier mobility (µ) was determined from a linear fit to the square root of I_{SD} as function of V_G utilizing equation 12.

2.4.2 Solar Cells

A bilayer configuration with a 40 nm thick polymer and a 40 nm evaporated C_{60} layer was chosen to eliminate the influence of the blend morphology on the device performance. The detailed configuration and the production method is given in chapter 3.2.5 and figure 3.5. To further ensure comparability the layer thicknesses were the same for all samples and the roughness was minimized as much as possible ensuring a similar interlayer area for charge separation.

The evaporation of the C_{60} layer and the characterization of the solar cells was performed in the group of Prof. D. Neher with the help of B. Tornow and Dr. S. Albrecht. Three different methods were used to characterize the solar cells:

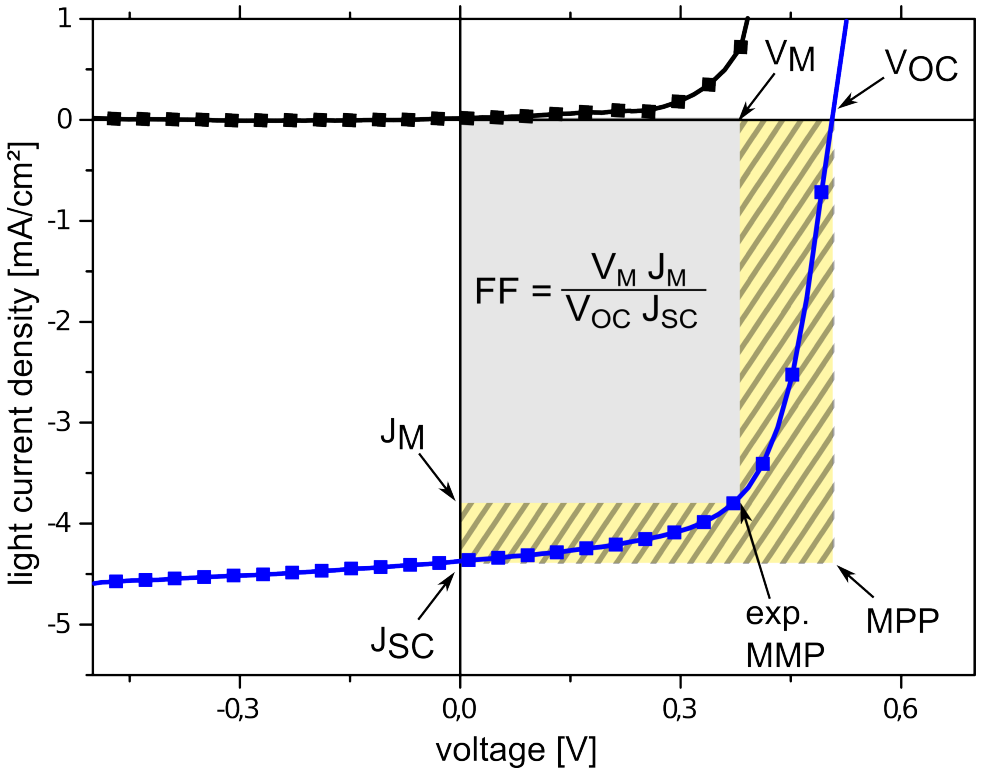

Fig. 2.7: Schematic J-V curve of an illuminated (blue) and a non-illuminated (black) device with the current density and the voltage on the y- and x-axis, respectively. The characteristic solar cell values are labeled as: short circuit current (J_{SC}), open circuit voltage (V_{OC}), fill factor (FF) (grey area) and the experimental maximum power point (exp. MPP). The theoretical values are additionally labeled as: maximum power point: (MPP) and J_M and U_M as the current and voltage of the experimental maximum power point.

Solar cell characteristics are typically taken from current-voltage curves (J-V curves) measured with and without illumination and give a general overview over the solar cell performance and their characteristic values. A general J-V curve is shown in figure 2.7 with labels highlighting the characteristic points: short circuit current (J_{SC}), open circuit voltage (V_{OC}) and fill factor (FF). To allow comparison of different sized solar cells not the current but the current density (mA/cm^2) is typically plotted.

The current flowing when no voltage is applied to an illuminated cell is called short circuit current (J_{SC}) and is a value for the maximal extractable current from a solar cell. This current at zero voltage flows because of a small internal electric field which is induced by the potential difference between the two electrodes (ITO and Al).

The open circuit voltage (V_{OC}) is defined as the point where no current is flowing caused by an compensation between the internal and external electric fields. The V_{OC} is directly correlated to the band gap between the HOMO of the donor and the LUMO of the acceptor phase and is sometimes referred to as the bulk heterojunction band gap, figure 1.5.[27] Further the fill factor (FF) is defined as the ratio between the theoretical maximum power point (MPP) and the experimentally achieved maximum power point (exp. MPP):

$$FF = \frac{J_M V_M}{J_{SC} V_{OC}} \tag{14}$$

with J_M and V_M as the current and voltage of the experimental maximum power point, respectively.

The shape of the curve gives further information about the field dependency of the solar cell which is a measure for how equally charges can be extracted over the applied voltage range. A low field dependency means that the current density stays constant over a large voltage range and the curve is assuming a rectangular form showing that the charges are extracted independent of the externally applied electrical field. It should be point out that the amount of extracted charges is determined by the interplay of the generation and recombination processes. To determine which of the processes is responsible for the observed field dependency additional measurements such as time delayed collection field (TDCF) have to be performed since it can not be extracted solely from the J-V curves.

The solar cell energy conversion efficiency (η) can be calculated by dividing the exp. MPP by the irradiated photon power density (P_{light} [W/cm^2]):

$$\eta = \frac{J_M V_M}{P_{light}} = \frac{FF \cdot J_{SC} \cdot V_{OC}}{P_{light}} \tag{15}$$

The measurements were performed in a nitrogen atmosphere at a constant temperature (25 °C) of the sample. The current was measured in relation to an applied voltage using a Keithley 2400 source meter. During the measurement the solar cell was illuminated with a simulated solar spectrum from a Sol2A sun simulator (*Newport*, Model 94042A) calibrated to 100 mW/cm^2 in accordance with the Air Mass 1.5 Global solar spectrum (AM1.5G). The simulator calibration was performed with a KG3 filtered mono crystalline silicon reference cell calibrated at Fraunhofer ISE (Potsdam-Golm). No mismatch correction was done, since the focus in this thesis lied on the comparison of different morphologies and on the field dependence of the curves.

External quantum efficiency (EQE) is a technique which measures the ratio between extracted charges and irradiated photons per second as function of the wavelength. The data are typically plotted as function of EQE against the wavelength and reveal the distribution of generated charges over the wavelengths. These data can therefore be used to understand which absorption bands are involved in generating free charges and often allow to separate between e.g. the polymer and the fullerene phases. The EQE is defined as:

$$EQE = \frac{\#electrons}{\#photons} = \frac{I(\lambda)e^{-1}}{P(\lambda)\left(\frac{hc}{\lambda}\right)^{-1}} \tag{16}$$

with I(λ) and P(λ) as the wavelength dependent current [C/s] and irradiated photons [J/s], respectively. The further constants are e the elementary charge [1.60×10^{-19} C], h the Planck constant [6.62×10^{-34} J/s], c the speed of light [299 792 458 m/s] and λ the wavelength [nm].

In addition an external field can in-situ be applied to the solar cell during the EQE measurements, which is then called field dependent external quantum efficiency (FEQE). From such measurements current-voltage curves can be extracted for certain wavelengths and be compared to the J-V curves.

The EQE measurements were performed in a nitrogen atmosphere after the solar cell characteristics were measured. A high-pressure halogen lamp (*Philips*, model 7724) was used to generate monochromatic light and was chopped to 90 Hz for the detection with a lock-in amplifier (Princeton Applied Research, model 5302) over a 1 kΩ resistor. The intensity of the light was checked with an UV enhanced crystalline silicon solar cell (*Newport* 818-UV), calibrated at Newport. For field dependent measurements an additional Keithley 2400 was used to apply the external field.

Time delayed collection field (TDCF) allows to measure the total generated free charges (Q_{tot}) before non-geminate recombination occurs (a bimolecular recombination of two charges generated during different absorption processes).[27,120] Changing the applied pre-bias the field dependence of the free charge generation (Q_{tot}) can be investigated and discriminated from the non-geminate recombination process. TDCF is based on the knowledge that the free charge generation is completed within a few picoseconds as shown by several groups[124–126] utilizing transient absorption spectroscopy and that the non-geminate recombination takes place after a few tens of nanoseconds.[127] These different time scales allow to extract all generated charges before non-geminate recombination takes place which was shown in detail for the conjugated polymer P3HT by Neher et al.[128]

Figure 2.8 is a schematic of the time (x-axis) and the applied bias (y-axis) for a TDCF measurement. At the beginning a pre-bias is applied to the solar cell and kept constant while free charges are generated by a 5 ns laser pulse (t_0) and a delay time of 10 ns. After the delay period the collection voltage (V_{coll}) is applied to extract all charges from the device.

A too intense laser pulse would lead to a much higher charge density than in a normally operated solar cell resulting in an additional bimolecular recombination process which could falsify the measurement. In the group of Prof. Neher the effect of the laser intensity was investigated using the same polymers as in this thesis.[127] Using these results the laser intensity was optimized measuring outside of the bimolecular recombination regime.

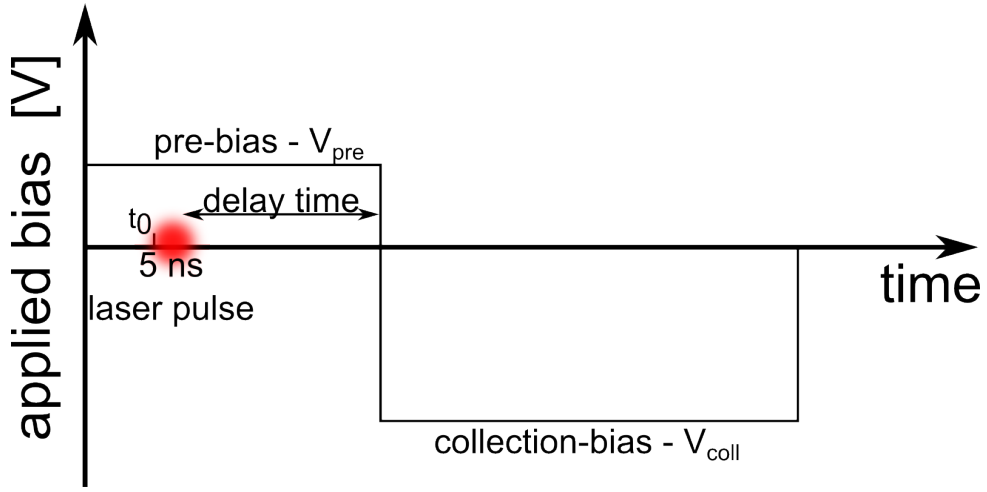

Fig. 2.8: Applied bias as function of time during a typical TDCF measurement. A pre-bias is applied before a 5 ns laser pulse which generates free charges. After a delay time of 10 ns during which the pre-bias is kept constant a collection bias is applied to extract all free charges (Q_{tot}) from the solar cell.

The TDCF measurements could not be performed inside a glovebox and were therefore performed after the J-V-curve and EQE measurements. Before the TDCF measurement the solar cells were encapsulated by gluing a glass slide on top of the solar cell using an epoxy resin. The charge generation was induced by a laser pulse (5.5 ns pulse width, 500 Hz repetition rate, 10 ns jitter) of a diode-pumped, Q-switched Nd:YAG laser (NT242, EKSPLA). The pre- and collection bias was applied by an Agilent 81150A pulse generator. The measurement of the current through the device was performed with an Agilent DSO 9054H oscilloscope via a 50 Ω resistor which was connected in series with the sample. To trigger the pulse generator a fast photo diode (EOT, ET-2030TTL) was utilized . The internal latency time of the pulse generator was compensated by delaying the laser pulse with a 85 m long multi-mode fiber (LEONI) with respect to the trigger diode. The pulse

fluence was determined with a power meter (Ophir, Vega) equipped with a crystalline silicon photo diode sensor (PD300-UV).

2.5 Polymer Analysis

2.5.1 Thermal Analysis

Thermal analysis was performed to investigate the decomposition and glass transition temperatures as well as the melting points of the investigated polymers. Without the knowledge of the thermal transitions an optimized thermal post-annealing is impossible since the temperature protocol must be adapted. For thermal annealing the temperature must be chosen such that a polymer chain mobility is possible (above the glass-transition) but earlier induced order is not destroyed (below the melting point). The decomposition temperatures, glass transitions temperatures and melting points were determined by thermal gravimetric analysis and differential scanning calorimetry, respectively:

Thermal gravimetric analysis (TGA) was performed on a *NETZSCH* STA 449C, in the group of Dr. J. Kerres (Institute for Chemical Process Engineering, University of Stuttgart) using an Al_2O_3 pan in the purging gas mixture O_2/CO_2 (1:1 Vol.) with a flow rate of 50 ml/min each.

Differential scanning calorimetry (DSC) was performed on a DSC-6000 from *Perkin Elmer*. The normal procedure consisted of two heating and two cooling cycles with heating/cooling rates of 10 K/min. To investigate the thermal behavior of highly crystalline samples the polymers were solvent vapor annealed inside of DSC pans before the measurement. Therefore a DSC pan was filled with a few mg of the polymer and annealing solvent (45 µl). The filled pan was then placed inside a solvent chamber of saturated solvent vapor and the solution equilibrated for several hours at elevated temperatures (50 °C) in the vapor. In a second step crystallization was induced by decreasing the vapor pressure over night to a pure nitrogen atmosphere. To remove any remaining solvent residues the nitrogen dried samples were afterwards vacuum treated for at least 12 h before thermal analysis.

2.5.2 High Temperature Gel Permeation Chromatography - HT-SEC

All polymers were characterized by high temperature size exclusion chromatography (PL-GPC 220 from *Agilent*) at 160 °C equipped with the column "PLgel Olexis" from *Agilent* optimized for molecular weights between 2000 to 10 000 000 g/mol. The HT-SEC was calibrated against polystyrene standards (figure A.21) and at least one standard was

checked together with each batch of polymers to ensure comparable results. The polymers were dissolved in 1,2,4-trichlorobenzene over night at 130 °C (ca. 1 mg/ml) and measured using a refractive index detector at 160 °C.

3 Experimental

3.1 Materials

3.1.1 Polymers

The batches of the three PCPDTBT (poly[2,6-(4,4-bis-(2-ethylhexyl)-4H-cyclopenta [2,1-b;3,4-b'] dithiophene)-*alt*-4,7-(2,1,3-benzothiadiazole)]) derivatives used in this thesis are summarized in table 3.1. The chemical structures are shown in figure 3.1. The molecular weights were determined by high temperature size exclusion chromatography (HT-SEC, trichlorobenzene, 1 mg/ml, 160 °C, against polystyrene, see figure A.21 for molecular weight distributions). Throughout this thesis the three derivatives will be referred to as PCPDTBT, F-PCPDTBT (poly[2,6-(4,4-bis-(2-ethylhexyl)-4H-cyclopenta[2,1-b;3,4-b']dithiophene)-*alt*-4,7-(5-fluoro-2,1,3-benzothiadiazole)]) and Si-PCPDTBT (poly[(4,4'-bis(2-ethylhexyl)dithiene-[3,2-b:2',3'-d]silole)-*alt*-4,7-(2,1,3-benzothiadiazole)]) Only in the case of Si-PCPDTBT different molecular weights were available. Throughout this thesis the respective molecular weights are always stated for the particular used Si-PCPDTBT batch.

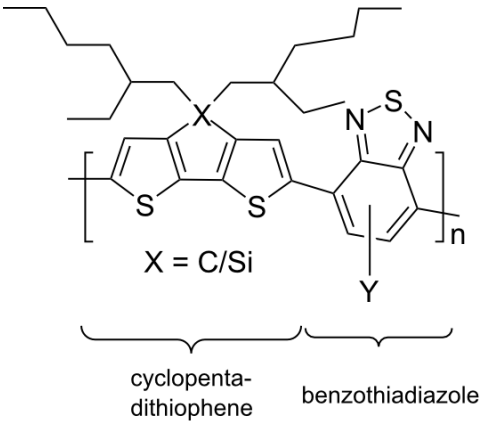

Fig. 3.1: Chemical structure of PCPDTBT (X = C, Y = H), Si-PCPDTBT (X = Si, Y = H) and F-PCPDTBT (X = C, Y = F).

Tab. 3.1: High temperature SEC measured on a *PL-GPC 220 (Agilent Tecnologies)* at 160 °C in trichlorobenzene against polystyrene. The molecular weight distributions and calibration are shown in figure A.21.

Polymer	batch	M_n [kg/mol]	M_w [kg/mol]	PDI
PCPDTBT	YY3-023CH[a]	14.7	26.7	1.8
F-PCPDTBT	KE11/3[b]	6.7	10.8	1.6
Si-PCPDTBT	*unknown*[c]	11.0	32.3	2.9
Si-PCPDTBT	YY5130B[a]	4.9	11.3	2.3
Si-PCPDTBT	SX6243[a]	2.9	10.5	3.6
Si-PCPDTBT	YY3091[a]	2.0	4.4	2.3

[a] The material was bought from *1-material*.
[b] Synthesized by the group of Prof. Janietz.[5]
[c] The material was bought from *Konarka* and was provided by the group of Prof. Neher.

3.1.2 Solvents, Chemicals and Substrates

All solvents, chemicals and substrates in this study were purchased from different manufactures and were used without further purification. A detailed summary is given in table 3.2. The surface of the substrates were cleaned before thin film deposition; detailed cleaning protocols are are given in chapter 3.2.1.

Substrates

Thin films (10 to 50 nm) investigated in this study were prepared on five different substrates depending on the requirements of the intended measurements: Si-wafer (AFM, SEM), SiO_x-wafer (ED/TEM), quartz-slides (absorption-, photoluminescence spectroscopy), glass-slides (absorption spectroscopy, transistor measurements) and ITO-slides (electrochemistry, solar cell characterization).

Silicon wafers were purchased from *CrysTec* as wafers of 150 mm diameter and divided using a glass cutter into ca. $2 \times 2\,cm^2$ pieces. The Si-wafer either contained a native (5 nm) or a thermally grown (300 nm) silicon oxide layer.

Transparent substrates were used for transmission spectroscopy. Absorption measurements between 350 to 2000 nm were often performed on pure glass-slides. In cases where solvent vapor annealing was performed or lower wavelength absorption (<350 nm) and photoluminescence was measured quartz-slides of 0.9 mm thickness were used.

Transistor substrates were prepared by evaporating gold source- and drain-electrodes (30 nm) on $2 \times 2\,cm^2$ SiO_x-wafers (cleaned by SnowJet and O_2-plasma) with a thin chromium layer (3 nm) as adhesion layer below the gold electrodes. The evaporation was performed through a polyimide shadow mask (*CADiLAC Laser GmbH*) at 10×10^{-6} bar with evaporation rates of 0.25 Å/s and 2.0 Å/s for chrome and gold, respectively. The final substrates contained 16 transistors with channels of 1 mm width divided in four transistor sets (a,b,c and d) of different channel lengths: 100, 150, 200 and 250 µm. A layout of the source-drain-electrodes is shown in figure A.1C.

ITO coated glass slides were used for the (spectro) electrochemistry (without patterning) and for solar cells (pre-patterned) purchased from *pgp* and *Lumtec*, respectively. The unstructured ITO substrates were cut into $2 \times 0.8\,cm^2$ peaces. The layout of the pre-patterned ITO-substrates is shown in figure A.1B.

Tab. 3.2: Summary of solvents, chemicals and substrates used in this thesis.

solvent	manufacturer	purity	boiling point [°C]	nomenclature
Acetonitrile	Sigma-Aldrich	p.a.	82	MeCN
Carbon disulfide	Sigma-Aldrich	p.a.	32	CS_2
Chlorobenzene	Sigma-Aldrich	p.a.	130	CB
Chloroform	Sigma-Aldrich	p.a.	61	$CHCl_3$
1-Chloronaphthalene	Sigma-Aldrich	technical[a]	259	1-CN
1,2-Dichlorobenzene	Sigma-Aldrich	p.a.	181	DCB
1,8-Diiodooctane	Sigma-Aldrich	98 %	167	DIO
1,2,4-Trichlorobenzene	Sigma-Aldrich	p.a.	213	TCB
Propylene carbonate	Sigma-Aldrich	p.a.	242	PC
Tetrahydrofurane	Sigma-Aldrich	p.a.	65	THF
Methylene chloride	Sigma-Aldrich	p.a.	40	CH_2Cl_2
chemicals	manufacturer	purity		nomenclature
Tetrabutylammonium hexafluorophosphate	Sigma-Aldrich			$TBAPF_6$
Tetrahexylammonium hexafluorophosphate	Sigma-Aldrich			$THAPF_6$
Ferrocen	Sigma-Aldrich			Fc
PEDOT:PSS	Heraeus[b]			
Bathocuproine	*MER Corp.*	sublimed 99.99 %		BCP
substrates	manufacturer	thickness		nomenclature
Silicon wafer[c]	CrysTec	675 ± 25 nm		Si-wafer
Silicon oxide wafer	CrysTec	675 ± 25 nm		SiO_x-wafer
Quartz	VWR	0.9 mm		quartz-slides
Glass	Thermo Scientific (Menzel-Gläser)			glass-slides
ITO[d]	PGP	0.7 ± 0.1 mm		
pre-patterned ITO[e]	Lumtec Taiwan	0.7 mm		

[a] technical, ≥85 % (GC), contains ˜10 % impurities of 2-chloronaphthalene.
[b] CLEVIOS^{TM} P VP AI 4083, PEDOT:PSS ratio 1:6 (by weight).
[c] polished, p-type (boron doped), resistivity 1 to 30 Ωcm
[d] Indium tin oxide, used in the electro chemistry, ≤50 Ohm/sq, product code: CEC050S
[e] used for solar cells.

3.2 Sample Preparation

In general all samples during this study were prepared as thin films (10 to 50 nm thickness) on adequate substrates for the intended measurements. The few exceptions in which thin films were not used is the thermal analysis by thermogravimetry (TGA) and differential scanning calorimetry (DSC). The respective procedures are described in the particular chapters. In this chapter first a description of the general cleaning procedures for all substrates and the typical thin film preparation methods are given followed by detailed summaries of the specific sample preparation techniques.

3.2.1 Substrate Cleaning

All substrates were cleaned right before thin film preparation. The cleaning procedure was generally performed at ambient air and the substrates were transfered into the glovebox directly after cleaning for thin film preparation. Mainly three methods were used for cleaning depending on the substrates and the requirements for further analysis: Snow jet, O_2-plasma and solvent cleaning.

The **snow jet** cleaning procedures was used for Si-, SiO_x-wafer, glass-slides and quartz-slides as first cleaning step to remove dust particles from the top surface. The snow jet (GunJet 30) from *Spraying Systems Deutschland GmbH* (Hamburg) produces a high-velocity carbon dioxide jet (purity 4.5) through an orifice which consists of small dry ice particles caused by the strong cooling during the gas expansion. Directing this jet onto a heated (ca. 200 °C) substrate surface leads to an abrupt sublimation of the dry ice particles, mechanically sweeping away any contamination from the surfaces. This cleaning procedure could only be used for substrates without any evaporated or thermally grown structures such as gold or ITO since they were partly lifted off by the snow jet.

O_2-plasma was generally used for Si-, SiO_x-wafer, glass-slides and quartz-slides as a second and for ITO substrates as first cleaning step to remove any organic contaminations from the surface. The oxygen plasma (10 min at 100 W) was applied utilizing a Femto plasma cleaner from *Diener electronic GmbH + Co.* (Ebhausen).

The following thin film preparation was always carried out directly after removing the substrates from the oxygen plasma and transferring them into the glovebox to prevent any fresh contamination.

Solvent cleaning was only applied to pre-patterned ITO coated glass slides when preparing bilayer solar cells. The procedure was adapted from the group of Prof. Neher, Potsdam. The substrates were cleaned by a 10 min ultrasonic treatment in the following

solvents: acetone, detergent, deionized (DI) water, isopropanol. The substrates were dried afterwards in an argon stream (purity 5.5) followed by a 10 min oxygen plasma treatment (10 min at 100 W).

3.2.2 Thin Film Preparation

In this study the thin films were prepared from solutions with concentrations around 3 mg/ml in most cases. In general the thickness of the films was checked by AFM and the processing conditions adapted to obtain film thicknesses between 10 to 40 nm. The solutions were prepared inside the glovebox and stirred for at least 2 h at 10 to 20 K below the boiling point of the respective solvent, but never at temperatures higher 80 °C. After removing the solutions from the hotplate the processing was performed within 5 to 10 min. In general no solutions older than 5 days were used.

Spin coating is the method which was mainly used in this study for thin film preparation except from occasional drop casting. Spin coating was carried out inside the glovebox using a Delta 6RC from *SUESS*. A droplet of 20 to 50 µl polymer solution is placed on a substrate, which then is spun with speeds varying between 600 to 2000 rpm for 30 to 1800 s depending on the intended film thickness, solution concentration and boiling point of the processing solvent. To gain homogeneous films the acceleration period was in some cases increased from the standard 500 ms. Within the first spinning step the majority of the film is formed and only at the substrate edges thicker areas of solution remain. Therefore the first step was always followed directly by an additional step of 6000 rpm for 10 to 15 s producing a homogeneous film with only very little artifacts at the substrate edges. In a final step the films were exposed to vacuum atmosphere to remove remaining solvent. The exact processing conditions for each sample are stated throughout this thesis.

3.2.3 Annealing Procedures

The quick drying process during spin coating allows almost no control over the film formation and possible crystallization. Therefore a standard procedure in this study was an additional annealing step such as solvent vapor or temperature annealing to increase the order within the films. Annealing of the spin coated films either by temperature or solvent vapor increases again the mobility of the polymer chains and allows a reorganization or recrystallization into a thermodynamically more favorable state. The annealing steps were performed under a nitrogen or argon atmosphere to avoid degradation. A detailed description is given in the following.

Thermal Annealing

In this study thermal annealing was performed in an argon atmosphere utilizing a hot stage (THMS600 from *Linkam*) with active cooling by liquid nitrogen. This allowed slow and accurate cooling rates. The annealing was followed in-situ either with an optical microscope or an UV–Vis–NIR spectrometer. For the absorption spectroscopy a specialized lit and bottom were fabricated from the mechanics workshop allowing in-situ transmission measurements under argon.

Solvent Vapor Annealing and Crystallization

Solvent annealing is a well known method from literature[129–131] and was the standard annealing method in this study to increase the morphological order of precasted polymer films. A lot of experience regarding this method was gained in our group during the study of P3HT as described in several publications from Crossland et al.[15,16,83] which were used as base for this thesis. The basic idea behind solvent annealing is to increase the polymer chain mobility within a thin film by swelling it in a vapor of a good solvent. After the film reaches a dissolved like state the solvent vapor pressure is reduced to a point where recrystallization occurs. The advantage compared to temperature annealing is that the process can take place at moderate temperatures far below the melting point or even decomposition temperature which particularly lowers the possibility of degradation during post annealing.

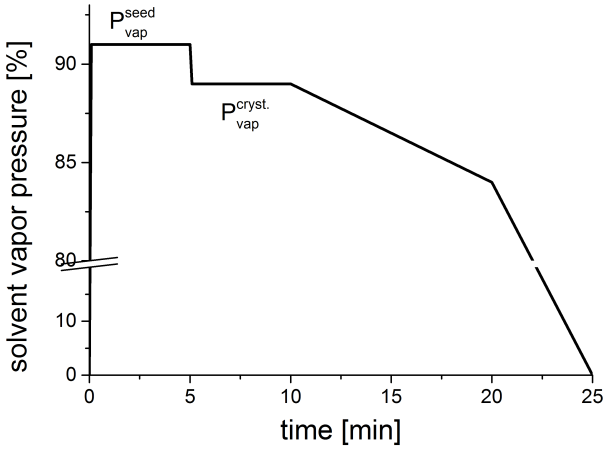

Fig. 3.2: Typical solvent vapor annealing protocol.

The self-built setup is schematically shown in figure 3.3. The temperature of the vapor is controlled by the water bath in which the whole setup is embedded ($T_{vap} = T_{bath}$). Only the top of the annealing chamber protrudes beyond the water level allowing in-situ observation and was additionally heated to prevent condensation on the quartz glass lid. On the left side the adjustment of the solvent vapor pressure ($P_{vap} = \frac{P_{sol}}{P_{N_2}}$) is shown: A dry nitrogen stream (P_{N_2}) is mixed with a nitrogen stream saturated with the annealing solvent (P_{sol}) by bubbling through a solvent filled washing bottle. The mixing ratio is controlled by two gas flow controllers (labeled at A and B) from *MKS* with an accuracy of

±0.01 sccm. The sample is mounted within the solvent chamber on top of a thermoelectric element which allows an independent control of the sample temperature. To ensure a swelling of the film a temperature difference between the vapor and the substrate of 2 to 8 K was generally necessary.

A typical solvent annealing protocol comprises two steps: swelling of a film and recrystallizing, figure 3.2. In the first step the film is swollen as much as possible without dewetting (P_{vap}^{seed}) to increase the polymer chain mobility and dissolve aggregates and crystals present in the pre-casted film. Depending on the chosen vapor pressure either all aggregates are dissolved or the thermodynamically most stable aggregates remain undissolved and can act in the following recrystallization as seeds.[83] In the second step the solvent vapor pressure is dropped to a pressure at which crystallization takes place ($P_{vap}^{cryst.}$), figure 3.2. It was observed that increasing or decreasing the vapor pressure too fast often leads to a dewetting of the films instead of a homogeneous swelling. This was prevented by using ramps which slowly change the vapor pressure. The exact annealing protocols including the used ramps for all samples are given throughout this thesis at the respective locations.

The success of solvent annealing strongly depends on the choice of the solvent. It was found, for example, that for P3HT highly crystalline films with low nucleation density can be obtained with carbon disulfide (CS_2) as annealing solvent. Mainly two factors

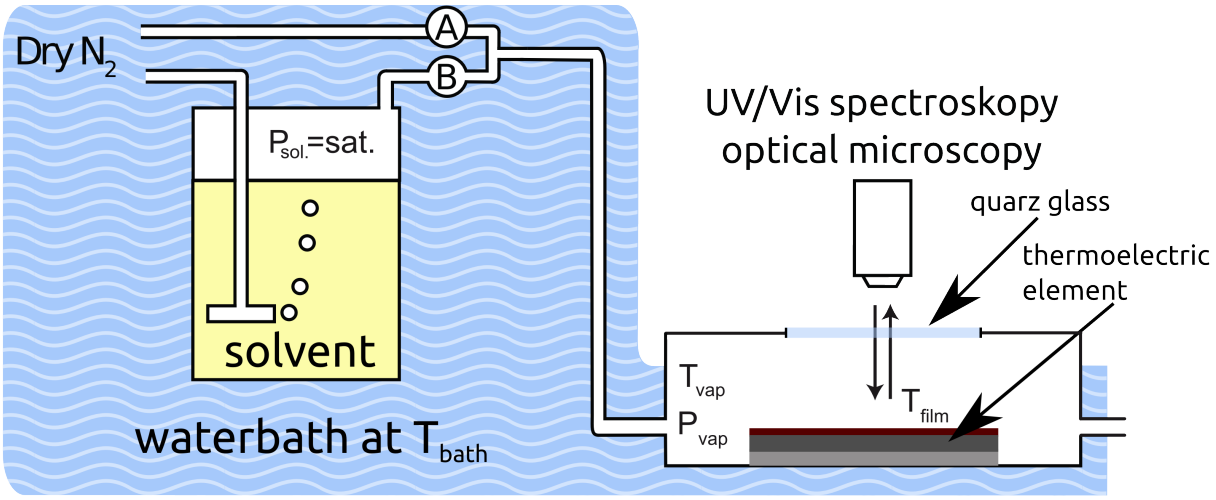

Fig. 3.3: Schematic illustration of the solvent vapor annealing setup. To control the vapor temperature (T_{vap}) the complete setup is embedded within a water bath except the top of the annealing chamber allowing in-situ investigations. One pure stream of nitrogen (purity 4.5) is split such that one half is saturated by bubbling through a washing bottle of the annealing solvent (P_{sol}). A defined vapor pressure within the annealing chamber is achieved by mixing the saturated with the dry nitrogen stream at a defined ratio ($P_{vap} = \frac{P_{sol}}{P_{N_2}}$). The sample is mounted within the chamber on a thermoelectric element controlling the temperature of the sample (T_{film}). A quartz glass within the chamber lit allows in-situ absorption spectroscopy and optical microscopy investigations.

make CS_2 such a good annealing solvent: First the good solubility of P3HT in CS_2 and second the low boiling point (46 °C) which allows high vapor pressures already at room temperature. In this study new solvents (mainly chlorobenzene) were tested often with boiling points above 100 °C. Such high boiling point solvents cause two new problems: i) at room temperature already the saturated vapor has such a low vapor pressure that the films will not swell. ii) if the temperature of the water bath and therefore also the vapor temperature is increased above room temperature condensation occurs at every part of the setup which is not within the water bath. One of the previous built setups was therefore modified such that not only the washing bottle but also the connection between washing bottle and the annealing chamber itself are kept at the same temperature.

Solvent crystallization is a variation of the solvent annealing method and was started during this study, because some polymers could not be swollen by traditional solvent annealing. It was assumed that because of their strong tendency to form aggregates the films consisted after spin coating already of poorly soluble aggregates. Therefore instead of pre-casting thin films a cleaned substrate was placed into the solvent chamber and covered with a drop of a highly diluted polymer solution of the annealing solvent (0.01 to 0.1 mg/ml). Before the drying of the droplet started, a vapor pressure similar to the swelling step during the solvent annealing was applied and an equilibrium between solution and vapor was reached. To crystallize the polymer the vapor pressure was slowly lowered over several hours inducing crystallization.

3.2.4 Polymer Backbone Alignment in Thin Films

For a crystal structure analysis it is often needed to obtain diffraction patterns along the polymer backbone direction. Therefore the polymer films must be oriented with the backbone parallel to the substrate. high-temperature rubbing[132,133] and epitaxy[134,135] are two methods proven to align conjugated polymers in thin films.

High-Temperature Rubbing

High-temperature rubbing (HT-rubbing) was performed on a self-built setup in the group of Dr. Brinkmann at the *Institut Charles Sadron* (ICS) of the *Centre national de la recherche scientifique* (CNRS) in Strasbourg.

For HT-rubbing polymer films were prepared on glass-slides and fixated by vacuum on a heatable translation stage under a rotating cylinder covered with a microfiber cloth, figure 3.4. Prior and during the rubbing the polymer film was heated under a nitrogen atmosphere to prevent degradation. The respective heating temperature is given

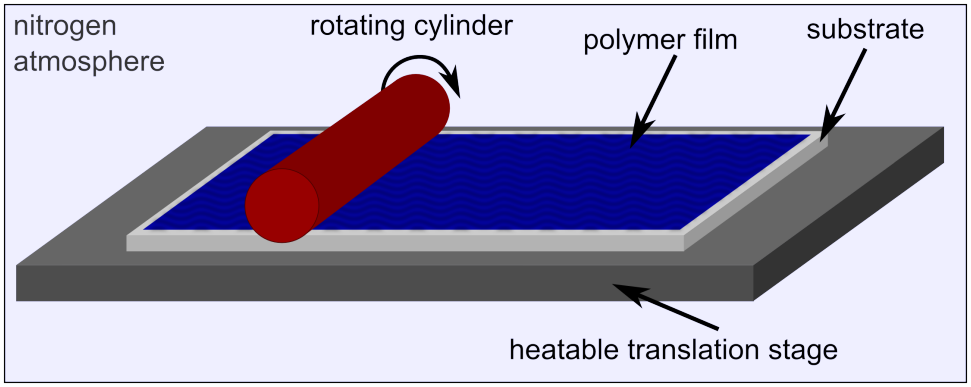

Fig. 3.4: Sketch of the self-built high-temperature rubbing setup.

throughout the thesis for the respective samples. While pressing the rotating cylinder with 2 bar onto the polymer film the substrate was moved at a constant speed (1 cm/s). This leads to shearing forces which align the backbones in the rubbing direction. To increase the alignment several rubbing cycles can be performed for each film.

Epitaxy

Epitaxy means the crystal growth of polymer films on pre-oriented substrates. In this thesis pre-oriented polytetrafuorethylen (PTFE) layers were used as pre-oriented substrates. The pre-oriented layers were prepared by sliding a PTFE cylinder with a pressure of 5 bar over a glass substrate which was held at 250 to 300 °C. It was shown in literature that by employing this method PTFE films with the backbone (c_{PTFE}) aligned in the rubbing direction can be obtained.[134, 135]

PCPDTBT layers were prepared on top of such aligned PTFE substrates by spin coating from chlorobenzene solutions (3 mg/ml). Melt-annealing was finally used to induce epitaxial growth of the PCPDTBT. Therefore the films were heated up to 290 °C, cooled with 0.25 K to 280 °C and held for 4 h, before cooling with 0.25 K back to room temperature.

3.2.5 Specific Sample Preparations

TEM grid preparation

Samples for TEM/ED investigations were prepared by spin coating and different annealing steps on SiO_x substrates (300 nm thick thermally grown silicon oxide layer) or on pure glass slides. The films were coated with a thin amorphous carbon layer to prevent charging during the TEM measurements. Afterwards a polarized optical microscope (*Leica* DMR-X) was used to select areas of interest and the areas were labeled by cutting circles with

a diameter of the TEM grids into the film. The films were then floated onto a diluted aqueous hydrofluoric acid (5 to 10 %) and transfered onto TEM copper grids. The transfer was performed right before the TEM/ED measurements in the group of Dr. Brinkmann at the *Institut Charles Sadron* (ICS) of the *Centre national de la recherche scientifique* (CNRS).

Solar Cell Preparation

The solar cells were prepared on pre-patterned ITO-substrates (see chapter 3.1.2) which were cleaned in an ultrasonic bath with different solvents followed by an oxygen plasma treatment (10 min at 100 W, see chapter 3.2.1). On the cleaned substrates a 40 nm hole injection PEDOT:PSS layer (Clevios Ai 4083) was spin coated (30 sec at 2400 rpm) and dried by annealing for 10 min at 180 °C. The samples were vacuum treated for at least 1 h and transfered into the glovebox.

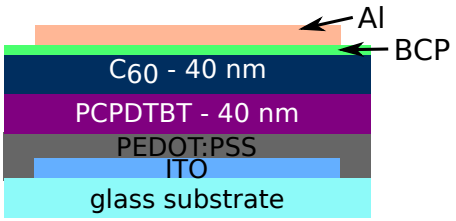

Fig. 3.5: Schematic of the layers in bilayer solar cells.

The polymer layers were then spin coated from $CHCl_3$ or chlorobenzene/diiodooctane (CB/DIO, 2 w% DIO) solutions of 3 mg/ml and 10 mg/ml, respectively. The spin coating conditions were adjusted to achieve film thicknesses of 40 ± 3 nm for all samples and were checked by AFM. For the CS_2-annealed samples pre-casted $CHCl_3$ films were additionally solvent annealed, applying the annealing protocol given in figure A.10.

The samples were transfered under nitrogen atmosphere to the group of Prof. Neher, University of Potsdam and finalized by evaporation at 10^{-6} mbar a 40 nm C_{60} layer followed by 5 nm of bathocuproine (BCP) and a 100 nm Al top electrode. Schematics of the prepared solar cell configuration is shown in figure 3.5 and figure A.1

Transistor Preparation

For mobility measurements organic field effect transistors (OFETs) were used. Figure 3.6 shows a top-gate, bottom-contact configuration as used throughout this thesis. For preparation a glass substrate was cleaned via snow jet and O_2-plasma. As source- and drain electrodes gold (30 nm, Au with a 3 nm Cr adhesion layer) was evaporated at 10^{-6} mbar with 5 Å/s through a

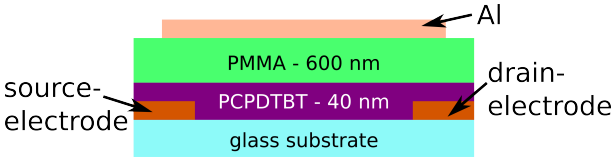

Fig. 3.6: Schematic of a bottom-contact (source- and drain-electrode), top-gate (Al) transistor setup.

shadow mask (polyimide, $50 \pm 5\,\mu m$ bought from *CADiLAC Laser GmbH*, Hilpoltstein) resulting in sixteen transistors of four different channel lengths: 100, 150, 200 and 250 µm and each with a channel width of 1 mm. An exact layout of the shadow mask is shown in figure A.1. The polymer films were prepared directly after evaporation forming 30 to 50 nm thick films. The detailed preparation of the polymer layers is given during the discussion of the respective samples. The PMMA layer was spin coated (90 s at 1200 rpm) from a 60 mg/ml solution, dissolved at 80 °C over night in n-butyl acetate and cross-linked after spin coating within 30 min at 80 °C on a heating plate under nitrogen. To ensure a good contact during the measurement a toothpick was used to remove the PMMA layer from the source- and drain-electrodes. The OFETs were then finalized by evaporating the Al gate electrode through a shadow mask (*CADiLAC Laser GmbH*) at 10^{-6} mbar with 2.5 Å/s (figure A.1).

4 Correlation between Morphology and Absorption Properties

In the literature it is well known that the absorption behavior of conjugated polymers is influenced by their morphology. In chapter 1.2.5 it was shown for P3HT how changes in the molecular weight and the packing of the polymer backbones can induce shifts and additional aggregation bands in the absorption signature. Spano et al.[7–9,84,136] studied the influence of morphology on the absorption of several polymer systems over the last years. They showed that it was possible to model the absorption as well as the photoluminescence spectra from solutions and films using the Franck-Condon principle, chapter 1.2.5. These studies investigated the properties of homopolymers such as poly(3-hexylthiophene) (P3HT),[8,9] poly(p-phenylene vinylene) (PPV),[94] poly[2-methoxy-5-(2'-ethylhexyloxy)-p-phenylene vinylene] (MEH-PPV)[93,137] and polyfluorene (PFO)[95]

All conjugated polymers investigated by the model of Spano et al.[7–9,84,136] are, to the best of my knowledge, homopolymers. There is one copolymer that has been intensively investigated in the literature by Brinkmann et al.,[138] with respect to correlations between absorption and morphological properties: poly[N,N'-bis(2-octyldodecyl)-1,4,5,8-naphthalene-dicarboximide-2,6-diyl]-*alt*-5,5'-(2,2'-bithiophene) (P(NDI2OD-T2)) (chemical structure shown in figure 1.2). Its absorption spectrum shows a typical donor-acceptor copolymer signature with both a high (380 nm) and a low (600 nm) energy absorption band. In addition a fine structure is revealed when going from the dissolved to the solid state.[139]

Brinkmann et al.[138] used different annealing protocols and high resolution TEM (HR-TEM) to identify two polymorphs in P(NDI2OD-T2) thin films, called form I and form II. Interestingly the two polymorphs display two different polymer backbone stackings, resulting in different absorption spectra. For form I a segregated stacking of the bithiophene donor units (T2) and the naphthalene diimid acceptor units (NDI) was found. The corresponding absorption spectra of form I shows a broad, structured absorption with a maximum at 700 nm and a second vibronic band around 810 nm. Form II on the other hand revealed a stacking in which every second backbone is shifted by $c/2$ leading to a mixed π-stacking of the T2 and the NDI units. This polymer arrangement results in an absorption with a maximum at 700 nm and a shoulder around 640 nm. Brinkmann et al. suggested that the different chain packings of the two polymorphs influence the interchain exciton coupling and lead thereby to the different absorption signatures.

This demonstrates that especially for the case of copolymers, where the number of different stacking possibilities is increased, the polymer morphology can strongly effect the

optical properties. Exactly such considerations were taken into account for this study of the donor-acceptor copolymer PCPDTBT.

4.1 Aggregation in Solution

In solution a high control over the aggregation tendency can be obtained by changing either the temperature or the concentration of the solution. In-situ absorption spectroscopy allows to study the evolution of the optical properties during aggregation. In the following chapters the spectroscopic behavior of PCPDTBT and its derivatives in solution is studied. The transition of the polymers from the dissolved to the aggregated state is analyzed using the Franck-Condon method and discussed in detail. The results lay the foundation for the understanding of the UV–Vis–NIR-absorption and PL spectra of aggregated thin films which will be discussed later on in this thesis. The contents of this chapter with respect to PCPDTBT have been published in [11, Fischer et al. 2013].

4.1.1 Absorption and PL Behavior in Solution

In preliminary experiments, the completely dissolved polymers (PCPDTBT, F-PCPDTBT and Si-PCPDTBT) were investigated by absorption and photoluminescence (PL) spectroscopy in solution. Figure 4.1A (left axis) shows the typical UV/Vis-spectra of PCPDTBT dissolved in good solvents (0.01 mg/ml). The spectrum reveals two main absorption bands: one at low energies around 730 nm accompanied by a shoulder around 670 nm and one high energy band around 420 nm. The photoluminescence (MTHF, 67 °C, 0.25 mg/ml) shown in figure 4.1A (right axis) resembles a classic mirror image of the absorption with a maximum around 780 nm.

Lanzani et al.[140] investigated the absorption of PCPDTBT by DFT calculations and ultrafast spectroscopy. They showed that the low energy absorption is correlated to a charge-transfer (CT) transition between the delocalized HOMO and the LUMO which is localized on the benzothiadiazole units (BT). The shoulder of the low energy band at 670 nm was further assigned to a vibronic mode and the high energy absorption to a S_0 to S_n transition. Besides our study [10, Scharsich and Fischer et al. 2015] there are, to the best of my knowledge, until today no further studies on the detailed PL behavior of the pure PCPDTBT.

To better understand the absorption behavior DFT//B3LYP/6-31G** calculations were performed for PCPDTBT in cooperation with M. C. Ruiz Delgado (Department of Physical Chemistry, University of Málaga, Campus de Teatino, Spain) employing an oligomer approach.[11,141] Figure 4.1B displays for a $(CPDTBT)_3$ oligomer the molecular

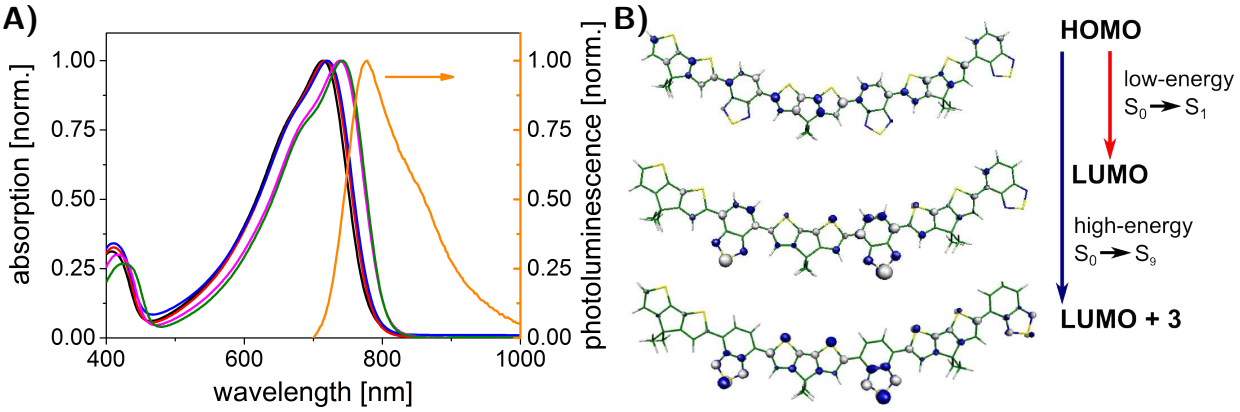

Fig. 4.1: A) Left axis: Absorption spectra of a $0.01\,\mathrm{mg/ml}$ solution of PCPDTBT in THF (black, $\epsilon = 7.4$), $CHCl_3$ (red, $\epsilon = 4.6$), CB (blue, $\epsilon = 5.6$), 1-CN (pink, $\epsilon = 5.04$) and CS_2 (green, $\epsilon = 2.6$).[142] Right axis: Photoluminescence of PCPDTBT dissolved in 2-Methyltetrahydrofuran (MTHF, $0.25\,\mathrm{mg/ml}$) at $67\,^{\circ}\mathrm{C}$. **B)** Molecular orbitals calculated by DFT//B3LYP/6-31G** of the low ($S_0 \rightarrow S_1$) and the high energy ($S_0 \rightarrow S_9$) transition from the $(CPDTBT)_3$ oligomer (adapted from[11]).

orbitals involved in the low energy ($S_0 \rightarrow S_1$) and the high energy ($S_0 \rightarrow S_9$) transition. For the oligomers $(CPDTBT)_n$ (n = 1-5) a strong red shift of the absorption was found going from n = 1 to n = 3. The red shift increase no further for n > 3, indicating that already three to four conjugated CPDTBT units are sufficient to develop the characteristic absorption spectra of PCPDTBT.

4.1.2 Influence of Solvent Polarity

In donor-acceptor copolymers the low energy peak is caused by the charge-transfer character of the HOMO/LUMO transition. Such a transition is always associated with a transfer of charge density from the donor to the acceptor unit which causes a change in the dipole moment of the polymer. Since such a change in the dipole moment can be stabilized (destabilized) by a polar (non-polar) solvent a shift in the absorption maxima of a given polmyer in solvents of varying polarity can be observed.[143] The absorption of PCPDTBT was therefore investigated in a range of processing solvents such as CS_2 (polarity: $\epsilon = 2.6$), $CHCl_3$ ($\epsilon = 4.6$), 1-CN ($\epsilon = 5.04$), CB ($\epsilon = 5.6$) and THF ($\epsilon = 7.4$), ϵ taken from [142, Handbook of Chemistry and Physics]. Figure 4.1 shows the observed hypsochromic shift of the absorption spectra with increasing solvent polarity. Looking at the low energy band, the absorption maxima is shifted in CS_2 (carbon disulfide, bp = $46\,^{\circ}\mathrm{C}$, $\epsilon = 2.6$) to THF (bp = $66\,^{\circ}\mathrm{C}$, $\epsilon = 7.4$) by almost 30 nm to lower energies. It should be noted that when shifting the spectra along the x-axis such that all low energy maxima appear at the same wavelength, the shapes of the spectra match each other perfectly. This

strongly indicates that the hypsochromic shift is due to the different solvent polarities and not caused by aggregation effects.

Further investigations of CPDTBT trimers in different solvents were performed by M. C. Ruiz Delgado. Using the polarizable continuum model (PCM) approach together with the optimized geometries from the DFT calculations, the molecules in the ground state were modeled.[11] Furthermore the excited state dipole moments were calculated using the RhoCI density together with the TDDFT-PCM vertical electronic excitation energies. In accordance to the experimental data, a blue shift upon increasing solvent polarity was predicted. It was suggested that the blue shift is due to an increased charge-transfer in the ground state which is caused by both the increased dipole moment in the ground state and the decreased dipole moment in the excited state. For example when comparing the solvents CS_2 ($\epsilon = 2.6$) and THF ($\epsilon = 7.4$) an increase of the ground state dipole moment from 3.83 D (CS_2) to 4.04 D (THF) was found and a decrease in the S_1 state from 9.63 D (CS_2) to 9.03 D (THF). The same trend was also found for highly polar solvents, for example, dimethyl sulfoxide (DMSO, $\epsilon = 46.7$) which unfortunately could not be experimentally investigated due to the insufficient solubility of PCPDTBT in DMSO.

Si-PCPDTBT and F-PCPDTBT

The absorption spectra of Si-PCPDTBT (M_W = 10.5 kg/mol) and F-PCPDTBT (M_W = 10.8 kg/mol) in different solvents reveal similar behavior as found for PCPDTBT, figure 4.2. Both show a blue shift upon increasing solvent polarity. In contrast to PCPDTBT, the spectra of F-PCPDTBT can not be matched perfectly when shifting along the x-axis. The THF solution for example shows an increased absorption around 800 nm and a more prominent shoulder around 670 nm than the other solutions. This can probably be attributed to a stronger aggregation tendency of F-PCPDTBT which will be confirmed later on during the investigation of the aggregation behavior.

Since a red shift in the absorption band was observed in the DFT calculations of PCPDTBT oligomers of different lengths, the absorption spectra were measured of several Si-PCPDTBT batches of different molecular weights (M_W between 4 to 32 kg/mol), figure 4.2C. As predicted by the calculations a strong red shift of the spectra was observed with increasing molecular weight (M_W = 4.4 to 10.5 kg/mol), likely due to an increase of the conjugation length. The two polymers with the highest molecular weight (M_W = 11.3 and 32.3 kg/mol) show only a small red shift but a remarkable change in the shape of the spectra. Both reveal a splitting of the low energy absorption band. This is again probably due to aggregation effects however this claim could not be proven. The

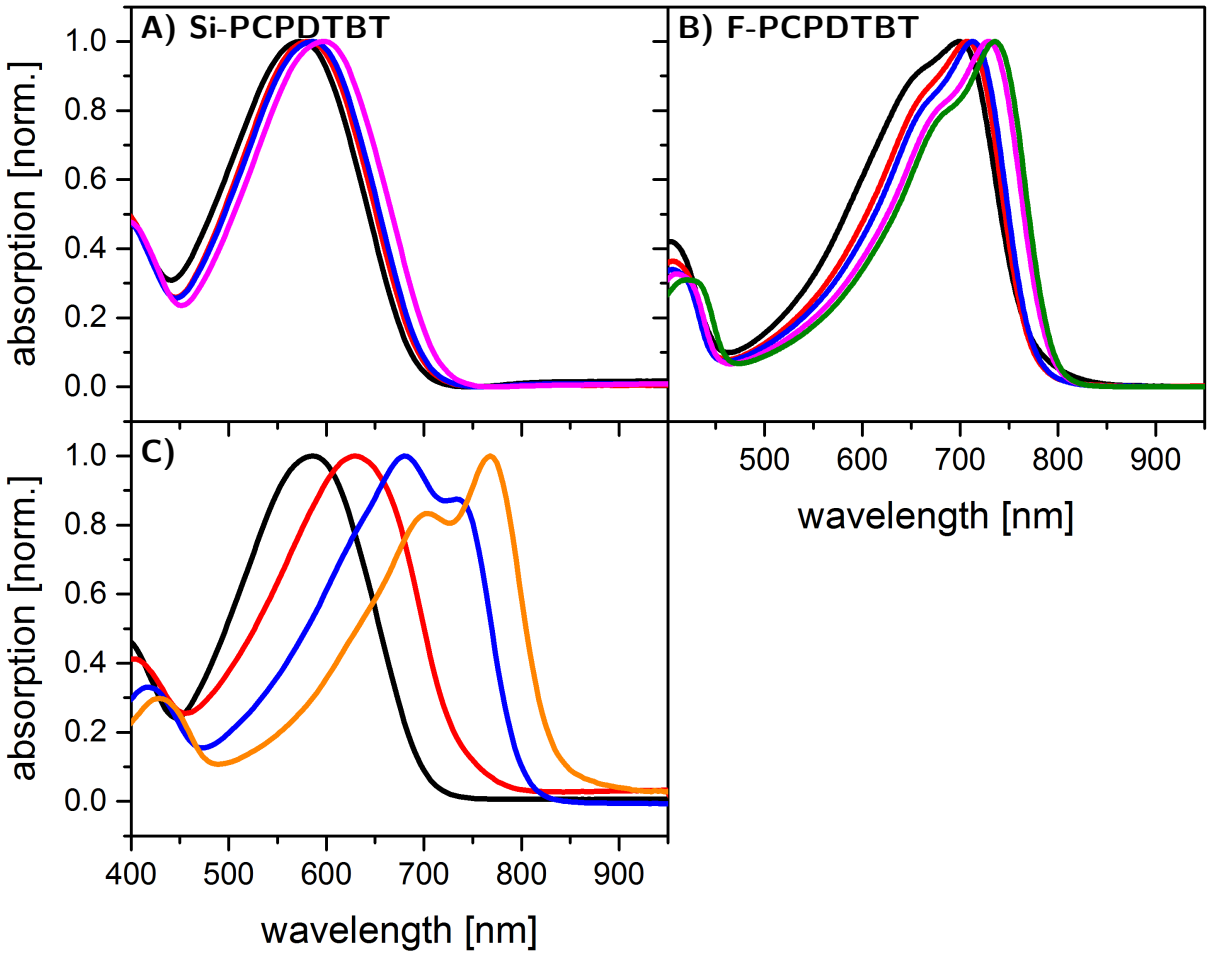

Fig. 4.2: A) and B) Absorption spectra of a $0.01\,\mathrm{mg/ml}$ solution of Si-PCPDTBT (A, $M_W = 10.5\,\mathrm{kg/mol}$) and F-PCPDTBT (B) in THF (black, $\epsilon = 7.4$), $CHCl_3$ (red, $\epsilon = 4.6$), CB (blue, $\epsilon = 5.6$), 1-CN (pink, $\epsilon = 5.04$) and CS_2 (green, $\epsilon = 2.6$).[142] **(C)** Si-PCPDTBT absorption spectra in CB solutions ($0.01\,\mathrm{mg/ml}$) of different molecular weights (M_W): $4.4\,\mathrm{kg/mol}$ (black), $10.5\,\mathrm{kg/mol}$ (red), $11.8\,\mathrm{kg/mol}$ (blue) and $32.3\,\mathrm{kg/mol}$ (orange).

extent of aggregation could not be reduced through dilution of the solutions. No changes in the spectral shape was observed and eventually the detection limit of the employed spectrometer was reached. The fine structure seen in figure 4.2C will be discussed in more detail when analyzing the aggregation behavior in the next chapter.

Summary

In summary the absorption spectra of PCPDTBT and its derivatives in solution showed a high and low energy band which was correlated by DFT calculations to a HOMO/LUMO and a HOMO/LUMO+3, transition respectively. It was shown that the low energy band has a strong charge-transfer character which leads to a hypsochromic shift with increasing solvent polarity due to a change in the dipole moments of the ground and excited states.

As predicted in the DFT calculations an increase in conjugation length leads to a red shift of the spectra. However, in polymers with high molecular weights, aggregation effects dominate the shape of the absorption spectra.

4.1.3 Change in the Absorption Signature during Aggregation

After discussing the UV/Vis-absorption and PL behavior of the fully dissolved polymers, the optical properties during aggregation were investigated. The aggregation behavior of conjugated polymers is best probed in solution because the transition between the dissolved and aggregated state can be controlled by changing either the temperature, the concentration or the solvent itself. This gives access to in-situ investigations utilizing spectroscopy methods as UV/Vis-absorption, PL, Raman et cetera.[7,8,92,93,139]

Temperature and Concentration Dependency

The aggregation behavior was first investigated in THF which is a moderate solvent for PCPDTBT, thereby, making it possible to switch between the dissolved and aggregated states by: i) lowering the temperature or ii) increasing the polymer concentration. In the first approach, the polymer was dissolved at elevated temperatures. Lowering the temperature leads then to a decreased solubility and therefore to an either inter- or intrachain aggregation. Changing the concentration of the solution while keeping the temperature constant on the other hand does not change the solubility of the polymer, but leads instead to a saturation of the solution and therefore to a pure interchain aggregation.

For PCPDTBT, both of the experiments above mentioned, decreasing temperature and increasing concentration, revealed an additional absorption band around 800 nm. The effect was best observed when cooling a THF solution of 3 mg/ml down to −15 °C. Figure 4.3A shows how a strong 800 nm band appears as the temperature decreases. The concentration dependent measurements showed a less distinct effect, probably because the absorption could only be measured up to 3 mg/ml due to the strong absorption of PCPDTBT. Nevertheless, the THF solution reveals with increasing concentration a clear increase of the absorption around 800 nm, figure 4.3B. The same experiment was performed in a variety of solvents, shown in figure A.2.

The appearance of this band at 800 nm was attributed to aggregation, as it has been seen in other conjugated polymers, e.g. P3HT[8,92] (610 nm) or MEH-PPV[93] (590 nm), chapter 1.2.5. This observation is in further agreement with the findings of Peet et al.[17] They gradually decreased the solvent quality of a PCPDTBT solution by going from a

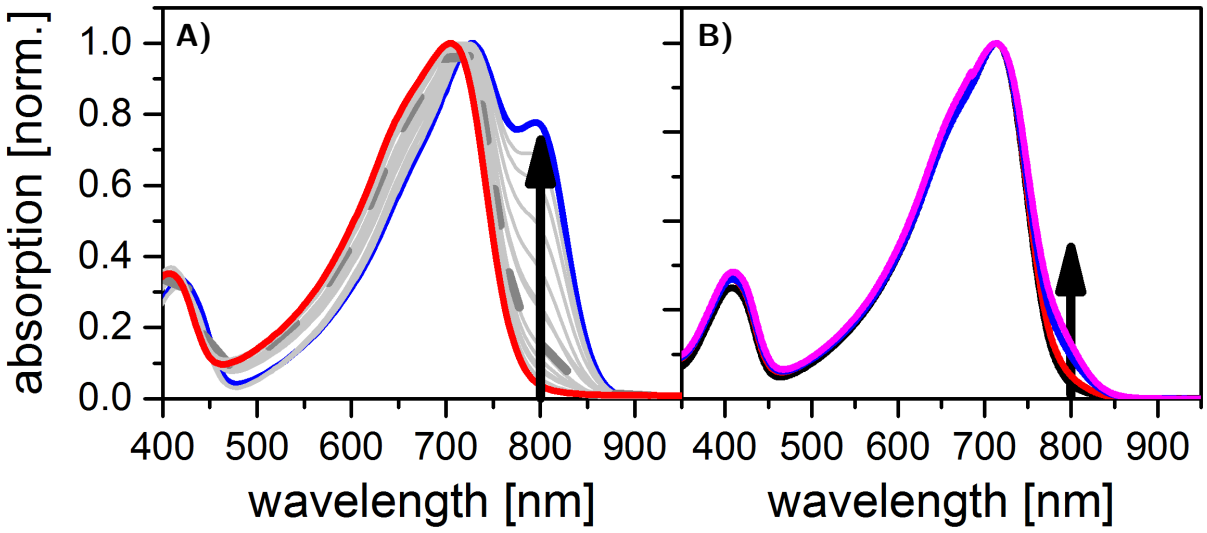

Fig. 4.3: A PCPDTBT temperature dependent absorption spectra of a 3 mg/ml THF solution between −15 °C (blue) and 55 °C (red) taken every 5 K (RT: dashed). **B)** Absorption spectra of PCPDTBT in THF at four different concentrations 0.01 mg/ml (black), 0.1 mg/ml (red), 1 mg/ml (blue) and 3 mg/ml (pink).

good solvent (chlorobenzene) to a bad solvent (diiodooctane) and found an coinciding increase of the absorption around 800 nm.

Low Temperature Investigations

Following up on these experiments, low temperature (−163 °C) UV/Vis-absorption and PL of PCPDTBT was measured in cooperation with C. Scharsich in the group of Prof. A. Köhler, in Bayreuth. The setup used in Bayreuth allowed for in-situ absorption and PL measurements while cooling of the solution down to a few Kelvin. The experiments were performed in the low melting point solvent 2-methyltetrahydrofuran (MTHF) due to its low freezing point, by cooling a solution (0.25 mg/ml) down to −163 °C (110 K) and heating it up again in steps of 20 K to 67 °C (340 K) while following the absorption and PL.

The resulting in-situ absorption and PL spectra are shown in figure 4.4. At 67 °C (red) the absorption consist of two broad and unstructured bands: a high (405 nm) and a low (690 nm) energy transition. For both no notable difference compared to the spectra in other solvents were found (compare figure 4.1A). After cooling the solution to −163 °C (blue) both absorption bands are red shifted and increased significantly in intensity. In addition, the low energy band was split into two bands with prominent maxima at 750 nm and 840 nm ($\Delta E = 194$ meV). Going from the dissolved (red) to the aggregated (blue) absorption spectrum, first the low energy maximum (690 nm) is red shifted until room temperature (280 K, dashed). Upon further cooling, this redshift is followed by the

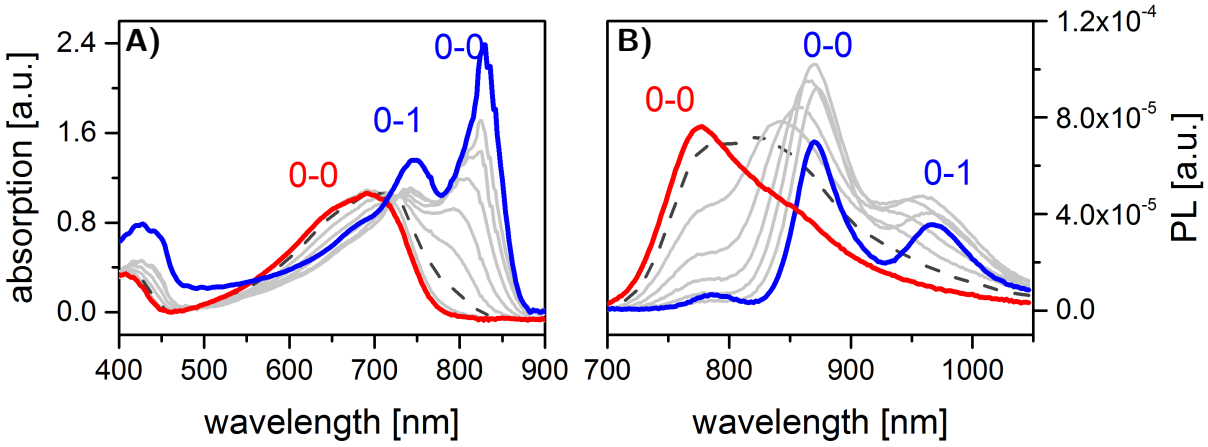

Fig. 4.4: UV/Vis (A) and PL (B) spectra of PCPDTBT dissolved in MTHF (0.25 mg/ml) between 67 °C (red, 340 K) and −163 °C (blue, 110 K) with spectra taken every 20 K in between (dashed: room temperature). For the PL spectra the excitation wavelength was 405 nm (adapted from[10,144]).

appearance of a shoulder at approximately 830 nm due to the formation of aggregates. Furthermore the isosbestic point around 730 nm (1.7 eV) indicates that the additional absorption band is caused by a second phase and is not due to a planarization of the polymer backbone during aggregation.

In figure 4.4B the results of the in-situ PL (excitation: 405 nm) experiments are shown. In accordance with the absorption spectra in the same solutions, the single band of the dissolved spectra (red) at 775 nm is shifted to lower energies during cooling, and splits into two vibronic bands which were further red-shifted to 870 nm and 965 nm.

Comparing these results (a red shift, an increase in intensity and an isosbestic point) to experiments carried out with other conjugated polymers such as P3HT,[8,92] MEH-PPV[93] and P(NDI2OD-T2),[139] they all show similar behavior as a result of aggregation. It is therefore fair to assume that the low temperature spectra, demonstrating strong absorption at 800 nm, is a result of an increased conjugation length (red shift) of a new aggregated phase (isosbestic point).

Si-PCPDTBT and F-PCPDTBT

Only a few studies on the optical properties of pure Si-PCPDTBT and F-PCPDTBT are found in literature. Both derivatives are reported to aggregate similar to PCPDTBT in solution and are typically processed form chlorobenzene or ortho-dichlorobenzene (o-DCB) forming thin films with an aggregation band at 800 nm.[6,112]

As suggested earlier both tend to aggregate, more strongly than PCPDTBT. Therefore for the Si and F containing derivatives, other solvents than those used for PCPDTBT had do be employed to ensure a transition from a dissolved state to an aggregated phase in the

temperature range investigated. Figure 4.5 shows the temperature dependent absorption spectra performed in CB and 1-CN (3 mg/ml) for Si-PCPDTBT and F-PCPDTBT, respectively. Both polymers reveal a red shift and an increase in intensity upon decreasing the temperature, in accordance with PCPDTBT. In CB, Si-PCPDTBT ($M_W = 11.3\,kg/mol$) reveals a broad absorption band at 650 nm. Upon cooling of the solution, the absorption band is red shifted and an isosbestic point is formed at around 660 nm. Finally, the charge-transfer band becomes more broad and is split into two peaks with maxima at approximately 690 nm and 750 nm.

In the dissolved state the main absorption of F-PCPDTBT is found at 700 nm which is shifted to 730 nm as a result of aggregation. In contrast to PCPDTBT and Si-PCPDTBT, F-PCPDTBT shows no splitting of the aggregation band. Still the isosbestic point at 700 nm and the increased intensity indicate the formation of a new phase.

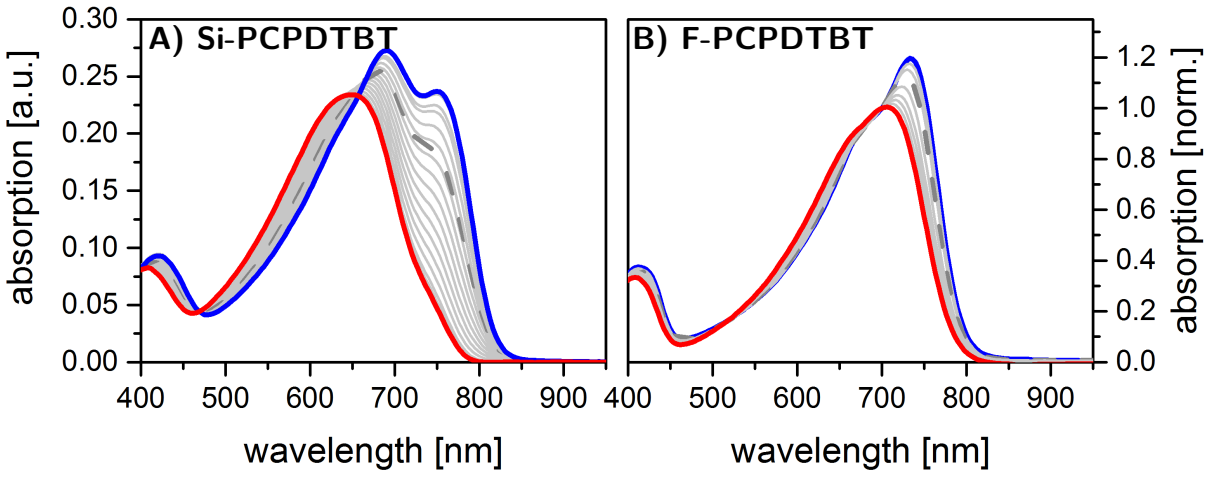

Fig. 4.5: Temperature dependent absorption spectra of $3\,mg/ml$ polymer solutions **A)** Si-PCPDTBT ($M_W = 11.3\,kg/mol$) in CB measured in the temperature range between $120\,°C$ (red) and $-20\,°C$ (blue) with $10\,K$ temperature steps (gray). **B)** F-PCPDTBT in 1-CN measured between $130\,°C$ (red) and $-5\,°C$ (blue) with $5\,K$ temperature steps (gray, RT: dashed line).

4.1.4 Franck-Condon Analysis of the Absorption and PL

Despite the differences in the basic polymer structure and the origins of the optical transitions of donor-acceptor copolymers versus homopolymers such as P3HT and MEH-PPV, there are also similarities. One important difference for donor-acceptor copolymers such as PCPDTBT is that the main HOMO/LUMO transition has a strong CT character. Furthermore DFT calculations have shown that the absorption spectrum is much less sensitive to changes in conjugation length for copolymers in comparison to homopolymers.[11,140] Nevertheless, the strong aggregation band at low energies and the splitting of

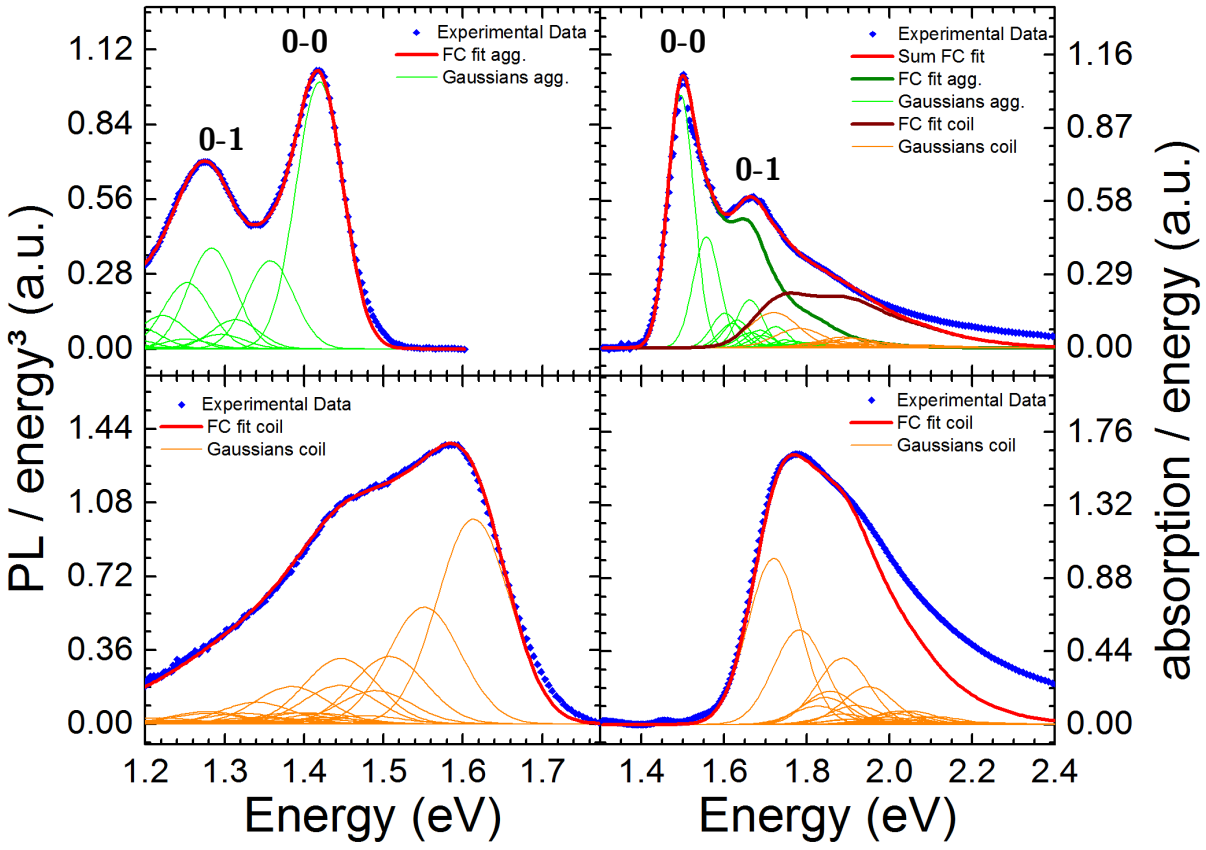

Fig. 4.6: Franck-Condon analysis of the PL (left) and absorption (right) spectra of a PCPDTBT solution (MTHF, 0.25 mg/ml). **Top**: Spectra at 180 K representing a pure aggregated phase. **Bottom**: Spectra at 340 K representing a coiled state of the polymer chains in solution. The experimental data are indicated by blue squares and the calculated spectra by red lines. The Gaussian curves which were used to fit the spectra are shown in green and orange, respectively. The sum over all Gaussian curves for each phase are shown in dark red (coiled) and dark green (aggregated) (adapted from[10,144]).

the band during aggregation is reminiscent of homopolymer absorption behavior known from P3HT, chapter 1.2.5. Hence, a Franck-Condon analysis was performed in accordance with the investigations of the homopolmyers reported by Spano et al.[7–9,91,92] A detailed description of the Franck-Condon analysis is given in chapter 1.2.5. To the best of my knowledge, investigating the origins of fine structure of the absorption and PL signatures using only vibrational modes was up till now, only applied on homopolmyers such as P3HT. In the following section a description of the Franck-Condon based analysis is given.

4.1.4.1 Modeling the Aggregated and Coiled Phases

The Franck-Condon analysis was performed in cooperation with C. Scharsich from the group of A. Köhler, in Bayreuth using the absorption and PL spectra measured in

MTHF, chapter 4.1.3. A publication including the results shown here has been submitted recently [10, Scharsich and Fischer et al.].

The spectra of varying temperatures (180 to 340 K) were fitted by sums of Franck-Condon transitions based on several vibrational modes correlated to the HOMO/LUMO transition in the harmonic approximation (e.g. PL: $S_1(0) \rightarrow S_0(m_i)$ with the vibrational quantum number $m_i = 0, 1, 2, 3, ..$ in S_0). The vibrational energies ($\hbar\omega$) were kept the constant for the ground and excited states. The intensity of a single vibrational mode ($I_{0\rightarrow m_i}$) is given by the product of the density of states and the Franck-Condon factor:[26]

$$I_{0\rightarrow m_i} \propto n_f^3(\hbar\omega)^3 \frac{S_i^{m_i} exp(-S_i)}{m_i!} \tag{17}$$

with n_f^3 as the real part of the refraction index (assumed to be constant over the fitted spectral range) and the Huang-Rhys parameter S_i. The absorption (Abs.) and the PL spectra can then be fitted by considering different oscillators (i) and summing over all vibrational quantum number of the ith vibrational modes ($m_i = 0, 1, 2, 3, ..$):[8, 26, 137]

$$PL(\hbar\omega) \propto n_f^3(\hbar\omega)^3 \sum_{m_i} \prod_i \left[\frac{S_i^{m_i} exp(-S_i)}{m_i!}\right] \cdot \Gamma\delta \left[\hbar\omega - \left(\hbar\omega_0 - \sum_i m_i\hbar\omega_i\right)\right] \tag{18}$$

$$Abs.(\hbar\omega) \propto n_f(\hbar\omega) \sum_{m_i} \prod_i \left[\frac{S_i^{m_i} exp(-S_i)}{m_i!}\right] \cdot \Gamma\delta \left[\hbar\omega - \left(\hbar\omega_0 + \sum_i m_i\hbar\omega_i\right)\right] \tag{19}$$

were ω_0 is the 0-0 frequency and Γ is a Gaussian line shape function with constant standard deviation σ, chapter 1.2.5.

The frequencies (ω_i) of the oscillators were taken from Raman measurements shown in figure A.4. The five vibrational modes with the energies of 62, 106, 136, 167 and 190 meV (500, 854, 1096, 1347 and 1532 cm^{-1}) were included into the calculations.

Two different absorption and PL spectra were found for the dissolved and aggregated phase, figure 4.6: one at elevated temperature (340 K, bottom) belonging to a completely dissolved phase of probably coiled polymer chains with short conjugation lengths and no interchain coupling. Another at 180 K (top) with a spectrum shape known from aggregation experiments when increasing the polymer concentration, figure 4.3B. These two extreme cases were fitted using equation 18 and 19, figure 4.6 (green and red lines). The used Franck-Condon parameters are summarized in table 4.3.

Dissolved Phase

Figure 4.6 shows the spectra of the dissolved PCPDTBT at 340 K. The spectra reveal broad and unstructured PL and absorption bands with the maxima of the 0-0 transition at 1.6 eV (PL) and 1.7 eV (Abs.). The 0-1 transitions are not resolved and can only be seen as shoulders of the 0-0 transition around 1.46 eV (Abs.) and 1.88 eV (PL). The fits are in good agreement with the observed spectra. Compared to the fits of the aggregated spectra a larger Gaussian standard deviation (band width) was used. This was necessary due to the greater vibrational freedom of the polymer chains at higher temperatures. In addition a blue shift of the 0-0-transition of around 0.2 eV compared to the aggregated phase had to be assumed probably caused by the decreased conjugation length in the dissolved phase.

Aggregated Phase

In the aggregated phase at 180 K the maxima of the 0-0 transition were found to be around 1.4 eV (PL) and 1.5 eV (Abs.). The 0-1 transition was observed as a separate peak and nicely matches the fitted spectra. The PL spectra could be fitted using just one emission state. The absorption spectrum on the other hand could only be fitted if assuming that not all polymer chains were aggregated but some remained in a dissolved-like state with probably coiled backbones. The complete fit of the spectra consists therefore out of a mixture of a calculated aggregated phase (dark green) and a coiled phase (dark red) in

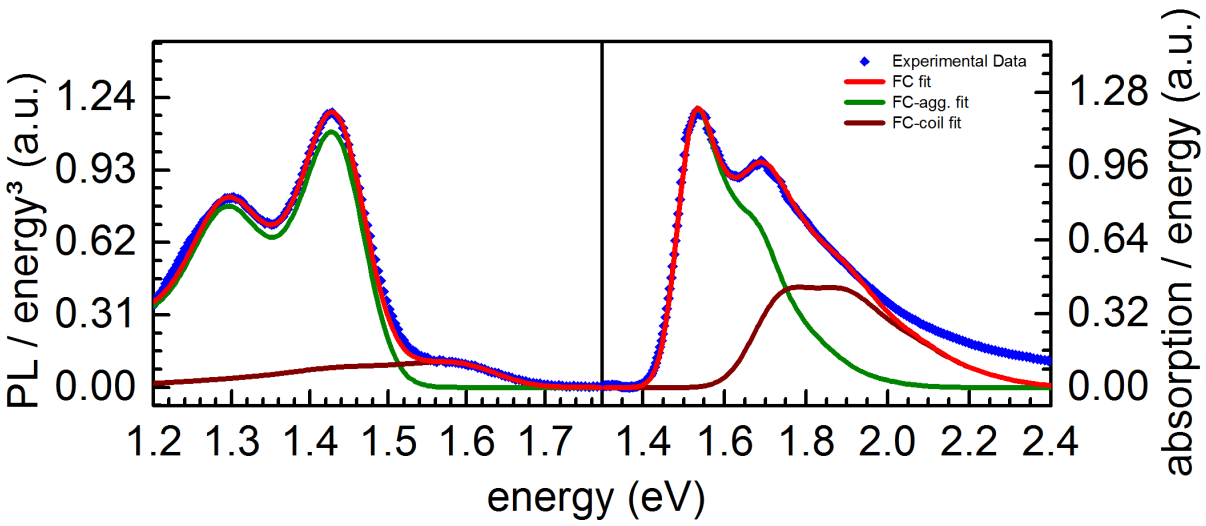

Fig. 4.7: Comparison between the Franck-Condon (FC) fit (red) and the experimental data (blue squares) of PCPDTBT dissolved in MTHF at 240 K. The FC fit was calculated from a mixture of the aggregated (green) and the coiled/dissolved (dark red) phases with the exact parameters shown in table 4.3 (adapted from[10, 144]).

the ratio 67/33. It should be noted that in the corresponding PL spectrum, only the aggregated phase is seen. This is probably due to the relaxation of the excited states into the lowest vibrational state which is located in the aggregated phase. As a result the PL originates from the aggregated phase. This is probably always the case if a majority of the polymer is aggregated and only small amorphous domains exist.

Mixed Phase

At 240 K the solution contains both phases: an aggregated and a coiled (dissolved) phase. Therefore the absorption and PL spectra seem to be a mixture of both, figure 4.7.

To confirm our fittings of the pure phases we used the parameters obtained from the 180 K and 340 K spectra to calculate the mixed spectra of the solution at 240 K. The calculated spectra nicely resemble the experimental data, figure 4.7. The percentage of the aggregated phase was determined to 86 % and 57 % in the PL and absorption, respectively, see table 4.3. The higher percentage of the emission belonging to the aggregated phase in the PL can again be explained by a relaxation from the coiled to the aggregated phase in the excited state. Further the 0-0 transition energies had to be slightly shifted in between the coiled and the aggregated phases to match the experiment.

Tab. 4.3: Franck-Condon parameters for the fitting of the PL and absorption spectra shown in figure 4.6 and figure 4.7. f is the relative ratio between the aggregated and coiled/dissolved phase, $\hbar\omega_0$ the energy of the 0-0 transition, σ the Gaussian standard deviation and I_{0-0}/I_{0-1} the peak ratio between the 0-0 and 0-1 peak intensity.

	photoluminescence				**absorption**			
	f [%]	$\hbar\omega_0$ [eV]	σ [meV]	I_{0-0}/I_{0-1}	f [%]	$\hbar\omega_0$ [eV]	σ [meV]	I_{0-0}/I_{0-1}
180 K **agg.**	100	1.420	30	0.94	67	1.495	33	1.06
180 K **coil**	0	-	-	-	33	1.720	60	0.70
340 K **agg.**	0	-	-	-	0	-	-	-
340 K **coil.**	100	1.614	46	0.76	100	1.720	63	0.76
240 K **agg.**	86	1.434	37	0.98	57	1.520	40	0.94
240 K **coil.**	14	1.598	46	0.76	43	1.720	63	0.66

Summary

In summary, two phases: an aggregated and a dissolved/coiled phase, were observed in solution. Both could be fitted in good agreement with the experimental data using a Franck-Condon analysis, analogous to a method reported for homopolymers in literature,

chapter 1.2.5. In accordance with conjugated homopolymers such as P3HT it was shown that PCPDTBT undergoes a phase transition from a dissolved to an aggregated phase when cooled in solution. The phase transition temperature was found to be around room temperature (300 K) which is particular relevant for processing thin films using PCPDTBT solutions. Furthermore, the red shift of the aggregated phase compared to the coiled phase suggests a planarization of the polymer backbone during aggregation.

The Franck-Condon analysis proved to be a valuable tool for modeling the absorption spectra of a typical donor-acceptor copolymer such as PCPDTBT. It was possible to not only fit the pure aggregated and coiled phases, but also the spectra of the intermediate phase at 240 K which contains a mixture of both. Particularly the latter confirms the legitimacy of this approach. These results suggest that not only the absorption and PL of homopolymers but also of donor-acceptor copolymers such as PCPDTBT can be fitted employing a Franck-Condon analysis.

4.2 Optical Properties of Spin Coated Films

In literature most studies focus on the absorption and morphology properties of PCPDTBT/fullerene blends,[61,127,145] instead of the pure PCPDTBT copolymer, even though it is well known that the morphology of the individual phases plays an important role for device performance in photovoltaic applications and OFETs.[15,16,25,60,146,147]

The few groups[17,140] who study the pure copolymer PCPDTBT typically prepared films by spin coating from chlorobenzene (CB) and did not investigate any other processing solvents. The absorption spectra of those films described in the literature[11,17,140] are similar to the aggregated solution discussed in chapter 4.1.3:[11] Two main maxima around 410 nm (high energy) and 770 nm (low energy) are reported. The 770 nm band is often accompanied by a shoulder around 725 nm. Comparing solution and film spectra a broadening and red-shift of the low energy band from around 720 nm (solution) to 770 nm (film) is described. In the literature[17] a shift of the maximum up to almost 800 nm was only reported for polymer/PCBM blends or when additional solvent additives such as haloalkanes or alkyl thiols were added to the processing solvent. The role of the additive was therefore attributed to an increase of the aggregation.[58,102]

Regarding morphology, literature studies[58,102,108,110] only provide few and weak reflections from X-ray scattering. PCPDTBT is therefore often regarded as hardly crystallizable polymer. The groups who investigated the pure PCPDTBT films used mainly AFM and grazing incidence wide angle X-ray scattering (GIWAXS). They describe the films spin coated from CB solutions as featureless with an increased aggregation when processed with the solvent additive 1,8-diiodooctane (DIO, 2 w%). In analogy to P3HT an edge-on morphology with a π-stacking distance of around 3.8 Å causing the 800 nm absorption is suggested. A detailed discussion on literature regarding the crystal structure is given at the beginning of chapter 4.4.

In the last chapter the absorption and PL properties of PCPDTBT and its derivatives during aggregation in solution were discussed and the spectra were fitted utilizing a Franck-Condon analysis. Two phases were identified: i) A dissolved phase with probably coiled non-interacting polymer chains and a maximum absorption around 720 nm. ii) An aggregated phase with the absorption shifted to lower energies and a strong aggregation band around 800 to 840 nm. Compared to the absorption shift reported for thin films in literature this is a surprisingly large shift and could indicate that the films are only partially aggregated. In the following section the influence of different processing solvents and solvent additives on film morphology and their optical properties will be discussed.

4.2.1 PCPDTBT

Using different processing solvents with high (e.g. 1-CN, CB) and low (e.g. CS_2, THF, $CHCl_3$) boiling points (bp.) allows the influence of the time frame of film formation during spin coating. This often affects the crystallinity and morphology of thin films. A similar effect can be accomplished by adding high boiling point solvent additives to the processing solvent.[17, 58, 102] PCPDTBT was therefore dissolved and spin coated from five different solvents (3 mg/ml): CS_2 (bp.: 46 °C), $CHCl_3$ (bp.: 61 °C), THF (bp.: 66 °C), chlorobenzene (CB, bp.: 131 °C) and 1-chloronaphthalene (1-CN, bp.: 259 °C).[142] It should be noted that at 3 mg/ml all of these solutions except for THF showed no indication of aggregation in the absorption spectra before deposition, figure A.3. The spin coating conditions were adjusted for each solvent to obtain film thicknesses of 20 to 40 nm, verified by AFM. The detailed processing conditions are given in table 4.4. Hereafter, films spin coated from a certain solvent are named according using the following nomenclature: *solvent-spincoated* film.

Tab. 4.4: Spin coating conditions for the thin film preparation using different solvents. All substrates were cleaned by SnowJet and O_2-plasma and the films spin coated under nitrogen atmosphere from 3 mg/ml solutions. The processing conditions were not changed if the solvent additive 1,8-diiodooctane (DIO) was added. After the first spinning step all films were rotated for additional 10 s at 6000 rpm to remove remaining solution from the edges of the substrates.

Solvents with and without 2 w% DIO	CS_2	$CHCl_3$/ THF	CB	1-CN
rpm	2000	1500	1000	800
time [s]	30	30	800	1800

Spin Coating from Pure Solvents

The absorption spectra of the thin PCPDTBT films, shown in figure 4.9A, reveal two kinds of spectra depending on the processing solvent. It should be noted that only the low energy band changes, whereas the high energy part of the spectra reveals a maximum around 410 nm.

The spectra of the films prepared from low boiling point solvents ($CHCl_3$ and CS_2) show a broad low energy absorption between 600 to 750 nm. The spectral signatures probably originate from a combination of the absorption due to the amorphous (similar to the solution, compare figure 4.4) and the aggregated domains. The films prepared from the high boiling point solvents (CB and 1-CN) on the other hand show absorption spectra similar to the aggregated solution with a strong maximum at around 800 nm and a shoulder around 740 nm. This is in accordance with the increased time for the polymer

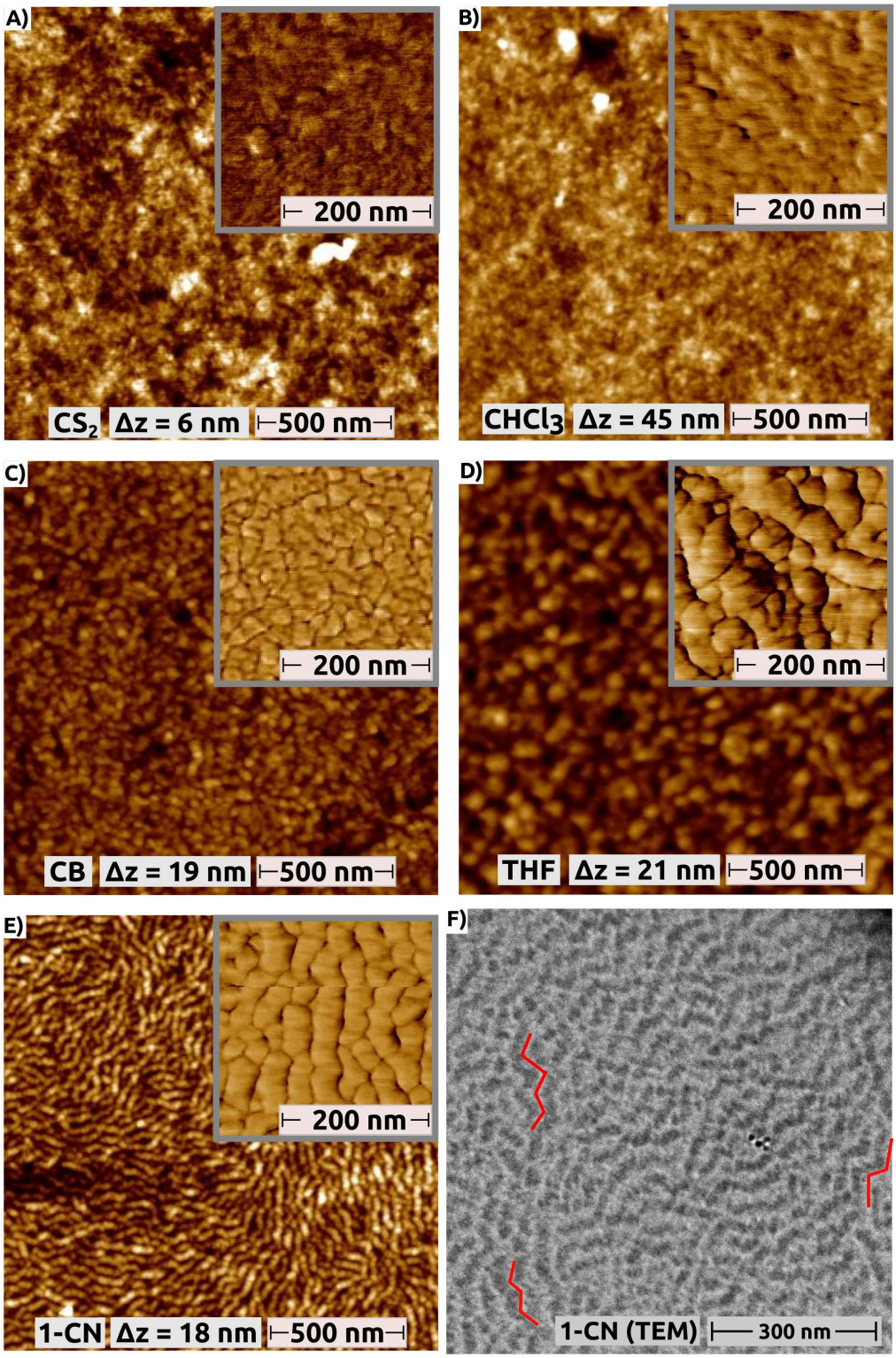

Fig. 4.8: AFM height images of PCPDTBT films spin coated from $3\,\mathrm{mg/ml}$ CS_2 (A), $CHCl_3$ (B), CB (C), THF (D) and 1-CN (E and F) without solvent additives. The corresponding AFM phase image are shown in figure A.7 **E)** TEM bright field images of a 1-CN-spincoated film with red lines highlighting the zig-zag pattern discussed in the text (adapted from[11]).

chains to rearrange during the spin coating process due to a slower evaporation of the high boiling point solvents.

The spectra of the films spin coated from THF show despite its low boiling point (66 °C) a strong aggregation band. It is suggested that in the THF solution PCPDTBT is already pre-aggregated and the aggregates are deposited randomly during the spin coating processes. This is further supported by the concentration dependent absorption spectra in solution, chapter 4.1.3, figure A.3, which revealed a small aggregation band for 3 mg/ml THF solutions.

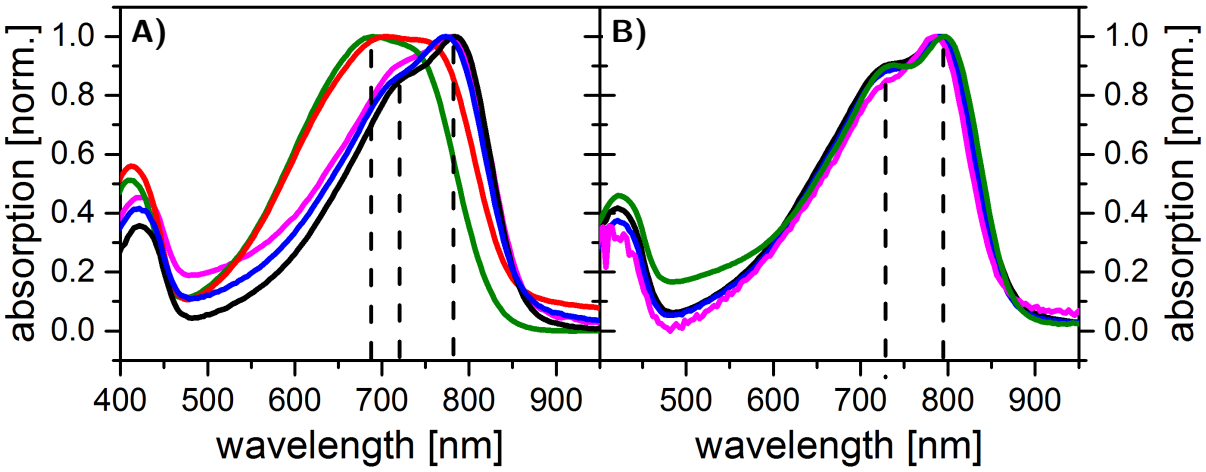

Fig. 4.9: Absorption spectra of PCPDTBT films processed by spin coating from 3 mg/ml solutions of CS_2 (green), $CHCl_3$ (red), CB (blue), 1-CN (pink) and THF (black) without (**A**) and with (**B**) 2 w% of the solvent additive DIO (adapted from[11]).

The AFM images in figure 4.8 reveal that the film surfaces evolve from a rather disordered structure in CS_2- and $CHCl_3$-spincoated films (low boiling point) to a fiber-like morphology in the 1-CN-spincoated film (high boiling point). This further confirmed the assumption that an increased 800 nm band is correlated to an increased order. The nanofibers in the 1-CN-spincoated film show at higher magnification (see inset figure 4.8E) a substructure along the fiber axis of around 40 ± 3 nm. The films spin coated from intermediate boiling point solvents such as CB and THF show also aggregates in the region of around 40 ± 3 nm but no fiber-like morphology. The similar size of the substructure within the nanofibers and the aggregates indicate that the fibers are composed of such aggregates. The longer drying time of the high boiling point solvent might give the aggregates enough time to reorient and align in the fiber-like morphology.

Using transmission electron microscopy (TEM) in the bright field mode the substructure of the fibers could be further confirmed, figure 4.8F. Additionally a zig-zag pattern and a strong contrast between the fibers was noticed. It is proposed that the contrast could be

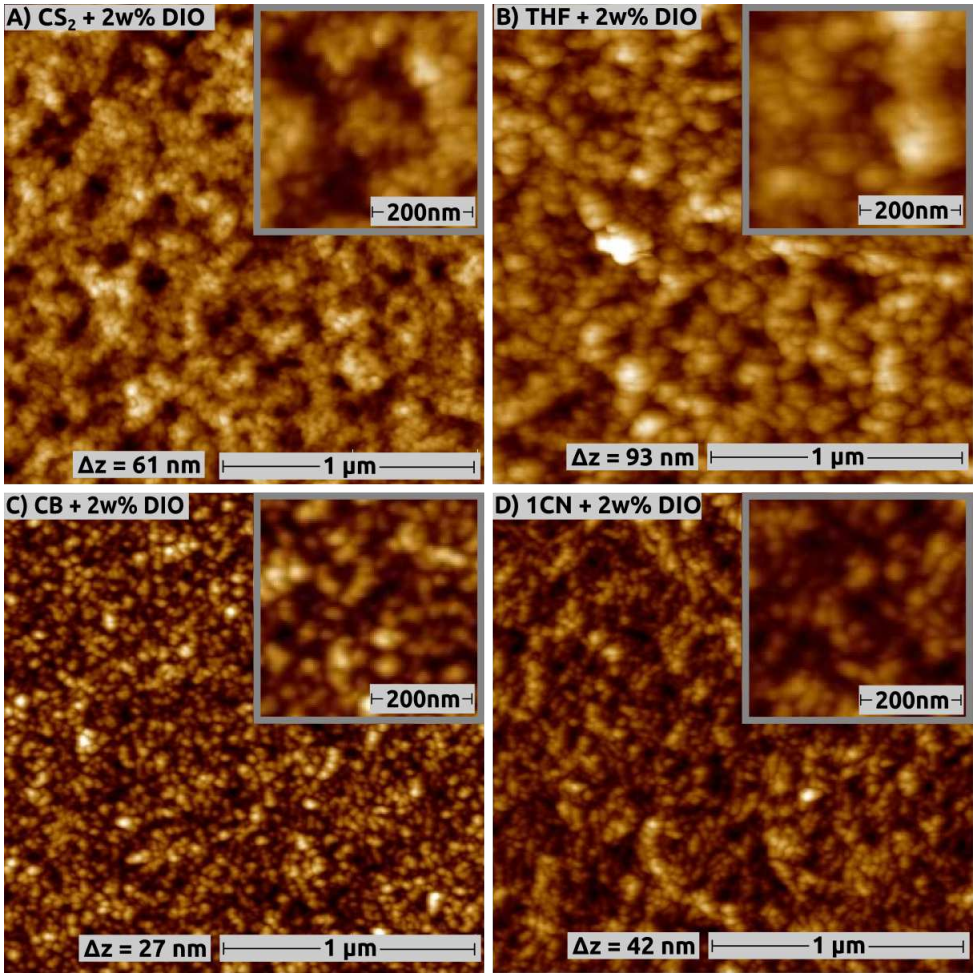

Fig. 4.10: AFM height images of PCPDTBT films processed by spin coating from $3\,\mathrm{mg/ml}$ CS_2 (A), THF (B), CB (C) and 1-CN (D) with $2\,\mathrm{w\%}$ of the solvent additive DIO. The corresponding AFM phase images are shown in figure A.5

induced by alternating crystalline (dark) and amorphous (bright) regions, similar to what was seen in semi-crystalline P3HT films.[148]

Spin Coating from Solutions Containing Solvent Additives

In the literature, often a high boiling point solvent such as 1,8-diiodooctane (DIO) is added as solvent additive ($2\,\mathrm{w\%}$) into the processing solvent (chlorobenzene) to improve the thin film and blend morphology.[17,58,102] The spectra of the thin films prepared from different processing solvents containing DIO as solvent additive are shown in figure 4.9B. Independent of the used solvent they reveal a strong 800 nm absorption indicating an increased aggregation.

The corresponding AFM images of the films spin coated from solutions containing $2\,\mathrm{w\%}$ DIO are shown in figure 4.10. In accordance to the absorption spectra similar surface

morphologies were found for all samples revealing aggregates in the sizes of 40 ± 3 nm. Surprisingly, even for the 1-CN-spincoated samples the aggregates do not form fiber-like structures. Instead they are randomly distributed on the substrate with no preferred orientation.

Hence, the solvent additive DIO seems to increase the aggregation tendency without assisting the assembly of the fiber-like structure. It is not understood why even from the high boiling point solvent, from which a fiber-like morphology can be prepared without solvent additive, no fibers are formed in the presence of DIO. It could be suggested that the aggregates are formed during the drying process at a time when the drying is already so far advanced that no more reorganization of the aggregates into fibers is possible.

TEM/ED of the Highly Ordered Films

Using TEM electron diffraction (TEM/ED) the morphology of the films with the most intense 800 nm bands prepared from 1-CN and CB/DIO were investigated, figure 4.11. Both ED patterns show three reflections at around 3.8, 5.7 and 11.0 Å, similar to the distances found in literature.[58,102,108,110] The CB/DIO sample shows only a pattern of three circles probably due to the small and randomly spread aggregates. The 1-CN-spincoated film on the other hand reveals a more defined reflection pattern due to the long range order of the fibers. The reflections at 3.8 Å and 5.7 Å are oriented perpendicular to each other which could indicate an edge-on morphology with the π-stacking and the polymer chain direction correlated to the 3.8 Å and 5.7 Å reflections, respectively. The 11 Å reflection is very weak and it is unknown if it is correlated to the polymer backbone or the alkyl side chain direction. A more detailed discussion regarding the crystal structure and an overview about the PCPDTBT morphologies reported in literature will be given in chapter 4.4.

Summary

In summary it was shown that for the film formation via spin coating the boiling point of the processing solvent and solvent additives are key factors which define the established thin film morphology. For PCPDTBT higher boiling point solvents and the solvent additive DIO lead to a strong aggregation band around 800 nm in the absorption spectra. Independent of the formation of small aggregates a fiber-like structure with long range order can be established by spin coating PCPDTBT from the high boiling point solvent 1-CN. Apparently its slow evaporation rate leaves enough time for the aggregates to reorganize into fibers during the film formation. Furthermore the typical distances proposed for an

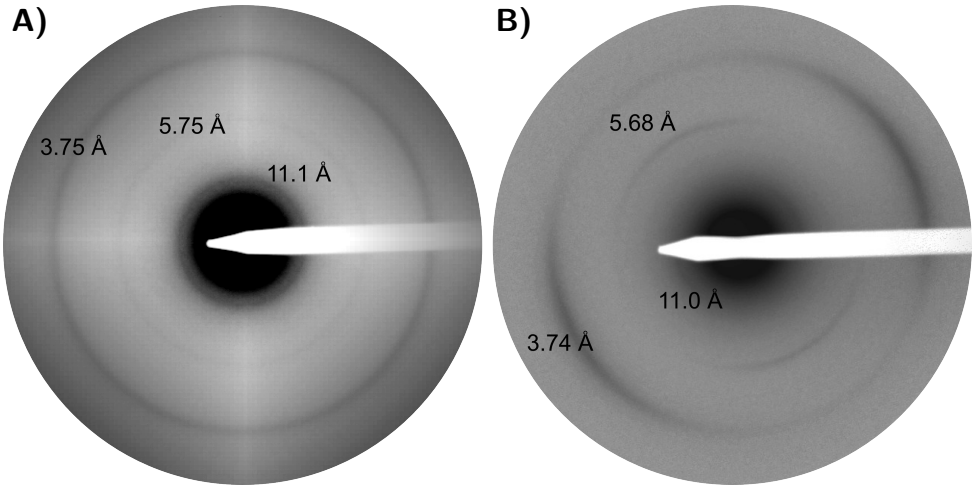

Fig. 4.11: TEM/ED pattern of PCPDTBT films prepared by spin coating from **A)** CB/DIO (3 mg/ml) and **B)** 1-CN (3 mg/ml).

edge-on morphology in literature with a π-stacking of around 3.8 Å was confirmed by TEM/ED measurements. The TEM bright field images also suggest a semi-crystalline nature of the fiber structure in the 1-CN-spincoated films.

These results are important for later device preparation, as shown in chapter 5.2, since it is reported[1,3,17] that a strong 800 nm band and structural order is necessary for high performing organic solar cell devices.

4.2.2 F-PCPDTBT

In the literature F-PCPDTBT is typically spin coated from either chlorobenzene (CB) or ortho-dichlorobenzene (o-DCB) and the few studies focusing on the pure copolymer report a similar behavior as for PCPDTBT.[5,6] For thin films, an aggregation band in the absorption at around 800 nm accompanied by a disordered thin film morphology was reported.

Neher et al.[5] investigated the effect of the solvent additive diiodooctane (DIO) on the F-PCPDTBT/PCBM blend morphology and found that the 800 nm aggregation band increases when up to 1 w% DIO is added into the processing solvent (CB). Increasing the DIO ratio above 3 w% led again to a decrease of the aggregation band, but this observation was not further discussed.

GIWAXS measurements of spin coated films by Jen et al.[114] suggest for F-PCPDTBT an edge-on morphology with typical π- and lamellar stacking distances. Jen et al.[114] reported a π-stacking of 3.8 Å and a lamellar stacking of 11 Å which is very similar to the values reported for PCPDTBT.

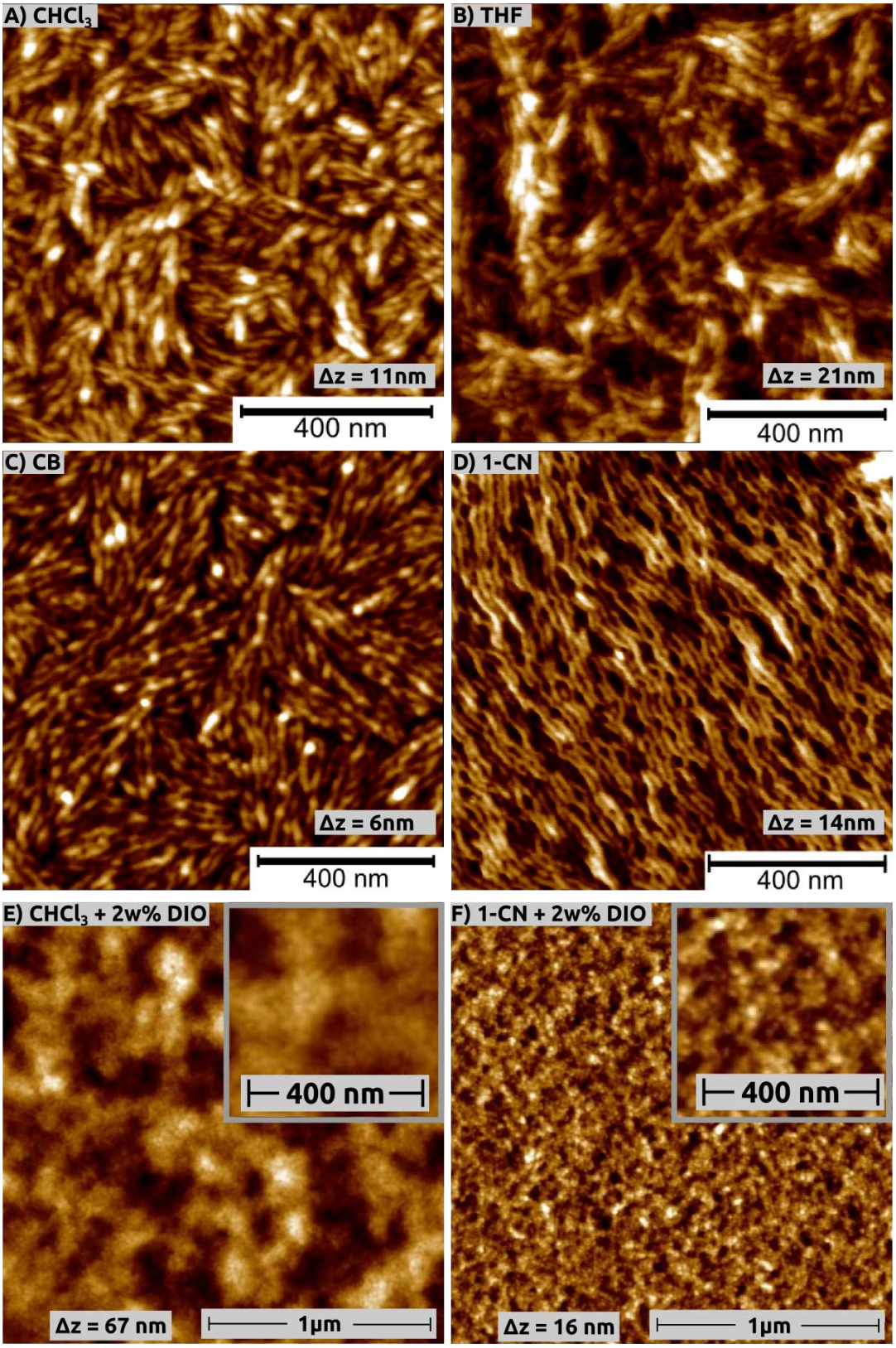

Fig. 4.12: AFM height images of F-PCPDTBT films processed by spin coating from **A)** $CHCl_3$, **B)** THF, **C)** CB, and **D)** 1-CN ($3\,\mathrm{mg/ml}$) without DIO and from **E)** $CHCl_3$ and **F)** CB with $2\,\mathrm{w\%}$ DIO as solvent additive. The corresponding AFM phase images are shown in figure A.7 and figure A.8 (partially measured by D. Trefz during his Master thesis).[149]

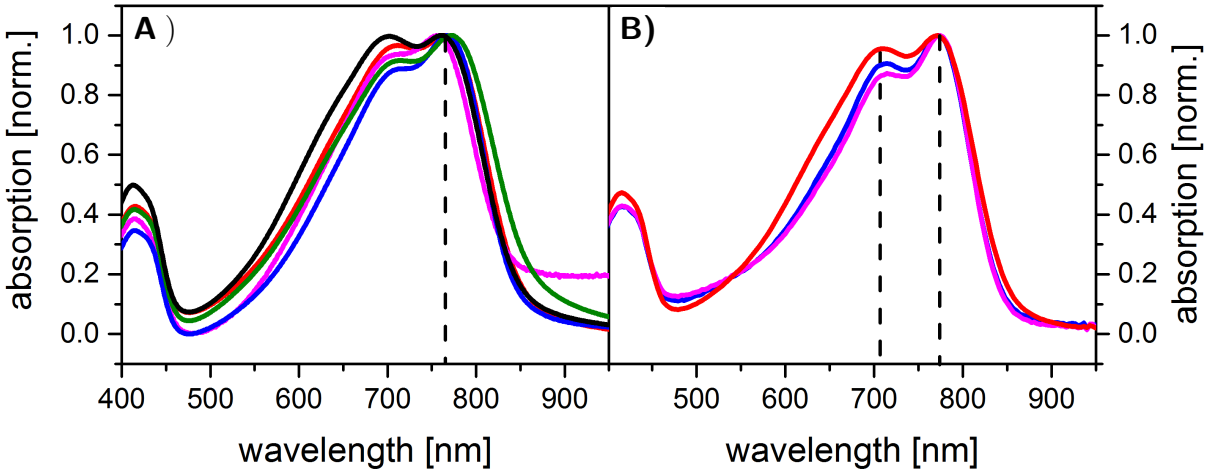

Fig. 4.13: Absorption spectra of F-PCPDTBT films processed by spin coating from 3 mg/ml solutions of THF (black), $CHCl_3$ (red), CB (blue), 1-CN (pink) and CS_2 (green) with (A) and without (B) 2 w% of the solvent additive DIO (partially measured by D. Trefz during his Master thesis).[149]

Spin Coating from Pure Solvents

In this thesis F-PCPDTBT was spin coated from different solvents (3 mg/ml) using the same conditions as for PCPDTBT, table 4.4. Figure 4.13A shows the absorption spectra of the samples after spin coating. They reveal for all prepared films an aggregation band at around 765 nm independent of the processing solvent. These findings are in good agreement with the concentration dependent absorption measurements in solution, figure A.2 and A.3. In all solvents the absorption spectra revealed at 3 mg/ml already a small aggregation band around 800 nm. This indicates that F-PCPDTBT already aggregates in solution and therefore partially, probably pre-formed, aggregates are deposited.

The film surfaces were investigated employing AFM, figure 4.12. They reveal already for low boiling point processing solvents, such as $CHCl_3$, a fiber-like structure. Going from low to high (1-CN) boiling point solvents the morphology evolves to a more and more ordered structures. The fiber length increases until a structure similar to the one of 1-CN-spincoated PCPDTBT films is found. A closer analysis shows that the fibers also consist of small aggregates of around 35 to 45 nm, similar to PCPDTBT.

Spin Coating from Solutions Containing Solvent Additives

For F-PCPDTBT also 2 w% DIO was added to the solutions and thin films prepared by spin coating, table 4.4. The spectra of films prepared from solutions containing DIO are marginally red shifted (10 nm) to 775 nm and the aggregation band is slightly more prominent than without DIO, figure 4.13B.

Figure 4.12E and F show the AFM height images of films spin coated from $CHCl_3$ and 1-CN solutions containing 2 w% DIO. Similar to PCPDTBT no fiber-like structure was obtained. Instead small aggregates of around 35 to 45 nm were found randomly spread on the substrate. The only exception is the CB/DIO-spincoated films which still reveal some fiber-like structures, figure A.8.

In summary F-PCPDTBT was found to behave in a similar fashion as PCPDTBT regarding the thin film morphology and absorption properties. These results together with the GIWAXS data known from literature[114] give reason to believe that spin coated F-PCPDTBT films also consist of an edge-on morphology similar to PCPDTBT and P3HT. The main difference to PCPDTBT seems to be a somewhat stronger aggregation tendency, which was also suggested by Zhang et al.[6]

4.2.3 Si-PCPDTBT

In the literature, also for Si-PCPDTBT only few publications were found regarding the pure polymer and its morphology. GIWAXS measurements of spin coated films by the group of Yang et al.[112] suggest also for Si-PCPDTBT an edge-on morphology. The GIWAXS patterns from films prepared by drop-casting from CB solutions revealed slightly different distances compared to PCPDTBT and F-PCPDTBT: 3.4 Å for the π-stacking and 15.5 Å for the lamellar stacking.

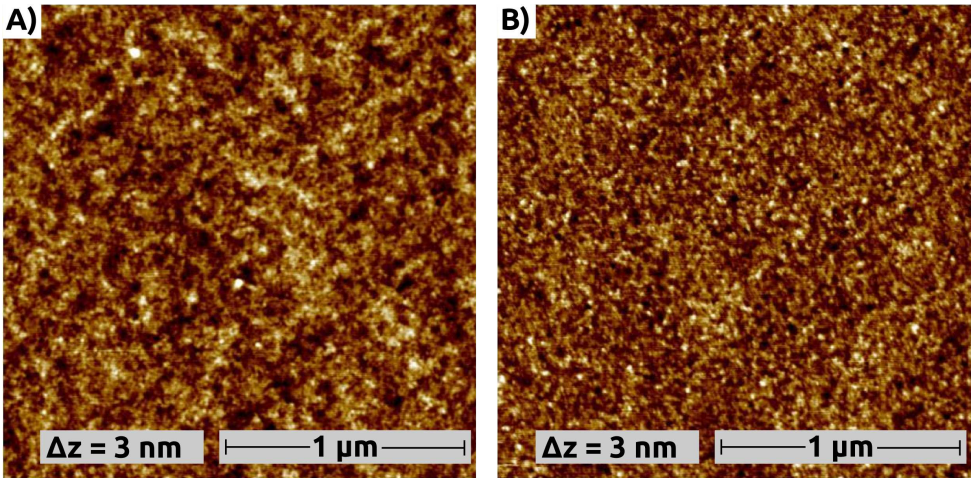

Fig. 4.14: AFM height images of Si-PCPDTBT (10 kg/mol) spin coated from $CHCl_3$ (A) and chlorobenzene (B) solutions (3 mg/ml). The corresponding phase images are shown in figure A.7 (measured by M. Jasch during his Master thesis).[150]

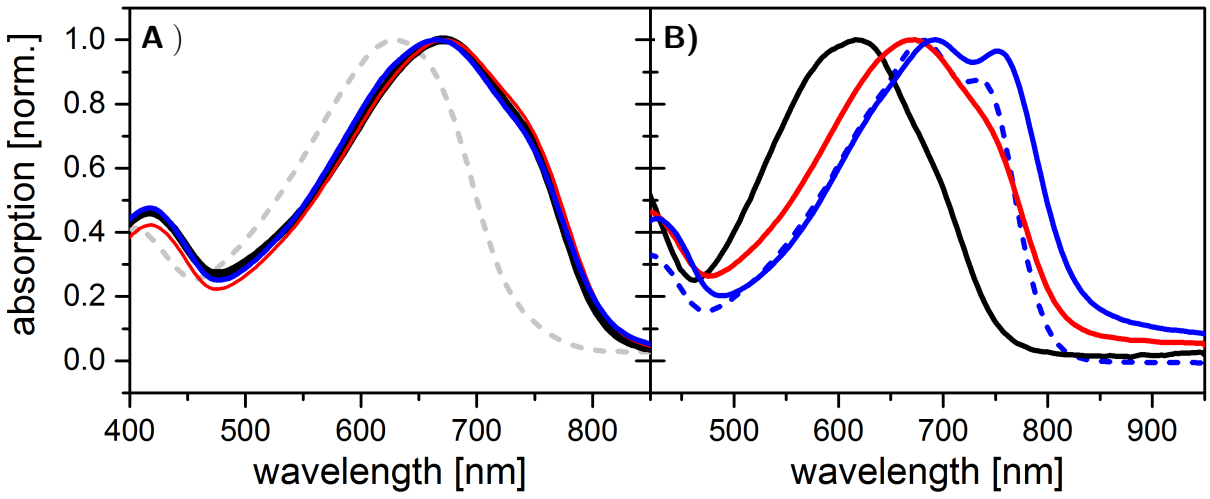

Fig. 4.15: A) Absorption spectra of Si-PCPDTBT (M_w=10 kg/mol) films processed by spin coating from 3 mg/ml solutions of THF (black), $CHCl_3$ (red), CB (blue). As comparison the solution spectrum (0.01 mg/ml) in CB is added (dashed grey). **B)** Absorption spectra of Si-PCPDTBT films with a molecular weight (M_W) of 4 kg/mol (black), 10 kg/mol (red) and 11 kg/mol (blue) processed by spin coating from 3 mg/ml solutions (measured by M. Jasch during his Master thesis).[150]

The discrepancies of the distances compared to PCPDTBT and F-PCPDTBT are probably due to the increased C-Si bond length in the cyclopentadithiophene which leads to a slightly stronger bended (19° compared to 10°) polymer backbone.[113]

The absorption spectra of Si-PCPDTBT solutions (0.01 mg/ml, chapter 4.1.3, figure 4.2C) revealed for molecular weights >11 kg/mol (M_W) already an aggregation in solution evident by strong red shifted aggregation bands. Therefore the 10.5 kg/mol batch was used to prepare thin films from solution. Figure 4.14 shows the AFM height images of Si-PCPDTBT films prepared from a high (CB) and a low ($CHCl_3$) boiling point solvent. In all prepared films a disordered surface morphology evident by the AFM images was found.

In accordance to the thin film morphologies the absorption spectra of the films all reveal the same absorption behavior, figure 4.15A. Compared to the spectra of a diluted solution (CB, 0.01 mg/ml, grey dashed) the absorption is red shifted and a small aggregation shoulder around 750 nm was found.

The absorption spectra of thin films prepared from different molecular weight polymers are shown in figure 4.15B. The absorption bands are red shifted with increasing molecular weight indicating an increased conjugation length. For the 11.8 kg/mol Si-PCPDTBT (blue) the absorption of a diluted solution (CB, 0.01 mg/ml) is additionally plotted (dashed line). The difference found between the film and the solution spectra is much smaller compared to the lower molecular weight polymer, figure 4.15A. This indicates that aggregates were

pre-formed in solution. It is therefore assumed that for the higher molecular weight Si-PCPDTBT only pre-aggregates are deposited during the spin coating process.

These results show that Si-PCPDTBT has a much stronger tendency to aggregate compared to F-PCPDTBT and PCPDTBT. The AFM image revealed only disordered films and no additional investigations were performed on these films without further annealing.

4.3 Solvent Vapor Annealing as Method to Obtain Highly Crystalline Samples

In the previous section it was shown that highly ordered films of PCPDTBT and F-PCPDTBT can be prepared by spin coating from 1-CN or CB/DIO solutions. Nevertheless, TEM/ED and DSC measurements of these films revealed only weak reflections and no melting point could be determined. Literature suggests for spin coated films an edge-on morphology but the reported GIWAXS data only give a rough picture of the crystal structure.[58,102] In this chapter solvent vapor annealing is therefore used as method to prepare thin films of higher crystallinity. All results from this chapter regarding PCPDTBT were also published by us in [12, Fischer et al. 2015].

Post-treatment of polymer films by solvent vapor annealing has been proven highly successful in the last years both for block copolymer self-assembly and polymer/PCBM blend phase separation. It further allows control over crystallization of semi-crystalline polymers. Due to the milder conditions, solvent vapor annealing has become a good alternative to conventional temperature annealing protocols since degradation at high temperature is avoided.[15,16,62,83,129,131,151–153]

Most research groups perform solvent vapor annealing by treating thin films with a saturated vapor, e.g. by placing a film for several minutes in a closed vial in which the bottom is covered by the annealing solvent. After several minutes the recrystallization is induced by opening the vial and quenching with pure nitrogen or air. Some other groups, including ourselves, built setups which allow to control the solvent atmosphere over a range of solvent vapor pressures and temperatures.[16,83,152] The strategy is to initially swell the film at very high vapor pressures forming thin films of highly concentrated solutions and to erase thereby any "deposition" history from the pre-cast films. Crystallization can subsequently be induced from this solution-like state by reducing the vapor pressure in a controlled manner which allows a high control over the crystallization conditions such as the drying time and evaporation rate, chapter 3.2.3. Hereafter samples annealed within a certain solvent vapor will be referred to as: *solvent-annealed* films.

Pre-cast films of polymers which show a high tendency to aggregate can sometimes not be swollen by solvent vapor annealing. In these cases it is possible to use a pre-dissolved highly concentrated solution and add few microliters onto a bare substrate in the solvent chamber. After several minutes at a high vapor pressure (around 90 to 94 %) a homogeneous film of the solution is formed. Recrystallization can be induced by reducing the vapor pressure similar as after the swelling of a pre-cast film. This technique is hereafter called *solvent-crystallization* and a detailed description is given in chapter 3.2.3.

Low boiling point solvents such as CS_2 (bp. 46 °C) are beneficial for solvent vapor annealing, since one can work at room temperature and still achieve high solvent content in the vapor, enabling the dissolution of the polymer film. For higher boiling point solvents such as CB (bp. 132 °C) it is required to increase the solvent and vapor temperature in order to gain a sufficient vapor pressure, chapter 3.2.3. Upon increasing the temperature, often also the critical issue of dewetting becomes more relevant. Dewetting means that if too much solvent condensates onto the sample the highly concentrated solution begins to form small droplets or holes. If dewetting occurs, typically the complete film is destroyed within several minutes and can not be recrystallized as a homogeneous film. Therefore the process becomes more complex and the experimentalist has less control over the annealing when using higher boiling point solvents and increased annealing temperatures.

All three derivatives of PCPDTBT were solvent vapor annealed in CS_2 and chlorobenzene (CB) vapor and will be discussed in the following section.

4.3.1 PCPDTBT

For the solvent vapor annealing experiments $CHCl_3$-spincoated films were used since the absorption spectra and the rather featureless top surface evident by AFM indicate a rather amorphous nature of these films, chapter 4.2 figure 4.8. Therefore pre-cast films of around 40 nm thickness were prepared by spin coating from a 3 mg/ml $CHCl_3$ solution on different substrates (table 4.4) and solvent vapor annealed in either CS_2 or CB.

CS_2 Solvent Vapor Annealing

A typical crystallization protocol for CS_2-annealing involves swelling of the film in an atmosphere of $P/P_{sat} = 92\%$ (P_{vap}^{sol}) CS_2 to increase the polymer chain mobility within the film as much as possible. The annealing step is followed by a recrystallization carried out by reducing the vapor pressure first down to $P/P_{sat} = 88\%$ ($P_{vap}^{cryst.}$) and in a second step decreasing it within 10 min to 85 %. After quenching with pure nitrogen the films were dried in vacuum. The detailed standard protocol is given in figure A.10B.

Figure 4.16A shows a polarized optical microscopy image of a film after CS_2 vapor annealing. The strong birefringence indicates already an increased order in the CS_2-annealed films. AFM investigations of the top surface revealed a highly ordered fiber-like structure in accordance with the POM images, figure 4.16B.

In general the film morphologies seem to be similar to the 1-CN-spincoated films. TEM/ED diffraction of PCPDTBT, shown in figure A.11, reveal a pattern of only weak

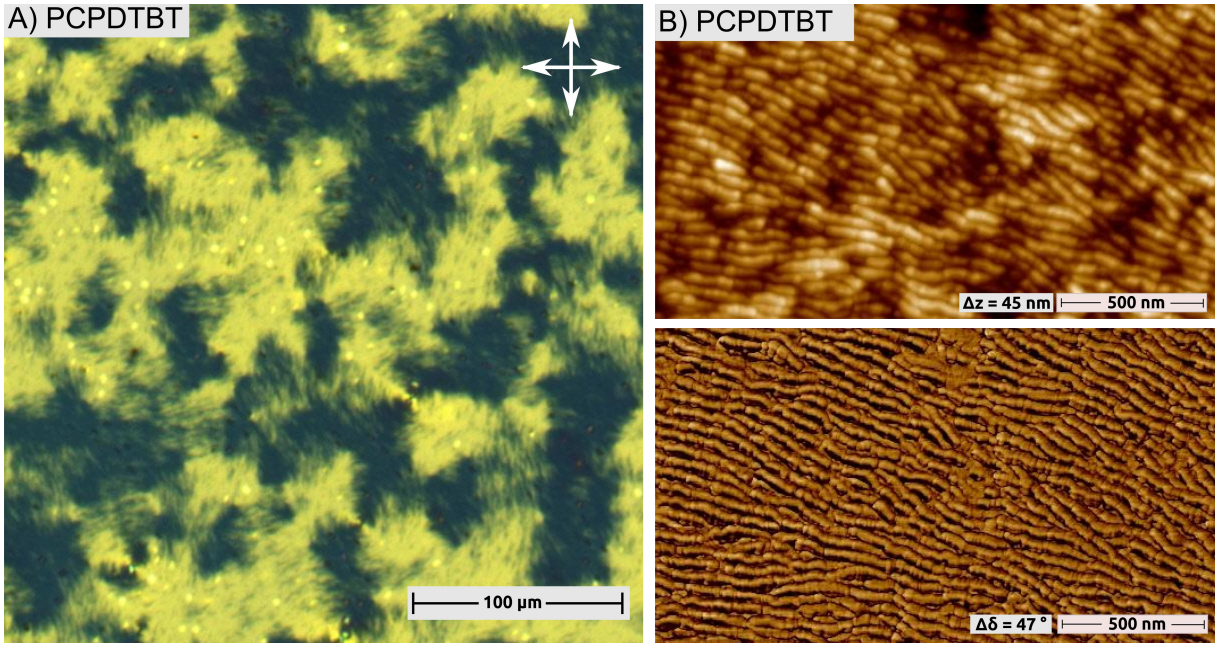

Fig. 4.16: POM (A) and AFM (B, top: height, bottom: phase) images of a thin PCPDTBT film prepared by CS_2 solvent vapor annealing. A detailed annealing protocol is given in figure A.10B (adapted from[12]).

reflections with specific orientations and distances at around 5.9 Å and 6.5 Å. Overall the reflections were too weak as to allow further crystal structure analysis.

CB Solvent Vapor Annealing

Since CS_2 solvent vapor annealing did not lead to films of increased order and crystallinity compared to the spin coated films the solvent CB was used for further annealing experiments. Due to the high boiling point of 132 °C a new annealing setup had to be built. The new setup allowed to heat the solvent reservoir and the whole vapor path such that uncontrolled condensation during operating at elevated temperatures was prevented, figure 3.3. After screening several temperatures for the solvent annealing, 50 °C was found to be an optimum temperature between controllable condensation and a high enough solvent content in the vapor to dissolve the films. It was therefore used in all following annealing protocols. The details of the setup are described in chapter 3.2.3.

Again, similar to the CS_2 solvent vapor annealing, pre-cast PCPDTBT films (3 mg/ml, $CHCl_3$, 1500 rpm) of around 40 nm thickness were placed into the solvent chamber and heated by a Peltier element to 42.2 °C. Using different annealing protocols in which the vapor pressures were varied for the swelling and recrystallization steps allowed to tune the nucleation density. The POM images in figure 4.17 demonstrate the control gained over the crystallization by solvent vapor annealing. The nucleation density and size of

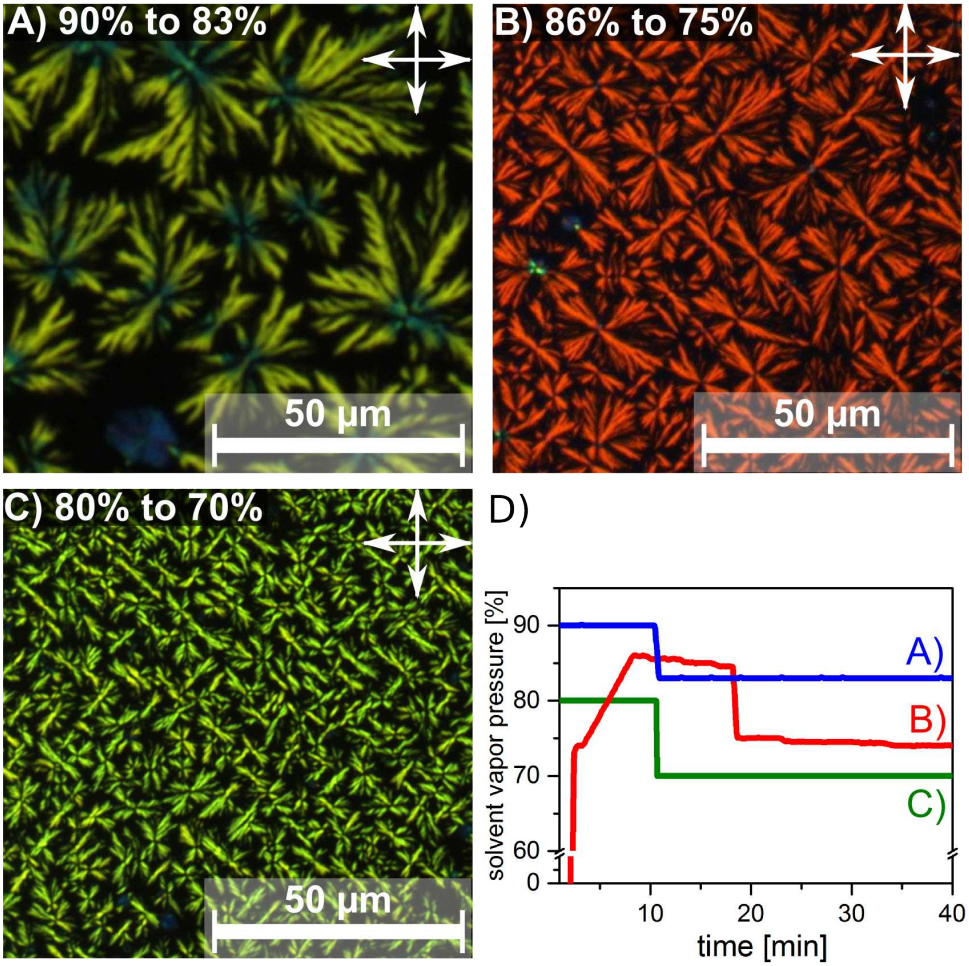

Fig. 4.17: A to C) Polarized microscopy images with crossed polarizers of CB vapor annealed films employing different annealing protocols. **D)** Annealing protocols of the films shown in A) to C) (adapted from[12]).

the spherulites was controlled by changing the time and vapor pressure (figure 4.17D) used for the swelling and recrystallization of the thin films. Similar results were already reported from our group for the semi-crystalline polymer P3HT.[83] It was shown that the vapor pressure of the swelling controls the number of seeds which later act as nucleation points during the recrystallization. While swelling the film all but the thermodynamically most stable crystals are dissolved which then act as seeds (nucleation centers) during subsequent recrystallization. The best and reproducible crystallization condition was found when recrystallizing the samples at vapor pressures between 70 to 73 % ($P_{vap}^{cryst.}$) after they had been dissolved in a CB vapor of around 80 to 90 % (P_{vap}^{sol}) for around 15 min. A detailed annealing protocol is given in figure A.10A. It should be pointed out that the here described morphologies were achieved on a variety of substrates including: Si-, SiO_x-, glass-, quartz- and gold-wafer.

Microscopy Investigations

The morphology of the CB-annealed samples was investigated by several microscopical techniques such as POM, AFM and SEM on the micrometer to nanometer scale. Additionally a structural characterization employing X-ray and electron diffraction was performed and is discussed in the next chapter. Figure 4.18A shows the polarized microscopy (POM) images of the CB-annealed films revealing a strong birefringence and the typical Maltese Crosses of spherulitic structures which indicate a radial growth starting from specific nucleation points. It should be noted that these structures are similar to P3HT spherulites prepared by CS_2-annealing, which typically consist of an edge-on morphology.[83] The size of the spherulites varies with the used annealing protocol and reaches diameters of up to 40 µm, figure 4.17.

SEM images of the spherulites reveal a dendritic structure, figure 4.18C. In the center of the spherulites a small region of parallel lamellae (inset) was found which splay and branch radially into fibers away from the center. Such fiber or lamella growth is typical for conjugated polymers in which one crystallographic direction grows faster than the others, chapter 1.2.4.

Besides the spherulites a second deep blue, almost circular structure, was found in the POM images, figure 4.18B. These structures are especially prominent in samples with low nucleation density, figure 4.17A. Interestingly, these structures show no Maltese Cross or fiber-like structures suggesting a different growth mechanism than the radial growth observed for the spherulites. Further investigations by TEM and AFM, shown in figure 4.18D and E, respectively, suggest areas of different thicknesses. An AFM height profile confirmed distinct height steps of 15 ± 3 nm between the different regions indicating a terrace-like structure. Such structures are likely to originate form standing polymer chains and will be discussed further in the next chapter utilizing electron and X-ray diffraction for a more in-depth structural characterization. In summary the microscopy methods suggest the existence of two morphologies of rather high crystallinity and different polymer chain orientations relative to the substrate.

Melting Point

In literature, no differential scanning calorimetry (DSC) measurements of PCPDTBT were found. Attempts during this thesis to determine a melting point of PCPDTBT by conventional DSC measurements of powders prepared by drying PCPDTBT from different solvents remained unsuccessful. Therefore the crystalline CB-annealed samples were investigated employing DSC measurements.

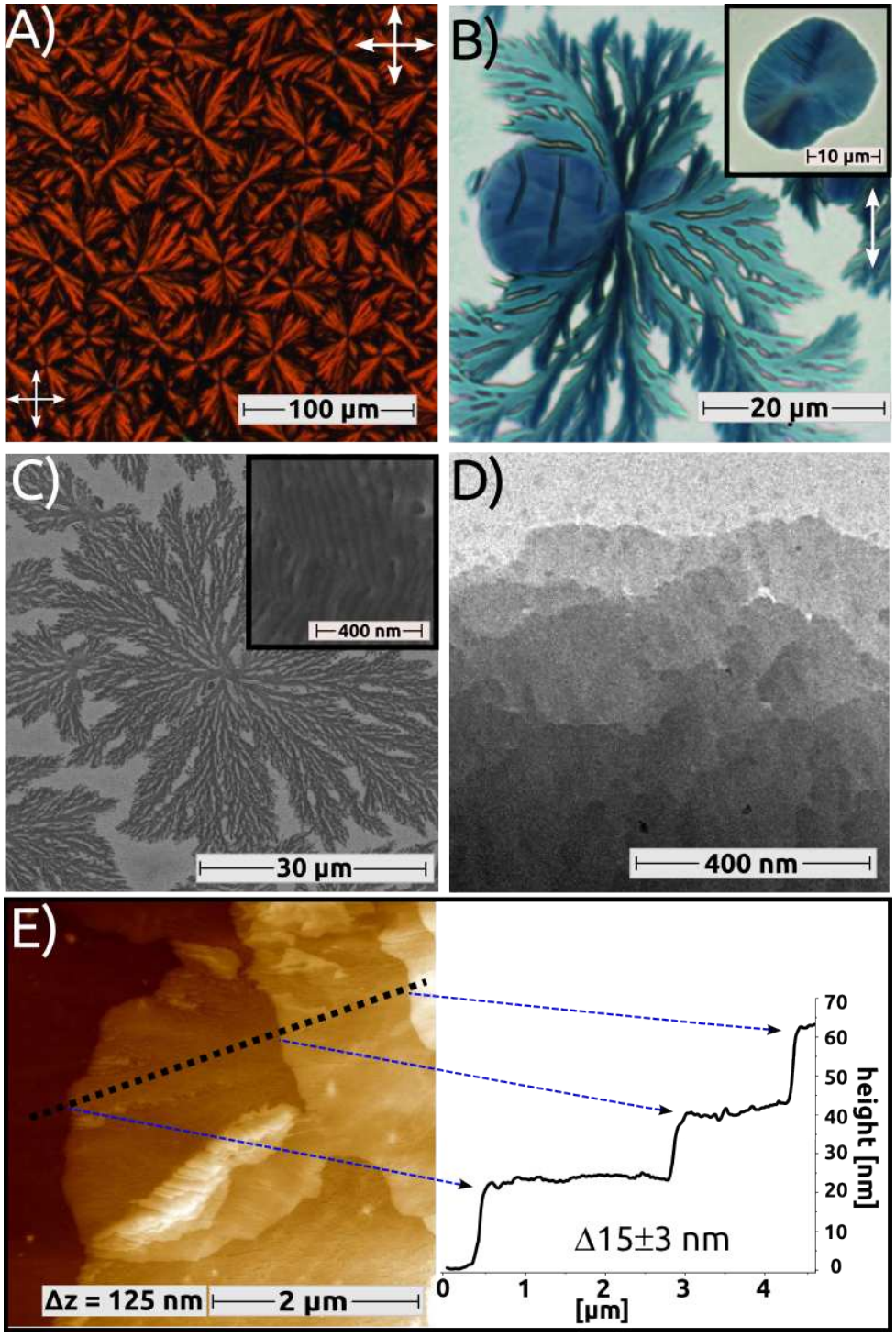

Fig. 4.18: Morphology of PCPDTBT thin films prepared by CB solvent vapor annealing. The spin coated films ($3\,\mathrm{mg/ml}$, $CHCl_3$, $1500\,\mathrm{rpm}$) were swollen at vapor pressures between 70 to $73\,\%$ after they had been dissolved in CB vapor of around 80 to $90\,\%$. **A)** POM image (reflection mode) of a thin film consisting only of spherulites (substrate: Si-wafer). **B)** POM image (transmission mode) of a single spherulite together with a terrace-like structure, inset: magnification of an individual terrace-like structure (glass-wafer). **C)** SEM image of the dendritic structure of a spherulite (Au-substrate). The image was measured at $1.0\,\mathrm{kV}$ with a secondary electron detector in $12.1\,\mathrm{mm}$ distance of the sample. **D)** TEM bright field image of the edge of a terrace-like structure. **E)** AFM height image of the edge of a terrace-like structure with the height profile showing the distinct height steps (adapted from[12]).

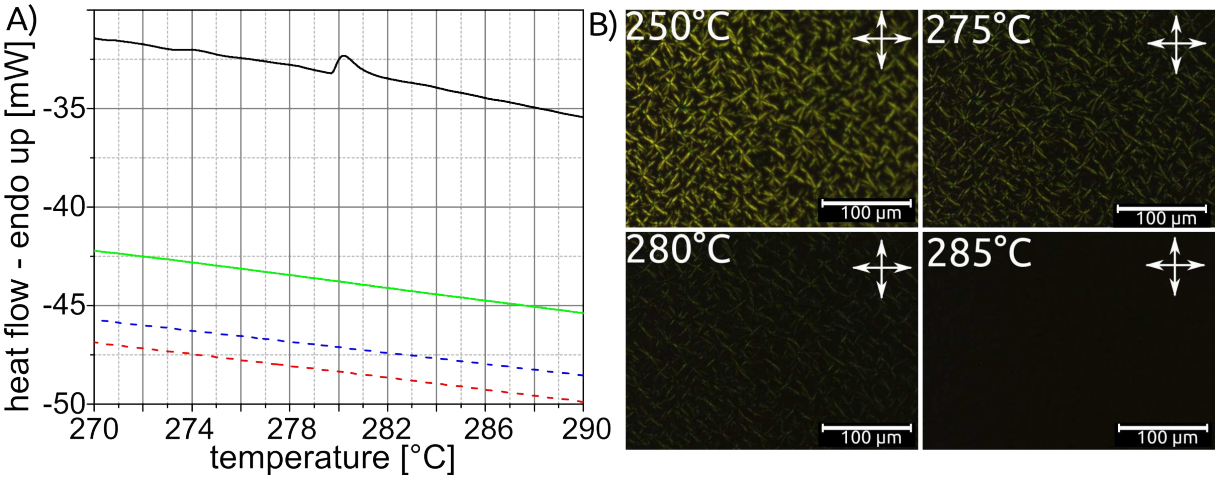

Fig. 4.19: PCPDTBT samples prepared by CB vapor annealing. **A)** DSC measurement heated from $-50\,°C$ to $370\,°C$ (black), cooled to $-50\,°C$ (dashed blue), heated again to $370\,°C$ (green) and cooled to $-50\,°C$ (dashed red) with $10\,K/min$. **B)** POM images taken of a CB-annealed PCPDTBT film during heating under an argon atmosphere with $10\,K/min$. All images were taken with the same exposure settings (adapted from[12]).

The annealing procedure had to be slightly adapted to prepare enough CB-annealed PCPDTBT material for a DSC measurement. The recrystallization was therefore performed directly inside a DSC pan. A highly concentrated CB solution (110 mg/ml) was filled into a 50 µl (Al) pan and placed into a saturated CB vapor atmosphere. Slowly reducing the vapor pressure over several hours led to a crystallization of the polymer solution. POM images taken of the material in the DSC pans confirmed that spherulitic structures similar to the thin films were obtained. After drying in vacuum the DSC pans were closed under nitrogen atmosphere and measured by heating/cooling cycles between -50 to $370\,°C$ with $10\,K/min$, figure 4.19A. Earlier TGA measurements had shown the stability of the polymer up to $400\,°C$ excluding degradation during the DSC measurements, figure A.22.

In figure 4.19A the first heating curve (black) reveals a distinct melt transition at $280 \pm 2\,°C$. A recrystallization of the polymer during the following cooling and heating cycle was not observed. This underlines the finding that conventional temperature annealing does not seem to give rise to crystallization in PCPDTBT polymers. Only under more dynamic conditions such as solvent vapor annealing crystallization can be induced.

Employing a hot-stage, the melting point was further confirmed by in-situ POM measurements. POM images were taken during the heating of a CB-annealed film under an argon atmosphere. Figure 4.19B shows how the characteristic Maltese Crosses of the spherulitic structures vanish between 275 and $285\,°C$ which is in perfect agreement to the DSC results.

Finding a melting point for the CB-annealed samples, which was impossible for the non solvent vapor annealed material, confirms the increased crystallinity compared to the spin coated samples discussed in chapter 4.2.

4.3.2 F-PCPDTBT

CS_2 Solvent Vapor Annealing

CS_2 solvent vapor annealing of F-PCPDTBT films was performed with the same protocol as used for PCPDTBT, figure A.10B. $CHCl_3$-spincoated films were swollen in a CS_2 atmosphere of $P/P_{sat} = 92\%$ (P_{vap}^{sol}). Recrystallization was subsequently induced by reducing the vapor pressure down to $P/P_{sat} = 88\%$ ($P_{vap}^{cryst.}$) and further decreasing it within 10 min to 85 %.

The polarized optical microscopy images of the solvent annealed films show only a weak birefringence, figure A.12. The AFM investigations revealed a fiber-like morphology with two regions of different fiber density, figure 4.20. In some parts of the films the fibers form a network-like structure in which only few fibers are arranged parallel to each other, figure 4.20A. In other regions a higher fiber density with thick bundles of parallel arranged fibers was found, figure 4.20B. In-situ microscopy observation during the CS_2 vapor annealing revealed an inhomogeneous swelling of the F-PCPDTBT films which could have caused the two different regions.

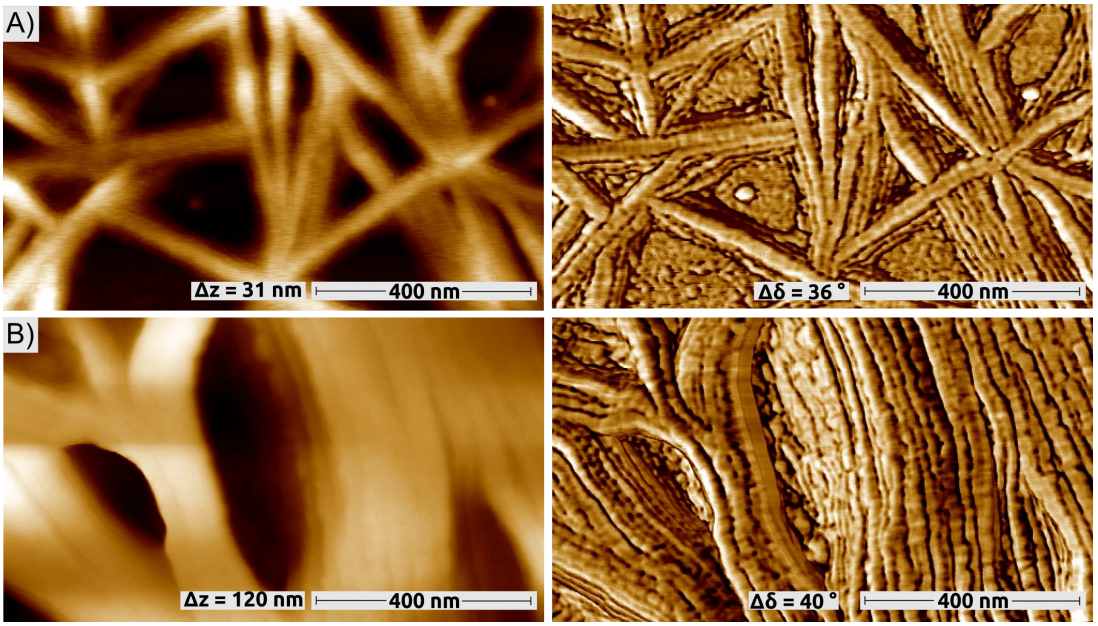

Fig. 4.20: AFM height (left) and phase (top) images of CS_2-annealed F-PCPDTBT films. A) and B) display different areas of the same sample.

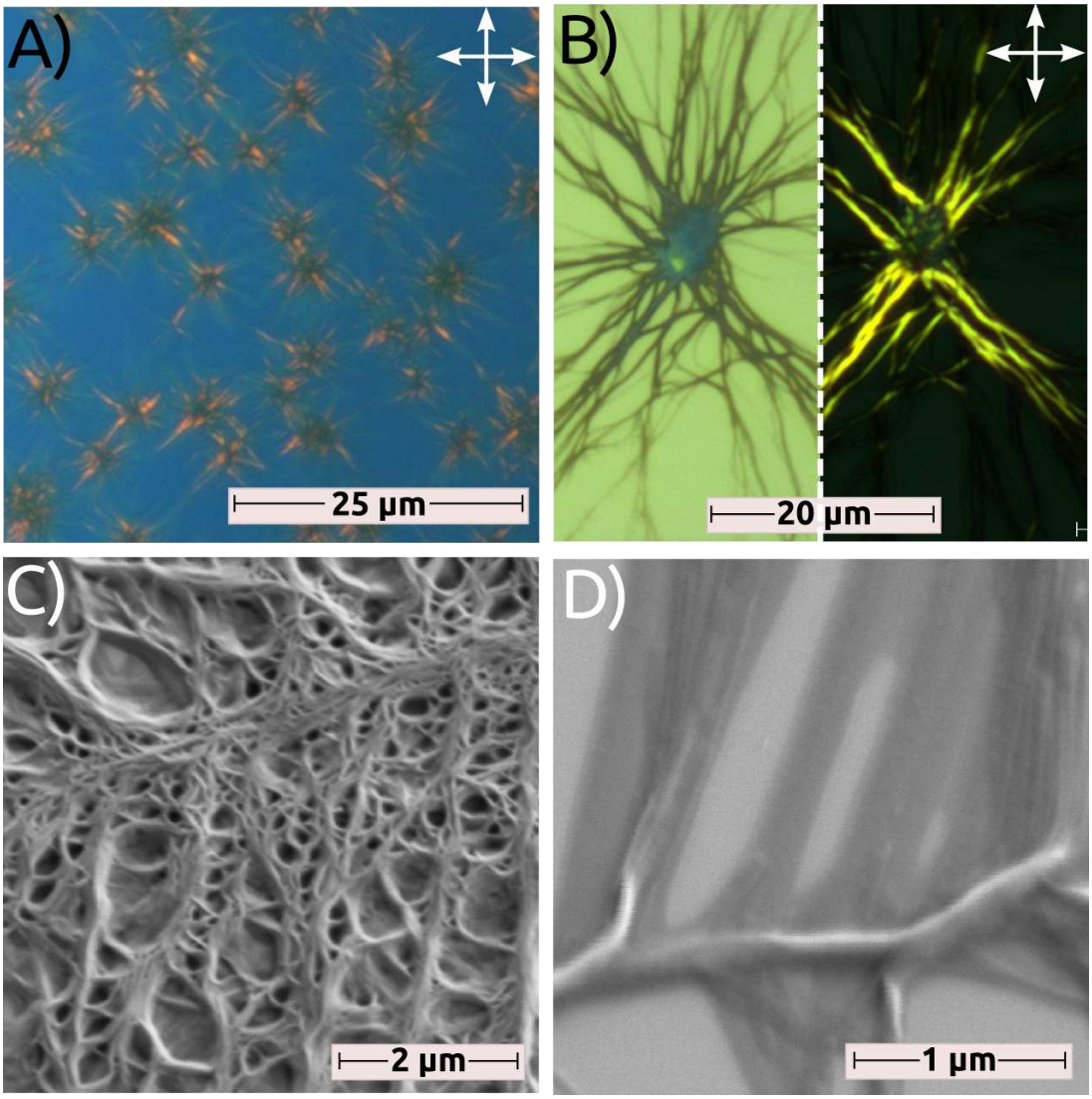

Fig. 4.21: Morphology of F-PCPDTBT thin films prepared by CB solvent crystallization. A diluted solution of $0.01\,\mathrm{mg/ml}$ was crystallized in a $74\,\%$ CB vapor pressure within $900\,\mathrm{min}$. **A)** POM image of a thin film after CB solvent crystallization (substrate: SiO_x-wafer). **B)** Microscopy image of a single star-like structure without (left) and with (right) crossed polarizers (Si-wafer). **C)** SEM image from the center of a spherulite (Au-substrate). **D)** SEM image of a single fiber in the outer region of a star-like structure (Au-substrate). The SEM images were acquired at $2.0\,\mathrm{kV}$ with a secondary electron detector in $8.4\,\mathrm{mm}$ distance to the sample.

Since no homogeneous structure and crystallization could be obtained using CS_2 solvent vapor annealing no further investigations employing CS_2 were performed for F-PCPDTBT.

CB Solvent Vapor Crystallization

Using pre-cast films of F-PCPDTBT and similar annealing protocols as described for PCPDTBT always led to either no change in the thin film structure or to a strong dewetting of the swollen films. Therefore instead of using a pre-cast film a diluted CB

solution (0.1 mg/ml) was placed onto a clean substrate inside the solvent chamber. The substrate was held at 42 °C while the chamber was purged with a 92 % (P_{vap}^{sol}) CB vapor at 50 °C for 10 min. During this step a homogeneous film of the solution was formed on the substrate which was afterwards crystallized by decreasing the vapor pressure to 74 % ($P_{vap}^{cryst.}$). Within 900 min at 74 % the solvent evaporated completely and crystalline appearing star-like structures remained, figure 4.21. A detailed annealing protocol is shown in figure A.10C.

Morphology

Figure 4.21 shows POM and SEM images taken from CB-crystallized F-PCPDTBT films. They reveal isolated star-like features of around 20 µm in diameter and show a strong birefringence and Maltese Crosses in the POM images. The center of these structures is formed by a couple of parallel fibers surrounded by a disordered network of fibers from which only few grow radially away as can be seen from the SEM image in figure 4.21C. Further magnification of single fibers in the SEM (figure 4.21D) shows a thick core which is surrounded by a thinner structure. Interestingly, no defined nucleation points were found as in the PCPDTBT spherulites. It is therefore considered that few in solution pre-aggregated fibers act as nucleation points when deposited on the substrates. It should be noted that, in contrast to the PCPDTBT samples, for F-PCPDTBT no terrace-like features were found.

4.3.3 Si-PCPDTBT

The absorption spectroscopy in solution and thin films already suggested lower solubility of Si-PCPDTBT, chapter 4.1. This was further confirmed by the CS_2 solvent vapor annealing which showed either no effect or a very strong dewetting of the samples. Therefore no experiments using CS_2 solvent vapor annealing are shown.

Using chlorobenzene as annealing solvent and protocols similar to the ones applied for PCPDTBT and F-PCPDTBT revealed also for the higher molecular weight samples (M_w = 32.3 and 11.3 kg/mol) that they can not be solvent vapor annealed. Even solvent crystallization as successfully used for F-PCPDTBT was found to lead to uncontrolled film crystallization and inhomogeneous films. Therefore the higher molecular weights were also not further investigated.

The lower molecular weight samples (M_w = 4.4 and 10.5 kg/mol) reveal better solubility and the CB-annealing protocol could be optimized during the master thesis of M. Jasch[150] under my supervision. Si-PCPDTBT films were spin coated from 3 mg/ml $CHCl_3$ solutions

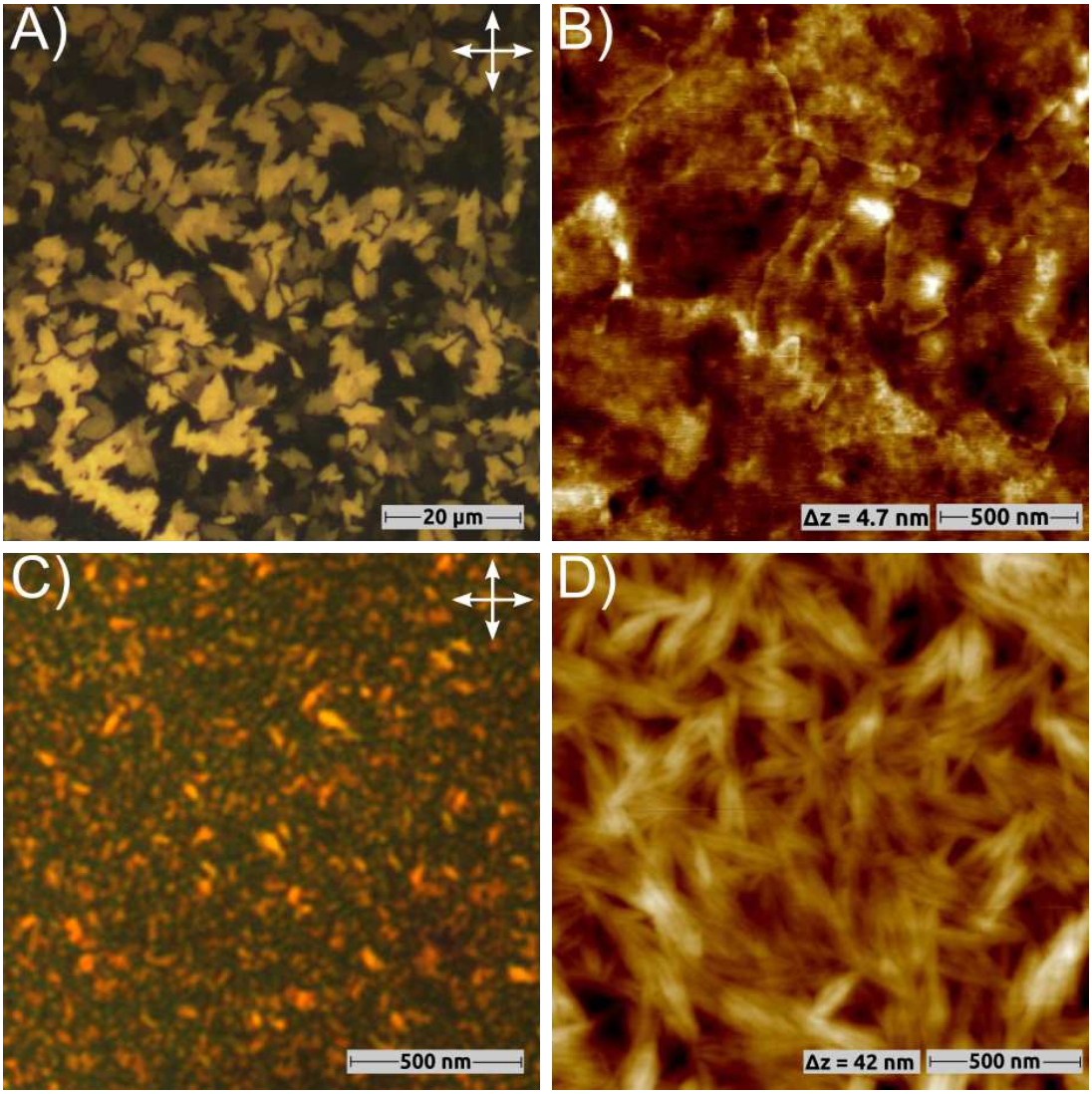

Fig. 4.22: POM and AFM height images of Si-PCPDTBT (A/B: M_w 4.4 kg/mol, C/D: 10.5 kg/mol) thin films prepared by CB solvent vapor annealing. CB-annealed films of Si-PCPDTBT were prepared from pre-cast films (spin coated, 3 mg/ml, $CHCl_3$) by annealing in CB vapor (50 °C) whereas the samples were cooled down to A/B: 47 °C and C/D: 45 °C. (Measured by M. Jasch during his master thesis).[150]

and recrystallized at 70 to 60 % ($P_{vap}^{cryst.}$) solvent vapor after swelling the films at 77 % (P_{vap}^{sol}). The detailed protocol is given in figure A.10D. The CB vapor temperature was set to 50 °C for both polymers and the cooling of the sample was adjusted to 47 and 45 °C for the 4.4 and 10.5 kg/mol (M_w) samples, respectively.

The POM and AFM images of the CB-annealed Si-PCPDTBT films are shown in figure 4.22. The morphologies of the two molecular weight samples strongly differ from each other. The lower molecular weight (M_w = 4.4 kg/mol) film consists of around 5 µm large irregularly formed regions of high birefringence. No correlation between birefringence

and the polarizer positions was found which indicates a morphology of standing chains. The AFM images confirmed a flat structure with sharp grain boundaries. Height profiles taken from several samples revealed no distinct height steps.

Figure 4.22C/D displays the POM and AFM images of the 10.5 kg/mol (M_w) sample. The POM images reveal a structure of high nucleation density and strong birefringence. Probably due to the small feature size no Maltese Crosses could be identified. The AFM height image reveals a structure comprised of short fibers with no specific nucleation point similar as seen for F-PCPDTBT samples prepared by spin coating, figure 4.12.

4.3.4 Absorption Properties of Solvent Annealed Films

PCPDTBT and F-PCPDTBT

The POM, AFM, DSC and TEM measurements of CB-annealed PCPDTBT and F-PCPDTBT suggested the formation of highly ordered crystalline films. For both polymers the aggregation experiments in solution had revealed a prominent 800 nm band during the formation of aggregates at low temperatures. In literature the 800 nm band was correlated to an edge-on morphology with a π-stacking of the polymer backbones, chapter 4.1.3.

Due to the high crystallinity, evident from POM and DSC, a strong 800 nm absorption was expected to confirm the crystallinity of the solvent annealed films. For the following absorption measurements samples consisting of only the spherulitic structures were used, since the rare and small circular blue structures could not be measured exclusively without locally resolved spectroscopy.

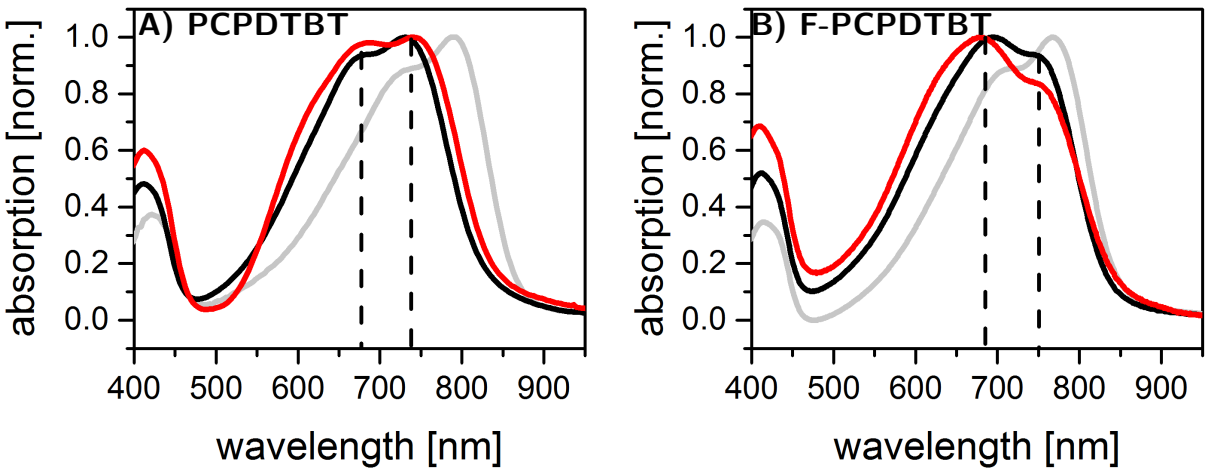

Fig. 4.23: Absorption spectra of CS_2- (black) and CB-annealed (red) PCPDTBT (A, adapted from[12]) and F-PCPDTBT (B) films. As comparison the spectra of spin coated films from PCPDTBT (3 mg/ml CB+2 w% DIO, A) and F-PCPDTBT (3 mg/ml CB, B) are added (light gray).

Surprisingly, for both polymers the CS_2- and CB-annealed films do not show an 800 nm absorption band. Instead they reveal an additional blue-shifted absorption band with a maximum around 680 nm, figure 4.23. For comparison reasons spectra of CB/DIO-spincoated films were added (gray) to the graph. This is remarkable since these two samples consist of a much higher crystallinity (see discussion above) than the CB/DIO-spincoated films. This leads to two possible conclusions: i) The films are not crystalline, which is unlikely since DSC and POM results indicate a highly crystalline film or ii) the films consist of a new crystal structure with a different absorption signature. This would mean that the solvent-annealed films form a structure which is different from the aggregates found in solution and after spin coating. The second conclusion seems more likely and would be in accordance with the absorption behavior known from the donor-acceptor polymer P(NDI2OD-T2). As discussed in the introduction of this chapter the absorption of P(NDI2OD-T2) depends strongly on the crystal structure, mainly the stacking of the donor/acceptor units.[138]

Temperature-Dependent UV/Vis-Spectroscopy

To further compare the two structures with and without the 800 nm absorption additional temperature-dependent absorption spectroscopy was performed. Therefore the evolution of the absorption while heating from room temperature to 250 °C was measured. Figure 4.24 shows the temperature-dependent film spectra of the solvent-annealed samples (left) and the CB/DIO-spincoated samples (right). For PCPDTBT (top) as well as F-PCPDTBT (bottom) the spectra were taken during a heating process of 5 K/min under nitrogen atmosphere.

For both polymers the evolution of the differently prepared films strongly differs: The spectra of the CB/DIO-spincoated sample (figure 4.24B and D) reveal at room temperature (black) a strong 800 nm band. At 100 °C (dashed, blue) the 800 nm absorption is almost completely gone and the maximum of the absorption is shifted to around 730 nm. Further increasing the temperature up to 250 °C shifts the absorption to even higher energies up to 700 nm.

The CB-annealed films of both polymers show no 800 nm absorption at room temperature, figure 4.24A/C (black). Instead they reveal a blue-shifted absorption with a maximum around 680 nm and a shoulder around 760 nm. Interestingly, when heating the CB-annealed films up to 100 °C almost no change in the absorption was observed, figure 4.24A/C (blue dashed). At 250 °C (red) the 680 nm absorption is still present but the shoulder around 760 nm decreased in intensity during the heating process.

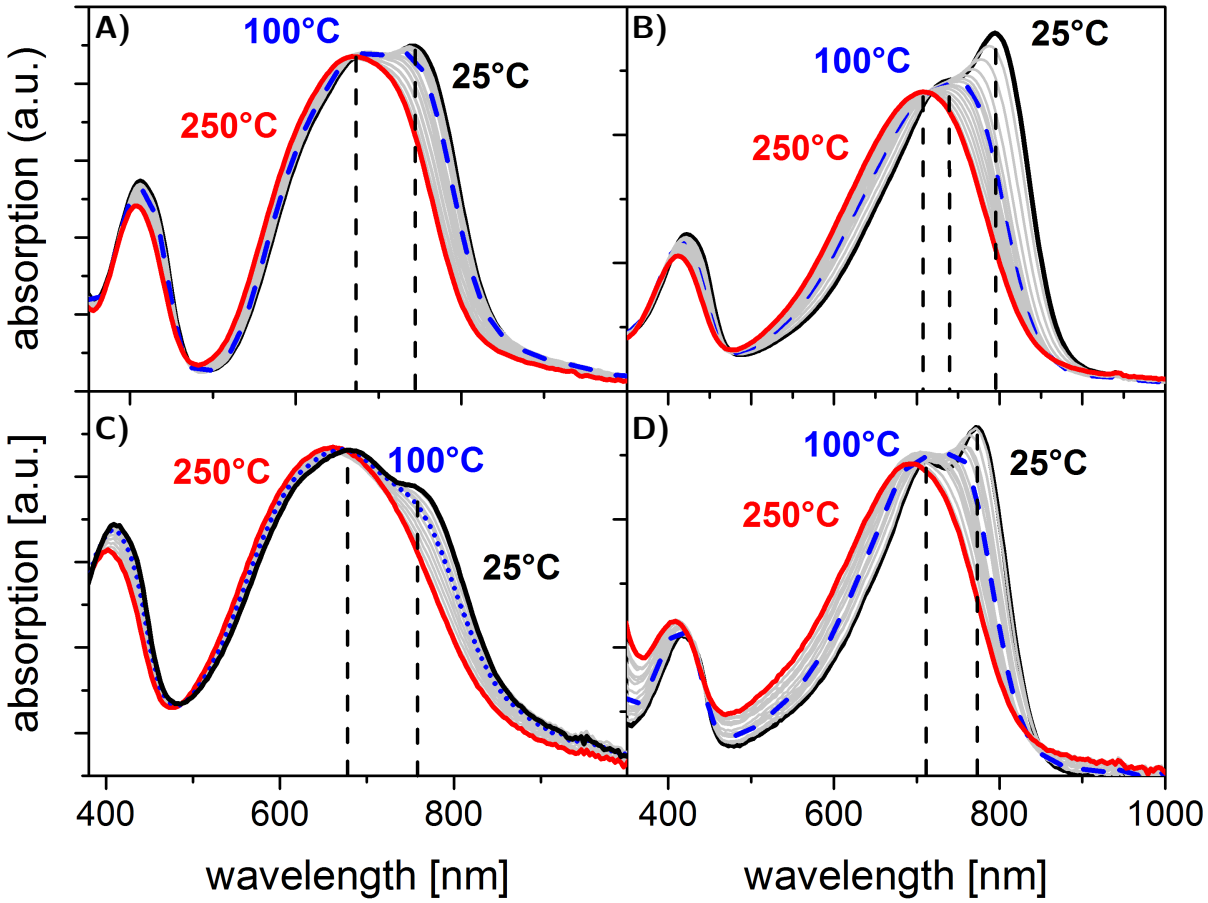

Fig. 4.24: UV/Vis-absorption spectra during the heating (5 K/min) of PCPDTBT (A and B) and F-PCPDTBT (C and D) films prepared by CB vapor annealing (A,C) and spin coating from CB with 2 w% DIO (B,D).

The main difference between the CB-annealed and the CB/DIO-spincoated samples is that in the CB/DIO-spincoated samples an evolution of the absorption spectra already takes place while heating up to 100 °C. The absorption signature of the CB-annealed samples on the other hand does not change until close to the melting point.

The PCPDTBT films were additionally heated to 320 °C which is 40 °C above the melting point. At this temperature the spectra of both samples (CB-annealed and CB/DIO-spincoated) look almost identical with a low (400 nm), a high energy (670 nm) absorption and without any fine structure, figure A.13. This is expected since in both cases the respective crystal structure should be completely destroyed.

All findings indicate that the solvent vapor annealed films comprise a thermodynamically more stable polymorph than the CB/DIO-spincoated films. POM and DSC support the assumption of a highly crystalline structure compared to the CB/DIO-spincoated films. Further the absence of the 800 nm band in the absorption supports a new polymorph and

the temperature dependent spectra indicate that this new polymorph is thermodynamically favored.

Si-PCPDTBT

The different molecular weights of Si-PCPDTBT were investigated by absorption spectroscopy after CB-annealing and compared with the absorption of the spin coated films. In agreement with the POM and AFM investigations the high molecular weight samples (M_w = 11 and 32 kg/mol) reveal no change in the absorption of the thin films before and after CB vapor annealing, figure 4.25 (orange and blue).

For the lower molecular weights (M_w = 4 and 10 kg/mol) an increase of the low energy absorption band was observed after CB solvent vapor annealing, figure 4.25 (black). The spectra show a small increase of the shoulder around 730 nm for the M_w = 4 kg/mol and an even smaller increase for the M_w = 10 kg/mol sample. These results suggest that the films do still consist of a large amorphous portion, even though the POM and AFM images suggested increased crystallinity. Another possibility could be that almost no change of the absorption between the aggregated and non-aggregated structure exists. This is unlikely when considering the strong effects found for PCPDTBT and F-PCPDTBT.

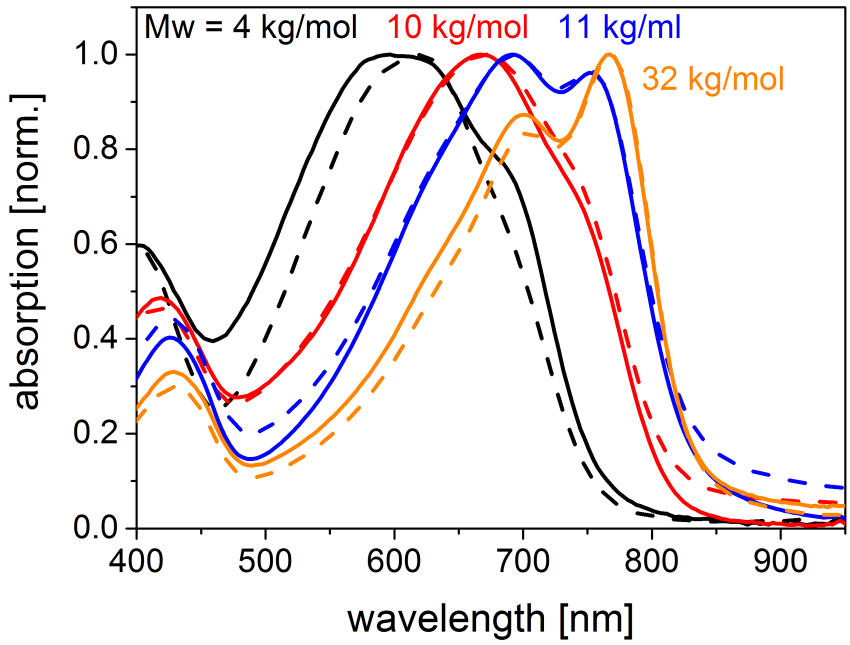

Fig. 4.25: Absorption spectra of Si-PCPDTBT films with different molecular weights before (dashed) and after CB annealing (solid). The pre-cast films (spin coated, 3 mg/ml CB) were CB solvent vapor annealed at 50 °C and a substrate temperature of around 45 to 47 °C. The detailed vapor annealing protocol is given in figure A.10D.

Si-PCPDTBT seems in summary to either aggregate already in solution (M_w = 11 and 32 kg/mol) or seems to be only slightly effected by CB solvent vapor annealing (M_w = 4 and 10 kg/mol). Even though or maybe despite the fact that the optical properties of Si-PCPDTBT are completely unaffected by processing conditions Si-PCPDTBT performs very well in organic solar cells.[4]

4.3.5 Summary

In this chapter solvent vapor annealing was used to control the crystallization of PCPDTBT and its derivatives. The two solvents CS_2 and chlorobenzene (CB) were employed and a high control over the crystallization of PCPDTBT and F-PCPDTBT was obtained. Highly crystalline structures could be obtained for polymers when CB solvent annealing was used.

For PCPDTBT and F-PCPDTBT a spherulitic structure consisting of a fiber-like substructure was found. In PCPDTBT additionally small regions of a second morphology with a terrace-like structure and deep blue absorption was found. It was possible to determine the melting point of the CB-annealed samples to 280 °C by DSC measurements.

Absorption measurements and a comparison to the earlier discussed CB/DIO-spincoated films revealed that the solvent-annealed samples consist of a new and different polymorph. This becomes evident from the absence of the characteristic 800 nm absorption found in the CB/DIO-spincoated samples. The polymorph obtained by CB-annealing revealed in contrast a blue-shifted absorption with a new maximum around 680 nm.

Further temperature-dependent absorption measurements revealed for the CB-annealed films an unchanged absorption above 100 °C. On the contrary, the characteristic 800 nm band of the CB/DIO-spincoated samples decreased already upon heating to 100 °C. These findings suggest that the new polymorph found in the solvent annealed samples is thermodynamically favored compared to the CB/DIO-spincoated structure.

For Si-PCPDTBT on the other hand it was impossible to obtain control over the crystallization due to its strong tendency to aggregate already in solution. Only the two smallest molecular weight polymers could be crystallized. Surprisingly almost no effect on the absorption spectra was found.

4.4 Polymorphism as Function of Film Preparation

The previous chapters have already shown how difficult it is to crystallize PCPDTBT. This is probably also the reason why only few groups investigated the crystal structure of PCPDTBT. Russel et al.,[58] Bazan et al.[108] and Nelson et al.[102] employed mainly grazing incidence wide angle X-ray scattering (GIWAXS) to resolve the structure of PCPDTBT samples. The samples investigated were prepared by spin coating from CB solutions with and without solvent additives such as 1,8-diiodooctane (DIO) or 1,8-octanedithiol (ODT). In this thesis the samples prepared by following the standard processing conditions from literature (spin coating from CB with 2 w% DIO) will be hereafter called *CB/DIO-spincoated*.

From AFM and POM data such samples are generally described as featureless in the literature.[58,102,108] From the GIWAXS data the authors suggest a morphology with long range π-stacking in analogy to P3HT, figure 1.15C. Two main reflections were reported: an in-plane (IP) π-stacking distance (0 1 0) of 3.8 Å (q = 1.6 $Å^{-1}$) and an out-of-plane (OOP) lamellar stacking distance (1 0 0) around 11 Å, chapter 1.3.1. The values for the lamellar stacking (1 0 0) vary in the literature from 10.5 Å (q = 0.6 $Å^{-1}$) without and 12 Å (q = 0.51 $Å^{-1}$) with solvent additive in the processing solvent. It was therefore suggested that the solvent additives influence the alkyl side chain crystallization, chapter 1.3.1.[58,102]

Bazan et al. further reported two polymorphs: one with an edge-on orientation and the (1 0 0)-OOP reflex at 11.4 Å (q = 0.55 $Å^{-1}$) and another with a face-on morphology and a (1 0 0)-IP reflex at 11.6 Å (q = 0.50 $Å^{-1}$). Independent of the (1 0 0) reflection all publications reported a diffuse π-stacking reflection around 3.8 Å which increased in intensity when processing with solvent additives, figure 1.15B.

GIWAXS data from Nelsen et al.[102] further revealed two weak in-plane reflections at 11.1 Å (q = 0.58 $Å^{-1}$) and 5.8 Å (q = 1.08 $Å^{-1}$). For the CPDTBT unit DFT calculations suggested a length of around 11 to 12 Å. The reflections were therefore correlated to the polymer chain direction (0 0 l) and indexed as (0 0 1) and (0 0 2), respectively.

The structure of PCBM/PCPDTBT blends prepared from solutions containing 2 w% DIO was described by Russel et al.[58] as non-equilibrium crystalline fibrils, but the authors did not further comment on these structures. Chassé et al.[110] applied near edge X-ray absorption fine structure spectroscopy (NEXAFS) and confirmed the edge-on structure based on analogies to other conjugated thiophene-based polymers such as P3HT.

Summarizing these literature data the structure of thin films prepared by spin coating with and without solvent additives is described as an edge-on morphology with π-stacked polymer chains similar to P3HT. The data do not allow for a detailed crystal structure

analysis. In chapter 4.2 the films spin coated from CB with and without solvent additive were also investigated by TEM/ED, figure 4.11 and the reflections, reported in literature from GIWAXS, were confirmed. To the best of my knowledge there is up to today no report, besides our,[12] which used solvent vapor annealing or suggests a crystal structure for PCPDTBT and its derivatives.

It should be noted that the highly crystalline structures found after solvent vapor annealing, chapter 4.3, most likely consist of a completely different morphology than the CB/DIO-spincoated samples reported in literature. This assumption is built on the fact that the solvent annealed structures reveal a rather blue-shifted UV/Vis-absorption without any indication of the 800 nm band as typical for the CB/DIO-spincoated structure, chapter 4.2. Since literature[17,58] proposes that the 800 nm absorption is caused by the long range π-stacking in the edge-on morphology it is probable that the solvent annealed structure is not dominated by such π-stacking.

In the next section, first the crystal structure analysis of the solvent annealed samples is discussed. These samples reveal the structure of the polymer chains in the a,b-plane of the unit cell, but do not give any information along the direction of the polymer backbone. Additional methods had to be used to align the polymer chains within the film plane, chapter 3.2.4. From these samples further information along the c-axis (polymer backbone) of the unit cell was obtained and gives more experimental evidence to allow a crystal structure analysis. All diffraction data of the solvent annealed samples give further evidence of a new crystal structure compared to the CB/DIO-spincoated samples. Parts of this chapter have been submitted in [13, Fischer et al. 2015].

The GIWAXS measurements were performed together with the beam scientist Kevin Yager from the *Center for Functional Nanomaterials* at Brookhaven National Laboratory and the group of Prof. Alamgir Karim from the University of Akron at the X9 beamline at Brookhaven's National Synchrotron Light Source. All TEM/ED experiments were performed in cooperation with M. Brinkmann and N. Kayunkid at the *Institut Charles Sadron* in Strasbourg.

4.4.1 Structural Information from Solvent Annealed Films

4.4.1.1 PCPDTBT

The last chapter showed that PCPDTBT can be crystallized by employing solvent vapor annealing, contradicting the often suggested amorphous nature of PCPDTBT. POM, AFM, SEM and DSC measurements all confirmed a very high order and crystallinity indicating the possibility of a successful crystal structure analysis. Employing TEM/ED

and GIWAXS measurements the solvent vapor annealed samples were used to obtain a first tentative crystal structure for PCPDTBT which was published by us in [12, Fischer et al. 2015].

CB-annealed

The transmission electron microscopy (TEM) bright field images in figure 4.26A of CB-annealed PCPDTBT films reveal the same two features already found in the AFM and SEM images discussed in chapter 4.3.1: i) A spherulitic structure composed out of lamellar substructure as already seen in the POM images, figure 4.18A. ii) A terrace-like structure which appeared as circular blue regions in the polarized optical microscope (POM), figure 4.18B. In the AFM height images distinct height steps were found for these terraces, figure 4.18E. These AFM and POM images were discussed in the previous chapter 4.3.1 and it was suggested that the terrace-like structures of PCPDTBT most likely consist of standing polymer chains.

Using TEM/ED distinct electron diffraction (ED) patterns were found for the terrace-like structures. They reveal reflections up to the sixth order and high symmetry, figure 4.26B. This indicates a very high crystallinity in accordance with the DSC and POM measurements. Assuming standing chains for the terrace-like structure the ED pattern were indexed corresponding to a [001] zone and the unit cell parameters were determined to: a = 12.5 Å and b = 19.8 Å. Further strong (h k 0) reflections which should be noted are the (1 1 0) and the (1 5 0) in the inner and outer region of the ED pattern, respectively.

Figure 4.26C shows the ED pattern of the spherulitic structures. Compared to the terrace-like regions they reveal a much less distinct reflection pattern. Employing rotation tilt TEM/ED experiments the meridian reflection (2 0 0) could be identified as the same reflection found along the meridian of the terrace-like pattern, figure 4.26B. This was shown by tilting the sample relative to the electron beam around the fiber axis finding that the meridian reflection (2 0 0) remained unchanged, whereas other peaks appeared or disappeared. At a tilt of 45 to 50° the same ED pattern as seen for the terrace-like structure arises, figure 4.26D. This proved that both structures comprise the same polymorph and that their unit cells are just differently tilted relative to the substrate by around 45 to 50°, as schematically shown in figure 4.26E and F.

Even though a good set of reflections for PCPDTBT was already found by TEM/ED some samples were additionally measured by GIWAXS at the X9 beamline at Brookhaven's National Synchrotron Light Source to expand the structural model. The experiments were performed by K. Yager from the *Center for Functional Nanomaterials* at Brookhaven

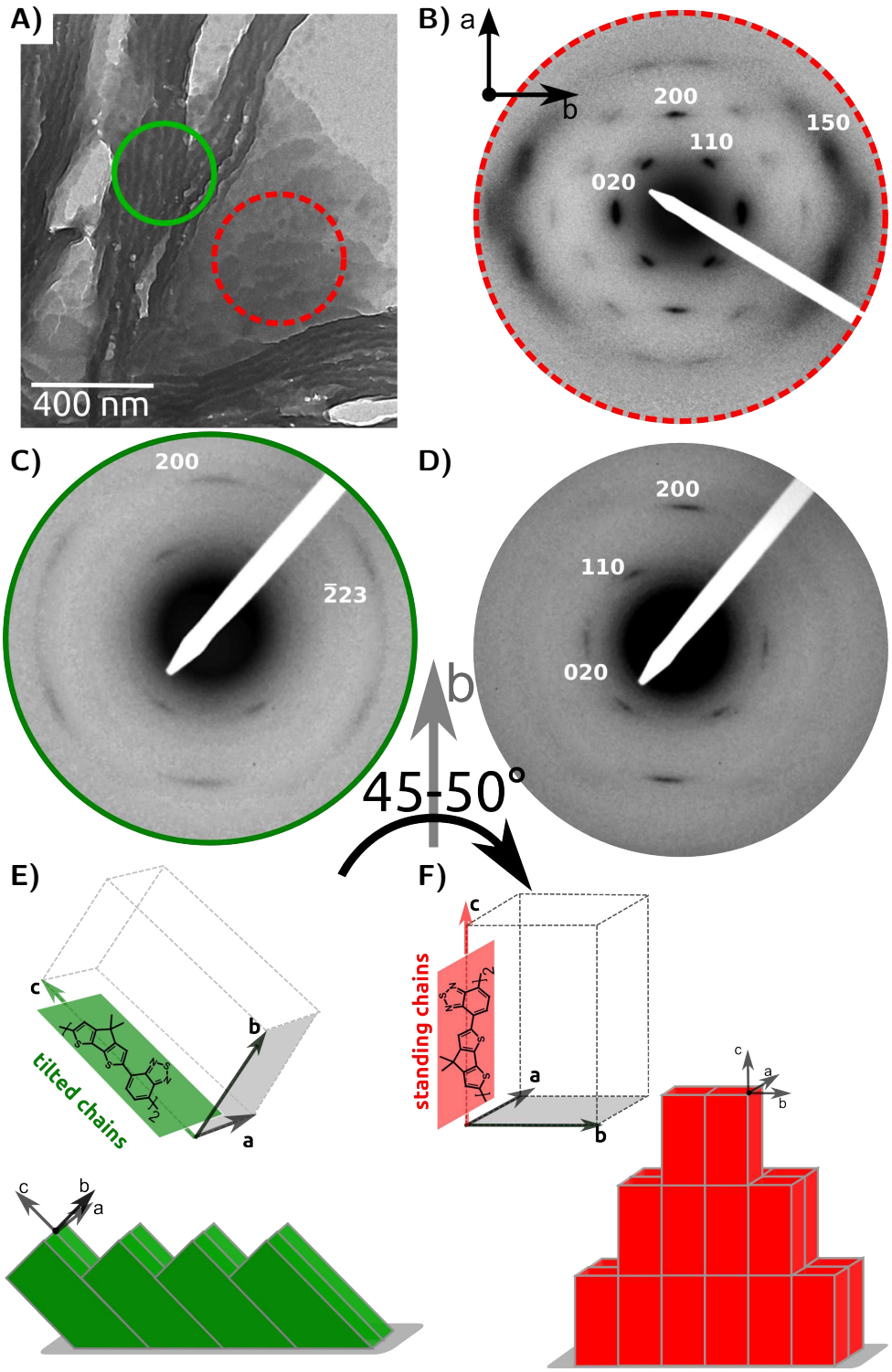

Fig. 4.26: TEM studies of CB-annealed PCPDTBT films. **A)** Bright field image with lamellar (green, solid circle) and terrace-like structures (red, dashed circle) of a PCPDTBT film. **B)** TEM/ED pattern of a terrace-like region as marked in A (red dashed circle). **C)** and **D)** TEM/ED patterns of the lamellar region (A, green, solid circle) (C) and after tilting the TEM grid around the fiber axis (020) by 45 to 50° (D). **E) and F)** Scheme of the unit cell orientation with tilted (spherulites, green) and standing (terrace-like, red) polymer chains with respect to the substrate (adapted from[12]).

Tab. 4.5: Summarized GIWAXS data of CB- and CS_2-annealed PCPDTBT films obtained from the patterns shown in figure 4.27 and figure 4.28.

Sample	q [Å^{-1}]	[Å]	hkl-value	orientation
PCPDTBT				
CB-annealed	0.42	15.0	011	OOP
	0.59	10.6	110	IP
	0.37	17.0		ca. 40°
CS_2-annealed	0.66	9.5	020	OOP
	0.58	10.8	110	ca. 40°
	1.07	5.9	004	IP

National Laboratory. GIWAXS often gives a better signal to noise ratio compared to TEM/ED due to the higher brilliance of the source. In addition GIWAXS probes the in-plane (IP) and the out-of-plane (OOP) direction of thin films, chapter 2.1.

In the CB-annealed films the TEM experiments indicated a coexistence of two different regions: i) mostly spherulites with a lamellar substructure and a tilted polymer chain orientation and ii) fewer terrace-like structures with a standing chain orientation. While TEM/ED is a selective area method, GIWAXS averages over large sample areas of about 1 to 2 cm^2. Therefore mainly reflections of the lamellar regions consisting of tilted chains were expected to be found. Figure 4.27 shows the ED pattern of a CB-annealed film. As expected for tilted chains, a (0 1 1) reflection at around 15 Å (q = 0.42 Å^{-1}) in the out-of-plane direction was found. Another strong reflection was found at around 17 Å (q = 0.42 Å^{-1}) at an angle of around 45°. Its origin is still unclear and it could not be indexed or correlated to any data found by TEM/ED.

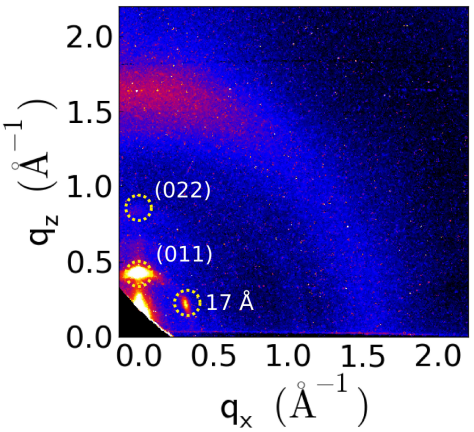

Fig. 4.27: GIWAXS pattern of a CB-annealed sample. The majority of the film consisted of the spherulitic structure (preparation see chapter 4.3.1, adapted from[12]).

In summary the GIWAXS pattern of the CB-annealed films further supports the TEM/ED data but did not reveal any additional information.

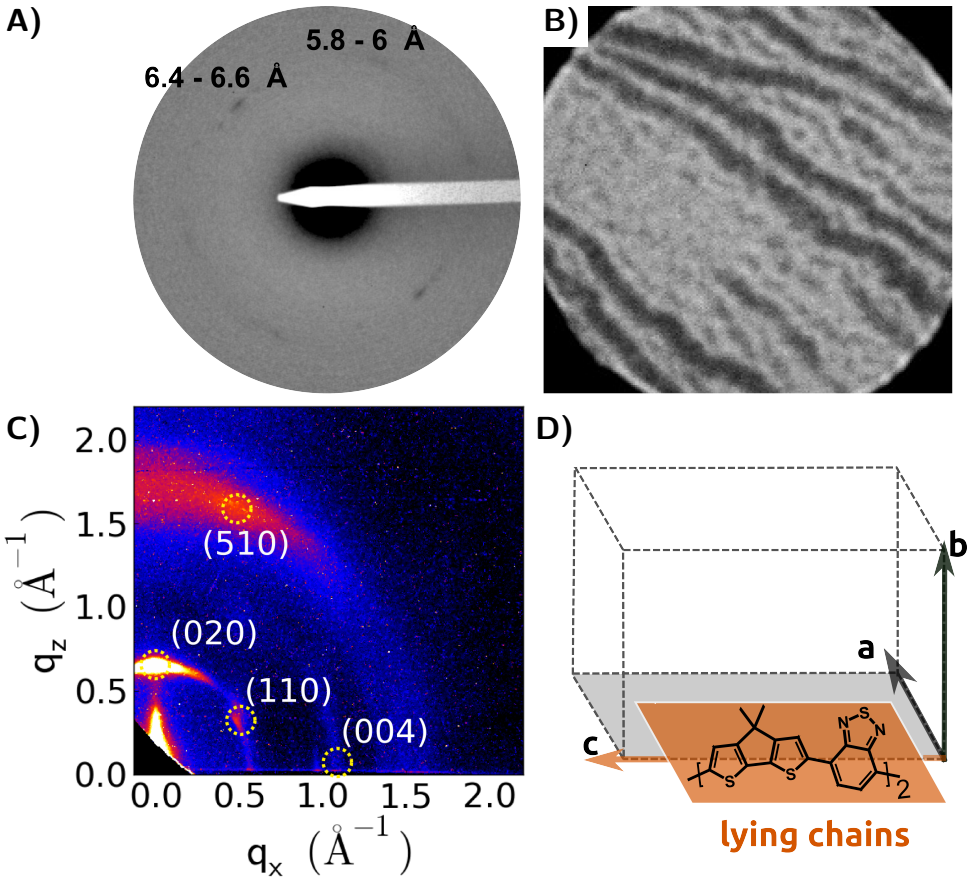

Fig. 4.28: TEM/ED and GIWAXS investigations of CS_2-annealed PCPDTBT films (preparation see chapter 4.3.1). **A)** Selected area TEM/ED pattern of the region shown in the bright field image in B). **C)** GIWAXS data of a CS_2-annealed PCPDTBT film. **C)** Proposed polymer chain orientation based on the GIWAXS pattern (adapted from[12]).

CS_2-annealed

The TEM/ED of CS_2-annealed films revealed only very weak and few reflections which could not be indexed, figure 4.28A. These results contradicted the highly ordered lamellar structure seen by AFM and TEM in figure 4.16 and figure 4.28B, respectively.

Therefore the main focus during the GIWAXS investigations was on the CS_2-annealed samples for which the absorption spectra suggested the same polymorph as in the CB-annealing samples, chapter 4.3.4. Figure 4.28C reveals the GIWAXS pattern obtained from CS_2-annealed samples prepared as described in chapter 4.3.1. One intense reflection was found out-of-plane (OOP) around 9.5 Å, one in-plane (IP) around 5.9 Å and one at about 45° with a distance of 10.8 Å. Reflections with the same distances were found in the CB-annealed samples and therefore the same polymorph was assumed. The main reflection in the OOP direction was indexed as (0 2 0) which suggests a morphology with the polymer backbone oriented in-plane to the substrate, figure 4.28D. The structure is

further supported by the finding of the (1 1 0) reflection at about 45°, which was also very prominent in the TEM/ED pattern of the CB-annealed films. Furthermore, some weak reflection was found along the in-plane direction of the pattern at around 5.9 Å and was indexed as (0 0 4), figure 4.28C. In accordance with the findings of Nelson et al.[102] this reflection was correlated to the polymer chain direction and further support an in-plane orientation of the polymer backbones.

A summary of all GIWAXS data is given in table 4.5. They suggest that the CS_2-annealed films consist of the same polymorph as the CB-annealed films but with a polymer chain orientation parallel to the substrate. In contrast to the CB-annealed films, the CS_2-annealed films homogeneously cover the complete substrate. This is of great importance since it allows to use them for device preparation.

4.4.1.2 F-PCPDTBT

The TEM bright field images of CB-annealed F-PCPDTBT films reveal only one morphology which consists of long fibers, figure 4.29A and resembles the structures found in the AFM and SEM images shown in the previous chapter 4.3.2. The ED pattern shown in figure 4.29B is quite similar in symmetry to the PCPDTBT ED pattern, however it reveals even sharper and more defined reflections. Therefore the F-PCPDTBT pattern was also indexed as [001] zone and the unit cell parameters were determined to: a = 11.0 Å and b = 20.6 Å.

One very important difference between the patterns of PCPDTBT and F-PCPDTBT should be pointed out: Both ED patterns show at the outer edge a pair of strong, smeared out reflections, 1 5 0 in the case of PCPDTBT and 3 1 0 in the case of F-PCPDTBT. In

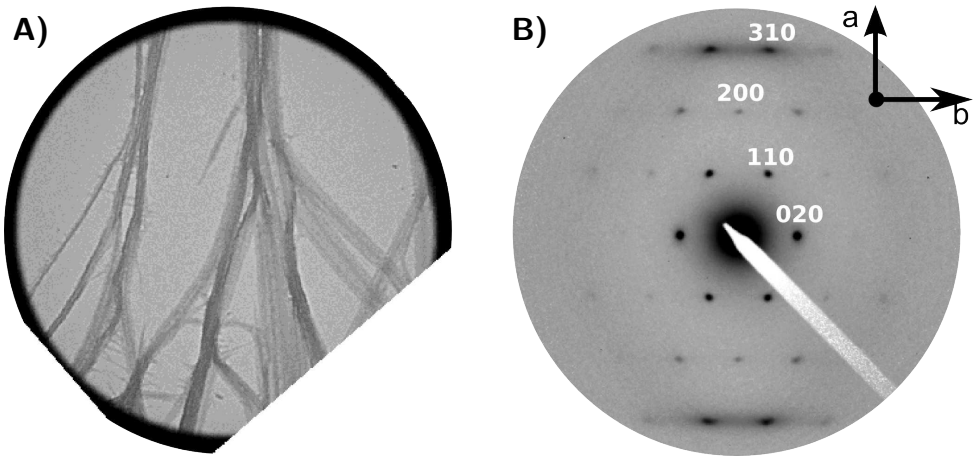

Fig. 4.29: TEM bright field image (A) and the corresponding electron diffraction pattern (B) of a CB-annealed F-PCPDTBT film (preparation see chapter 4.3.2) (adapted from[13]).

the case of PCPDTBT they are oriented along the b-axis whereas for F-PCPDTBT they are rotated by 90° and found in the direction of the a-axis. The distance of 3.8 Å found for these reflections is typical for interchain π-stacking of conjugated polymers. This indicates that there must be an essential difference in the orientation of the stacking between the PCPDTBT and F-PCPDTBT backbones.

4.4.1.3 Structural Characterization

Besides the well known edge-on structure, dominated by long-range π-stacking, also dimer-like structures are known for a few conjugated polymers such as poly(9,9'-di-n-octyl-2,7-fluorene) (PFO).[154] TEM electron diffraction of the α-PFO polymorph shows that PFO can crystallize in an orthorhombic unit cell comprising 8 polymer chains and a space group identified as $P\,n\,b\,2_1$.

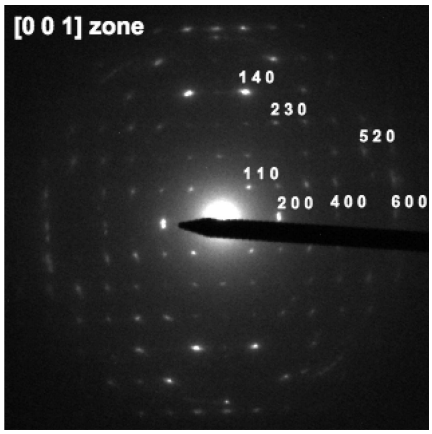

Fig. 4.30: TEM/ED pattern of a α-PFO thin film sample. Reprinted with permission from [154, M. Brinkmann 2007]. Copyright (2007) American Chemical Society.

Interestingly, PFO forms a dimer-like structure with 4 dimer units inside the orthorhombic unit cell. Such a dimer structure reveals a characteristic ED pattern shown for α-PFO in figure 4.30. The ED pattern reveals a symmetry and intensity distribution with an hexagonal pattern around the center induced from the orthorhombic unit cell. In the outer region of the pattern two strong reflections ($\pm 1\,4\,0$) are caused by the dimers and resemble the interchain distance between the polymer backbones. Also typical for a dimer-like pattern is the low intensity of the reflections between the inner and the outer regions of the ED pattern (figure 4.30 ($2\,3\,0$) and ($4\,0\,0$)). This leads in general to a pattern which can be described by an inner ring of strong reflections, followed by a ring of weak reflections, and two intense outer reflections along the direction of the dimer stacking.

Both [001] patterns of PCPDTBT and F-PCPDTBT are in good accordance with such an intensity distribution indicating a dimer-like structure, figure 4.26B and figure 4.29B. Inspired by the similarity to the PFO patterns[154] the PCPDTBT and F-PCPDTBT patterns were interpreted by assuming a dimer formation: The six intense, inner reflections, which form a quasi-hexagonal pattern, were indexed as $\pm 2\,0\,0$ and $\pm 1\,\pm 1\,0$ corresponding to an orthorhombic unit cell with distances in the range of 9 to 11 Å. The two intense outer reflections were indexed as $\pm 1\,5\,0$ and $\pm 3\,1\,0$ for PCPDTBT and F-PCPDTBT, respectively, and correlate to a short π-stacking distance of 3.6 to 3.8 Å between two

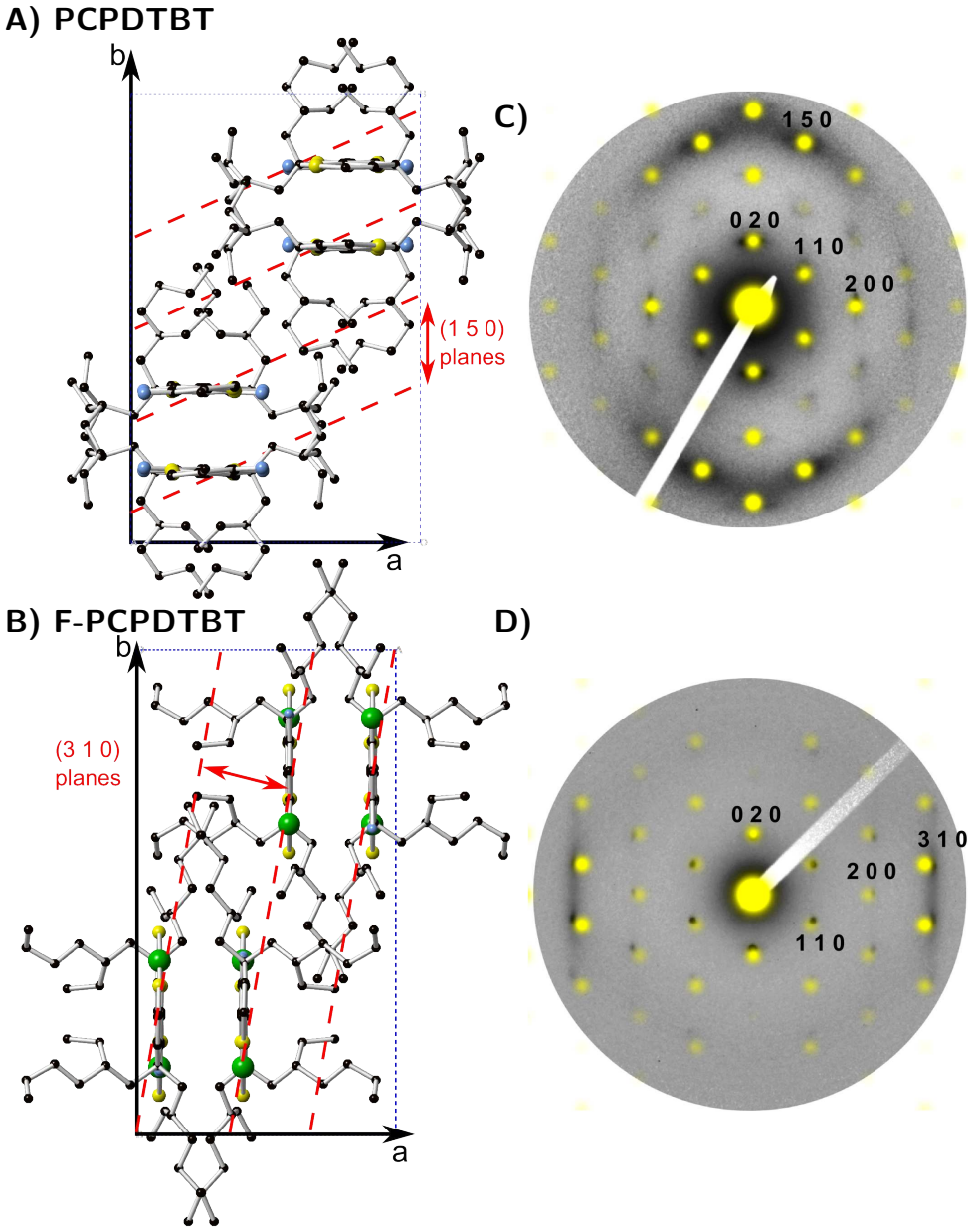

Fig. 4.31: A) and B) Proposed structure for the polymer chain orientation along the c-axis of the crystal structure based on the ED patterns obtained from the solvent annealed films shown in figure 4.26 and figure 4.29 for PCPDTBT (A) and F-PCPDTBT (B), respectively. **C) and D)** Experimental (background) and calculated (yellow) ED patterns of the [001] zone from the model shown on the left (adapted from[13]).

polymer chains comprising a dimer. The slight smearing of the outer reflections is therefore most likely caused by a slight disorder in the packing of the dimers and not by the dimer orientation within the unit cell. This is further supported by the fact that the inner reflections, which are correlated to the dimer position within the orthorhombic unit cell, are very distinct and sharp.

Although both patterns look quite similar the arrangement of the dimers in the unit cell must be different. The two main reasons for this conclusion are: i) Both structures show different unit cell parameters and ii) The two outer reflections which correspond to the dimer stacking had to be differently indexed. As shown in figure 4.31 it is suggested that the dimers in PCPDTBT and F-PCPDTBT are rotated with respect to one another by 90° around the c-axis. The plane of the π-stacking is therefore oriented along the a-axis in the case of PCPDTBT and along the b-axis in the case of F-PCPDTBT, in accordance with the (1 5 0) and (3 1 0) reflections seen in the respective ED patterns.

Simulated patterns of the a,b-planes of both structures are shown in figure 4.31C and D with the measured ED patterns in the background. They clearly resemble the symmetry and the intensity distribution of the measured patterns.

4.4.2 Structural Information from In-Plane Oriented Polymer Backbones

The measurements of the solvent annealed films gave an in-depth insight into the crystal structure of the a,b-plane along the alkyl side chains and dimer stacking direction. However, without further information along the polymer chain direction (c-axis) no complete crystal structure could have been proposed. In the literature only one publication from Nelson et al.[102] reported a reflection around 11.8 Å which was suggested to be correlated to the polymer chain direction and was indexed as 0 0 1. This finding was supported by DFT calculations which suggest the length of one repeating unit (CPDTBT) to be around 11 Å.

Since TEM/ED is limited to the in-plane direction of thin films a method was needed to align the polymer chains within the film plane. Since both epitaxy[134,135] and high-temperature rubbing[132,133] have previously been successful in aligning conjugated polymers in-plane, both methods were investigated.

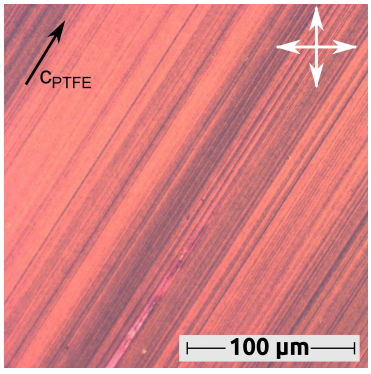

Fig. 4.32: POM image of a melt-annealed PCPDTBT film (300 °C) prepared on an aligned PTFE layer with the rubbing direction (c_{PTFE}) indicated by an arrow.

4.4.2.1 Methods to Achieve In-Plane Alignment

Epitaxial Growth of PCPDTBT

An in-plane chain orientation for PCPDTBT was obtained by epitaxial growth on pre-oriented polytetrafluoroethylene (PTFE) substrates (preparation see chapter 3.2.4). In the literature[134,135] it has been shown that polymer films prepared on top of such layers can be aligned parallel to the PTFE backbone by melt-annealing.

Therefore thin PCPDTBT films of around 30 to 40 nm thickness were prepared on aligned PTFE layers by spin coating from chlorobenzene (CB, 3 mg/ml) solutions. After drying under vacuum the films were melt-annealed under an argon atmosphere. The samples were heated above the melting point of PCPDTBT to 290 °C, cooled with 0.25 K/min to the melting point at 280 °C, where they were held for 4 h, before cooling at a rate of 0.25 K/min back to room temperature. A POM image of a epitaxially grown PCPDTBT layer is shown in figure 4.32.

High-Temperature Rubbing of F-PCPDTBT

High temperature rubbing (HT-rubbing) was intensively studied and developed over the last years by Brinkmann et al.[25, 80, 132, 133, 155] The authors showed that a great variety of conjugated polymers such as P3HT, poly(2,5-bis(3-dodecyl-2-yl)-thieno[3,2-b]thiophene) (C12-pBTTT) or poly[N,N'-bis(2-octyldodecyl)-1,4,5,8-naphthalene-dicarboximide-2,6-diyl]-*alt*-5,5'-(2,2'-bithiophene) (P(NDI2OD-T2)) can be aligned with their backbone along the rubbing direction. Rubbing is typically performed on thin films prepared by spin coating or blade-coating. The substrates are fixated by vacuum on a heatable translation stage under a rotating cylinder covered with a microfiber cloth. Pressing the rotating cylinder down on the film and moving the substrate at a constant speed leads to shearing forces which align the backbones in the rubbing direction, chapter 3.2.4.

Thin films of PCPDTBT were prepared on glass slides from a chlorobenzene solution (8 mg/ml) by blade-coating. Subsequently the films were rubbed on a self-built rubbing machine under nitrogen at the *Institut Charles Sadron* in Strasbourg. The rubbing was performed by applying a rotating cylinder with a 2 bar pressure on the translating sample (1 cm/s) which was heated to 240 °C beforehand. A post-annealing treatment to further increase the alignment was performed in a *Linkam* hot stage under nitrogen by holding the sample for 1 min at 260 °C, followed by cooling with 0.5 K/min down to room temperature.

4.4.2.2 TEM/ED Investigation of In-Plane Aligned Samples

The TEM bright field images of the aligned PCPDTBT and F-PCPDTBT films are shown in figure 4.33. An arrow indicates the PTFE backbone direction (c_{PTFE}) and the rubbing direction. A lamellar-like structure running perpendicular to the alignment direction with periods of 29 nm (PCPDTBT) and 13 nm (F-PCPDTBT) was found. This is typical for aligned polymers with the backbones oriented parallel to the alignment direction. The long axis of the lamellae comprises a stacking of the polymer chains perpendicular to the backbone direction often due to the strong interaction of the π-systems. The

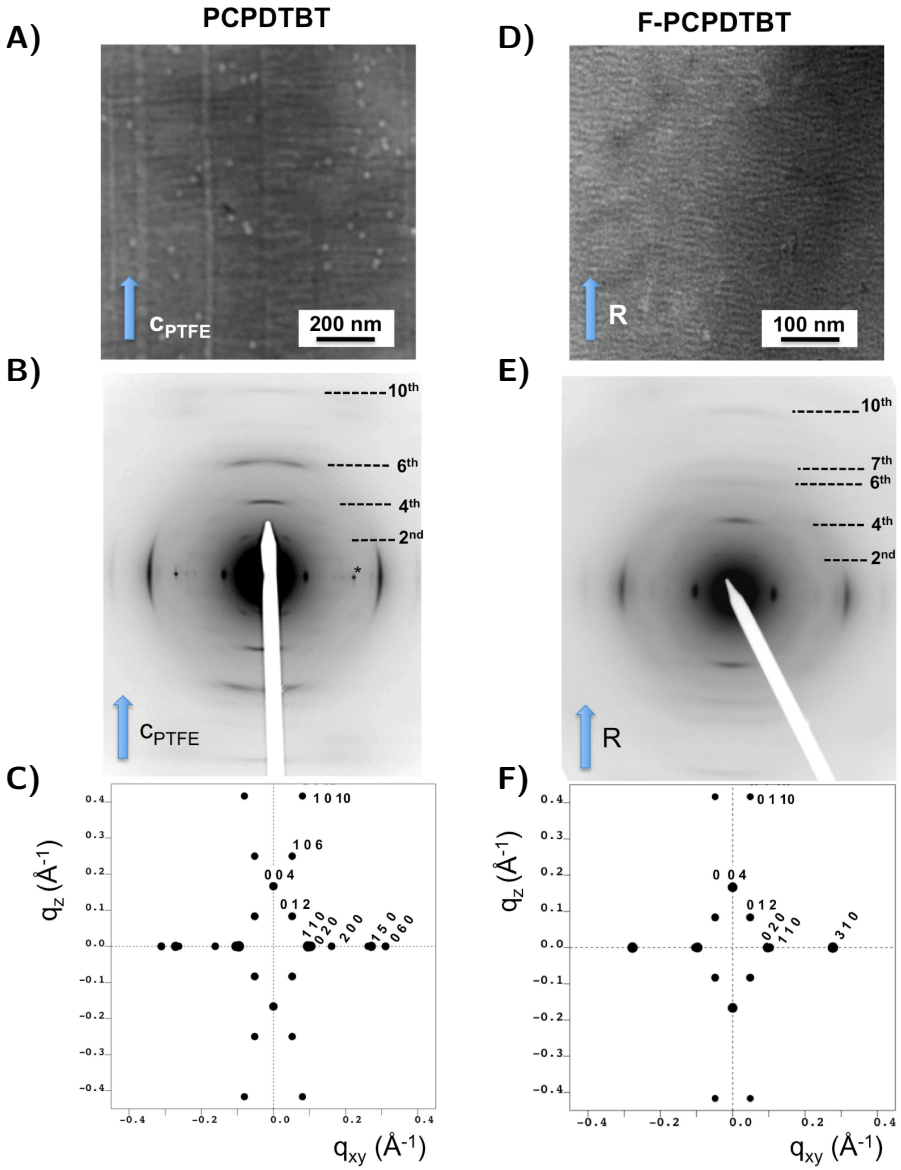

Fig. 4.33: TEM bright field images (top) and ED patterns (middle) of melt-annealed PCPDTBT (left) and rubbed F-PCPDTBT (right) samples. Bottom: calculated ED patterns with the c-axis (polymer backbone) along the meridian employing the models shown in figure 4.35. **A to C)** PCPDTBT film prepared on a rubbed PTFE substrate by drop casting (0.1 mg/ml) and subsequent melt-annealing at 284 °C (Annealing program: cooling with 0.25 K/min from 290 °C to 284 °C, holding at 284 °C for 2 h and further cooling to room temperature). **D to F)** Blade-coated F-PCPDTBT film which was rubbed at 240 °C and subsequently annealed at 260 °C (adapted from[13]).

bright/dark lamellae are caused by alternating crystalline and amorphous domains due to the semi-crystalline nature of conjugated polymers.

The ED patterns (figure 4.33B and E) reveal several characteristic reflections along the equator and therefore perpendicular to the alignment direction. The same reflections were already found in the patterns of the a,b-plane in the solvent annealed samples. In

PCPDTBT for example a dominant (1 1 0) reflection at 10.5 Å with a diffuse satellite reflection close to 9.7 Å (0 2 0) is seen. Furthermore the (1 5 0) reflection of the interchain stacking in the dimers is found together with several other (h k 0) reflections along the equator. This proves a backbone orientation parallel to the PTFE backbone and that the rubbed samples consist of the same polymorph as the CB-annealed films. Similar reflections along the equator of the F-PCPDTBT pattern allow the same conclusion suggesting a structure with the polymer backbone aligned along the rubbing direction.

Hence, the reflection intensity distribution along the meridian of the ED patterns is correlated to the polymer chain direction (c-axis) and allows to extract structural information along the polymer backbone.

The ED pattern of the PCPDTBT sample reveals along the meridian strong reflections on the 4th, 6th and 10th layer line. For the F-PCPDTBT samples strong reflections mainly on the 4th and some weaker on the 6th and 10th layer line were observed. In both cases the most intense reflection was indexed as 0 0 4. For the later structural characterization it is important to notice that no (0 0 2n+1) reflections are present. From both patterns the c-axis unit cell parameter was extracted: $c = 23.6 \pm 1.0$ Å (PCPDTBT) and $c = 23.2 \pm 1.0$ Å (F-PCPDTBT). All found reflections and corresponding distances are also summarized in table 4.6.

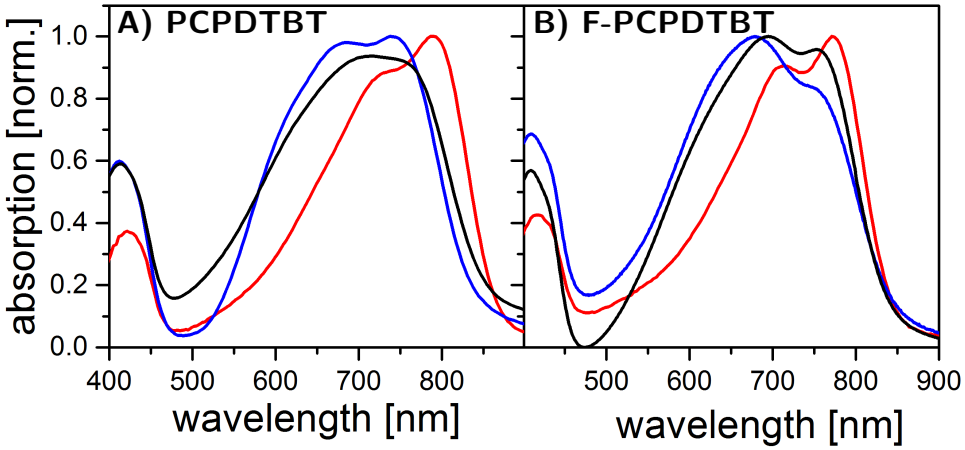

Fig. 4.34: Absorption spectra of thin PCPDTBT and F-PCPDTBT films prepared by different techniques. **A)** PCPDTBT absorption spectra of thin films prepared by spin coating from CB/DIO (2 w%, red), CB-annealing (blue) and melt-annealing (290 °C) on PTFE (black). **B)** F-PCPDTBT absorption spectra of thin films prepared by spin coating from CB/DIO (2 w%, red), CB-annealing (blue) and HT-rubbing (240 °C, black) (adapted from[12, 13]).

4.4.2.3 Absorption Properties of In-Plane Aligned Samples

The ED patterns of both polymers suggest already that the aligned samples comprise the same polymorph as the CB-annealed films and not the one found in the literature after spin coating (CB/DIO-spincoated). UV/VIS absorption spectroscopy can further be used to distinguish between the two polymorphs. In the previous chapter 4.3.4 it was shown that the solvent annealed films have a characteristic absorption signature with a 680 nm and a 740 nm band. The CB/DIO-spincoated films on the other hand reveal a strong 800 nm band with a shoulder around 740 nm, chapter 4.2. In the literature this 800 nm absorption was correlated to an edge-on morphology with long range π-stacking.[17]

In figure 4.34 the absorption spectra of the aligned PCPDTBT and F-PCPDTBT samples are plotted together with the absorption spectra of CB-annealed and CB/DIO-spincoated films. The CB/DIO-spincoated film spectra (red) reveal a strong 800 nm band whereas the CB-annealed samples reveal a blue shifted absorption with a 680 nm absorption band. The films aligned by melt-annealing on PTFE (black, PCPDTBT) and by HT-rubbing (black, F-PCPDTBT) reveal clearly an absorption signature similar to the CB-annealed samples. This supports the findings from the TEM/ED that the aligned samples comprise the same polymorph as the solvent annealed samples.

This is an important finding which shows that several techniques (melt-annealing, HT-rubbing and solvent vapor annealing) lead to the same polymorph. Particularly the fact that slow crystallization methods such as melt-annealing and solvent vapor annealing induce this new polymorph suggests that it is the thermodynamically stable structure.

4.4.3 Tentative Crystal Structure

Although the number of reflections found for PCPDTBT and F-PCPDTBT is much smaller than compared to other conjugated polymers such as P3HT or PFO it was possible to construct a first tentative crystal structure during this PhD thesis. However, it was not possible to determine the exact side chain conformation. Instead the side chain conformation was optimized by reproducing the correct reflection intensities along the 0 0 l layer of the aligned patterns and assuming reasonable atom/atom distances.

The first step towards finding a crystal structure was to determine the space group by identifying selection rules from the ED patterns. For both polymers the following selection rules were extracted from the ED patterns of the solvent annealed samples, figure 4.26:

$$\begin{aligned} (\mathrm{h\,0\,0}) \text{ with } \mathrm{h} &= 2\mathrm{n}, \\ (\mathrm{0\,k\,0}) \text{ with } \mathrm{k} &= 2\mathrm{n}, \\ (\mathrm{h\,k\,0}) \text{ with } \mathrm{h{+}k} &= 2\mathrm{n}. \end{aligned}$$

From the aligned sample patterns one additional rule was extracted:

$$(0\ 0\ \mathrm{l}) \text{ with } \mathrm{l} = 2\mathrm{n}.$$

These four selection rules allow several orthorhombic space groups from which the most likely four are P n 2 n, P n c n, C c c 2 and P c c n and will be discussed in the following.[156]

Considering the unit cell parameters, the molecular weight of the CPDTBT repeating unit, and a reasonable crystal density of around 1 g/cm^3, a number of 8 CPDTBT units within one unit cell would be coherent, table 4.6. Therefore the P n 2 n symmetry was

Tab. 4.6: Summary of distances of the TEM/ED patterns of PCPDTBT and F-PCPDTBT prepared by solvent vapor annealing (figure 4.26 and 4.29), high temperature rubbing (figure 4.33B) and epitaxial growth on PTFE (figure 4.33A). Bottom: extracted unit cell parameter and calculated crystal density.

hkl-value	PCPDTBT [Å]	F-PCPDTBT [Å]
2 0 0	6.2[a]	5.5
0 2 0	9.9	10.3
1 1 0	10.5	9.8
1 5 0	3.8	
3 1 0	-	3.8
0 0 4	5.9[c]	5.8[b]
0 0 6	3.7[c]	3.8[b]
0 0 7		3.3[b]
0 0 10	2.3[c]	2.2[b]
a	12.5	11.0
b	19.8	20.6
c	23.6	23.2
ρ_{calc} (g/cm^3)	1.08	1.18

a) Terrace-like structures. b) Rubbed samples. c) Epitaxial growth on PTFE.

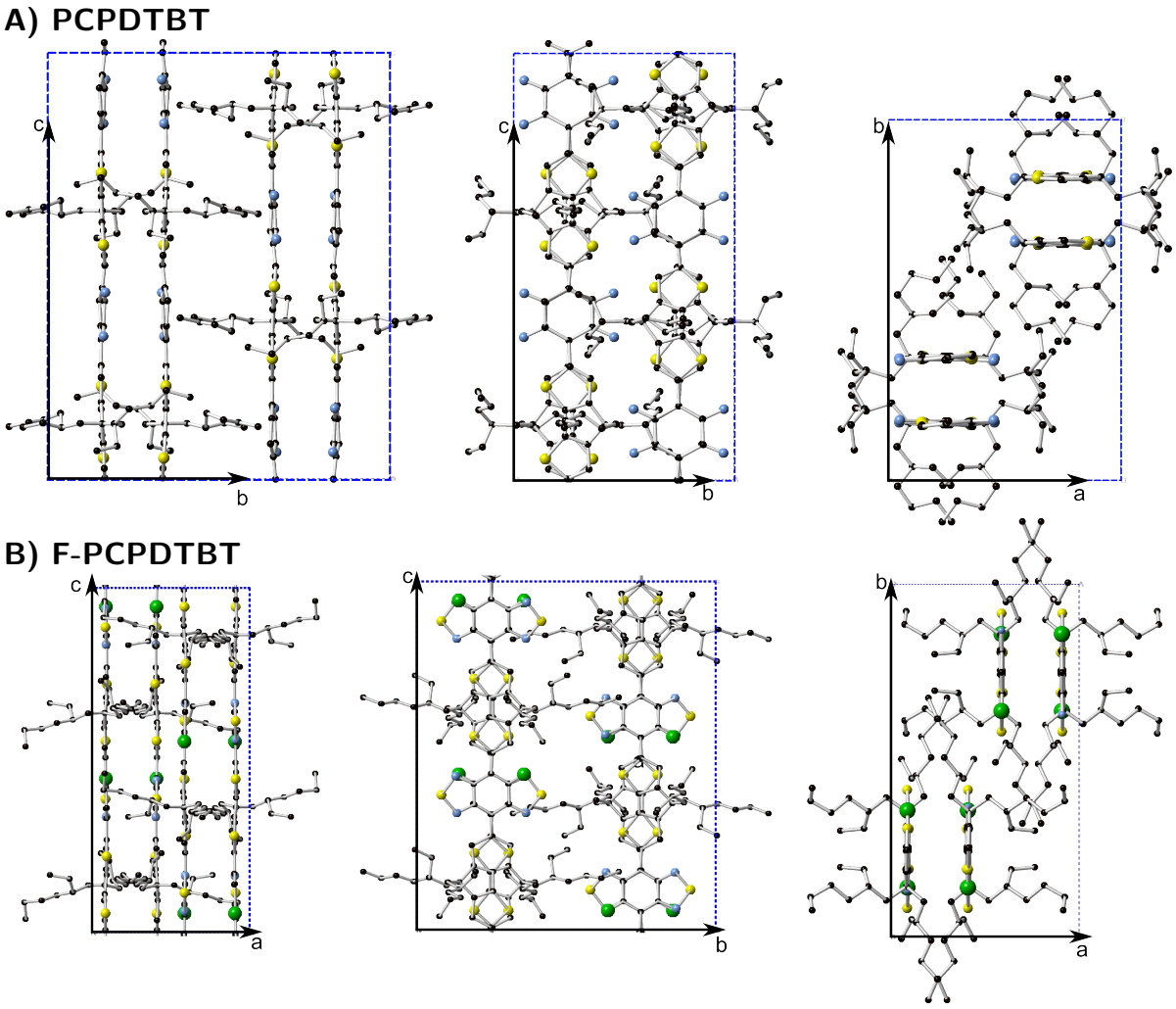

Fig. 4.35: Model of the proposed crystal structure of PCPDTBT (**A**) and F-PCPDTBT (**B**) along the b-, a- and c-axis of the unit cell employing the P c c n symmetry. The exact crystal structures are given also in the appendix A.6 (adapted from[13]).

discarded since it generates only 4 asymmetric units within one unit cell. P n c n, C c c 2 and P c c n on the other hand generate 8 asymmetric units as needed for a reasonable crystal density and are considered hereafter.

For the three remaining space groups molecular models (figure A.15) were built and their possible ED patterns calculated employing a *Silicon Graphic Station* using the *Cerius2* program and the software *CrystalMaker 9.1* together with the extension *SingleCrystal 2.3*.

The ED patterns along the polymer backbone direction for the C c c 2 symmetry always corresponded to a segregated stacking which induced a strong 0 0 2 reflection in the simulated ED patterns. Since the experimental patterns show no indication of any 0 0 2 reflection, the C c c 2 space group was ruled out.

Comparing the two space groups P n c n and P c c n it was found that the P n c n group has several drawbacks compared to P c c n. The ED patterns calculated from the possible models using the P n c n space group matches best the experimental data when assuming a non-planar backbone conformation with a tilting angle between the planes of the BT and CPDT units, figure A.14. Such a twisted backbone is unlikely since DFT calculations suggest a planar backbone for PCPDTBT, figure A.16.[106] Further unrealistic short distances between neighboring atoms of different chains were also found in this configuration, making this space group unlikely.

For the P c c n space group, on the other hand, several strong arguments were found supporting this symmetry. A recent study[157] on CPDT-BT oligomers proposed a face-to-face anti-parallel stacking of the BT units similar to the models found when employing the P c c n symmetry. Furthermore the P c c n space group allows a π-stacking within the dimer units despite the presence of the bulky ethyl-hexyl side chains which could further stabilize this structure. Figure 4.35 shows three different projections of the proposed crystal structure employing the P c c n space group for PCPDTBT and F-PCPDTBT.

It should be pointed out that the stacking direction of the dimers is parallel to the a,c-plane in PCPDTBT whereas in F-PCPDTBT it is parallel to the b,c-plane. This is in accordance with the smeared out reflections found in the ED patterns of the solvent annealed samples. It was earlier discussed that these reflections are correlated to the interchain stacking within the dimers and that in the [001] zone they are rotated by 90° comparing PCPDTBT and F-PCPDTBT. This is now perfectly mirrored in the structures by the different stacking orientations of the dimers. The calculated ED patterns for this structure resemble nicely the experimental data as shown in figure 4.31 and figure 4.33.

Having this in mind and comparing both structures it is most interesting that just the substitution of one single hydrogen atom per benzothiadiazole unit in the conjugated backbone causes a 90° change in the packing of the dimers. At the moment theoretical calculations of these structures are performed at the MPI in Mainz by Anton Melnyk in the group of Dr. Denis Andrienko. Those seem to confirm the stability of these structures and will hopefully help to better understand the influence of the fluorine on the crystal structure.

4.4.4 Evidence for another Polymorph

While optimizing the preparation methods for the epitaxial growth of PCPDTBT and F-PCPDTBT some transparent (non-absorbing) crystals in the melt-annealed samples (4 h at 300 °C, PTFE-substrate) were found. Interestingly the transparent character of

the crystals is completely independent of the light polarization. The transmission POM images, figure 4.36A, show that these crystals (red circle) do not change in color when rotating the polarizer. As comparison a spherulitic structure (blue circle) is highlighted in the same POM image. The absorption of the spherulitic structure changes strongly when rotating the polarizer whereas the new found structure stays transparent. Hence, these crystals seem to be completely different than any other structure of PCPDTBT and F-PCPDTBT discussed before.

TEM/ED of these regions reveal very sharp reflections up to the 8th order and a characteristic hexagonal-like pattern, figure 4.36B and C. The distances of the two main reflections at the equator and meridian were determined to 7.55 Å and 7.25 Å, respectively, for both polymers. Since these distances allow no indexation by the cell parameters discussed above, they were attributed to the [001] zone of a new orthorhombic polymorph with the respective unit cell parameters of a = 8.3 Å and b = 15.1 Å. Hereafter this new

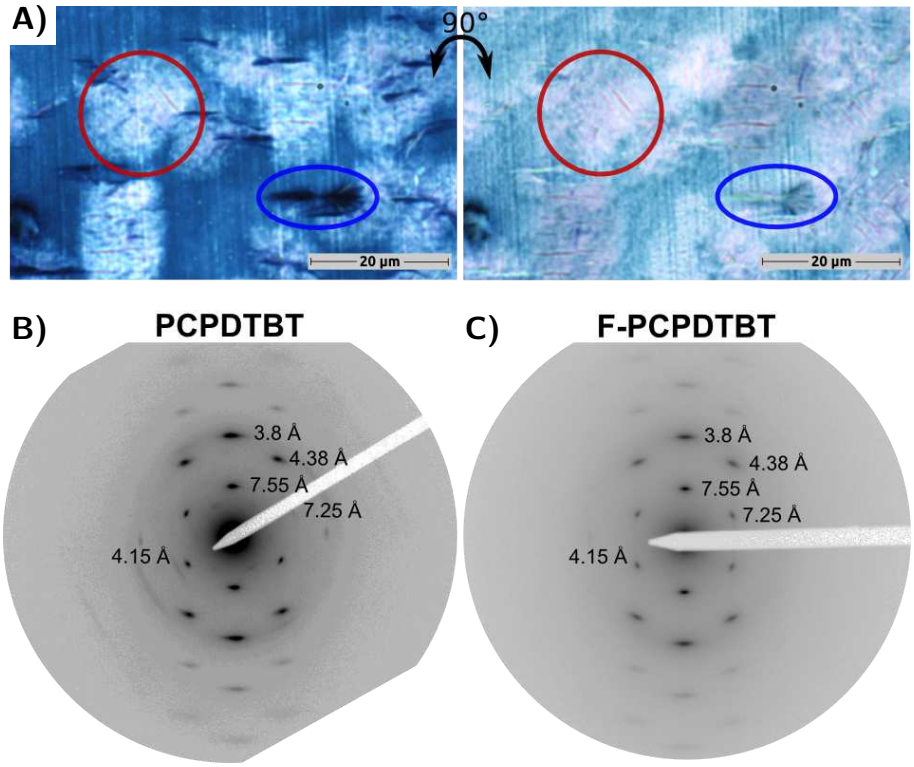

Fig. 4.36: A) POM images from the edge of a melt-annealed F-PCPDTBT sample. The circles label the different morphologies: The red circle indicates the transparent areas from which the ED-pattern in C) was taken. The blue circle labels a spherulitic structure. **B) and C)** ED-TEM pattern taken from transparent areas at the edges of PCPDTBT (A) and F-PCPDTBT (B) samples prepared by drop casting from a CB solution (0.3 mg/ml) on a glass slide covered with a rubbed PTFE layer. After drying the films at 50 °C in a nitrogen atmosphere the films were annealed for 4 h at 300 °C and cooled to RT with 0.25 K/min (adapted from[13]).

polymorph is referred to as form II whereas the previous discussed crystal structure is called form I.

It should be noted that the form II polymorph reveals the same ED patterns for PCPDTBT and F-PCPDTBT films. Therefore the same structure for both derivatives can be assumed. From the unit cell parameters the volume of the form II unit cell was calculated to be only half of the one found in form I. It can therefore be assumed that the unit cell consists of only two polymer chains instead of four as in form I. Another important observation is the missing of any strong smeared out reflections in the outer regions of the patterns. This indicates that neither a dimer-like structure nor a long range π-stacking is probable in this unit cell.

Since only small areas of these crystals were observed and it was not possible to obtain larger areas of form II no further investigations regarding this structure could be performed. To obtain a complete crystal structure of this second polymorph also additional information about the polymer backbone direction would be needed but are impossible to be obtained from such small crystalline regions.

4.4.5 Summary

Two polymorphs, form I and form II, were identified in PCPDTBT and F-PCPDTBT films after solvent vapor annealing, melt-annealing and HT-rubbing. For form I a complete crystal structure analysis was performed and a tentative crystal structure suggested, figure 4.35. For the structural characterization of the a,b-plane in form I the highly crystalline samples prepared by CB solvent vapor annealing were investigated. In the PCPDTBT samples two possible polymer backbone orientations relative to the substrate were found when employing rotation tilt TEM/ED experiments. The F-PCPDTBT films revealed after CB solvent vapor annealing a fiber-like structure which was comprised out of standing polymer chains. From the ED patterns the a and b parameters of the unit cell were obtained and are summarized in table 4.6.

Additional GIWAXS measurements allowed to determine the same polymorph (form I) in the homogeneous CS_2-annealed samples but with a different polymer chain orientation relative to the substrate. Interestingly, a lying chain morphology was found for the CS_2-annealed samples whereas in the CB-annealed samples the polymer chains were tilted with respect to the substrate.

Additional information of the polymer backbone direction was subsequently obtained from samples prepared by epitaxial growth on aligned PTFE layers for PCPDTBT and by high temperature rubbing of F-PCPDTBT thin films. The obtained ED patterns along the

polymer backbone revealed the missing unit cell parameter along the c-axis for PCPDTBT (c = 23.6 ± 1.0 Å) and F-PCPDTBT (c = 23.2 ± 1.0 Å).

Using all obtained ED patterns a complete tentative crystal structure of form I was suggested for both polymers. Interestingly the structures gave no evidence for a typical lamellar structure with alternating π-stacking and alkyl chain lamellae. Instead a dimer-like structure was found similar to the one reported for α-PFO. It should be noted that due to the dimer structure no long range π-stacking as in many other conjugated polymers, as e.g. P3HT, exists in form I.

Comparing the PCPDTBT and F-PCPDTBT structure they both consist of the same space group and similar unit cell parameters and differ only in their dimer orientation. For PCPDTBT the dimer stacking was found to be along the b-axis whereas the stacking of the dimers for F-PCPDTBT was rotated by 90° leading to a stacking along the a-axis, figure 4.35.

By chance a second polymorph, called form II, was found in the melt-annealed samples from epitaxy experiments. This second structure was first seen in POM as non-absorbing crystalline regions which showed no change in absorption while rotating the polarizers. In contrast to form I the unit cell parameter extracted from the [001] zone suggested that only two polymer chains per unit cell are needed. The ED pattern showed no further evidence for any π-stacking or dimer formation. Due to the small areas in which form II was exclusively found and missing information along the polymer backbone direction no complete crystal structure could be developed.

It should be noted that thin PCPDTBT films of two different polymorphs can be prepared: i) a dimer-like structure (form I) by solvent vapor annealing and high temperature alignment ii) a π-stacked structure by following the literature processing protocol (CB/DIO-spincoating). This will be used in the following chapters to build and compare electronic devices with long range π-stacking and dimer-like structures in the active layer.

5 Preparation and Characterization of Devices

In this chapter the energy levels of the polmyers, mixed with and without fullerenes as acceptor material, were determined and the absorpiton spectra of the charged species characterized. Spectroelectrochemistry was performed in solution and thin films of the pure materials and on the classical bulk-heterojunction polymer/fullerene blends as used in organic solar cells. In a second part the well controlled morphologies discussed in chapter 4.4 will be studied with respect to their device performance in organic field-effect transistors (OFET) and solar cells.

5.1 Energy Level Characterization of Homopolymers and Blends

For the improvement of the device performance often the optical and structural properties are considered as the most important factors.[16,25,125,146] Besides them the energy levels of the frontier orbitals defined by the oxidation and reduction potentials are often neglected even though they are of at least similar importance for the performance of organic solar cells and organic field effect transistors (OFET).[14,27] The energy levels determine the chemical stability and band gap of a material and in electronic devices the energy levels of connecting materials must be matched. For example in organic solar cells the energy levels of the donor and acceptor materials have to compatible for high device efficiencies, chapter 1.2.2. In OFETs the energy levels play a key role when choosing a suitable electrode material to ensure a good charge injection, chapter 1.2.3.[66]

Beside the electrochemical properties also the optical properties of the charged polymers and constituents in the blends need to be investigated to gain a deeper understanding of the mechanisms on the molecular level in organic solar cells. For example the absorption of the polaron and bipolaron can be of great value if they are combined with time-dependent ultrafast spectroscopy experiments which is typically used to investigate the recombination and charge generation processes in organic solar cells.[107,158,159] The simultaneous determination of both properties is provided by spectroelectrochemistry.

In this chapter the electrochemical and optical properties were investigated by cyclic voltammetry combined with in-situ absorption spectroscopy of pure PCPDTBT and Si-PCPDTBT in thin films and solutions. Furthermore, blends of polymers and fullerenes with a typical device configuration as used in organic solar cells are investigated.

Cyclic voltammetry with in-situ UV/Vis/NIR absorption spectroscopy was performed to obtain spectral signatures of neutral and charged species. In-situ spectra allowed to follow the change in absorption during oxidation up to the dication (bipolaron) which reveals

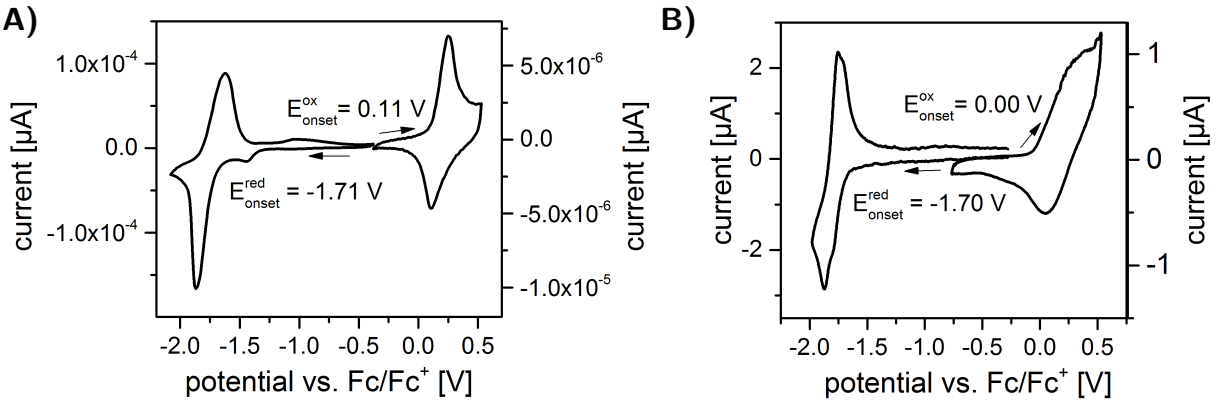

Fig. 5.1: Normalized cyclic voltammograms (2. cycle) of PCPDTBT (A) and Si-PCPDTBT (B). **A)** Thin PCPDTBT film measurement; preparation by spin coating from CB ($3\,\mathrm{mg/ml}$) (measuring conditions: MeCN/TBAPF$_6$, $0.1\,\mathrm{M}$, deaerated, scan rate: $20\,\mathrm{mV/s}$, RT, vs. Fc/Fc$^+$, reference electrode: Ag/AgCl, electrode: ITO; measured by A.-K. Saur[162]). **B)** Cyclic voltammogram of Si-PCPDTBT ($M_w = 27.7\,\mathrm{kg/mol}$) dissolved in dichlorobenzene (measuring conditions: concentration $1\,\mathrm{mg/ml}$, $0.1\,\mathrm{M}$ dichlorobenzene/TBAPF$_6$, deaerated, scan rate $100\,\mathrm{mV/s}$, RT, vs. Fc/Fc$^+$, reference electrode: Ag/AgCl).

typically a broad absorption band in the near IR region.[160] Furthermore, UV/Vis/NIR spectroscopy permits to correlate certain electron transfer reactions in blends to either the donor or acceptor phase establishing a more detailed picture of the redox processes within the active layer of organic solar cells.

The results presented in this chapter were used to investigate the charge separation process in polymer/fullerene solar cells (chapter 5.1.4) and were published in [14, Albrecht and Fischer et al. 2014]. In addition the absorption spectra of the charged species were used to study the photogeneration of polaron pairs in PCPDTBT employing pump probe spectroscopy and were published in [161, Di Nuzzo and Fischer et al. 2015].

5.1.1 Homopolymers

With the goal to obtain a general picture of the redox behavior of PCPDTBT ($M_w = 32.3\,\mathrm{kg/mol}$) and Si-PCPDTBT ($M_w = 27.7\,\mathrm{kg/mol}$) cyclic voltammetry was performed in solution and thin films. The highest molecular weight Si-PCPDTBT polymer was chosen for the following experiments because it revealed the best performances in organic solar cells. Furthermore the molecular weight and PDI is comparable to the PCPDTBT polymer.[14] In figure 5.1 the cyclic voltammograms of PCPDTBT and Si-PCPDTBT are shown. Whereas for PCPDTBT the cyclic voltammograms were obtained from thin films (spin coated from $3\,\mathrm{mg/ml}$ CB), for Si-PCPDTBT cyclic voltammograms with pronounced and well resolved redox waves were only obtained from dichlorobenzene (DCB, $1\,\mathrm{mg/ml}$) solutions. The detailed measuring conditions are given in the figure captions.

For both polymers a chemically reversible reduction and oxidation was found. The redox potentials were determined to: $E^{red}_{onset} = -1.71\,V$, $E^{ox}_{onset} = 0.11\,V$ for the PCPDTBT thin film and $E^{red}_{onset} = -1.70\,V$, $E^{ox}_{onset} = 0.00\,V$ for the Si-PCPDTBT solution (values vs Fc/Fc^+). Assuming an energy level of Fc/Fc^+ at $-4.8\,eV$ under the vacuum level[68] the HOMO/LUMO values were calculated to $-4.9\,eV/-3.1\,eV$ and $-4.8\,eV/-3.1\,eV$ for PCPDTBT (in the solid state) and Si-PCPDTBT (in solution), respectively.

Comparing the redox potentials in solution of both polymers (figure 5.1B and figure 5.2A) the HOMO/LUMO values were found to be the same: $-4.8\,eV$ (HOMO) and $-3.1\,eV$ (LUMO). It can therefore be concluded that the replacement of the bridging carbon by silicon has almost no effect on the HOMO/LUMO energies. A small difference of 100 mV is only found when comparing the reduction potential of films versus solutions. The reason therefore could be the interchain coupling of the polymer chains in the thin films or the difference in the setups, but this was not further investigated.

No cyclic voltammetry was performed on F-PCPDTBT since the amount of available material was limited and needed for other experiments. In literature Jen et al.[114] reported for F-PCPDTBT films ($M_n = 23\,kg/mol$, PDI = 1.6) HOMO and LUMO values of $-5.0\,eV$ and $-3.54\,eV$, respectively. Compared to the PCPDTBT and Si-PCPDTBT the HOMO seems to be unaffected but the LUMO is lowered by about 0.4 eV. An overview over the HOMO/LUMO values and the band gap of all three polymers is given in table 5.7.

Tab. 5.7: HOMO/LUMO values of PCPDTBT ($M_w = 32.3\,kg/mol$), Si-PCPDTBT ($M_w = 27.7\,kg/mol$) and F-PCPDTBT ($M_n = 23\,kg/mol$, PDI = 1.6) measured in solution.

	HOMO [eV]	LUMO eV	band gap [eV]
PCPDTBT	−4.8	−3.1	1.7
Si-PCPDTBT	−4.8	−3.1	1.7
F-PCPDTBT[114]	−5.0	−3.5	1.5

5.1.1.1 Absorption Signatures of the Neutral and Charged Species

Spectroelectrochemistry combines absorption and cyclic voltammetry in a single experiment which allows to record UV/Vis/NIR spectra in-situ during anodic and cathodic potential cycles. For spectroelectrochemical characterizations of solutions a self-built thin layer cell setup adapted from the description of C. Geskes et al.[117] was used, chapter 2.3. Deaerated solutions of the polymers of typically 1 mg/ml with 1 M supporting electrolyte were measured in a thin layer configuration with a AgCl coated Ag wire acting as pseudo reference electrode. A working electrode comprised of a polished platinum disk acted as

mirror for the absorption spectroscopy performed in reflection mode. A more detailed description is given in chapter 2.3.

The characterization of thin polymer films spin coated onto transparent ITO-substrates was performed in acetonitrile (MeCN) containing 0.1 M NBu_4PF_6 which does not dissolve the polymer film. The spectra were taken in transmission mode using a self-built setup described in chapter 2.3.

PCPDTBT

The spectroelectrochemical characterization of PCPDTBT was performed as part of the diploma thesis from Ann-Kathrin Saur[162] under my supervision and is shown in figure 5.2. The measurements were performed in a chlorobenzene solution (CB, 1.1 mg/ml with tetrabutylammonium hexafluorophosphate (NBu_4PF_6) 0.2 M as supporting electrolyte) and a THF solution (1 mg/ml THF with NBu_4PF_6 0.2 M) employing a thin layer setup.

The cyclic voltammogram of the reversible oxidation reveals an anodic and cathodic peak potential (E_{pa} and E_{pc}) around 0.28 V and 0.01 V for the forward and reverse scans, respectively. The onset potential was determined to 0.04 V resulting in a HOMO of −4.84 eV. Figure 5.2 shows the corresponding in-situ absorption spectra of the oxidation next to the cyclic voltammograms with the spectra colored in accordance to the potentials of the dots in the cyclic voltammogram.

In the spectra the appearance of two new absorption bands (blue and green) have been observed while going from neutral species at 0.0 V (red) to the dication. At potentials < 0.30 V the polymer is oxidized to a radical cation as seen in the cyclic voltammogram by a maximum peak current. In the absorption spectra the disappearing of the neutral band (red) around 720 and 410 nm and a simultaneous appearing of a broad absorption band (blue) around 1273 nm confirm the formation of the radical cation. Going to higher potentials a second oxidation takes place leading to a second broad absorption in the NIR region (green). Comparing the cyclic voltammogram and the absorption spectra the bands (green and blue) can be identified as a radical cation (polaron) and dication (bipolaron) absorption band. This is in further agreement with the fact that such broad absorption above 1500 nm are typical for conjugated polymers and are caused by the formation of polaron bands as discussed in chapter 1.1.[30,160]

In chlorobenzene the reduction of PCPDTBT revealed some unexplained strong current in the cyclic voltammogram before a change in the absorption spectra could be detected. This was probably due to impurity (most likely remaining O_2 in the solution) or other errors in the measurement and could not be resolved.

A more reliable measurement could be performed in a THF solution (1 mg/ml) shown in figure 5.2C and D. The cyclic voltammogram reveals a reversible reduction with anodic peak potentials at −1.47 and −1.95 V from which the half wave potential and LUMO values were calculated to $E_{red}^{1/2} = -1.71$ V and −3.09 eV, respectively. The corresponding absorption spectra show alike the oxidation a disappearing of the neutral bands (red) with a simultaneous appearing of first the radical anion band at 1080 nm (blue) until −2.09 V. Above this potential a dianion band appeared with a main absorption around 1500 nm (green).

In summary employing spectroelectrochemistry on PCPDTBT the HOMO/LUMO value were found to be around −4.9 and −3.1 eV, respectively and the electrochemical band gap was calculated to 1.8 eV. From the correlation between the cyclic voltammograms and the in-situ absorption spectra the polaron and bipolaron bands for the oxidation and reduction could be identified in the NIR region of the spectra, figure 5.2. Small differences were found between the solution and film which is probably due to crystalline domains and aggregation of the polymer chains in the thin films similar to what is known for P3HT.[163] An overview of the electrochemical values comparing thin film and solution data of PCPDTBT is given in table 5.8.

Tab. 5.8: Electrochemical data of the oxidation and reduction potentials determined for PCPDTBT from figure 5.2 and figure 5.1A by spectroelectrochemistry. HOMO and LUMO values were calculated assuming the energy level of Fc/Fc^+ at −4.8 V under vacuum level.

PCPDTBT	E_{onset}^{ox}	E_{onset}^{red}	$E_{red}^{1/2}$	HOMO	$LUMO_{onset}$	$LUMO_{E_{1/2}}$
		[V]			[eV]	
thin film	0.11	−1.71		−4.90	−3.1	
CB solution	0.04			−4.84		
THF solution		−1.57	−1.71		−3.23	−3.09

Si-PCPDTBT

In-situ spectroelectrochemistry in solution revealed already at small potentials a strong 800 nm absorption similar to the absorption signatures of the aggregated solutions in chapter 4.1.3. It was assumed that aggregation takes place and therefore the spectroelectrochemical characterization in a thin film configuration was chosen. The thin film configuration also allowed a better comparability to investigations of fullerene blended films which will be discussed in the next chapter.

The measurements of the Si-PCPDTBT films were all associated with two main problems: i) All films detached from the substrate during the reverse scan of the first cycle which

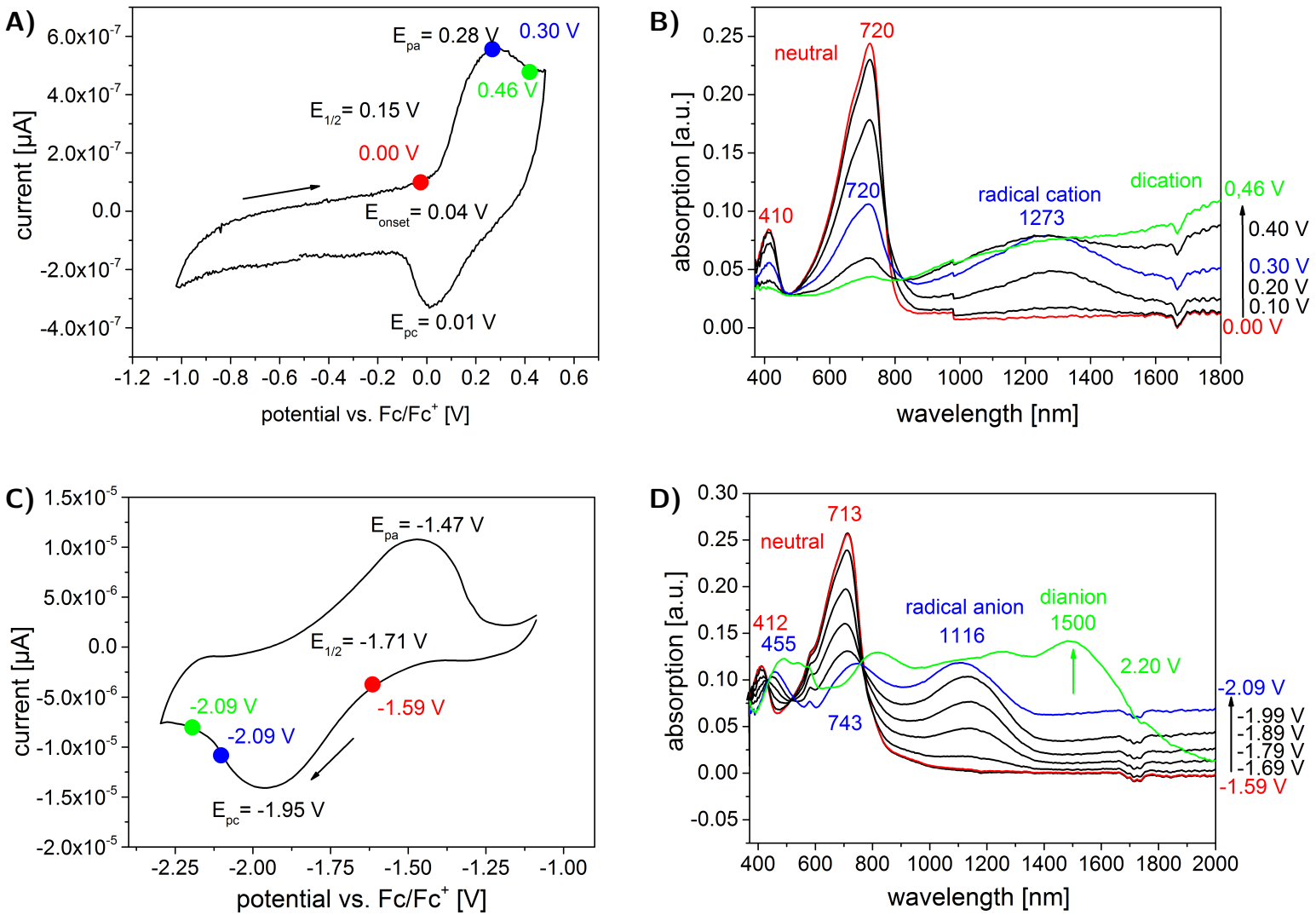

Fig. 5.2: Spectroelectrochemical characterization of PCPDTBT in solution. Cyclic voltammograms **A)** and **C)** with the corresponding in-situ absorption spectra (**B)** and **D)**) during the oxidation (top) and reduction (bottom). The line colors indicate the applied potentials and correspond to the labels given in the corresponding CVs in A) and C). The half wave potentials ($E_{1/2}$ and peak potentials (E_{pa} and E_{pc}) are given in the CVs. **A) and B)** The oxidation was measured in a solution of $1.1\,\mathrm{mg/ml}$ chlorobenzene/NBu_4PF_6 $(0.2\,\mathrm{M})$ using a scan rate of v=$10\,\mathrm{mV/s}$. **C) and D)** The reduction was measured in a solution of $1\,\mathrm{mg/ml}$ THF/NBu_4PF_6 $(0.2\,\mathrm{M}$, v=$20\,\mathrm{mV/s})$ (adapted from[11]).

prevented any measurements of the second cycle. ii) It was not possible to measure a reduction cycle in thin films. All attempts with different solvents and electrolytes ended with a destruction of the film before any absorption of the anionic species could be detected.

Thus, for the determination of the energy levels the first cycle of a thin film spin coated on ITO was used, figure 5.3A. The cyclic voltammogram reveals no distinct maximum peak potentials, therefore only the onset potential was determined to $E^{ox}_{onset} = 0.22\,V$ and the HOMO calculated to 5.0 eV. The corresponding absorption spectra show a similar behavior as found for PCPDTBT during oxidation. A disappearing of the neutral bands located at 610 and 760 nm and a simultaneous appearing of a polaron band around 1050 nm was observed, figure 5.3B.

The weak and broad signals of the cyclic voltammogram made it difficult to determine an exact value for the onset potential. Therefore additionally a plot of the intensity evolution as a function of applied potential from characteristic absorption bands was extracted and plotted into the CV graphs, figure 5.3A. From these plots the onset of the intensity evolution of the absorption can be determined and is hereafter denoted as *absorption onset* ($E^{ox/red,wavelength}_{Abs.onset}$).

In Figure 5.3A, right axis, the intensity evolution of the neutral absorption band at 760 nm (blue) and the radical cation absorption band at 950 nm (orange) is plotted. The absorption onsets were determined to $E^{ox,760nm}_{Abs.onset} = 0.20\,V$ and $E^{ox,950nm}_{Abs.onset} = 0.23\,V$, respectively. These results are in excellent agreement with the estimated current onset extracted from the cyclic voltammogram. This proves that the absorption onset is a valuable tool which can be additionally used to determine the onset potentials.

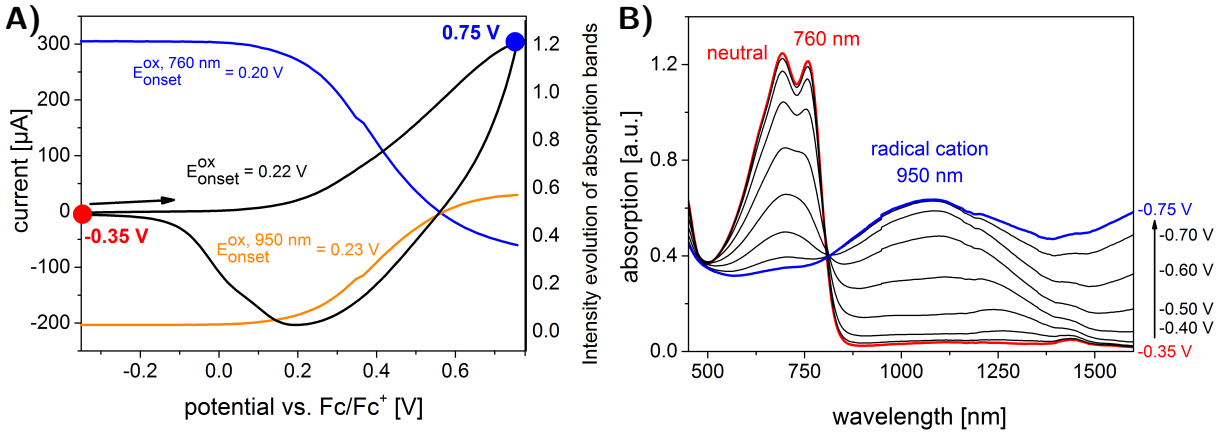

Fig. 5.3: In-situ spectroelectrochemical data of pure Si-PCPDTBT film on ITO-substrate (spin coated from o-DCB 20 mg/ml) and measured in acetonitrile. **A)** CV of the first oxidation cycle (current: left y-axis); the blue and the orange line depict the intensity evolution of the 760 nm and 950 nm absorption feature (Abs: right y-axis). **B)** Corresponding absorption spectra recorded during the forward scan (v = 10 mV/s) of the oxidation between −0.35 V and 0.75 V (adapted from[14]).

In summary the HOMO/LUMO values for Si-PCPDTBT were calculated to −4.8 eV/ −3.1 eV in the DCB solution, figure 5.1. This is in good agreement with the somewhat lower value of −5.0 eV of the HOMO found for thin Si-PCPDTBT films (figure 5.3) and is similar to the HOMO values of PCPDTBT.

5.1.2 Fullerenes as Electron-Acceptors

For later comparison with the blend systems the C_{60} fullerene derivatives PCBM, ICMA, ICBA and ICTA (figure 5.4) were characterized by classical cyclic voltammetry and spectroelectrochemistry. Figure 5.5 shows exemplarily for PCBM the cyclic voltammogram and the corresponding absorption spectra. In addition the intensity evolution of characteristic wavelengths are plotted into the cyclic voltammogram (right axis). The measurements of all derivatives are shown in figure A.17 and were performed in solution (3 mg/ml, 0.1 M $TBAPF_6$/methylene chloride, 20 mV/s, RT) under thin layer conditions.

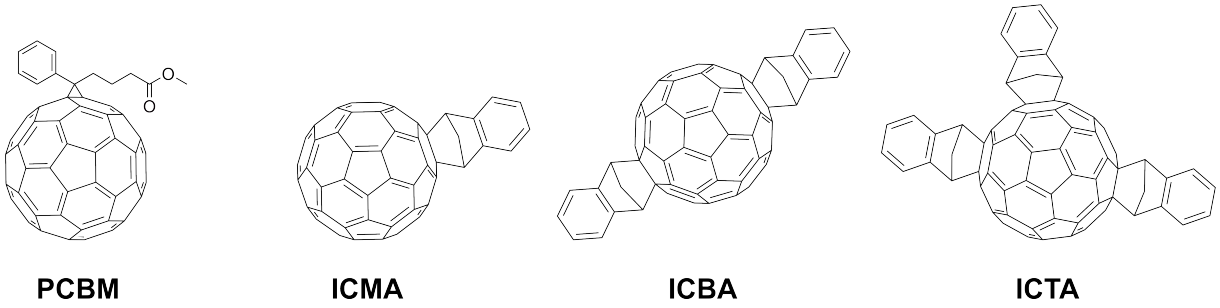

Fig. 5.4: Chemical structures of the used fullerene derivatives: [6,6]-phenyl-C_{61}-butyric acid methyl ester (PCBM), indene-C_{60} monoadduct (ICMA), indene-C_{60} bisadduct (ICBA) and indene-C_{60} trisadduct (ICTA).

Absorption Signatures during Reduction of the Fullerenes

The absorption spectra shown in figure 5.5B of PCBM in solution reveal an absorption band in the neutral state around 330 nm. Upon increasing the reduction potential to −1.20 V a first reduction peak is found in the cyclic voltammogram and in conjunction an absorption band at 1025 nm of the radical anion appears (green). Further increasing the reduction potential leads to a second reduction causing a decrease of the 1025 nm band and an increasing of two new main bands of the dianion around 780 and 900 nm.

A deeper insight of the absorption evolution is obtained when plotting the intensity evolution of characteristic absorption bands into the cyclic voltammogram as shown in figure 5.5A, right axis. Obviously, during the first reduction not only the 1025 nm band rises but also a slight increase in absorption at 900 and 370 nm (orange; blue) and a small decrease of the neutral band at 300 nm (red) occurs. After a plateau between the first

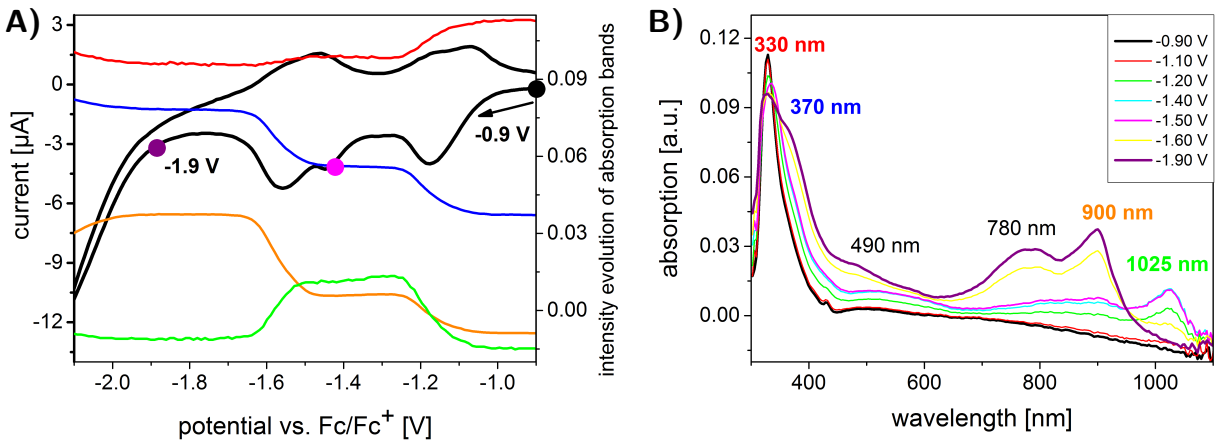

Fig. 5.5: In-situ spectroelectrochemical data of PCBM dissolved in methylene chloride (3 mg/ml with 0.1 M $TBAPF_6$, v = 20 mV/s). **A)** CV of the first reduction cycle (left axis). The colored lines correspond to the intensity evolution of characteristic absorption bands (Abs: right axis) with their wavelength labeled with the same color in B). **B)** Corresponding in-situ absorption spectra recorded during the forward scan of the reduction shown in A) (adapted from[14]).

and second reduction (−1.3 to −1.5 V) the intensity evolution shows a distinct decrease of the 1025 nm band back to its origin and a second increasing of the 900 and 370 nm bands during the second reduction.

In addition to the E^{red}_{onset} potentials from the cyclic voltammogram the onsets of the change in absorptions for specific wavelengths ($E^{ox/red,wavelength}_{Abs.onset}$) were determined. A summary of the values is shown in table 5.9. Similar absorption signatures were found for the other fullerene derivatives and are shown in figure A.20.

In addition to spectroelectrochemical characterization, the fullerenes were measured by classical solution voltammetry in methylene chloride using a Pt wire as counter electrode and a silver wire in 0.01 M $AgNO_3$ as reference electrode, figure A.20. These measurements were performed by Dr. Adrian Ruff and details of the measuring conditions are given in the figure captions. From these cyclic voltammogram the half wave potentials ($E^{red}_{1/2}$) of the first reduction were determined and compared to the values of the E^{red}_{onset} and $E^{ox/red,wavelength}_{Abs.onset}$ from the spectroelectrochemistry measurements, table 5.9.

It is noticeable that the absorption onsets ($E^{ox/red}_{Abs.onset}$) and the half wave potentials coincide in their values almost perfectly. The onset potentials on the other hand lie consistently lower. Therefore it should be possible to determine accurate reduction potentials from the absorption onsets even if it is not possible to identify the peak potential of the reduction from the cyclic voltammogram.

Summary

In summary the LUMO values of the fullerenes could be determined by employing spectroelectrochemistry measurements using the absorption onset and could be compared to the values obtained from conventional cyclic voltammetry in solution. Both measurements give similar results for the LUMO levels and are in good agreement with literature:[145] −3.70 eV PCBM, −3.68 eV ICMA, −3.53 eV ICBA and −3.33 eV ICTA. All values are summarized in table 5.9.

5.1.3 Polymer/Fullerene-Blends

In this chapter the energy level characterization of the polymer/fullerene blends will be discussed taking into account what was learned in the previous chapters regarding the redox processes of the pure materials. To ensure a good comparability to the organic solar cells, which will be discussed later, the preparation of the blends followed the processing protocols of the organic solar cells, chapter 5.1.4.[14] The Si-PCPDTBT/fullerene blends (1:1.5 by weight, M_w = 27.7 kg/mol) were spin coated on ITO-substrates from an o-dichlorobenzene solution (20 mg/ml, 70 °C, 600 rpm) and dried in vacuum. The main difference in the preparation compared to the organic solar cells was the missing PEDOT:PSS interlayer between ITO and blend but this should not influence the energy levels of the active layer. For a detailed preparation protocol see chapter 3.2.5.

It should be pointed out that only the Si-PCPDTBT could be investigated because the PCPDTBT/fullerene films detached from the electrodes during the measurements such that no data could be obtained.

Spectroelectrochemistry was used since it allows a more precise determination of the energy levels than conventional cyclic voltammetry. A second advantage of the spectroelectrochemistry is that together with the knowledge of the absorption behavior of the pure materials it was possible to assign certain redox reactions to specific phases of the blends.

Reduction

The reduction of the blend films was performed in propylene carbonate (0.1 M $TBAPF_6$/ propylene carbonate, v=20 mV/s, RT). The cyclic voltammograms together with the intensity evolution of characteristic absorption bands are plotted in figure 5.6 and the corresponding in-situ absorption spectra are shown in figure A.18. In the cyclic voltammograms the forward scans reveal up to three anodic redox waves. The backward scans revealed almost no (PCBM, ICMA) or less (ICBA, ICTA) oxidation peaks. It was observed that the films started to detach from the substrate during the backward scan of the

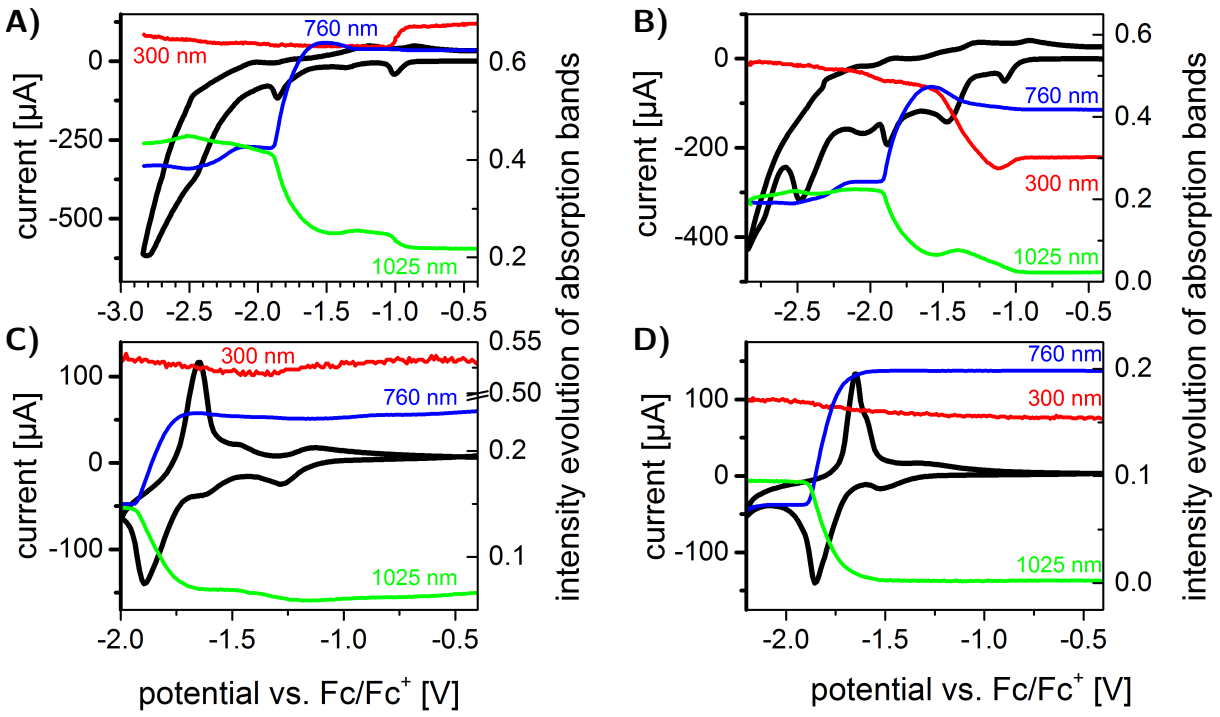

Fig. 5.6: In-situ spectroelectrochemical data of Si-PCPDTBT/fullerene blends of the first reduction cycle with **A)** PCBM, **B)** ICMA, **C)** ICBA and **D)** ICTA. Measurements were performed on thin films spin coated on ITO-substrates in propylene carbonate (0.1 M $TBAPF_6$/propylene carbonate, v=20 mV/s, RT). Left axis: CVs of the first reduction cycles. Right axis: Intensity evolution of characteristic fullerene bands: 300 nm (red), 760 nm (blue) and 1000 nm (green) for ICMA (B) and ICBA (C) or 1025 nm (green) for PCBM (A) and ICTA (D) (adapted from[14]).

reduction. This could not be prevented even though several solvent/electrolyte combination were tried out (solvents: acetonitrile, propylene carbonate, 1-chloronaphthalene and (di)chlorobenzene; supporting electrolytes: $TBAPF_6$ and $THAPF_6$). Therefore only the first cycle was considered.

From the cyclic voltammograms and the intensity evolutions the half wave potentials ($E^{red}_{1/2}$) and the absorption onsets ($E^{ox/red}_{Abs.onset}$) of the first reductions were determined, table 5.9. No significant difference of more than ±10 mV between the two techniques were observed. Therefore the LUMO values for the polymer/fullerene blends were calculated to: −3.9 eV PCBM, −3.8 eV ICMA, −3.6 eV ICBA and −3.4 eV ICTA.

To distinguish between the reduction of the fullerene and the polymer phase the intensity of the neutral polymer band at 760 nm was plotted against the applied potentials, figure 5.6. From the characterization of the pure Si-PCPDTBT it is known that the 760 nm band decreases in intensity when the polymer is reduced. Following the absorption intensity of the 760 nm band during the first reduction of the blend no changes were detected, except for the ICTA blend. On the other hand for the fullerenes an increase of the

anionic 1025 nm band and a decrease of the neutral 300 nm was observed. From the pure fullerene investigations both bands are known to be correlated with the first reduction of the fullerenes. It can therefore be assumed that during the first reduction of the PCBM, ICMA and ICBA blends only the pure fullerene phases are reduced and the Si-PCPDTBT is not charged. This is not surprising since the potential to reduce the pure polymer film ($E_{1/2}^{red} = -1.70\,V$) was found to be 0.5 to 0.8 V higher than the first reduction of the blends (PCBM: $-0.92\,V$, ICMA: $-0.99\,V$, ICBA: $-1.21\,V$). It should be pointed out that this observation also excludes a charge transfer from the fullerene to the polymer in the blend.

The cyclic voltammograms of ICTA blends revealed a first small reduction peak around $-1.4\,V$ which is not correlated to any change of the absorption, figure 5.6D, but matches the first reduction potential of the pure ICTA. In the cyclic voltammogram this peak is followed by a strong second reduction peak and a simultaneous decrease of the 760 nm neutral band of the polymer and the increase of an 1025 nm fullerene anionic band. This was interpreted as a coinciding reduction of the polymer and fullerene phases.

Compared to the other fullerene derivatives the LUMO level of ICTA ($-3.3\,eV$) lies close to the LUMO of Si-PCPDTBT ($-3.1\,eV$). It is therefore possible that only few larger domains of pure ICTA are reduced during this first small reduction peak at around $-1.4\,V$ followed by a reduction of the complete blend. From these observations it was assumed that in polymer/ICTA blends the ICTA can not be reduced without reducing the polymer phase. This should have a strong effect on the solar cell efficiency and will be discussed later.

In summary the LUMO levels of the blend films were found to be stabilized compared to the LUMO levels of the pure fullerenes. Interestingly, the stabilization of the LUMO (defined as the difference between the LUMO values of the fullerenes in blend and solution) decreases with the number of addends going from 170 meV in PCBM to 70 meV in ICTA. The reason for this observation is unclear but it can be speculated that this is due to the approaching of the fullerene LUMO towards the LUMO of PCPDTBT ($-3.1\,eV$) with increasing number of addends (PCBM $-3.70\,eV$ and ICTA $-3.33\,eV$).

The reduced difference between the fullerene and polymer LUMO values could provide a stronger interaction between them and lead to an electron-transfer between the fullerene and polymer during the reduction. This would also be in agreement with the findings of the ICTA blends (LUMO: $-3.40\,eV$). Here a coinciding reduction of PCPDTBT and ICTA was found. It is therefore suggested that in the Si-PCPDTBT/ICTA blends an electron-transfer reaction from the ICTA to the polymer occurs as soon as the fullerene is reduced.

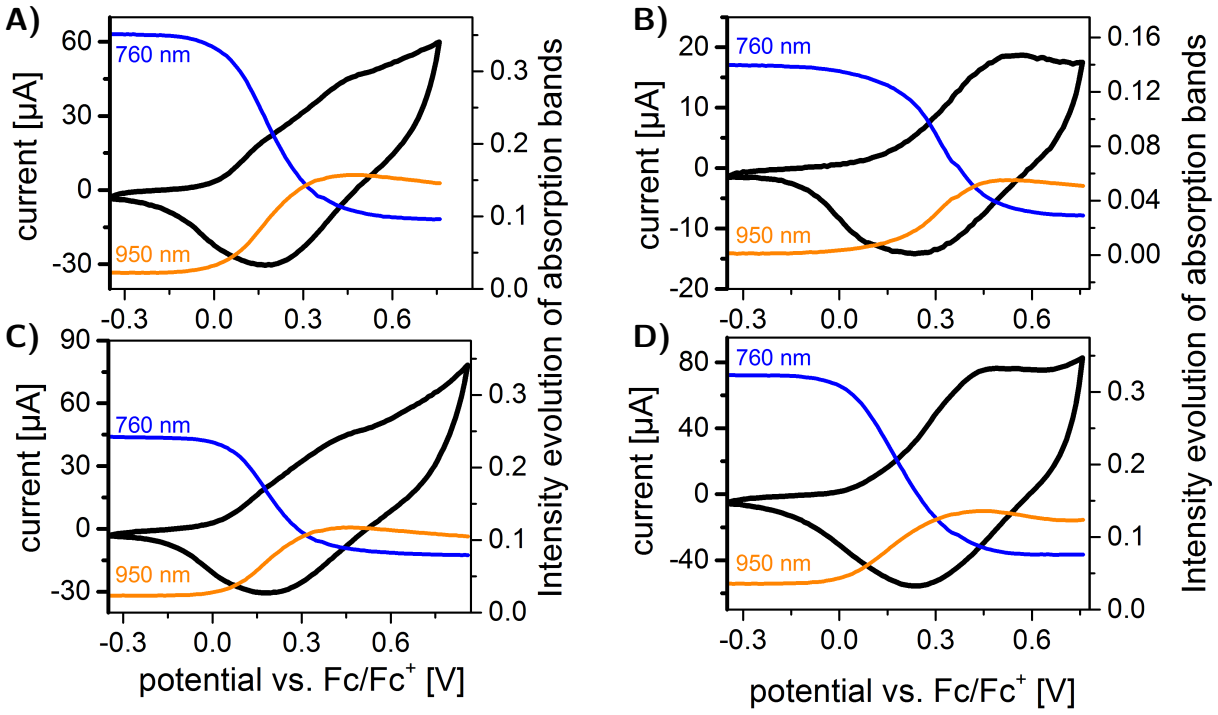

Fig. 5.7: In-situ spectroelectrochemical data of Si-PCPDTBT/fullerene blends from the first oxidation cycle with **A)** PCBM, **B)** ICMA, **C)** ICBA and **D)** ICTA. Measured as thin film on ITO-substrates in MeCN (0.1 M $TBAPF_6$, v=20 mV/s, RT). Left axis: cyclic voltammograms. Right axis: Intensity evolution of characteristic absorption bands: 950 nm (orange) and 760 nm (blue) (adapted from[14]).

Oxidation

The oxidations of the blend films were measured in acetonitrile (0.1 M TBAPF6/MeCN, v = 20 mV/s, RT), shown in figure 5.7. The corresponding absorption spectra are shown in figure A.19. For the oxidation no destruction or detaching of the film from the substrates was observed. Therefore the easier to handle and often used solvent acetonitrile (MeCN) was used for these measurements. The spectroelectrochemical characterization of all four Si-PCPDTBT/fullerene blends (PCBM, ICMA, ICBA and ICTA) reveals almost the same behavior as seen for the pure Si-PCPDTBT films, figure 5.3. An increased current in the cyclic voltammogram (E^{ox}_{onset}), a decrease of the neutral band (blue, 760 nm) and a coinciding increase of the polymer radical cationic band (orange, 950 nm) indicates that the oxidation potential of the polymer is located between 0.00 and 0.10 V.

The absorption onsets were used to determine the oxidation potentials and to calculate the HOMO levels, summarized in table 5.9. Compared to the pure Si-PCPDTBT films (−5.0 eV) the polymer/PCBM blend showed a small increase in the HOMO level up to around −4.8 eV. With an increasing number of addends (ICMA to ICTA) the LUMO energy decreased to −4.9 eV for ICTA.

In summary the difference of the HOMO levels between the pure polymer and the blend films were found to be less than 100 mV considering an error of 50 meV. It should be noted that no oxidation of the fullerenes was detected neither in the cyclic voltammogram nor in the in-situ absorption spectra, figure A.19. It was therefore assumed that during the oxidation of the blends exclusively the Si-PCPDTBT phase is oxidized and the fullerenes remain in their neutral phase. No further investigations regarding the differences of the HOMO values in the pure films and blends were performed. In can be speculated that either different thin film morphologies[163] in the blends or the interaction between the polymer chains with the fullerenes are the reason for this observations.

5.1.4 Summary and Impact on Bulk-Heterojunction Solar Cells

For an overview all data obtained from the electrochemical experiments are summarized in table 5.9. The in-situ absorption spectra (figure A.19 and figure A.18) showed nicely that during oxidation or reduction of the blends exclusively the polymer or the fullerene phases are charged. An exception was found for Si-PCPDTBT/ICTA blend in which a simultaneous reduction of both phases was detected. It was assumed that this is due to the similar LUMO values of the Si-PCPDTBT and ICTA.

Further the intensity evolutions from characteristic absorption bands were plotted against the applied potential. Thereby the onset potentials of the changes from characteristic absorption bands ($E_{Abs.onset}^{ox/red,wavelength}$) could be determined. It was shown that this method introduces an alternative to determine redox potentials besides using the onset or half wave potentials from the cyclic voltammograms. The comparison between cyclic voltammetry and spectroelectrochemistry data of the pure fullerene derivatives showed that the values gained from the absorption onsets ($E_{Abs.onset}^{ox/red,wavelength}$) correspond perfectly to the half wave potentials obtained from conventional cyclic voltammetry in solution. They can therefore be used as substitutes for the half wave potential if no peak potentials can be determined.

Comparing the redox potentials of the pure materials in solution and the polymer/fullerene blends differences of up to 180 ± 10 mV in the reduction potentials were found. Furthermore, a stabilization of the LUMOs was observed. This stabilization became smaller as smaller the difference between the LUMO values of the polymer and fullerene became. It was therefore proposed that with declining difference between the LUMO values of the polymer (donor) and the fullerene (acceptor) phases a better electron-transfer from the fullerene LUMO to the polymer is possible. This was supported by the finding that in the ICTA/polymer blends only a coinciding reduction of the fullerene and the polymer occurred.

Tab. 5.9: Characteristic potential values and energy levels of the pure polymers, fullerenes and the spin coated polymer/fullerene blends (1/1.5 by weight). The HOMO and LUMO values were calculated assuming the energy level of Fc/Fc^+ at $-4.8\,V$ under vacuum level. As comparison the literature[145] LUMO values of the fullerenes and the Si-PCPDTBT are given in brackets. The detailed measurements from which the values were taken are given in the food notes.

	HOMO	LUMO	$E^{red}_{1/2}$	E^{red}_{onset}	$E^{red}_{abs.onset}$	E^{ox}_{onset}	$E^{ox}_{abs.onset}$
	[eV]		[V]				
pure components							
C-PCPDTBT	-4.8[a]	-3.1[b]	−1.71[b]			0.04[a]	
Si-PCPDTBT (-5.0)	-5.0[c]	-3.1[e]		−1.70[e]		0.22[c]	0.23[c]
PCBM[d] (-3.74)		-3.70	−1.10[f]	−1.04	−1.10		
ICMA[d] (-3.70)		-3.68	−1.12[f]	−1.01	−1.09		
ICBA[d] (-3.55)		-3.53	−1.27[f]	−1.11	−1.25		
ICTA[d] (-3.36)		-3.33	−1.47[f]		−1.45		
Si-PCPDTBT/fullerene blends[g]							
PCBM	-4.8(3)	-3.8(8)	−0.92		−0.93	0.03	0.04
ICMA	-4.8(8)	-3.8(1)	−0.99		−0.99	0.08	0.16
ICBA	-4.8(3)	-3.6(0)	−1.21		−1.20	0.03	0.06
ICTA	-4.9(1)	-3.4(0)	−1.40		–	0.11	0.03

a) Determined from a CB solution, figure 5.2A/B **b)** Determined from a THF solution, figure 5.2C/D **c)** Determined from a spin coated thin film, figure 5.3. The absorption onset was taken from the intensity evolution of the 950 nm band. **d)** Determined from a methylene chloride solution, figure 5.5. The absorption onset was taken from the intensity evolution of the 1025 nm band. **e)** Determined from a dichlorobenzene solution, figure 5.1B. The absorption onset was taken from the intensity evolution of the 1025 nm band. **f)** Determined from a methylene chloride solution, figure A.20 **g)** Oxidation: Values were taken from thin films measured in acetonitrile, figure A.19. Reduction: Values were taken from thin films measured in o-dichlorobenzene, figure 5.6.

These results show that especially the LUMO energies can be strongly shifted when fullerenes are blended with conjugated polymers. Hence, these results evince that for discussions about the role of frontier orbital energies in organic solar cells it is necessary to determine the HOMO/LUMO values directly from the active layers rather than using values of the pure materials.

Impact on Bulk-Heterojunction Solar Cells

These energy level characterizations of polymer/fullerene blends were used in a collaboration with Steve Albrecht during his PhD in the group of Prof. D. Neher in Potsdam. They were recently investigating the mechanism of the efficient charge separation in organic solar cells.[5, 14, 109] Up to today there is an ongoing discussion about the mechanism of

this efficient charge separation despite the existence of geminate electron-hole pairs bound by strong Coulomb forces.[109, 124, 126, 164, 165]

As driving force for the charge separation the energy difference between the lowest singlet state (E_{S1}, typically the donor band gap) in the system and the fully separated charge pair state (E_{CS}) is proposed ($E_{CS}^{eff} = E_{S1} - E_{CS}$). Whereby the E_{CS} is defined as the difference between the LUMO and HOMO of the acceptor and donor material, respectively. Typically energies larger as 0.1 eV are reported for high performing systems.[14, 57, 109, 166]

Besides the driving force for the charge separation also the mechanism of the charge separation is intensively discussed in literature.[14, 109] A theory is proposed where upon excitation of the polymer/fullerene blend a charge transfer (CT) state is formed from which the charge separation occurs. For this theory two possible routes are shown in figure 5.8A. Route 2 proposes that after excitation of the polymer an electronically and/or vibrationally excited CT-state is formed which possesses enough kinetic energy to overcome the Coulomb forces between the hole and electron resulting in charge separation. On the other hand a pathway over thermalized CT states is shown by route 1. Here, it is assumed that the CT state relaxes into the ground state from which then the charge separation occurs.[14, 166]

In this collaboration the goal was to investigate the effect of the driving force (E_{CS}^{eff}) on the charge separation and to distinguish between the two described routes.

Therefore organic solar cells with active layers composed of Si-PCPDTBT/fullerene blends were prepared using the fullerene derivatives, PCBM, ICMA, ICBA and ICTA

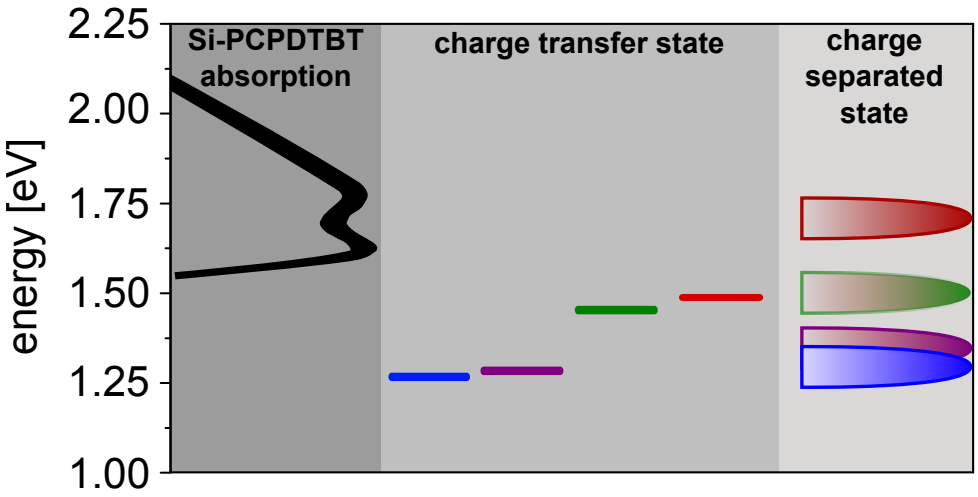

Fig. 5.8: Sketch of the energy diagram with two proposed pathways for charge separation in polymer/fullerene blends exemplary shown for ICTA. From left to right the main absorption of Si-PCPDTBT, the charge transfer (CT) state and the position of the charge separated (CS) states are indicated. Adapted with permission from [14, Albrecht and Fischer et al. 2014]. Copyright (2014) John Wiley and Sons.

with LUMO energies decreasing from −3.7 eV (PCBM) to −3.3 eV (ICTA), as discussed above. These active layers were studied by S. Albrecht employing a variety of solar cell characterization methods including external quantum efficiency (EQE), sensitive photo thermal deflection spectroscopy (PDS) and time-delayed collection field (TDCF) experiments. In addition morphology investigations using resonant polarized soft X-ray scattering (P-SoXs) and grazing incident wide angle X-ray scattering (GIWAXS) were performed.[14,166]

Furthermore, the knowledge of the energetic levels from not only the pure polymer and fullerenes but also of their energetic levels within the actual blends as used in organic solar cells was indispensable. Those were taken from the electrochemistry investigations discussed above. From the four blend systems investigated in this chapter the solar cell efficiencies were measured by S. Albrecht et al.[14,166] The efficiencies were found to decrease in the order of increasing number of addends to the fullerene and are summarized in table 5.10.

Tab. 5.10: Solar cell characteristics of the blend systems investigated also by electrochemistry with the short circuit current (J_{sc}), the open circuit voltage (V_{oc}), the fill factor (FF) and the solar cell power conversion efficiency (PCE). The solar cells were built and measured by S. Albrecht.[14,166]

	J_{sc} [mA/cm^2]	V_{oc} [mV]	FF [%]	PCE [%]
Si-PCPDTBT/PCBM	11.6	591	64	4.38
Si-PCPDTBT/ICMA	10.8	618	60	4.00
Si-PCPDTBT/ICBA	7.7	810	44	2.75
Si-PCPDTBT/ICTA	0.9	947	25	0.22

The charge separated states in the blends were calculated and are shown in figure 5.8.[14,166] Even though a direct comparison between the absolute values of the pure fullerenes and blend films is difficult, due to different local environments (solution vs. film), the fullerenes can be compared relative to each other. Therefore the stabilization energies (defined as difference between fullerene LUMO in blend and solution) were compared and a significant decrease from 0.18 eV (PCBM) to 0.07 eV (ICTA) was found. It was suggested that the decrease in the stabilization energies is responsible for the lower solar cell efficiency in ICTA blends compared to PCBM blends. On the other hand large differences in the solar cell efficiencies between ICBA and ICTA were found even though they showed similar values of stabilization energies. This made the stabilization energy as sole factor doubtful.

The spectroelectrochemistry further revealed that the LUMO energy of ICTA lies close to the LUMO of the pure Si-PCPDTBT and only a coinciding reduction of both phases was found. Figure 5.8 sketches the increase of the ICTA LUMO and the finding from Albrecht at al.[14, 166] that the charge transfer state is limited by the optical band gap of the Si-PCPDTBT. This leads to an increased energy gap between the charge separation and charge transfer state which limits the charge separation. These findings were further confirmed by a correlation between the charge generation efficiency and difference between the polymer LUMO and the charge transfer energy. It was shown that the generation efficiency decreases strongly when this difference between the polymer LUMO and the charge transfer energy becomes small. It was therefore concluded that the generation of free charges proceeds via the split-up of the relaxed CT state (Route 1) irrespective of the initial exciton energy and driving force. A detailed description of all findings and conclusions can be found in our publication [14, Albrecht and Fischer et al. 2014] and the PhD thesis of S. Albrecht.[166]

5.2 Morphology Dependence of the Hole Mobility in Organic Field Effect Transistors

It is well known from literature that the charge carrier mobility (μ) of conjugated polymers is strongly influenced by their molecular weight[16,45,96,105] and mesoscopic morphology.[15,16,25,45,96,167] A fast charge carrier mobility is important for most electronic devices and not only for organic field effect transistors (OFETs). For example, it is also a key factor for high efficiencies in organic solar cells since a fast charge carrier transport to the electrodes minimizes the chance of charge recombination.[126] The information about the correlation between charge transport and crystal structure, polymer backbone orientation and molecular weight is therefore a key element in finding the optimal mesoscopic morphology for electronic devices.

In particular for P3HT, theoretical investigations of Lan et al.[45,96] and experiments from our group [15, 16, Fischer et al. 2012 and Crossland et al. 2012] suggest a strong correlation between the charge carrier mobility (μ) and certain crystallographic directions depending on the molecular weight. It was shown that within crystalline domains the charge transport along the polymer chain direction is 2 to 3 decades faster than along the π-stacking direction.[45,96] Lan et al.[96] further suggested that within the amorphous regions the charge transport is several orders of magnitude slower compared to the crystalline domains, chapter 1.2.6.

Over macroscopic distances on the other hand the mesoscopic morphology must be considered. P3HT exhibits a semi-crystalline, edge-on structure which consists of alternating crystalline/amorphous domains in the direction of the polymer backbone and perpendicular to the π-stacking. Therefore the charges must cross amorphous domains of slower charge transport[96] when traveling over macroscopic distances in the direction of the polymer backbones. To cross such amorphous domains single polymer chains which connect two crystalline domains were suggested and called tie-molecules. They act as bridges over amorphous domains and allow a fast charge transport across the amorphous regions, chapter 1.2.6.

In order to access these tie-molecules the charges must move parallel to the amorphous regions within the crystalline domains. This means that for a fast charge carrier mobility over macroscopic distances a 2D charge transport along and parallel to the polymer backbones is necessary. For example in the edge-on morphology of P3HT charges can hop fast between π-stacked polymer backbones perpendicular to the polymer chain direction and move fast along the polymer backbones. The charges can therefore access tie-molecules to cross amorphous regions.

The model of tie-molecules was further supported by experiments performed during my diploma thesis.[16] Employing aligned P3HT films of different molecular weights it was shown that for polymers with molecular weight above 10 kg/mol a faster charge transport occurs compared to polymers with smaller molecular weight and PDI. This is probably because in the lower molecular weight polymers no backbones long enough to bridge the amorphous regions exist.[16,96]

In the literature the hole mobility of PCPDTBT was investigated in spin coated films by Turner et al.[119] The OFETs were prepared by spin coating from a chlorobenzene solution and subsequent temperature annealing at 100 °C. The measurements with a bottom-contact top-gate configuration revealed mobilities of around $3 \times 10^{-3}\,\mathrm{cm^2/Vs}$. Interestingly, mobilities of $> 3\,\mathrm{cm^2/Vs}$ were reported for PCPDTBT with linear C_{16} side chains by Müllen et al.[105] This high hole mobility is probably possible because of a different crystal structure with a better packing of the polymer chains due to the less bulky, linear side chains.

In this chapter different polymorphs of PCPDTBT with and without π-stacking are compared to understand the influence of long range π-stacking on the hole mobility in donor-acceptor copolymers.

5.2.1 Investigated Morphologies of PCPDTBT

The previous chapter 4 showed the possibility to obtain homogeneous films with different polymer chain orientations and crystal structures for PCPDTBT, figure 5.9. For the OFET investigations in this chapter thin films were prepared using the optimized protocols employing CS_2 vapor annealing (CS_2-annealed) and spin coating form CB/DIO solutions (CB/DIO-spincoated). Both preparation methods exhibit morphologies with the polymer backbone oriented parallel to the substrate (in-plane). The interesting difference between these two morphologies is the stacking of the polymer backbones. For the CB/DIO-spincoated films literature[58,102] reports a classical edge-on morphology, similar to P3HT, with an in-plane long-range π-stacking perpendicular to the polymer backbone. For the CS_2-annealed films on the other hand evidence was found for a dimer-like structure, without long range π-stacking, chapter 4.4.1.

These findings were further supported by absorption spectroscopy. The spectra of the CB/DIO-spincoated films reveal a strong 800 nm absorption which was shown to be characteristic for long range π-stacking of the polymer backbones, chapter 4.2.[17] For the CS_2-annealed films on the other hand the absorption is blue shifted and an absorption

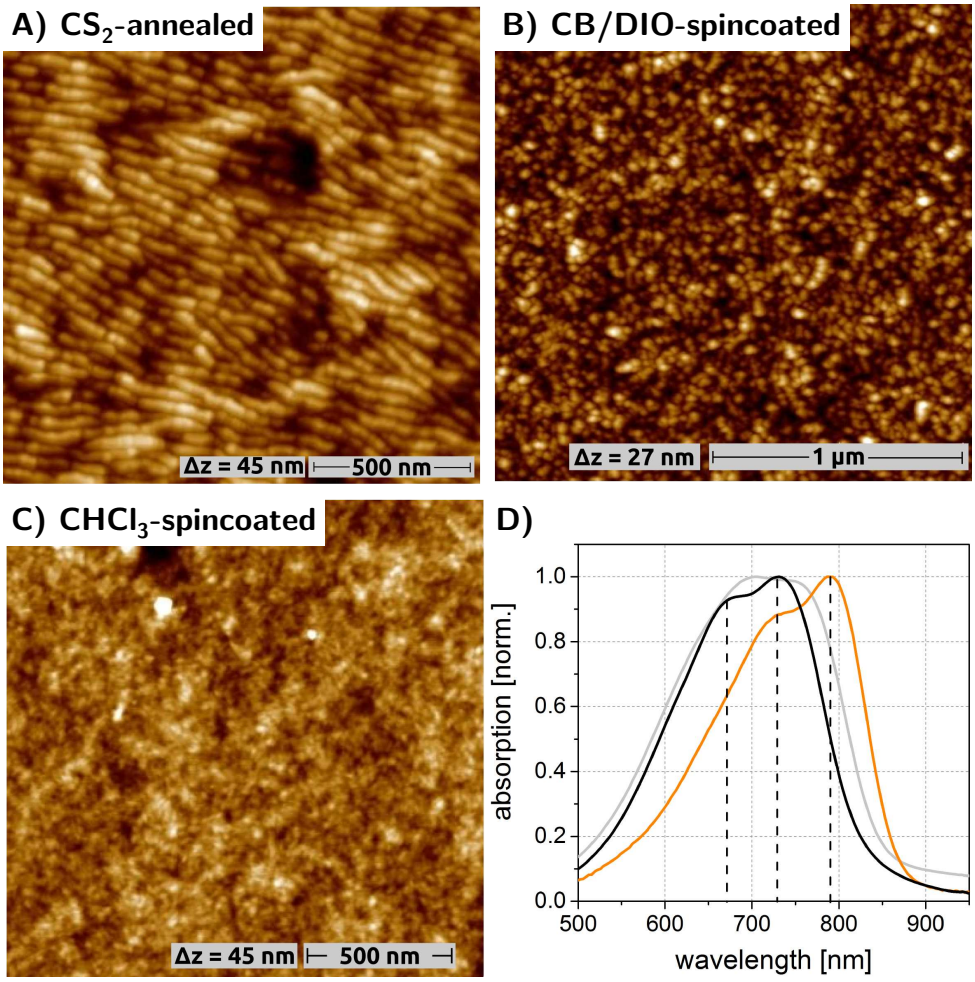

Fig. 5.9: A-C) AFM height images of PCPDTBT films prepared by A) CS_2 vapor annealing, B) spin coating from a CB solution with 2 w% DIO and C) spin coating from a $CHCl_3$ solution. **D)** Absorption spectra of the three differently prepared films shown in A-D: CS_2-annealed (black), CB/DIO-spincoated (orange) and $CHCl_3$-spincoated (gray).

band around 670 nm was found. The missing of the 800 nm band in the CS_2-annealed samples further confirms the absence of long range π-stacking, chapter 4.3.4.

A comparison between these two morphologies in OFETs allows therefore to investigate the influence of a long range π-stacking compared to a dimer-like structure on the charge carrier mobility. As suggested by investigations of other semi-crystalline polymers, e.g. P3HT, a 2D in-plane charge transport along the polymer backbones and the perpendiuclar π-stacking is necessary for high mobilities over macroscopic distances.[15,16,45,96] Therefore CB/DIO-spincoated films should reveal an increased mobility compared to the dimer-like structure of the CS_2-annealed samples.

In addition to the two ordered structures a $CHCl_3$-spincoated film (chapter 4.2) was investigated for comparison reasons. The $CHCl_3$-spincoated film reveals a weak 800 nm

absorption and is similar to the absorption spectra obtained from solutions. Therefore it can be assumed to be mostly amorphous with only few π-stacked aggregates.

OFET Preparation

A top-gate bottom-contact configuration was chosen for the OFET measurements, chapter 2.4. The main advantage of this configuration is that the charge transport is induced in the top few nanometers of the polymer film. This allows to correlate the charge carrier mobility to the morphologies measured by AFM.[15,121] A detailed structure analysis is given in chapter 4.4.

The OFETs were prepared on glass-substrates with evaporated source- and drain-electrodes (30 nm gold with 5 nm Cr adhesion layer) by spin coating from $CHCl_3$ (3 mg/ml, $CHCl_3$-spincoated) or CB solutions with 2 w% DIO as solvent additive (3 mg/ml, CB/DIO-spincoated). The CS_2-annealed films were prepared by subsequent CS_2 vapor annealing of the $CHCl_3$-spincoated films, following the procedure described in chapter 4.3.1. Each substrate consisted of sixteen transistors with four different channel lengths around 100, 170, 200 and 250 µm, each with a 1 mm channel width. The channel lengths varied from batch to batch and the actual channel lengths were determined for each sample with the optical microscope and are stated in the respective figure captions. After vacuum drying of the polymer films a dielectric PMMA layer was spin coated over the complete substrate (60 mg/ml, 1200 rpm) and annealed at 80 °C under nitrogen. For a detailed layout of the OFET see figure A.1A and chapter 3.2.5 for detailed preparation conditions.

5.2.2 Hole Mobility Characterization

For all three PCPDTBT morphologies (CS_2-annealed, CB/DIO-spincoated and $CHCl_3$-spincoated) output and transfer characteristics were measured from at least three different transistors for each of the four channel lengths. Figure 5.10 displays one representative set of output- and transfer curves obtained from the 170 µm channels for the different morphologies.

Output Characteristics

The output characteristics are shown in figure 5.10. The source-drain currents (I_{sd}) found in the saturation regime of the output characteristics at $V_G = -60\,V$ were always about one decade higher for the CB/DIO-spincoated films (3×10^{-8} A) compared to the CS_2-annealed samples (7×10^{-9} A). The output characteristics of the $CHCl_3$-spincoated films

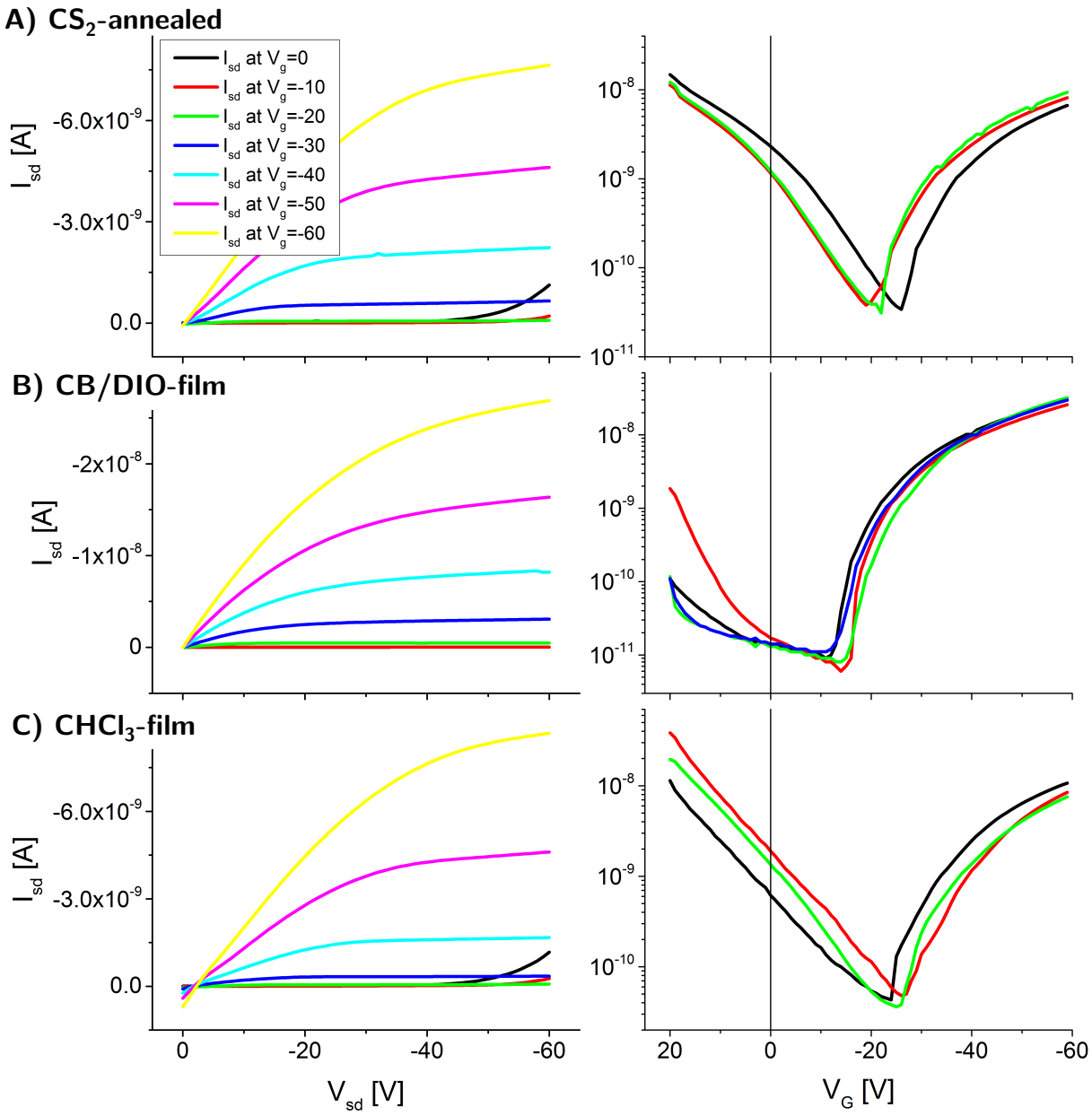

Fig. 5.10: Output (left) and transfer (right) characteristics ($170 \pm 5\,\mu m$ channel length) of PCPDTBT thin films obtained from the three morphologies described in the text: **A)** CS_2-annealed **B)** CB/DIO-spincoated and **C)** $CHCl_3$-film. **Left:** One representative set of output curves of one transistor for each morphology is shown. They were measured applying gate voltages (V_G) between 0 to $-60\,V$ in $10\,V$ steps. **Right:** Transfer curves obtained in the saturated regime ($V_{sd} = -60\,V$) by applying voltages between 20 to $-60\,V$ to the gate electrode. Each color represents a different transistor, each with a $170 \pm 5\,\mu m$ channel length (adapted from[168]).

behave similar to the CS_2-annealed films and reveal source-drain currents in the saturation regime at $V_G = -60\,V$ of around $7 \times 10^{-9}\,A$.

It should be pointed out that for the CS_2-annealed and $CHCl_3$-spincoated samples only above $V_G > -20\,V$ the typical output curve behavior was found: a linear regime for small V_{sd} and an increase of the current in the saturated regime with increasing gate voltages, chapter 2.4. At smaller gate voltages ($V_G < -20\,V$) the output curves reveal for high V_{sd} ($> -40\,V$) a small current which decreases with increasing gate voltages until gate voltages of $-20\,V$ and more are applied (e.g CS_2-annealed $V_G = 0\,V$, black line). Such a behavior indicates an ambipolar charge transport in the polymer which allows electron transport at low gate and high V_{sd} voltages and causes the observed current. For the CB/DIO-spincoated films on the other hand no evidence for such an ambipolar charge transport was found in the output curves.

The negative currents seen for the CS_2-annealed and the $CHCl_3$-spincoated samples close to $V_{sd} = 0\,V$ at high gate voltages are most likely caused by some leak currents through the PMMA dielectric layer.

Transfer Characteristics

The transfer characteristics were measured in the saturated regime ($V_{sd} = -60\,V$) by applying gate voltages between 20 to $-60\,V$, figure 5.10. All transfer characteristics show a high threshold voltage of around $-20\,V$ for the CS_2-annealed and $CHCl_3$-spincoated films and around $-17\,V$ for the CB/DIO-spincoated sample. This can be attributed to internal resistance between the polymer and the gold electrodes, most likely caused by a mismatch of the Fermi levels.

It should be pointed out that in all samples a current was detected when applying positive gate voltages. Since applying a positive gate voltage at the gate electrode induces negative charge accumulation in the polymer film, these currents must be correlated to an electron mobility. This is in accordance with the ambipolar behavior already seen in the output characteristics. In addition it should be noted that for positive gate voltages the CS_2-annealed and $CHCl_3$-spincoated films revealed a two order of magnitude higher current ($1 \times 10^{-8}\,A$) compared to the CB/DIO-films ($1 \times 10^{-10}\,A$).

Hole Mobility

The charge carrier mobilities of the respective samples were calculated from the transfer characteristics employing equation 12, chapter 2.4. The mobilities of the different morphologies are plotted for V_G between -30 to $-60\,V$ in figure 5.11A. To display the

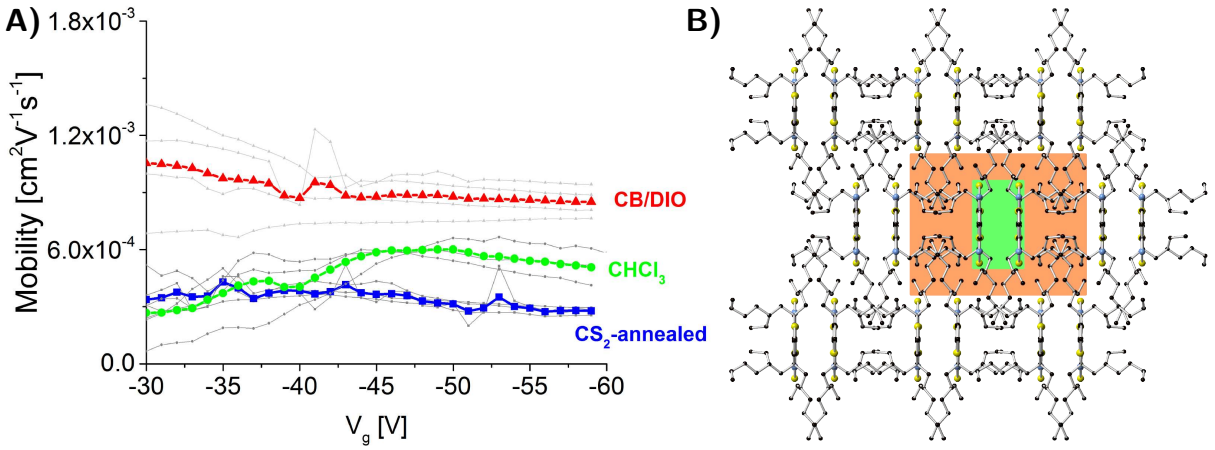

Fig. 5.11: A) Charge carrier mobility of three different PCPDTBT morphologies: CB/DIO-film (red, triangle), CS_2-annealed (blue, square) and $CHCl_3$-film (green, circle). For each morphology three different channel lengths were measured. The average over the different transistors of the same channel length (at least three per channel length) are displayed in gray. The averages over all channel lengths for each morphology are colored. **B)** Schematically view along the polymer backbone of a dimer structure including the alkyl side chains (orange) which separates the dimers (green).

fluctuations of the measurements the mobilities calculated from the transistors of each channel length were averaged (gray). The final mobilities were plotted as the average over the different channel lengths, figure 5.11A colored lines. The highest charge carrier mobility was found for the CB/DIO-spincoated samples (red) around $1 \times 10^{-3}\,\mathrm{cm}^2/\mathrm{Vs}$. For the CS_2-annealed (blue) and the $CHCl_3$-spincoated (green) samples the mobilities were determined to around $3 \times 10^{-4}\,\mathrm{cm}^2/\mathrm{Vs}$ and $5 \times 10^{-4}\,\mathrm{cm}^2/\mathrm{Vs}$, respectively.

It was discussed in the previous chapters that the CB/DIO-spincoated films comprise a semi-crystalline edge-on morphology with the polymer backbone and the long-range π-stacking in-plane of the film similar as P3HT.[17,58,102] It can therefore be assumed that in such films a charge transport along the π-stacking direction is possible. Hence, the higher charge carrier mobility in the CB/DIO-spincoated films is in good agreement with the above discussed need of a 2D charge transport in-plane of the polymer film, chapter 1.2.6. It is suggested that in the CB/DIO-spincoated films the charges cross amorphous regions by using tie-molecules which connect the crystalline domains, similar as suggested for P3HT by Lan et at.,[45,96] chapter 1.2.6.

In the dimer-like structure of the CS_2-annealed samples on the other hand the hopping between dimers is hindered by the bulky side-chains. The charges are therefore trapped within dimers and cannot transfer to better pathways of other polymer backbones as schematically shown in figure 5.11B. Therefore the charge carrier mobility seems to be dominated by the amorphous regions of the film. This is further in good agreement with the similar mobilities found in the rather amorphous $CHCl_3$-spincoated films. The

slightly higher charge carrier mobility of the $CHCl_3$-spincoated film can be explained by the more long range π-stacking character compared to the CS_2-annealed films, evident by the absorption spectra discussed in chapter 4.2.

5.2.3 Summary

In summary indications were found that the charge transport mechanism for crossing the amorphous regions in semi-crystalline donor-acceptor copolymer films is similar to P3HT, chapter 1.2.6. It was shown that PCPDTBT films with an in-plane long-range π-stacking backbone orientation provide charge carrier mobilities one order of magnitude higher than samples with a dimer structure. The further investigated rather amorphous sample revealed a similar charge carrier mobility as the dimer structure. This supports the assumption that without the π-stacking the charge carrier mobility seems to be dominated by the amorphous regions.

In literature high performance organic solar cells of PCPDTBT are only reported from active layers processed from CB/DIO solutions. Those exhibit a strong 800 nm band which indicates an increased long range π-stacking, chapter 4.2. With the results from this chapter this observation can be better understood since a high charge carrier mobility typically enhances charge extractions and therefore decreases the number of recombinations.

5.3 How Morphology Influences Bilayer Organic Solar Cells

In the same year PCPDTBT was introduced, Heeger et al.[3] reported solar cell efficiencies of 3.6 % using PCPDTBT/PCBM blends. In the same publication they suggested that efficiencies of up to 7 % should be possible if the morphology of the active layer could be optimized. Today solar cells of up to 5.5 % are reported when using solvent additives such as 1,8-diiodooctane (DIO) during the processing of the active layer, chapter 1.3.1.[1]

Over the last years most device improvements achieved in the field of organic solar cells included morphology optimizations. Thereby in literature the main focus typically lies on the optimization of the interface between the donor and the acceptor material and the blend morphology. Additional several other aspects such as e.g. crystallinity, polymer chain stacking and mesoscopic morphology must be considered when optimizing organic solar cells, chapter 1.2.2.[52,57,60,61,147,169,170]

Typically a bulk heterojunction of the donor and acceptor materials is used due to its easy preparation and high efficiencies. In this thesis bilayer devices were built to better understand the impact of morphology, chapter 1.2.2.

It is known that the chain orientation at the donor/acceptor and the electrode interfaces can strongly effect the charge separation.[170–172] Many groups investigated therefore the influence of the chain orientation using bilayer solar cells. In an theoretical and experimental study Cheng et al.[171] showed for the well known material systems pentacene (small molecule) and P3HT (polymer) that the molecular orientation at the interface to the PEDOT electrode is a key factor to maximize the number of extracted charges (short circuit current, J_{SC}). They showed that a face-to-face orientation between P3HT and PEDOT increases the hole mobility across the interface about 20 times compared to an edge-to-edge configuration at the interface.

Investigating the influence of the molecular orientation at the donor/acceptor interface Brédas et al.[172] used molecular dynamic simulation techniques to investigate different molecular packings at the 2,4-bis[4-(N,N-diphenylamino)-2,6-dihydroxy-phenyl] squaraine, (DPSQ) / C_{60} interface. They reported a strong influence on the electronic coupling depending on the molecular orientation of the two phases to each other. It was suggested that this coupling strongly influences the exciton dissociation and charge recombination processes at the donor/acceptor interface. Furthermore, using bilayer solar cells Brütting et al.[169] showed that the molecular orientation between α-sexithiophene (6T) and C_{60} can drastically change the rate of recombination. A considerable increase of the open circuit voltage was observed with the transition from a coexistence of standing and lying 6T molecules to a only standing morphology.

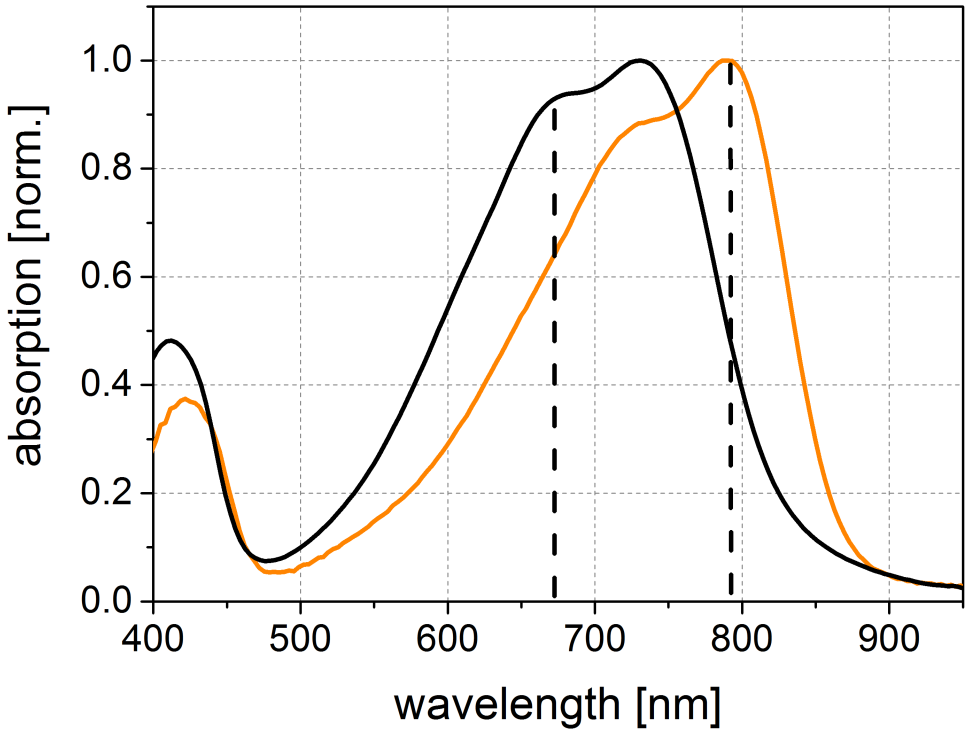

Fig. 5.12: Absorption spectra of the pure polymer layers used in the organic solar cells in this chapter. Black: CS_2-annealed polymer film. Orange: CB/DIO-spincoated film.

Further the charge carrier mobility in the pure phases of the blends must be considered, since it also has a strong influence on the solar cell performance, chapter 1.2.2. In conjugated polymers often an anisotropic charge transport mobility along specific crystallographic directions is found, chapter 1.2.6. In general the charge mobility is highest along the backbone and π-stacking direction but hindered in the direction of the alkyl side chains.[15,16,25,147,173] Since in organic solar cells the charges must be extracted as fast as possible after exciton separation to avoid non-geminal recombination a polymer chain orientation with the backbone standing on the electrodes is desired, chapter 1.2.2.

In the previous chapter 5.2 the charge carrier mobility of three different PCPDTBT morphologies was investigated. In the CB/DIO-spincoated films, which exhibit long range π-stacking, a charge carrier mobility of almost one order of magnitude higher compared to samples with a dimer structure (CS_2-annealed) or a rather amorphous structure ($CHCl_3$-film) was found. In this chapter the same three morphologies are used to build bilayer organic solar cells. The goal was to investigate the influence of the different morphologies and their in-plane charge carrier mobilities on the organic solar cell device performance.

5.3.1 Preparation of Bilayer Solar Cell

In earlier chapters it was discussed that thin PCPDTBT films with different crystal structures and molecular orientations can be fabricated by using the solvent additive DIO or applying solvent vapor annealing (CS_2- or CB-annealed). This provided the opportunity to investigate active layers consisting of different structures but the very same material in organic solar cells. To compare the different morphologies it was necessary to gain a high control over the polymer film formation and to investigate the individual layers making sure that they are comparable in terms of thickness and surface roughness. Therefore the bilayer solar cell configuration as described in chapter 1.2.2 and shown in figure 5.13C was chosen for the following investigations.

Polymer Film Preparation

Especially the comparisons between the CB/DIO-spincoated and the CS_2-annealed samples are of great interest. Both form homogeneous films with the polymer backbones oriented in-plane but reveal different crystal structures with and without long-range π-stacking, as proposed in literature and discussed in chapter 4.4.

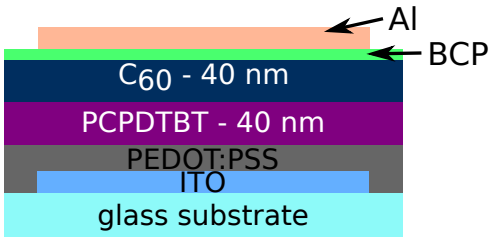

Fig. 5.13: Bilayer solar cell configuration.

Figure 5.12 shows the absorption spectra obtained from the different morphologies and confirms the different crystal structures, chapter 4.4. The CB/DIO-spincoated films reveal a strong 800 nm band correlated to the long-range π-stacking. In the CS_2-annealed samples this characteristic 800 nm band is absent and instead a blue shifted band at 670 nm appears.

The polymer layers were prepared on PEDOT:PSS coated pre-patterned ITO-substrates (figure A.1B) employing spin coating from $CHCl_3$ or CB/DIO (2 w% DIO) and post CS_2 vapor annealing of pre-cast $CHCl_3$-spincoated films. The processing conditions were optimized to gain films of 40 nm thickness and comparable roughness, table 5.11.

The $CHCl_3$-spincoated films were additionally included into this study as a reference film of low crystallinity and disordered chain orientations. It should be pointed out that from exactly the same morphologies the charge carrier mobility was already discussed in chapter 5.2.

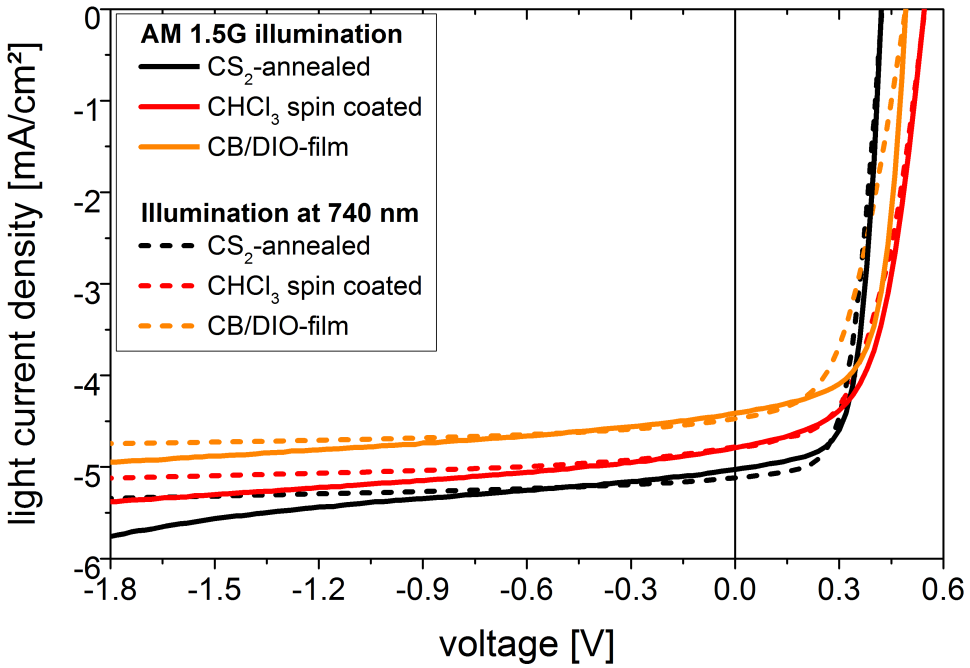

Fig. 5.14: J-V curves of $0.16\,\mathrm{cm}^2$ sized cells of CS_2-annealed (black), $CHCl_3$-spincoated (red) and CB/DIO-spincoated (orange) samples under AM 1.5G illumination with $100\,\mathrm{mW/cm}^2$ (solid) compared to J-V curves under $740\,\mathrm{nm}$ illumination (dashed) with the intensity adjusted to yield approximately the same J_{sc} as under AM 1.5G illumination (adapted from[12]).

Preparation of the Fullerene Acceptor Layer

The polymer films were transfered to Potsdam under a nitrogen atmosphere to prevent degradation. There the acceptor layer and top electrodes were added with the help of the master student B. Tornow at the University of Potsdam in the group of Prof. Neher.

The acceptor layers were prepared by evaporating a 40 nm thick C_{60}-layer on top of the polymer films. Evaporation was used to prevent penetration of the fullerenes into the polymer layers or changes in the polymer morphology as is likely when processing from solvents. Directly afterwards the cells were finalized by evaporation of a 5 nm bathocuproine (BCP) hole-blocking interlayer and an aluminum acceptor layer as top electrode. The complete device configuration is shown in figure 5.13. The detailed device preparation protocol is given in chapter 3.2.5.

5.3.2 Solar Cell Characterization

The following solar cell characterization was performed by me in the laboratories of Prof. D. Neher at the University of Potsdam together with the master student B. Tornow. Three different methods were employed: current-voltage-curves (J-V curves) under AM 1.5G and

740 nm illumination, external quantum efficiency (EQE) and time delayed collection field (TDCF) measurements.

J-V Curve Characteristics

Solar cell characteristics were measured directly after finalizing the solar cells under nitrogen atmosphere and the results are shown in figure 5.14. Each sample was investigated by illuminating with the entire solar spectrum (AM 1.5G, solid line) and with monochromatic 740 nm LED light (dashed line). The illumination with monochromatic 740 nm light induces a pure polymer excitation since C_{60} absorbs only below 700 nm.[174]

Surprisingly, despite the large differences in the film morphologies all J-V curves are quite comparable in shape, short circuit current (J_{SC}) and open circuit voltage (V_{OC}). It should be noted that all curves reveal a similar low field dependence of the photocurrent at reverse bias. Generally speaking the bilayer solar cells showed efficiencies of around 1.4 % and high fill factors between 66 % and 57 %. An overview of all performance data is given below in table 5.11.

Tab. 5.11: Bilayer solar cell performance data from the J-V curves in figure 5.14 under AM 1.5G illumination ($100\,mW/cm^2$) with an active area of $0.16\,cm^2$.

	CS_2-annealed	CB/DIO-spincoated	$CHCl_3$-spincoated
V_{OC} [V]	0.42	0.50	0.55
J_{SC} [mA/cm^2]	−5.03	−4.41	−4.79
FF [%]	66.7	64.7	57.2
ECE [%]	1.4	1.4	1.5
J_{SC}(EQE)[a] [mA/cm^2]	−5.07	−4.44	−4.97
R_q[b]	8.9	2.0	1

[a] Obtained from the EQE measurements without external applied bias (figure 5.15) by integration over the AM1.5G solar spectrum.
[b] Root mean squared roughness extracted from AFM images of the respective polymer films.

External Quantum Efficiencies - EQE

In general the external quantum efficiency is obtained by measuring the number of extracted charges (electrons) during irradiation at a certain wavelength with a known intensity. The EQE is then calculated from the ratio between the number of extracted charges (#electrons) and irradiated photons ($\frac{\#electrons}{\#photons}$, chapter 2.4.2) and plotted against the wavelength. EQE measurements with different external biases applied to the cells were additionally performed to be able to differentiate between the field dependence in the respective polymer and fullerene phases.

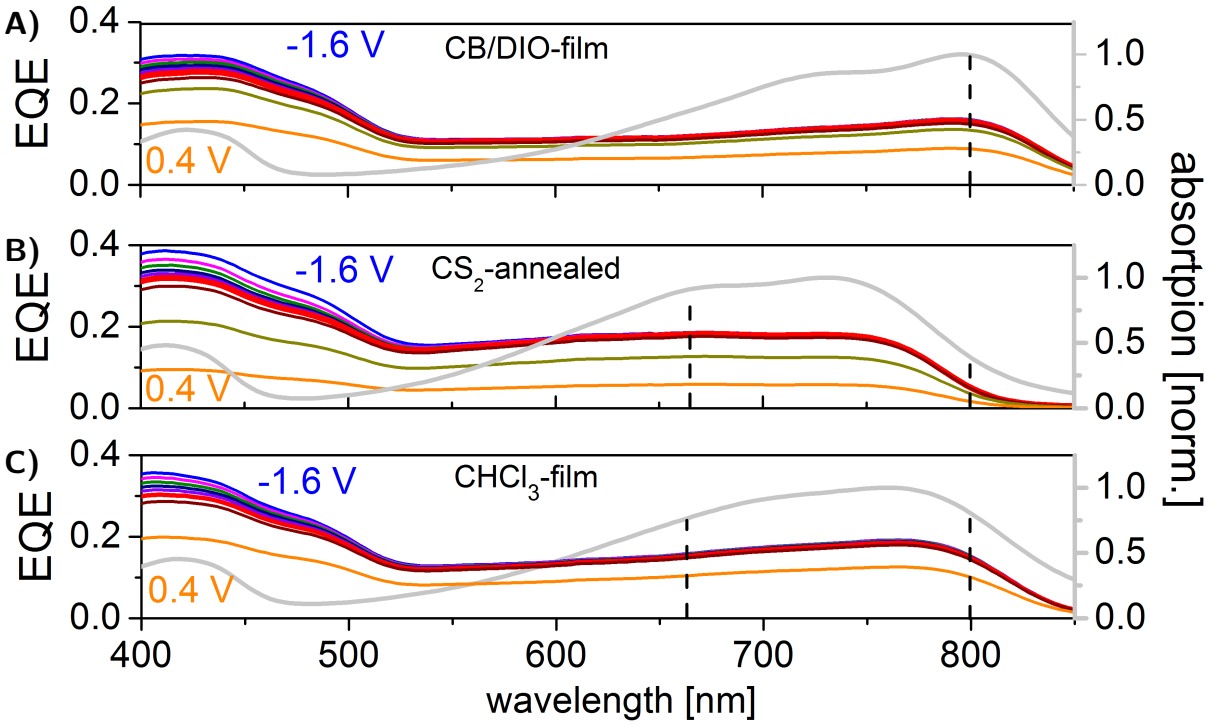

Fig. 5.15: Field dependent external quantum efficiency (EQE) spectra for different biases (-2.4 V to 0.4 V, left scale) of bilayer PCPDTBT/C_{60} cells are compared to the absorption spectra of the pure polymer layers (gray) without C_{60} (right scale). Three differently prepared polymer layers are compared: CB/DIO-spincoated **(A)**, CS_2-annealed **(B)** and $CHCl_3$-spincoated **(C)** samples (adapted from[12]).

For all samples figure 5.15 shows the plots of the EQEs against the wavelength (EQE: left axis). The absorption spectra of the pure polymer layers are added for comparison reasons (Abs: gray, right axis). The EQE in the high energy region (400 to 540 nm) is dominated by the C_{60} absorption (not shown) whereas the low energy region (600 to 900 nm) represents the polymer absorption. The characteristic absorption of the different morphologies is mirrored perfectly by the EQE spectra (dashed lines). For the CB/DIO-spincoated samples the 800 nm maximum, which was in earlier chapters correlated to long-range π-stacking (chapter 4.2), is only found in the EQE of the CB/DIO-spincoated samples. The CS_2-annealed sample on the other hand reveals a broad plateau from 600 to 740 nm which is perfectly consistent with the absorption of the dimer like crystal structure discussed in chapter 4.4. This indicates that the same polymer chains and aggregates causing the characteristic absorptions are also responsible for the charge generation within the polymer layer. The charge generation is therefore suggested to occur from excitons which are generated in the respective morphology of the polymer bulk and then diffuse to the donor/acceptor interfaces where they separate into electron/hole pairs.

Furthermore, the EQE peak maxima which are correlated either to the fullerene (430 nm) or polymer (700 to 800 nm) phase were compared. The comparison between the different samples revealed that the maxima differ only by 3 to 5 %. This indicates that the overall charge generation (including recombination processes) in all films is similar. This is also in good agreement with the J-V-curve results. To further ensure that the EQE data correspond to the measured J-V-curves the EQE spectra without externally applied bias (0 V) were integrated over the AM1.5G spectrum to obtain the current density (J_{SC}(EQE)). The calculated values are in good agreement with the J_{SC} values from the J-V-curves, table 5.11. This further supports that all three morphologies perform similar in bilayer solar cell devices.

In the region of the fullerene phase (400 to 500 nm) the comparison of the EQE spectra at different externally applied biases (−1.6 V – 0.2 V) reveals a high external field dependency for the light harvesting for all samples, figure 5.15. The same comparison in the polymer region (600 to 900 nm) showed almost no external field dependency. This indicates a much higher field dependence between −1.6 V and 0.2 V for the fullerene compared to the polymer phases.

The same trend of the field dependence as in the fullerene phase of the EQE was found in the J-V curves at high reverse biases (neg. potentials) when illuminating under solar AM 1.5G spectrum (solid line), figure 5.14. Whereas the field dependence in the J-V curves is smaller when only exiting the polymer phase with monochromatic light (740 nm, dashed line), figure 5.14. The same observation of increased field dependence of the charge generation in PCPDTBT:PCBM blends was found also by Brenner et al.[175] and has recently been attributed to the field-induced split-up of CT excitations in the fullerene phase.[176]

Time Delayed Collection Field - TDCF

TDCF is based on the following principle: after illumination all generated free charges (Q_{tot}) are extracted before non-geminate recombination occurs (a bimolecular recombination of two charges generated in different absorption processes). For this measurement free charges are generated by a monochromatic 5 ns laser pulse allowing the selective excitation of certain phases. After a delay time of 10 ns a collecting voltage is applied to extract all free charges before non-geminate recombination can occur. Additionally a pre-bias can be applied during the free charge generation allowing a field dependent measurement for the totally generated free charges. A detailed description of the TDCF technique is given in chapter 2.4.2.

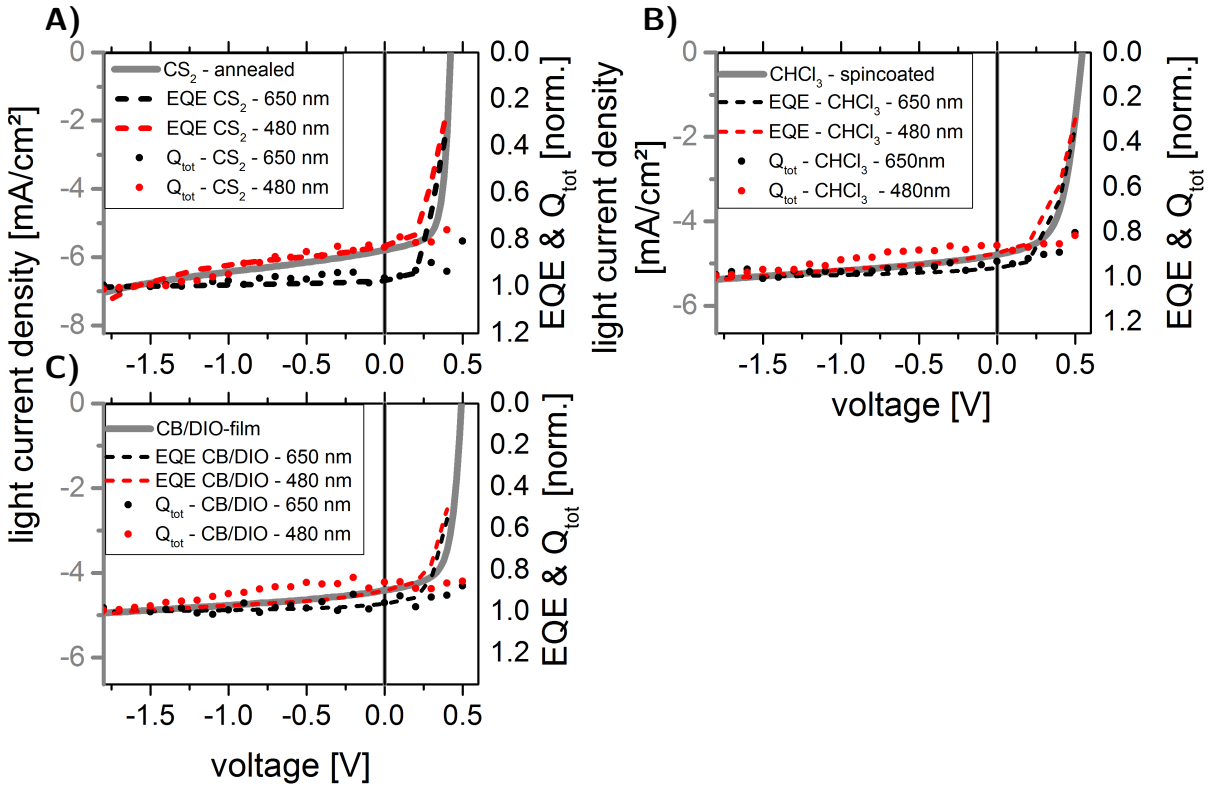

Fig. 5.16: J-V curves under AM 1.5G illumination with $100\,\mathrm{mW/cm^2}$ (gray, left scale) are compared to the normalized total charges (Q_{tot} from TDCF, dots) and the normalized field dependent EQE (right scale, dashed) excited at $650\,\mathrm{nm}$ (black) and $480\,\mathrm{nm}$ (red) for PCPDTBT/C_{60} bilayer cells normalized to $-1.8\,\mathrm{V}$. Three different preparation methods for the polymer layers are compared: CS_2-annealed **(A)**, $CHCl_3$-spincoated **(B)** and CB/DIO-spincoated **(C)** sample (adapted from[12]).

The TDCF measurements were performed outside the glovebox at ambient air. To protect the cells from degradation they were encapsulated by gluing a glass slide on top of the cell using an epoxy resin. The stability of the solar cells was tested by measuring a second set of J-V curves after the TDCF measurements. No significant signs of degradation was found.

In figure 5.16 the recorded data of the TDCF measurements (dots) are plotted against the applied voltage and compared with the J-V curves (gray) and the EQE data (dashed). The J-V curves were obtained under AM1.5G illumination whereas the EQE and TDCF data were measured for two characteristic absorption wavelengths (480 and 650 nm) corresponding to the fullerene (red) and the polymer (black) phase. The comparison between these two methods allows to differentiate between the total total number of extracted charges (EQE – including possible non-geminate recombination) and the totally generated charges (Q_{tot}) (TDCF – excluding non-geminate recombination). The plots of all samples show that the field dependence of the charge generation (Q_{tot}) at reverse bias follows the monochromatic photocurrent (EQE). This leads to the conclusion that the

field dependence is determined by the interplay between charge generation and geminal recombination and not by non-geminate recombinations. Only when going to low internal fields, close to the open circuit voltage (V_{OC}), the monochromatic EQE data differ from the Q_{tot} value. This means that at low internal fields non-geminate recombinations become the dominating factor for the overall photocurrent.

Further the EQE and TDCF data were compared with the J-V curves of the solar cells. This revealed that the field dependence observed in the J-V curves is almost exclusively determined by the fullerene phase. The curves in which only the polymer phase (680 nm) is excited show only a very weak field dependence of the generated and extracted charges. It can be speculated that the field dependence seen for the fullerene phase is due to the field-induced split-up of CT excitations in the pure fullerene phase.[176]

5.3.3 Summary

Three different preparation methods were used to obtain thin films of PCPDTBT comparable in thickness and surface roughness but with different crystal structures (CS_2-annealed vs. CB/DIO-spincoated) and degrees of crystallinity ($CHCl_3$-spincoated vs. CB/DIO-spincoated). To the best of my knowledge this is the first study comparing different morphologies of a conjugated donor-acceptor copolymer in a polymer/C_{60} bilayer solar cell devices. The results from the J-V curves as well as from the EQE and TDCF measurements show that the polymer morphology has only a minor impact on the efficiency and field dependence in these bilayer cells.

The almost completely field independent charge generation in the polymer phase leads to the conclusion that the split-up of the charge transfer excitons at the polymer/fullerene heterojunctions occurs rather barrier free. Surprisingly, regardless of the polymer morphology. These results are even more surprising considering the charge carrier mobilities determined for the different morphologies in the last chapter. It could be shown that the CB/DIO-spincoated samples possess an increased charge carrier mobility due to their long range π-stacking structure compared to the CS_2-annealed and $CHCl_3$-spincoated films.

All these results indicate that the efficiency of the here prepared bilayer solar cells does not depend on the polymer morphology but is rather determined by the electron delocalization in the highly crystalline C_{60} layer. It can be therefore assumed that the performance differences in bulk heterojunction solar cells reported for PCPDTBT[1,59,61,175,177] with efficiencies between 2.5 to 5.5 % are probably caused by different degrees of fullerene aggregation and blend morphology and not by changes in the polymer morphology.

6 Conclusion

The main goal of this thesis was to achieve a deeper understanding of how the mesoscopic morphology and crystal structure of donor-acceptor copolymers influence their optical and electrical properties. As a representative donor-acceptor copolymer the well known and high performance copolymer PCPDTBT[1–3] which is based on the electron-rich donor cyclopentadithiophene (CPDT) and electron-poor acceptor benzothiadiazole (BT) was investigated, figure 6.1A. In addition the two derivatives thereof Si-PCPDTBT[4] and F-PCPDTBT[5,6] were characterized and compared. Regarding molecular weights and PDI the following materials were studied: PCPDTBT (M_W = 26.7 kg/mol, PDI = 1.8) and F-PCPDTBT (M_W = 10.8 kg/mol, PDI = 1.6). Furthermore, the influence of the molecular weight on the optoelectronic properties was investigated using four different Si-PCPDTBT batches between 4 and 32 kg/mol (M_W).

In order to establish structure-function relationships first a fundamental understanding of the correlation between morphology and absorption in solution and thin films was established. The aggregation behavior was investigated by in-situ absorption and photoluminescence (PL) spectroscopy and modeled via a Frank-Condon-Analysis. Different processing solvents, with and without solvent additives, in addition to solvent vapor annealing, were used to control the mesoscopic morphology and crystal growth. TEM/ED and GIWAXS experiments were employed to establish a crystal structure and to identify different orientations of the unit cell relative to the substrate. The different morphologies were subsequently applied in field-effect transistors and organic solar cells in order to make correlations between the polymer morphology and device performances. In the following some of the key findings which also resulted in publications will be highlighted.

The optical properties in solution and the formation of aggregates were investigated employing UV/Vis and PL spectroscopy. In solution, the absorption spectra typical for donor-acceptor copolymers was found revealing a high energy band around 420 nm and a low energy band around 730 nm. Quantum chemical calculations suggest that the low energy band is caused by a charge-transfer (CT) transition between the HOMO and LUMO. The high energy band on the other hand was correlated to a HOMO to LUMO+3 transition. The charge-transfer character of the low energy band was further confirmed by a hypsochromic shift in solvents of increasing polarities. [11, Fischer et al. 2013]

The aggregation behavior of the polymers was probed in solution, by either changing the concentration or the temperature of the solution. Both experiments showed the appearance of a new red-shifted absorption band above 800 nm, figure 6.1B. Based on the fact that

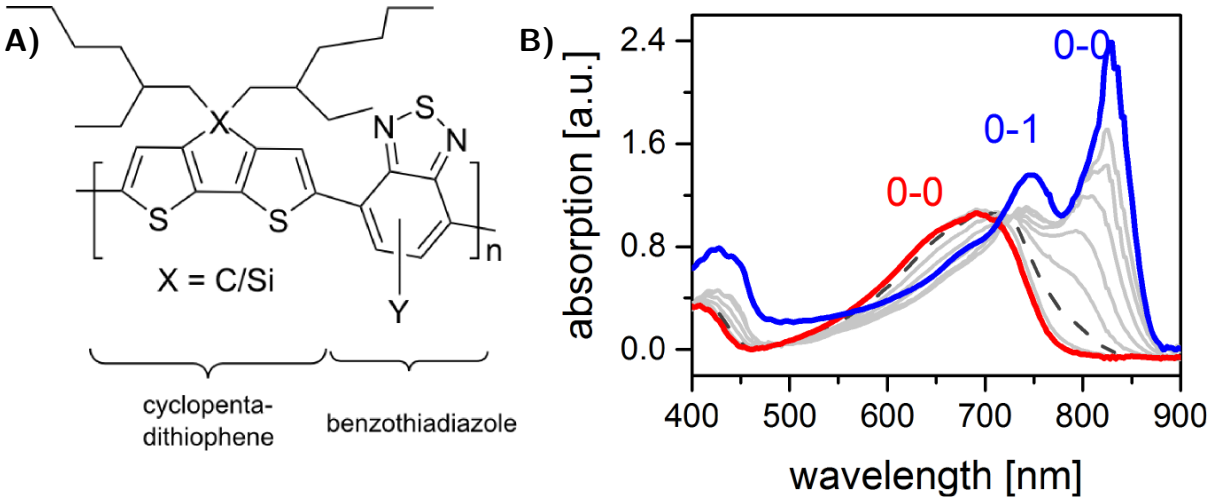

Fig. 6.1: A) Chemical structure of PCPDTBT (X = C, Y = H), Si-PCPDTBT (X = Si, Y = H) and F-PCPDTBT (X = C, Y = F). **B)** UV/Vis spectra of PCPDTBT dissolved in MTHF ($0.25\,\mathrm{mg/ml}$) between $67\,^{\circ}\mathrm{C}$ (red, $340\,\mathrm{K}$) and $-163\,^{\circ}\mathrm{C}$ (blue, $110\,\mathrm{K}$) with spectra taken every $20\,\mathrm{K}$ (gray) in between (dashed: room temperature; adapted from[10]).

aggregates of other conjugated polymers such as P3HT or MEH-PPV reveal a red shifted absorption, the 800 nm band was correlated to π-stacked aggregates of PCPDTBT.[17] Especially the concentration-dependent experiments confirmed the formation of interchain aggregates and excluded intrachain aggregation.

Spano et al.[7–9,85,93,137] had shown that the spectra of conjugated homopolymers such as P3HT and MEH-PPV can be modeled using a Frank-Condon analysis. The Spano approach could successfully be transfered to the PCPDTBT spectra. The absorption and PL spectra of PCPDTBT were further interpreted by modeling their absorption signatures in the dissolved and aggregated phase, employing the same technique as Spano et al. One important outcome was that the Spano model was used in this thesis for the first time to investigate the spectral signatures of a donor-acceptor copolymer. The experimental spectra could be nicely reproduced by employing two emissive states. In contrast to other conjugated polymers, such as P3HT, no J- or H-aggregation had to be assumed to explain changes in the 0-0/0-1 peak ratio when going from the solution to the aggregated phase. During aggregation, a red-shift, probably due to an increased conjugation length and planarization of the backbones, was found and at low temperatures, a sharpening of the vibrational bands was observed. [10, Scharsich and Fischer et al. 2015]

In a first attempt to understand and control the thin film morphology films spin coated from different processing solvents with and without solvent additives were investigated employing absorption spectroscopy and structural characterization. It was shown that the order of the thin film morphology increased with increasing boiling point of the processing

solvents. This was attributed to the probably increased drying time during the film formation due to the slower evaporation. Low boiling point solvents such as CS_2 revealed a featureless film morphology and absorption spectra reassembling those of the solution. With increasing boiling point randomly oriented aggregates of around 40 nm were found in the films by AFM. However, only when spin coating from the high boiling point solvent, 1-chloronaphthalene (bp. 259 °C), a distinct fiber morphology was observed. Such highly ordered films further revealed a strong 800 nm absorption band similar to the spectral signatures found in aggregated solutions. [11, Fischer et al. 2013]

In literature several publications[58, 102, 108] report on films processed from chlorobenzene (CB) solutions containing 1,8-diiodooctane (DIO) as solvent additive (CB/DIO-spincoated). An edge-on morphology with a long range π-stacking was suggested, even though only weak scattering was found by GIWAXS and no melting point could be obtained. TEM/ED and DSC experiments performed within this thesis confirmed the low crystallinity and the GIWAXS reflections reported in literature.

Interestingly, films spin coated from solvents containing 2 w% DIO revealed a strong 800 nm absorption and 40 nm aggregates independent of the processing solvent. It was therefore suggested that such high boiling point additives allow aggregation during the drying of the film regardless of the processing solvent. At the same time DIO seems to suppress the fiber formation observed in the 1-CN-spincoated films.

To further increase the crystallization tendency solvent vapor annealing was employed. In analogy to P3HT,[15, 16, 83] pre-cast PCPDTBT films (around 30 nm thickness) were annealed in CS_2 vapor atmosphere. AFM images showed a highly ordered fiber-like morphology for the CS_2-annealed films, figure 6.2A. TEM/ED and DSC measurements showed few weak reflections and no phase transitions, respectively, indicating low crystallinity for these samples.

In an attempt to further increase the crystallinity of the films the annealing solvent CS_2, was replaced by the often used processing solvent chlorobenzene (CB). Due to the higher boiling point i.e lower vapor pressure of CB, the temperature during the solvent vapor annealing had to be increased to 50 °C. While CS_2-annealed films resulted in fibre-like homogenous films, this led to highly crystalline samples of PCPDTBT with two distinct morphologies, figure 6.2B: i) dendritic spherulites of up to 40 µm in diameter which reveal a Maltese Cross in the POM images and a lamellar substructure in the AFM images. ii) Circular blue regions in the POM images with a terrace-like structure and distinct steps consisting of a height of around 15 nm. DSC measurements further revealed a melting

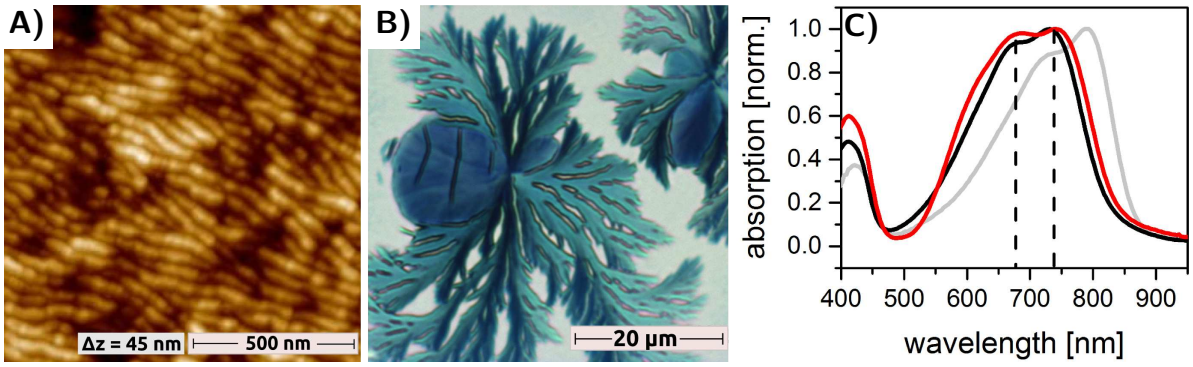

Fig. 6.2: A) AFM height image of a CS_2-annealed PCPDTBT thin film. **B)** POM image of a CB-annealed PCPDTBT film showing a spherulitic structure with an circular blue region attached. **C)** UV/Vis-absorption spectra of thin films prepared by CS_2 (black) and CB (red) vapor annealing. As comparison an absorption spectra of a CB/DIO-spincoated film (gray) was added (adapted from[12]).

point around 280 °C and confirmed the high crystallinity of these samples. [12, Fischer et al. 2015]

Interestingly, regardless of the annealing solvent no evidence of an 800 nm absorption band as in the spin coated films and aggregated solutions was found for the solvent-annealed samples, figure 6.2C. Instead a blue-shifted absorption with an additional band around 680 nm was measured. It was therefore suggested that the solvent annealed samples comprise a different polymorph compared to the aggregates found in solution and thin films. For F-PCPDTBT a very similar crystallization behavior as for PCPDTBT was found. On the contrary for Si-PCPDTBT, only the smallest molecular weight polymers could be recrystallized and no changes were found in the UV/Vis-absorption spectra before and after solvent vapor annealing. This was assumed to be because of the much higher aggregation tendency of Si-PCPDTBT compared to the other two derivatives.

The highly crystalline films obtained by solvent vapor annealing were used to establish a first crystal structure. The circular blue regions of the CB-annealed PCPDTBT samples revealed a high symmetry and distinct reflection pattern measured by TEM/ED. The pattern was accordingly indexed as [001] zone. Tilting experiments on the spherulitic structures confirmed that they consist of the same polymorph as the circular blue regions. The difference between the two structures was found to be only in the orientation of the polymer backbones relative to the substrate. In the spherulitic structure the chains are tilted by around 45°, figure 4.18. From the symmetry and intensity distribution of ED patterns obtained from CB-annealed films, a dimer-like structure in which 4 polymer chains build up an orthorhombic unit-cell was suggested. [12, Fischer et al. 2015]

The ED pattern of the CB-annealed F-PCPDTBT films revealed a similar symmetry and intensity distribution as the PCPDTBT samples. The main difference found was

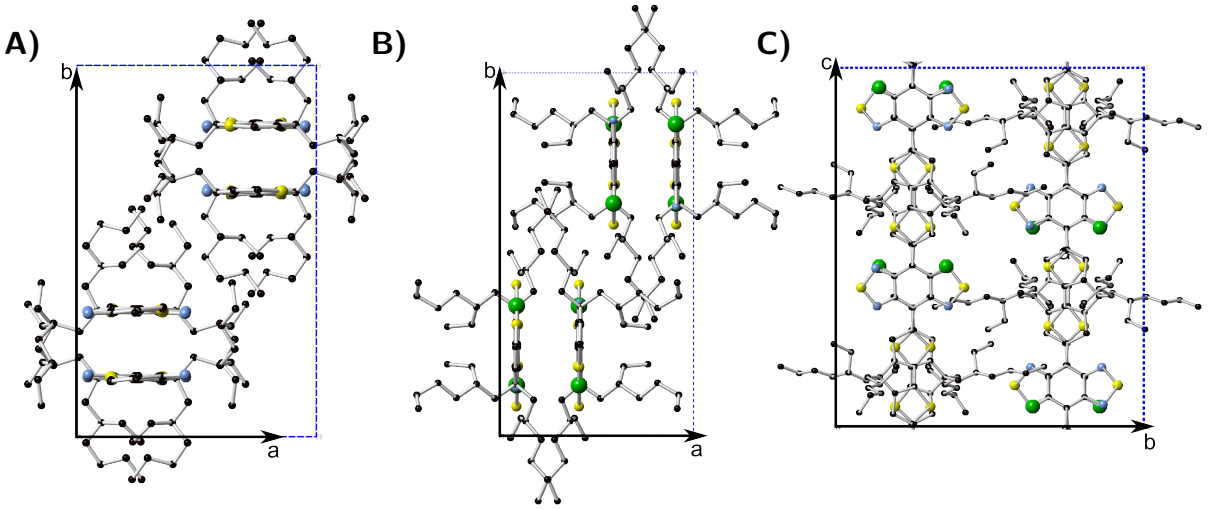

Fig. 6.3: Model of the proposed crystal structure for PCPDTBT (A) and F-PCPDTBT (B) and C). **A) and B)** show the dimer-like structure in the a,b-plane of the unit cell with the stacking direction rotated by 90° between PCPDTBT and F-PCPDTBT. **C)** View along the a-axis of the F-PCPDTBT structure revealing the anti-parallel stacking of the polymer chains found for both derivatives (adapted from[13]).

that the reflections correlated to the interchain stacking of the dimers were rotated by 90° compared to PCPDTBT. Therefore a similar dimer-like structure as in PCPDTBT but with the dimer stacking direction rotated by 90° was suggested for the fluorinated derivative, figure 6.3.

Further information along the polymer backbone direction was needed to complete the crystal structure. Two methods, epitaxy and high temperature rubbing, were employed to align the polymer backbones of PCPDTBT and F-PCPDTBT in the plane of the film. Using the aligned films, TEM/ED patterns were obtained showing a distinct intensity distribution along the polymer backbones. Four selection rules could be extracted from these patterns and a first tentative model for the crystal structure was constructed employing a P c c n space group. As shown in figure 6.3, both derivatives display a dimer-like structure with an anti-parallel stacking of the benzothiadiazole units within the dimers. [13, Fischer et al. 2015]

The PCPDTBT CS_2-annealed samples were additionally investigated by GIWAXS and the high brilliance allowed to obtain several additional reflections compared to the TEM/ED measurements. From the diffraction patterns of the CS_2-annealed films it was evident that they contain the same polymorph as the CB-annealed samples. In contrast to the CB-annealed films, the dimers are oriented parallel to the substrate. Hence, with CS_2 vapor annealing, a method was found to crystallize PCPDTBT in a homogeneous film of a dimer-like structure and with the polymer backbone oriented in-plane. This finding was of great importance since such films could afterwards be compared in organic field-effect

transistors (OFET) and organic solar cells with the long-range π-stacked morphology of CB/DIO-spincoated films.

At the moment Anton Melnyk from the group of Dr. Denis Andrienko at the MPI in Mainz is performing theoretical calculations based on the presented tentative crystal structure. It will be very interesting to see if the theoretical investigations can confirm the experimental structures. Furthermore, the theoretical investigations might help to better understand why the substitution of a single hydrogen atom by a fluorine changes the crystal structure so drastically.

Before actual devices were characterized the energy levels and absorption properties of the charged species of the different polymer derivatives were investigated via electrochemistry. The HOMO/LUMO values of Si-PCPDTBT and PCPDTBT were determined to $-5.0\,\text{eV}/-3.1\,\text{eV}$ and $-4.8\,\text{eV}/-3.1\,\text{eV}$, respectively. It was shown that the HOMO value does not change when blending Si-PCPDTBT with different fullerenes (PCBM, ICMA, ICBA and ICTA). The LUMO values on the other hand were shown to be stabilized by up to 100 meV when blending Si-PCPDTBT with fullerene derivatives. The in-situ spectroscopy further revealed that the first reduction occurs solely in the pure fullerene phases. Only in the most extreme case of ICTA lies the fullerene LUMO ($-3.3\,\text{eV}$) so close to that of Si-PCPDTBT ($-3.1\,\text{eV}$) that only one reduction peak for both the polymer and the ICTA appeared around $-1.4\,\text{V}$.

With the aim to better understand the efficient charge transfer state splitting in heterojunction PCPDTBT/fullerene solar cells, spectroelectrochemistry of both the pure polymer and the blended active layers were investigated together with S. Albrecht from the group of Prof. Neher. The spectroelectrochemistry provided a technique to investigate the HOMO/LUMO values not only in the pure phases but also in the blended active layers of the organic solar cells. This technique enabled the correlation of the redox processes to specific phases in the blends. Together with additional measurements (performed by S. Albrecht et al.) it was concluded that the generation of free charges in PCPDTBT/fullerene solar cells proceeds via the split-up of the relaxed CT state irrespective of the initial exciton energy and driving force. A detailed description of all findings and conclusions can be found in the respective publication [14, Albrecht and Fischer et al.] and the PhD thesis of S. Albrecht.[166]

In chapter 5, OFETs and solar cells were built from three different morphologies: i) CB/DIO-spincoated, with long-range π-stacking, ii) CS_2-annealed, with a dimer-like structure and iii) $CHCl_3$-spincoated, with a foremost amorphous morphology. In top-gate bottom-contact OFETs, the CB/DIO-spincoated films showed an one order of magnitude

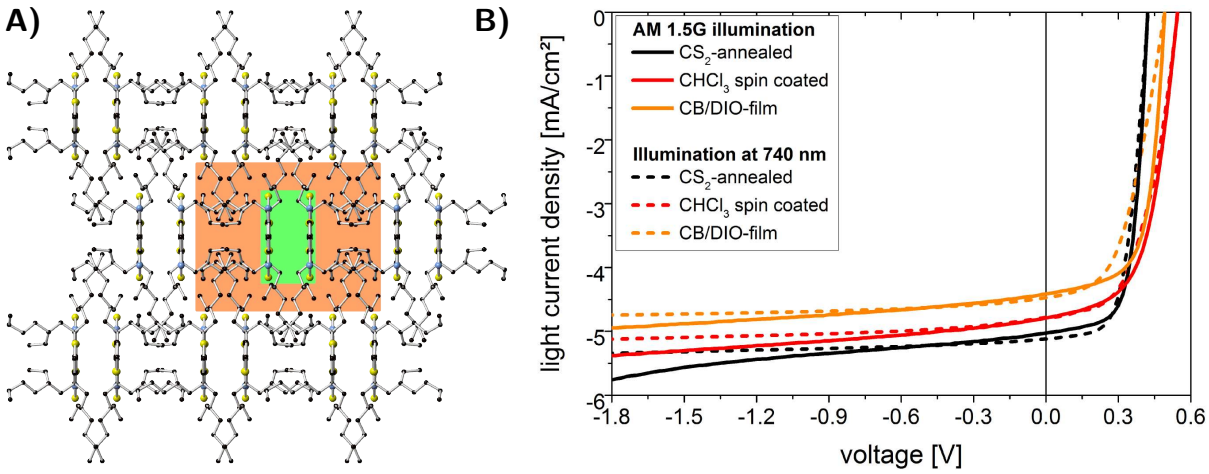

Fig. 6.4: A) Schematic of a dimer-like structure highlighting how the alkyl side chains form a barrier for charge transport between the dimers. **B)** J-V curves of solar cells prepared from CS_2-annealed (black), $CHCl_3$-spincoated (red) and CB/DIO-spincoated (orange) films under AM 1.5G illumination with $100\,\mathrm{mW/cm^2}$ (solid) compared to J-V curves under $740\,\mathrm{nm}$ illumination (dashed) with the intensity adjusted to yield approximately the same J_{sc} as under AM 1.5G illumination (adapted from[14]).

higher charge carrier mobility ($1 \times 10^{-3}\,\mathrm{cm^2/Vs}$) compared to the CS_2-annealed films ($1 \times 10^{-4}\,\mathrm{cm^2/Vs}$). Comparing the long-range π-stacking and the dimer-like structure it becomes obvious that a charge transport along the π-stacking is much more likely than between dimers. In the dimer-like structure the alkyl side chains form a barrier between the dimers, preventing an easy transition of the charges between two dimers. This packing prevents an efficient 2D charge transport and limits thereby the overall hole mobility on top of the polymer films, figure 6.4A. [168, Fischer et al. 2015]

The influence of the PCPDTBT structure was investigated using bilayer solar cells. The polymer layers were prepared using the same preparation methods as for the OFETs. As acceptor layer, C_{60} was evaporated and as electrodes ITO and aluminum electrodes were used. Using J-V-curve, EQE and TDCF measurements the solar cell characteristics and the recombination mechanisms were investigated and compared. The high charge carrier mobility in the CB/DIO-spincoated films gave reason to expect a better performance of the active layers prepared from CB/DIO. Surprisingly, all three morphologies revealed very similar device performances, figure 6.4B. A weak field dependence was found in all cells and was correlated to the field-induced charge generation of the fullerene phase. The similarity of the performance regardless of the morphology was surprising. It was speculated that the highly crystalline C_{60} provides such a good electron mobility that all free electrons are extracted via the fullerene phase before charge recombination can occur. This would probably mean that the small differences in the charge carrier mobility of the different polymer layers have only minor influence on the overall efficiency. [12, Fischer et al. 2015]

Future experiments can build up on the possibility to induce different polymorphs by the developed processing and annealing procedures. Using an amorphous C_{60} acceptor layer in bilayer solar cells to reduce the electron mobility in the acceptor layer such that the effect of the different polymer morphologies can be observed would probably be very interesting. The challenge hereby would be to apply the amorphous layer without destroying the polymer morphologies as it easily occurs when processing the fullerenes from solution. A possibility could be to evaporate a mixture of C_{60} and C_{70} or to use other fullerene derivatives.

In summary a general understanding of a representative donor-acceptor copolymer regarding influence of crystal structure and mesoscopic morphology on the opto-electronic properties and device performance was established. The additional investigation of two derivatives with typical backbone modifications such as fluorination of a monomer or substitution of the bridging carbon atom by a silicon atom further generalized this study. Many of the findings in this thesis such as aggregation behavior, annealing protocols or the charge carrier mobility-structure relationship can be used in future work regarding conjugated donor-acceptor copolymers.

References

[1] J. Peet, J. Y. Kim, N. E. Coates, W. L. Ma, D. Moses, A. J. Heeger and G. C. Bazan, *Nature Materials* **2007**, *6*(7), 497–500.

[2] D. Mühlbacher, M. Scharber, M. Morana, Z. Zhu, D. Waller, R. Gaudiana and Christoph J. Brabec, *Advanced Materials* **2006**, *18*(21), 2884–2889.

[3] I.-W. Hwang, C. Soci, D. Moses, Z. Zhu, D. Waller, R. Gaudiana, Christoph J. Brabec and Alan J. Heeger, *Advanced Materials* **2007**, *19*(17), 2307–2312.

[4] Jianhui Hou, Hsiang-Yu Chen, Shaoqing Zhang, Gang Li and Yang Yang, *Journal of the American Chemical Society* **2008**, *130*(48), 16144–5.

[5] Steve Albrecht, Silvia Janietz, Wolfram Schindler, Johannes Frisch, Jona Kurpiers, Juliane Kniepert, Sahika Inal, Patrick Pingel, Konstantinos Fostiropoulos, Norbert Koch and Dieter Neher, *Journal of the American Chemical Society* **2012**, *134*(36), 14932–14944.

[6] Yong Zhang, Jingyu Zou, Chu-chen Cheuh, Hin-lap Yip and Alex K.-Y. Jen, *Macromolecules* **2012**, *45*(13), 5427–5435.

[7] Frank C Spano and Carlos Silva, *Annual Review of Physical Chemistry* **2014**, *65*, 477–500.

[8] Jenny Clark, Carlos Silva, Richard H. Friend and Frank C Spano, *Physical Review Letters* **2007**, *98*(20), 206406.

[9] Frank C. Spano, *The Journal of Chemical Physics* **2005**, *122*(23), 234701.

[10] C. Scharsich, Florian S. U. Fischer, K. Wilma, R. Hildner, S. Ludwigs and A. Köhler, *Polymer Physics B* **2015**, *53*, 1416.

[11] Florian S. U. Fischer, Kim Tremel, A.-K. Saur, S. Link, Navaphun Kayunkid, Martin Brinkmann, D. Herrero-Carvajal, J. T. López Navarrete, M. C. Ruiz Delgado and Sabine Ludwigs, *Macromolecules* **2013**, *46*(12), 4924–4931.

[12] Florian S. U. Fischer, Daniel Trefz, Justus Back, Navaphun Kayunkid, Benjamin Tornow, Steve Albrecht, Kevin G. Yager, Gurpreet Singh, Alamgir Karim, Dieter Neher, Martin Brinkmann and Sabine Ludwigs, *Advanced Materials* **2015**, *27*, 1223–1228.

[13] Florian S. U. Fischer, N. Kayunkid, D. Trefz, S. Ludwigs and M. Brinkmann, *Macromolecules* **2015**, *48*, 3974.

[14] Steve Albrecht, Koen Vandewal, John R Tumbleston, Florian S. U. Fischer, Jessica D Douglas, Jean M J Fréchet, Sabine Ludwigs, Harald Ade, Alberto Salleo and Dieter Neher, *Advanced Materials* **2014**, *26*(16), 2533–9.

[15] Edward J. W. Crossland, Kim Tremel, Florian Fischer, Khosrow Rahimi, Günter Reiter, Ullrich Steiner and Sabine Ludwigs, *Advanced Materials* **2012**, *24*(6), 839–44.

[16] Florian S. U. Fischer, Kim Tremel, Michael Sommer, Edward J. W. Crossland and Sabine Ludwigs, *Nanoscale* **2012**, *4*(6), 2138–44.

[17] Jeffrey Peet, Nam Sung Cho, Sang Kyu Lee and Guillermo C. Bazan, *Macromolecules* **2008**, *41*(22), 8655–8659.

[18] C. K. Chiang, M. A. Druy, S. C. Gau, Alan J. Heeger, E. J. Louis, A. G. MacDiarmid, Y. W. Park and H. Shirakawa, *Journal of the American Chemical Society* **1978**, *100*, 1013–1015.

[19] C. Chiang, C. Fincher, Y. Park, Alan J. Heeger, H Shirakawa, E. Louis, S. Gau and Alan MacDiarmid, *Physical Review Letters* **1977**, *39*(17), 1098–1101.

[20] Hideki Shirakawa, Edwin J. Louis, Alan G. MacDiarmid, Chwan K. Chiang and Alan J. Heeger, *Journal of the Chemical Society, Chemical Communications* **1977**, *16*(16), 578.

[21] Hideki Shirakawa, *Angewandte Chemie* **2001**, *113*(14), 2642–2648.
[22] Alan J. Heeger, *Angewandte Chemie* **2001**, *113*(14), 2660–2682.
[23] Alan G. MacDiarmid, *Angewandte Chemie* **2001**, *113*(14), 2649–2659.
[24] Hae Jung Son, Feng He, Bridget Carsten and Luping Yu, *Journal of Materials Chemistry* **2011**, *21*, 18934.
[25] Kim Tremel, Florian S. U. Fischer, Navaphun Kayunkid, Riccardo Di Pietro, Roman Tkachov, Anton Kiriy, Dieter Neher, Sabine Ludwigs and Martin Brinkmann, *Advanced Energy Materials* **2014**, *4*(10), doi: 10.1002/aenm.201301659.
[26] Peter K. H. Ho, Ji-Seon Kim, Nir Tessler and Richard H. Friend, *The Journal of Chemical Physics* **2001**, *115*(6), 2709.
[27] Alan J. Heeger, *Advanced Materials* **2014**, *26*(1), 10–27.
[28] Marcel Schubert, Daniel Dolfen, Johannes Frisch, Steffen Roland, Robert Steyrleuthner, Burkhard Stiller, Zhihua Chen, Ullrich Scherf, Norbert Koch, Antonio Facchetti and Dieter Neher, *Advanced Energy Materials* **2012**, *2*(3), 369–380.
[29] Matthias Rehahn, *Chemie in unserer Zeit* **2003**, *37*(1), 18–30.
[30] Jean Luc Bredas and G. Bryan Street, *Accounts of Chemical Research* **1985**, *18*(10), 309–315.
[31] Muhammad E. Abdelhamid, Anthony P. O'Mullane and Graeme a. Snook, *RSC Adv.* **2015**, *5*(15), 11611–11626.
[32] Takakazu Yamamoto, Kenichi Sanechika and Akio Yamamoto, *Journal of Polymer Science: Polymer Letters Edition* **1980**, *18*(1), 9–12.
[33] John W-P. Lin and Lesley P. Dudek, *Journal of Polymer Science: Polymer Chemistry Edition* **1980**, *18*(9), 2869–2873.
[34] M. Kobayashi, J. Chen, T.-C. Chung, F. Moraes, Alan J. Heeger and F. Wudl, *Synthetic Metals* **1984**, *9*(1), 77–86.
[35] Takakazu Yamamoto, Atsushi Morita, Tsukasa Maruyama, Zhen-hua Zhou, Takaki Kanbara and Kenichi Sanechika, *Polymer Journal* **1990**, *22*(2), 187–190.
[36] I. Colon and G. T. Kwiatkowski, *Journal of Polymer Science Part A: Polymer Chemistry* **1990**, *28*(2), 367–383.
[37] Kohei Tamao, Koji Sumitani and Makoto Kumada, *Journal of the American Chemical Society* **1972**, *94*(12), 4374–4376.
[38] K. Tamao, S. Kodama, I. Nakajima, M. Kumada, A. Minato and K. Suzuki, *Tetrahedron* **1982**, *38*(22), 3347–3354.
[39] Takakazu Yamamoto, Ken-ichi Sanechika and Akio Yamamoto, *Bulletin of the Chemical Society of Japan* **1983**, *56*(5), 1497–1502.
[40] R.L. Elsenbaumer, K.Y. Jen and R. Oboodi, *Synthetic Metals* **1986**, *15*(2-3), 169–174.
[41] Kwan-Yue Jen, G. G. Miller and Ronald L. Elsenbaumer, *Journal of the Chemical Society, Chemical Communications* **1986**, *17*(17), 1346.
[42] K. Y. Jen, R. Oboodi and R. L. Elsenbaumer, *Polymeric Materials Science and Engineering* **1985**, *53*, 79–83.
[43] X.M. Jiang, R. Österbacka, O. Korovyanko, C.P. An, B. Horovitz, René A. J. Janssen and Z.V. Vardeny, *Advanced Functional Materials* **2002**, *12*, 587–597.
[44] Ralf Mauer, Marcel Kastler and Frédéric Laquai, *Advanced Functional Materials* **2010**, *20*(13), 2085–2092.

[45] Yi-Kang Lan, Cheng Han Yang and Hsiao-Ching Yang, *Polymer International* **2010**, *59*(1), 16–21.
[46] C. W. Tang, *Applied Physics Letters* **1986**, *48*(2), 183.
[47] G. Yu, J. Gao, J. C. Hummelen, F. Wudl and A. J. Heeger, *Science* **1995**, *270*(5243), 1789–1791.
[48] W. Ma, C. Yang, X. Gong, K. Lee and Alan J. Heeger, *Advanced Functional Materials* **2005**, *15*(10), 1617–1622.
[49] Kenji Kakiage, Yohei Aoyama, Toru Yano, Keiji Oya, Toru Kyomen and Minoru Hanaya, *Chemical communications* **2015**, *51*(29), 6315–7.
[50] Kim Tremel and Sabine Ludwigs, *P3HT Revisited - From Molecular Scale to Solar Cell Devices*, Springer, **2014**.
[51] National Renewable Energy Laboratory, AM 1.5G solar spectra, http://rredc.nrel.gov/solar/spectra/am1.5/astmg173/astmg173.html, online: 2015-04-20.
[52] W. Wiedemann, L. Sims, A. Abdellah, A. Exner, R. Meier, K. P. Musselman, J. L. MacManus-Driscoll, P. Müller-Buschbaum, G. Scarpa, P. Lugli and L. Schmidt-Mende, *Applied Physics Letters* **2010**, *96*(26), 263109.
[53] C. Groves, R. a Marsh and N. C. Greenham, *The Journal of chemical physics* **2008**, *129*(11), 114903.
[54] Oleksandr V. Mikhnenko, Hamed Azimi, Markus Scharber, Mauro Morana, Paul W. M. Blom and Maria Antonietta Loi, *Energy & Environmental Science* **2012**, *5*(5), 6960.
[55] Mauro Morana, Hamed Azimi, Gilles Dennler, Hans-Joachim Egelhaaf, Markus Scharber, Karen Forberich, Jens Hauch, Russell Gaudiana, David Waller, Zenghuo Zhu, Kurt Hingerl, Svetlana S. van Bavel, Joachim Loos and Christoph J. Brabec, *Advanced Functional Materials* **2010**, *20*(7), 1180–1188.
[56] Hai Wang, Hai-Yu Wang, Bing-Rong Gao, Lei Wang, Zhi-Yong Yang, Xiao-Bo Du, Qi-Dai Chen, Jun-Feng Song and Hong-Bo Sun, *Nanoscale* **2011**, *3*(5), 2280–5.
[57] Sung Heum Park, Anshuman Roy, Serge Beaupré, Shinuk Cho, Nelson Coates, Ji Sun Moon, Daniel Moses, Mario Leclerc, Kwanghee Lee and Alan J. Heeger, *Nature Photonics* **2009**, *3*(5), 297–302.
[58] Yu Gu, Cheng Wang and Thomas P. Russell, *Advanced Energy Materials* **2012**, *2*(6), 683.
[59] Jae Kwan Lee, Wan Li Ma, Christoph J. Brabec, Jonathan Yuen, Ji Sun Moon, Jin Young Kim, Kwanghee Lee, Guillermo C. Bazan and Alan J. Heeger, *Journal of the American Chemical Society* **2008**, *130*(11), 3619–23.
[60] Yuhang Liu, Jingbo Zhao, Zhengke Li, Cheng Mu, Wei Ma, Huawei Hu, Kui Jiang, Haoran Lin, Harald Ade and He Yan, *Nature Communications* **2014**, *5*(9), 5293.
[61] Huipeng Chen, Yu-Che Hsiao, Bin Hu and Mark Dadmun, *Advanced Functional Materials* **2014**, *24*(32), 5129–5136.
[62] Bobak Gholamkhass and Peyman Servati, *Organic Electronics* **2013**, *14*(9), 2278–2283.
[63] Haowei Tang, Guanghao Lu, Ligui Li, Jun Li, Yuzhen Wang and Xiaoniu Yang, *Journal of Materials Chemistry* **2010**, *20*(4), 683.
[64] Johannes Frisch, Marcel Schubert, Eduard Preis, Jürgen P. Rabe, Dieter Neher, Ullrich Scherf and Norbert Koch, *Journal of Materials Chemistry* **2012**, *22*(10), 4418.
[65] Xie Lin, Jeesoo Seok, Soyeon Yoon, Taehee Kim, BongSoo Kim and Kyungkon Kim, *Synthetic Metals* **2014**, *196*, 145–150.

[66] Dario Natali and Mario Caironi, *Advanced Materials* **2012**, *24*(11), 1357–87.
[67] G. Gritzner and J. Kuta, *Pure and Applied Chemistry* **1982**, *54*(8), 461–466.
[68] Jörn Pommerehne, Horst Vestweber, Werner Guss, Rainer F. Mahrt, Heinz Büssler, Michael Porsch and Jörg Daub, *Advanced Materials* **1995**, *7*(6), 551–554.
[69] Henning Sirringhaus, P. J. Brown, Richard H. Friend, M. M. Nielsen, K. Bechgaard, B. M. W. Langeveld-Voss, A. J. H. Spiering, René A. J. Janssen, E. W. Meijer, P. Herwig and D. M. de Leeuw, *Nature* **1999**, *401*(6754), 685–688.
[70] Leslie H. Jimison, Michael F. Toney, Iain McCulloch, Martin Heeney and Alberto Salleo, *Advanced Materials* **2009**, *21*(16), 1568–1572.
[71] R. Joseph Kline, Michael D. McGehee, Ekaterina N. Kadnikova, Jinsong Liu, Jean M. J. Fréchet and Michael F. Toney, *Macromolecules* **2005**, *38*(8), 3312–3319.
[72] A. Zen, J. Pflaum, S. Hirschmann, W. Zhuang, F. Jaiser, U. Asawapirom, J. P. Rabe, U. Scherf and Dieter Neher, *Advanced Functional Materials* **2004**, *14*(8), 757–764.
[73] P. Phillips, *Reports on Progress in Physics* **1999**, *53*(5), 549–604.
[74] Gert R. Strobl, *The Physics of Polymers*, Springer, **1996**.
[75] Jean-Marie Verilhac, Gilles LeBlevennec, David Djurado, François Rieutord, Mustapha Chouiki, Jean-Pierre Travers and Adam Pron, *Synthetic Metals* **2006**, *156*(11-13), 815–823.
[76] Jui-Fen Chang, Baoquan Sun, Dag W. Breiby, Martin M. Nielsen, Theis I. Sölling, Mark Giles, Iain McCulloch and Henning Sirringhaus, *Chemistry of Materials* **2004**, *16*(23), 4772–4776.
[77] Rui Zhang, Bo Li, Mihaela C Iovu, Malika Jeffries-El, Geneviève Sauvé, Jessica Cooper, Shijun Jia, Stephanie Tristram-Nagle, Detlef M Smilgies, David N Lambeth, Richard D. McCullough and Tomasz Kowalewski, *Journal of the American Chemical Society* **2006**, *128*(11), 3480–3481.
[78] Rodrigo Noriega, Jonathan Rivnay, Koen Vandewal, Felix P V Koch, Natalie Stingelin, Paul Smith, Michael F. Toney and Alberto Salleo, *Nature Materials* **2013**, *12*(11), 1038–44.
[79] Martin Brinkmann and Patrice Rannou, *Macromolecules* **2009**, *42*(4), 1125–1130.
[80] Lucia Hartmann, Kim Tremel, Sureeporn Uttiya, Edward J. W. Crossland, Sabine Ludwigs, Navaphun Kayunkid, Christelle Vergnat and Martin Brinkmann, *Advanced Functional Materials* **2011**, *21*(21), 4047–4057.
[81] Mukti Aryal, Krutarth Trivedi and Wenchuang Walter Hu, *ACS Nano* **2009**, *3*(10), 3085–90.
[82] Jiangang Liu, Yue Sun, Xiang Gao, Rubo Xing, Lidong Zheng, Shupeng Wu, Yanhou Geng and Yanchun Han, *Langmuir* **2011**, *27*(7), 4212–9.
[83] Edward J. W. Crossland, Khosrow Rahimi, Günter Reiter, Ullrich Steiner and Sabine Ludwigs, *Advanced Functional Materials* **2011**, *21*(3), 518–524.
[84] Frank C Spano, *Accounts of Chemical Research* **2010**, *43*(3), 429–39.
[85] Edwards T. Niles, John D. Roehling, Hajime Yamagata, Adam J. Wise, Frank C. Spano, Adam J. Moulé and John K. Grey, *The Journal of Physical Chemistry Letters* **2012**, *3*(2), 259–263.
[86] Robin M. Hochstrasser and Michael Kasha, *Photochemistry and Photobiology* **1964**, *3*(4), 317–331.
[87] Michael Kasha, *Radiation Research* **1963**, *20*(1), 55.
[88] J. Franck and E. G. Dymond, *Transactions of the Faraday Society* **1926**, *21*, 536.
[89] Edward Condon, *Physical Review* **1926**, *28*(6), 1182–1201.

[90] Heinz Bässler and Bernd Schweitzer, *Accounts of Chemical Research* **1999**, *32*(2), 173–182.
[91] Frank C Spano, Jenny Clark, Carlos Silva and Richard H. Friend, *The Journal of chemical physics* **2009**, *130*(7), 074904.
[92] Christina Scharsich, Ruth H. Lohwasser, Michael Sommer, Udom Asawapirom, Ullrich Scherf, Mukundan Thelakkat, Dieter Neher and Anna Köhler, *Journal of Polymer Science Part B: Polymer Physics* **2012**, *50*(6), 442–453.
[93] Anna Köhler, Sebastian T Hoffmann and Heinz Bässler, *Journal of the American Chemical Society* **2012**, *134*(28), 11594–601.
[94] Frank C Spano, *Chemical Physics Letters* **2000**, *331*(1), 7–13.
[95] Fernando B Dias, Jorge Morgado, António L. Maçanita, Fernando P. da Costa, Hugh D Burrows and Andrew P Monkman, *Macromolecules* **2006**, *39*(17), 5854–5864.
[96] Yi-Kang Lan and Ching-I Huang, *The Journal of Physical Chemistry B* **2009**, *113*(44), 14555–64.
[97] Gianni Zotti, Gilberto Schiavon, Anna Berlin, Giovanni Fontana and Giorgio Pagani, *Macromolecules* **1994**, *27*(7), 1938–1942.
[98] A. Dhanabalan, J. K. J. van Duren, P. A. van Hal, J. L. J. van Dongen and R. A. J. Janssen, *Advanced Functional Materials* **2001**, *11*(4), 255–262.
[99] Zhengguo Zhu, David Waller, Russell Gaudiana, Mauro Morana, David Mühlbacher, Markus Scharber and Christoph J. Brabec, *Macromolecules* **2007**, *40*(6), 1981–1986.
[100] Swaminathan Venkatesan, Jihua Chen, Evan C. Ngo, Ashish Dubey, Devendra Khatiwada, Cheng Zhang and Qiquan Qiao, *Nano Energy* **2014**, *12*, 457–467.
[101] P.G. Karagiannidis, S. Kassavetis, C. Pitsalidis and S. Logothetidis, *Thin Solid Films* **2011**, *519*(12), 4105–4109.
[102] Tiziano Agostinelli, Toby a. M. Ferenczi, E. Pires, Samuel Foster, Andrea Maurano, Christian Müller, Amy Ballantyne, Mark Hampton, Samuele Lilliu, Mariano Campoy-Quiles, Hamed Azimi, Mauro Morana, Donal D. C. Bradley, James Durrant, J. Emyr Macdonald, Natalie Stingelin and Jenny Nelson, *Journal of Polymer Science Part B: Polymer Physics* **2011**, *49*(10), 717–724.
[103] Robert C. Coffin, Jeffrey Peet, James T. Rogers and Guillermo C. Bazan, *Nature Chemistry* **2009**, *1*(8), 657–61.
[104] Suhao Wang, Michael Kappl, Ingo Liebewirth, Maren Müller, Katrin Kirchhoff, Wojciech Pisula and Klaus Müllen, *Advanced Materials* **2011**, *24*(3), 417–420.
[105] Hoi Nok Tsao, Don M Cho, Insun Park, Michael Ryan Hansen, Alexey Mavrinskiy, Do Y Yoon, Robert Graf, Wojciech Pisula, Hans Wolfgang Spiess and Klaus Müllen, *Journal of the American Chemical Society* **2011**, *133*(8), 2605–12.
[106] Dorota Niedzialek, Vincent Lemaur, Dmytro Dudenko, Jie Shu, Michael Ryan Hansen, Jens Wenzel Andreasen, Wojciech Pisula, Klaus Müllen, Jérôme Cornil and David Beljonne, *Advanced Materials* **2013**, *25*(13), 1939–47.
[107] Fabian Etzold, Ian A Howard, Nina Forler, Don M Cho, Michael Meister, Hannah Mangold, Jie Shu, Michael Ryan Hansen, Klaus Müllen and Frédéric Laquai, *Journal of the American Chemical Society* **2012**, *134*(25), 10569–83.
[108] James T. Rogers, Kristin Schmidt, Michael F. Toney, Edward J. Kramer and Guillermo C. Bazan, *Advanced Materials* **2011**, *23*(20), 2284–8.
[109] Koen Vandewal, Steve Albrecht, Eric T. Hoke, Kenneth R. Graham, Johannes Widmer, Jessica D. Douglas, Marcel Schubert, William R. Mateker, Jason T. Bloking, George F.

Burkhard, Alan Sellinger, Jean M. J. Fréchet, Aram Amassian, Moritz K. Riede, Michael D. McGehee, Dieter Neher and Alberto Salleo, *Nature Materials* **2014**, *13*(1), 63–8.

[110] Umut Aygül, David Batchelor, Ulf Dettinger, Seyfullah Yilmaz, Sybille Allard, Ullrich Scherf, Heiko Peisert and Thomas Chassé, *The Journal of Physical Chemistry C* **2012**, *116*(7), 4870–4874.

[111] Ergang Wang, Li Wang, Linfeng Lan, Chan Luo, Wenliu Zhuang, Junbiao Peng and Yong Cao, *Applied Physics Letters* **2008**, *92*(3), 033307.

[112] Hsiang-Yu Chen, Jianhui Hou, Amy E Hayden, Hoichang Yang, K N Houk and Yang Yang, *Advanced Materials* **2010**, *22*(3), 371–5.

[113] Markus C Scharber, Markus Koppe, Jia Gao, Fabrizio Cordella, Maria A Loi, Patrick Denk, Mauro Morana, Hans-Joachim Egelhaaf, Karen Forberich, Gilles Dennler, Russ Gaudiana, Dave Waller, Zhengguo Zhu, Xiaobo Shi and Christoph J. Brabec, *Advanced Materials* **2010**, *22*(3), 367–70.

[114] Yongxi Li, Jingyu Zou, Hin-Lap Yip, Chang-Zhi Li, Yong Zhang, Chu-Chen Chueh, Jeremy Intemann, Yunxiang Xu, Po-Wei Liang, Yu Chen and Alex K.-Y. Jen, *Macromolecules* **2013**, *46*(14), 5497–5503.

[115] David Nečas and Petr Klapetek, *Central European Journal of Physics* **2011**, *10*(1), 181–188.

[116] David B. Williams and C. Barry Carter, *Transmission Electron Microscopy*, Springer, **2009**.

[117] C. Geskes and J. Heinze, *Journal of Electroanalytical Chemistry* **1996**, *418*, 167–176.

[118] Chan Luo, Aung Ko Ko Kyaw, Louis a Perez, Shrayesh Patel, Ming Wang, Bruno Grimm, Guillermo C. Bazan, Edward J Kramer and Alan J. Heeger, *Nano Letters* **2014**.

[119] Masaki Horie, Jeff Kettle, Chin-Yang Yu, Leszek A. Majewski, Shu-Wei Chang, James Kirkpatrick, Sachetan M. Tuladhar, Jenny Nelson, Brian R. Saunders and Michael L. Turner, *Journal of Materials Chemistry* **2012**, *22*(2), 381–389.

[120] R. Street, Sarah Cowan and Alan J. Heeger, *Physical Review B - Condensed Matter and Materials Physics* **2010**, *82*(12), 121301.

[121] Qingshuo Wei, Kazuhito Hashimoto and Keisuke Tajima, *ACS applied materials & interfaces* **2011**, *3*(2), 139–42.

[122] Chang Hyun Kim, Yvan Bonnassieux and Gilles Horowitz, *IEEE Transactions on Electron Devices* **2013**, *60*(1), 280–287.

[123] Hagen Klauk, *Chemical Society reviews* **2010**, *39*(7), 2643–66.

[124] Natalie Banerji, Sarah Cowan, Mario Leclerc, Eric Vauthey and Alan J. Heeger, *Journal of the American Chemical Society* **2010**, *132*(49), 17459–70.

[125] Ian A Howard, Ralf Mauer, Michael Meister and Frédéric Laquai, *Journal of the American Chemical Society* **2010**, *132*(42), 14866–76.

[126] Jiamo Guo, Hideo Ohkita, Hiroaki Benten and Shinzaburo Ito, *Journal of the American Chemical Society* **2010**, *132*(17), 6154–64.

[127] Steve Albrecht, Sebastian Schäfer, Ilja Lange, Seyfullah Yilmaz, Ines Dumsch, Sybille Allard, Ullrich Scherf, Andreas Hertwig and Dieter Neher, *Organic Electronics* **2012**, *13*(4), 615–622.

[128] Juliane Kniepert, Marcel Schubert, James C. Blakesley and Dieter Neher, *The Journal of Physical Chemistry Letters* **2011**, *2*(7), 700.

[129] Huipeng Chen, Sheng Hu, Huidong Zang, Bin Hu and Mark D. Dadmun, *Advanced Functional Materials* **2013**, *23*(13), 1701–1710.

[130] Xiaodan Gu, Ilja Gunkel, Alexander Hexemer, Weiyin Gu and Thomas P. Russell, *Advanced Materials* **2014**, *26*(2), 273–81.

[131] Sabine Ludwigs, Alexander Böker, Andrej Voronov, Nicolaus Rehse, Robert Magerle and Georg Krausch, *Nature Materials* **2003**, *2*(11), 744–7.

[132] Laure Biniek, Nicolas Leclerc, Thomas Heiser, Rony Bechara and Martin Brinkmann, *Macromolecules* **2013**, *46*(10), 4014–4023.

[133] Laure Biniek, Stéphanie Pouget, David Djurado, Eric Gonthier, Kim Tremel, Navaphun Kayunkid, Elena Zaborova, Nicolas Crespo-Monteiro, Olivier Boyron, Nicolas Leclerc, Sabine Ludwigs and Martin Brinkmann, *Macromolecules* **2014**, *47*(12), 3871–3879.

[134] Jean Claude Wittmann and Paul Smith, *Nature* **1991**, *352*(6334), 414–417.

[135] Martin Brinkmann, Sabine Graff, Christine Straupé, Jean-Claude Wittmann, Christian Chaumont, Frank Nuesch, Anver Aziz, Michel Schaer and Libero Zuppiroli, *The Journal of Physical Chemistry B* **2003**, *107*(38), 10531–10539.

[136] Hajime Yamagata and Frank C Spano, *The Journal of Chemical Physics* **2012**, *136*(18), 184901.

[137] Hajime Yamagata, Nicholas J Hestand, Frank C. Spano, Anna Köhler, Christina Scharsich, Sebastian T Hoffmann and Heinz Bässler, *The Journal of Chemical Physics* **2013**, *139*(11), 114903.

[138] Martin Brinkmann, Eric Gonthier, Stéfan Bogen, Kim Tremel, Sabine Ludwigs, Martin Hufnagel and Michael Sommer, *ACS Nano* **2012**, *6*(11), 10319–26.

[139] Robert Steyrleuthner, Marcel Schubert, Ian Howard, Bastian Klaumünzer, Kristian Schilling, Zhihua Chen, Peter Saalfrank, Frédéric Laquai, Antonio Facchetti and Dieter Neher, *Journal of the American Chemical Society* **2012**, *134*(44), 18303–17.

[140] Daniele Fazzi, Giulia Grancini, Margherita Maiuri, Daniele Brida, Giulio Cerullo and Guglielmo Lanzani, *Physical Chemistry Chemical Physics* **2012**, *14*(18), 6367–6374.

[141] J. Gierschner, J. Cornil and H. J. Egelhaaf, *Advanced Materials* **2007**, *19*(2), 173–191.

[142] William M. Haynes, *Handbook of Chemistry and Physics, 93rd Edition*, CRC Press Taylor & Francis Group, **2012**.

[143] Christian Reichardt and Thomas Welton, *Solvents and Solvent Effects in Organic Chemistry*, Wiley-VCH Verlag GmbH & Co. KGaA, Weinheim, Germany, **2010**.

[144] Christina Scharsich, *The influence of conformational order on the excited state of organic semiconductors*, Dissertation, Universität Bayreuth, 2015.

[145] Mark a Faist, Thomas Kirchartz, Wei Gong, Raja Shahid Ashraf, Iain McCulloch, John C de Mello, Nicholas J Ekins-Daukes, Donal D C Bradley and Jenny Nelson, *Journal of the American Chemical Society* **2012**, *134*(1), 685–692.

[146] Mauro Morana, Matthias Wegscheider, Alberta Bonanni, Nikos Kopidakis, Sean Shaheen, Markus Scharber, Zhengguo Zhu, David Waller, Russell Gaudiana and Christoph J. Brabec, *Advanced Functional Materials* **2008**, *18*(12), 1757–1766.

[147] Yoann Olivier, Dorota Niedzialek, Vincent Lemaur, Wojciech Pisula, Klaus Müllen, Unsal Koldemir, John R Reynolds, Roberto Lazzaroni, Jérôme Cornil and David Beljonne, *Advanced Materials* **2014**, *26*(14), 2119–36.

[148] Martin Brinkmann and J.-C. Wittmann, *Advanced Materials* **2006**, *18*(7), 860–863.

[149] Daniel Trefz, *Morphologie von F-PCPDTBT Low Bandgap Polymers*, Diplomarbeit am Institut für Polymerchemie, Universität Stuttgart, 2013.

[150] Matthias Jasch, *Morphologiecharakterisierung von Si-PCPDTBT-Filmen*, Diplomarbeit am Institut für Polymerchemie, Universität Stuttgart, 2012.
[151] Steve Miller, Giovanni Fanchini, Yun-Yue Lin, Cheng Li, Chun-Wei Chen, Wei-Fang Su and Manish Chhowalla, *Journal of Materials Chemistry* **2008**, *18*(3), 306.
[152] Eric Verploegen, Chad E. Miller, Kristin Schmidt, Zhenan Bao and Michael F. Toney, *Chemistry of Materials* **2012**, *24*(20), 3923–3931.
[153] Soojin Park, Bokyung Kim, Ji Xu, Tommy Hofmann, Benjamin M. Ocko and Thomas P. Russell, *Macromolecules* **2009**, *42*(4), 1278–1284.
[154] Martin Brinkmann, *Macromolecules* **2007**, *40*(21), 7532–7541.
[155] Martin Brinkmann, Lucia Hartmann, Laure Biniek, Kim Tremel and Navaphun Kayunkid, *Macromolecular Rapid Communications* **2014**, *35*(1), 9–26.
[156] Th. Hahn (Hrsg.), *International Tables for Crystallography*, Band 50, Springer Netherlands, Chester, England, **1986**.
[157] Shu-Wei Chang, Huw Waters, Jeff Kettle and Masaki Horie, *Organic Electronics* **2012**, *13*(12), 2967–2974.
[158] Florian Kanal, Stefan Ruetzel, Han Lu, Michael Moos, Marco Holzapfel, Tobias Brixner and Christoph Lambert, *The Journal of Physical Chemistry C* **2014**, *118*(41), 23586–23598.
[159] Christian Wiebeler, Raphael Tautz, Jochen Feldmann, Elizabeth von Hauff, Enrico Da Como and Stefan Schumacher, *The Journal of Physical Chemistry B* **2012**.
[160] C Kvarnström, H Neugebauer, A. Ivaska and N. S. Sariciftci, *Journal of Molecular Structure* **2000**, *521*, 271.
[161] Daniele Di Nuzzo, Daniele Viola, Florian S. U. Fischer, Giulio Cerullo, Sabine Ludwigs and Enrico Da Como, *The Journal of Physical Chemistry Letters* **2015**, *6*(7), 1196–1203.
[162] Ann-Kathrin Saur, *Spektroelektrochemie von Donor-Akzeptor Systemen*, Diplomarbeit am Institut für Polymerchemie, Universität Stuttgart, 2012.
[163] Magdalena Skompska and Artur Szkurlat, *Electrochimica Acta* **2001**, *46*(26-27), 4007–4015.
[164] Andrey E Boguslavskiy, Jochen Mikosch, Arjan Gijsbertsen, Michael Spanner, Serguei Patchkovskii, Niklas Gador, Marc J J Vrakking and Albert Stolow, *Science* **2012**, *335*(6074), 1336–40.
[165] G. Grancini, M. Maiuri, D. Fazzi, A. Petrozza, H.-J. Egelhaaf, D. Brida, G. Cerullo and G. Lanzani, *Nature Materials* **2013**, *12*(1), 29–33.
[166] Steve Albrecht, *Generation, Recombination and Extraction of Charges in Polymer:Fullerene Bulk Heterojunction Solar Cells*, Dissertation, Cumulative, Universität Potsdam, 2014.
[167] Haiyang Wang, Yaozhuo Xu, Xinhong Yu, Rubo Xing, Jiangang Liu and Yanchun Han, *Polymers* **2013**, *5*(4), 1272–1324.
[168] Florian S. U. Fischer, G. L. Schulz, Daniel Trefz, A. Melnyk, Martin Brinkmann, D. Andrienko and Sabine Ludwigs, A family of PCPDTBT derivatives: correlations between polymer morphology and transport properties in organic field-effect transistors, submitted, 2015.
[169] Ulrich Hörmann, Christopher Lorch, Alexander Hinderhofer, Alexander Gerlach, Mark Gruber, Julia Kraus, Benedikt Sykora, Stefan Grob, Theresa Linderl, Andreas Wilke, Andreas Opitz, Rickard Hansson, Ana Sofia Anselmo, Yusuke Ozawa, Yasuo Nakayama, Hisao Ishii, Norbert Koch, Ellen Moons, Frank Schreiber and Wolfgang Brütting, *The Journal of Physical Chemistry C* **2014**, *118*(46), 26462–26470.

[170] Keiichirou Yonezawa, Alexander Hinderhofer, Takuya Hosokai, Kengo Kato, Rintaro Makino, Frank Schreiber, Nobuo Ueno and Satoshi Kera, *Advanced Materials Interfaces* **2014**, *1*(5), doi: 10.1002/admi.201400004.

[171] Fu-Ching Tang, Fu-Chiao Wu, Chia-Te Yen, Jay Chang, Wei-Yang Chou, Shih-Hui Gilbert Chang and Horng-Long Cheng, *Nanoscale* **2014**, *7*(1), 104–12.

[172] Yao-Tsung Fu, Demetrio a. da Silva Filho, Gjergji Sini, Abdullah M. Asiri, Saadullah Gary Aziz, Chad Risko and Jean-Luc Brédas, *Advanced Functional Materials* **2014**, *24*(24), 3790–3798.

[173] Robert Steyrleuthner, Riccardo Di Pietro, Brian A Collins, Frank Polzer, Scott Himmelberger, Marcel Schubert, Zhihua Chen, Shiming Zhang, Alberto Salleo, Harald Ade, Antonio Facchetti and Dieter Neher, *Journal of the American Chemical Society* **2014**, *136*(11), 4245–56.

[174] J. Catalán and P. Pérez, *Fullerenes, Nanotubes and Carbon Nanostructures* **2002**, *10*(2), 171–180.

[175] Thomas J. K. Brenner, Zhe Li and Christopher R. McNeill, *The Journal of Physical Chemistry C* **2011**, *115*(44), 22075.

[176] George F. Burkhard, Eric T. Hoke, Zach M. Beiley and Michael D. McGehee, *The Journal of Physical Chemistry C* **2012**, *116*(50), 26674.

[177] Yi Yang, Kamil Mielczarek, Anvar Zakhidov and Walter Hu, *ACS Applied Materials & Interfaces* **2014**, *6*(21), 19282–19287.

[178] George M Sheldrick, *Acta crystallographica. Section A, Foundations of crystallography* **2008**, *64*(Pt 1), 112–22.

[179] Miquel Planells, Bob C Schroeder and Iain McCulloch, *Macromolecules* **2014**, *47*, 5889.

A Appendix

A.1 Substrates

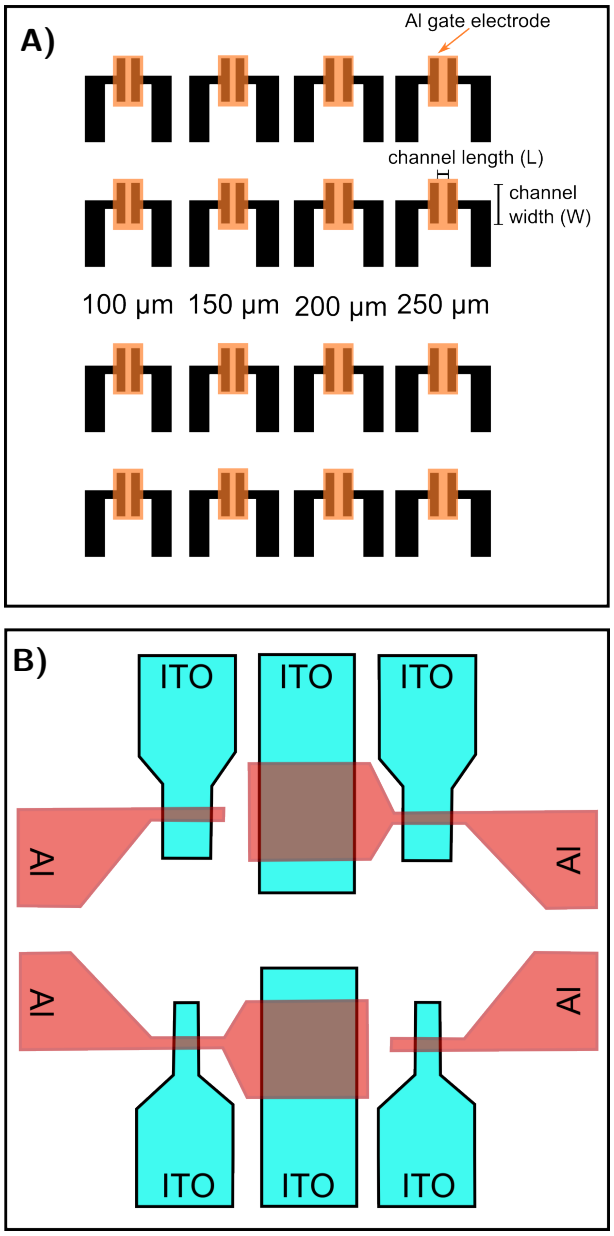

Fig. A.1: A) Layout of the bottom-contact (Au, black), top-gate (Al, orange) transistors with channel lengths between 100 to $250\,\mu\mathrm{m}$ and a channel width of $1\,\mathrm{mm}$. **B)** Layout of the bottom- and top-electrodes used for the preparation of solar cells. Each substrate includes 6 active areas defined by the overlap of ITO structure (cyan) and the evaporated Aluminum top-electrodes (red).

A.2 Absorption and PL in Solution

PCPDTBT

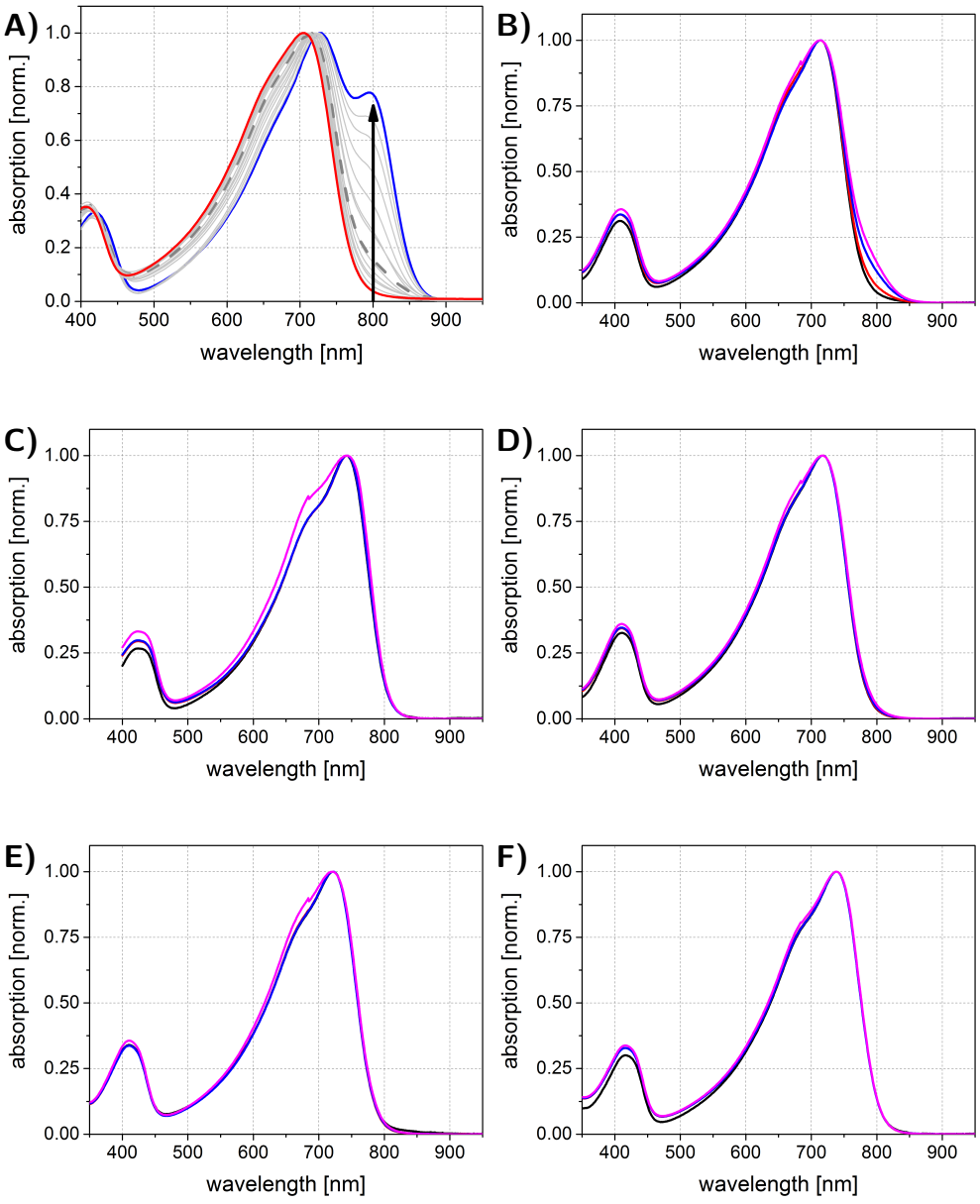

Fig. A.2: A) Temperature-dependent absorption spectra of $3\,\mathrm{mg/ml}$ PCPDTBT in THF in the temperature range between $-20\,^{\circ}\mathrm{C}$ (blue) and $55\,^{\circ}\mathrm{C}$ (red) in steps of $5\,\mathrm{K}$ (gray). **B-F)** Absorption spectra of PCPDTBT in THF (B), CS_2 (C), $CHCl_3$ (D), CB (E) and 1-CN (F) each at four different concentrations $0.01\,\mathrm{mg/ml}$ (black), $0.1\,\mathrm{mg/ml}$ (red), $1\,\mathrm{mg/ml}$ (blue) and $3\,\mathrm{mg/ml}$ (pink).

F-PCPDTBT

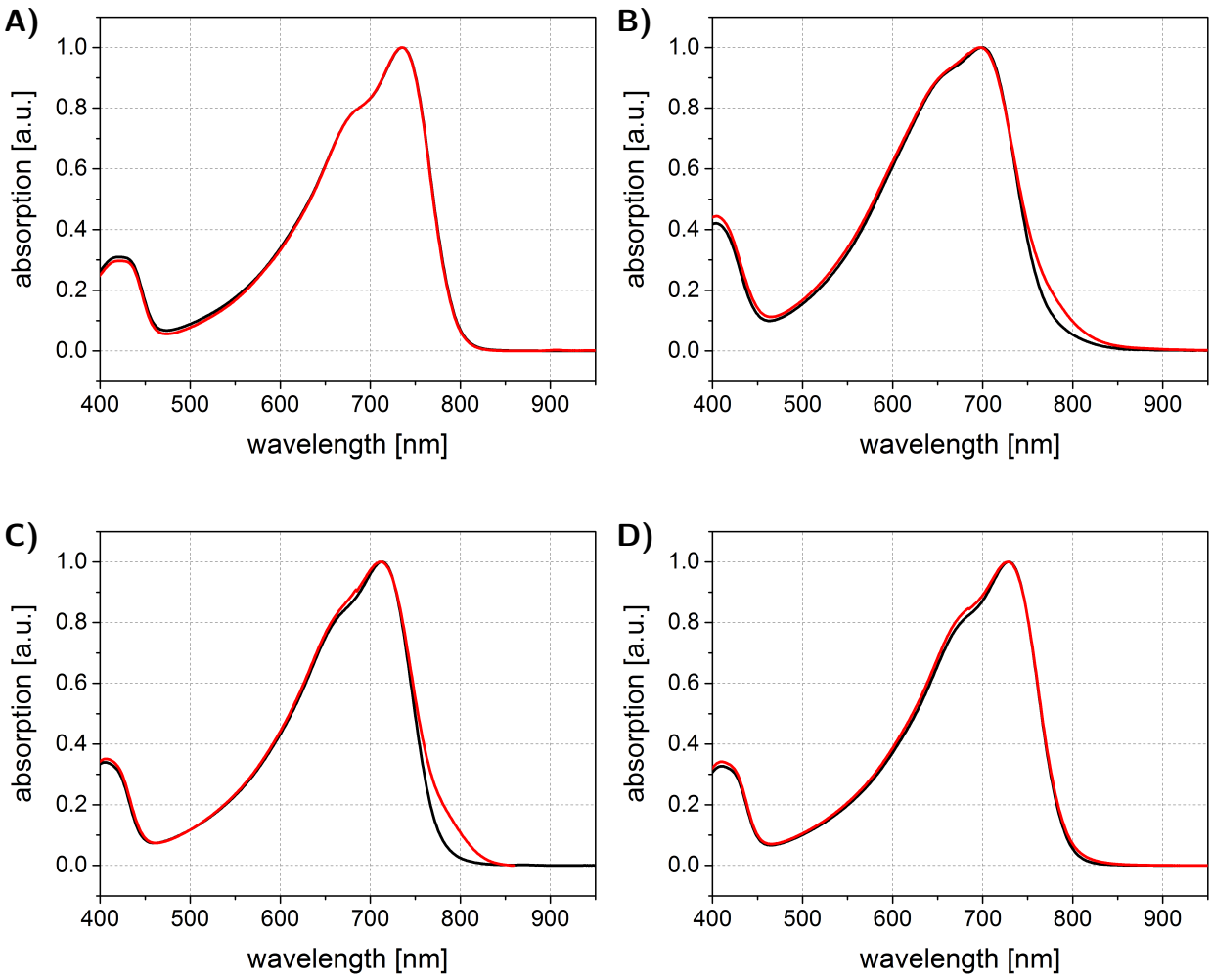

Fig. A.3: A-D) Absorption spectra of F-PCPDTBT in CS_2 (A), THF (B), CB (C) and 1-CN (D); each at two different concentrations $0.01\,\mathrm{mg/ml}$ (black) and $3\,\mathrm{mg/ml}$ (red).

A.3 Raman Spectroscopy

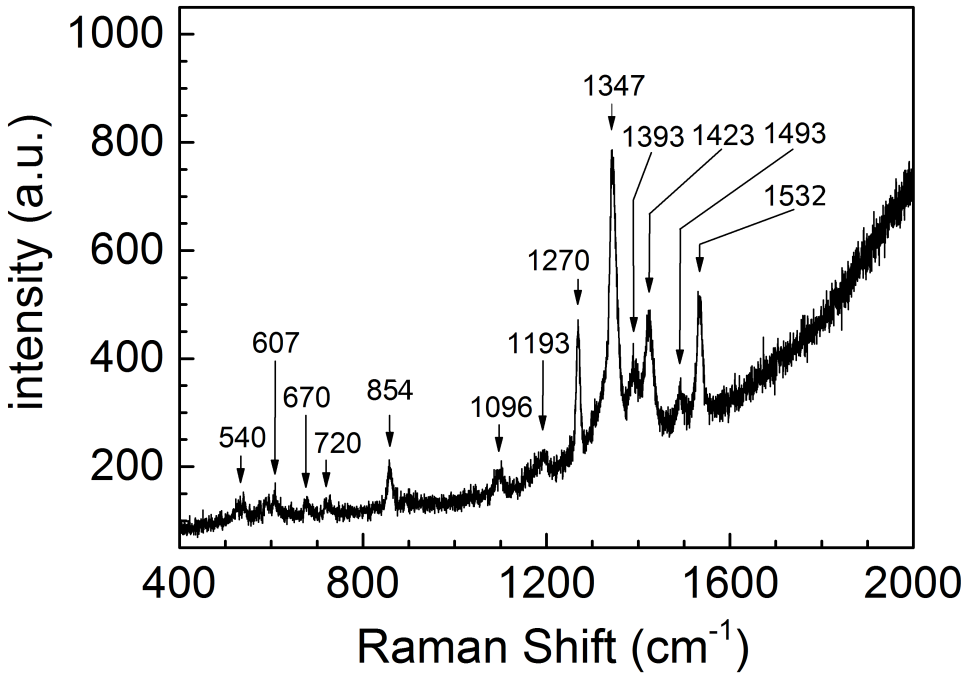

Fig. A.4: Raman spectrum of a PCPDTBT thin film spin coated from $CHCl_3$ on a SiO_x-substrate (adapted from[10]).

A.4 Thin Films

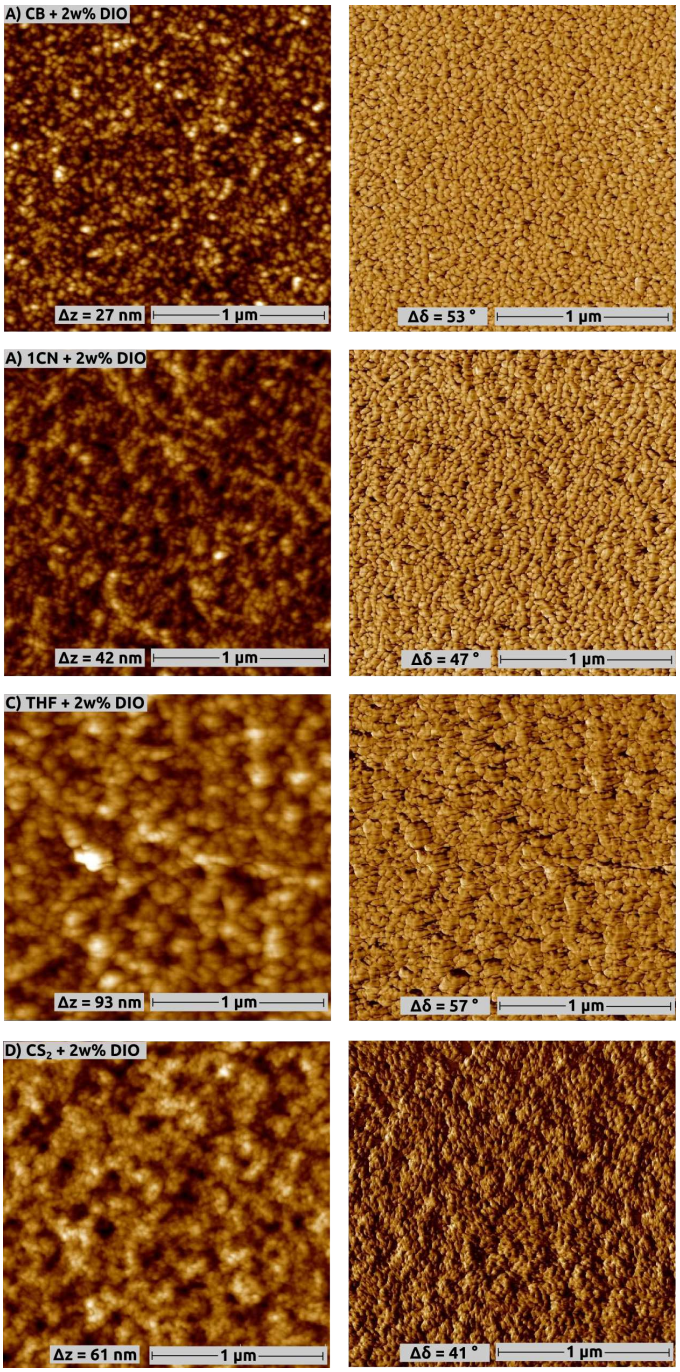

Fig. A.5: Height- (left) and Phase- (right) AFM images of PCPDTBT films on Si-wafer after spin coated from $3\,\mathrm{mg/ml}$ CB (A), 1-CN (B), THF (C) and CS_2 (D) solutions with $2\,\mathrm{w\%}$ DIO as solvent additive.

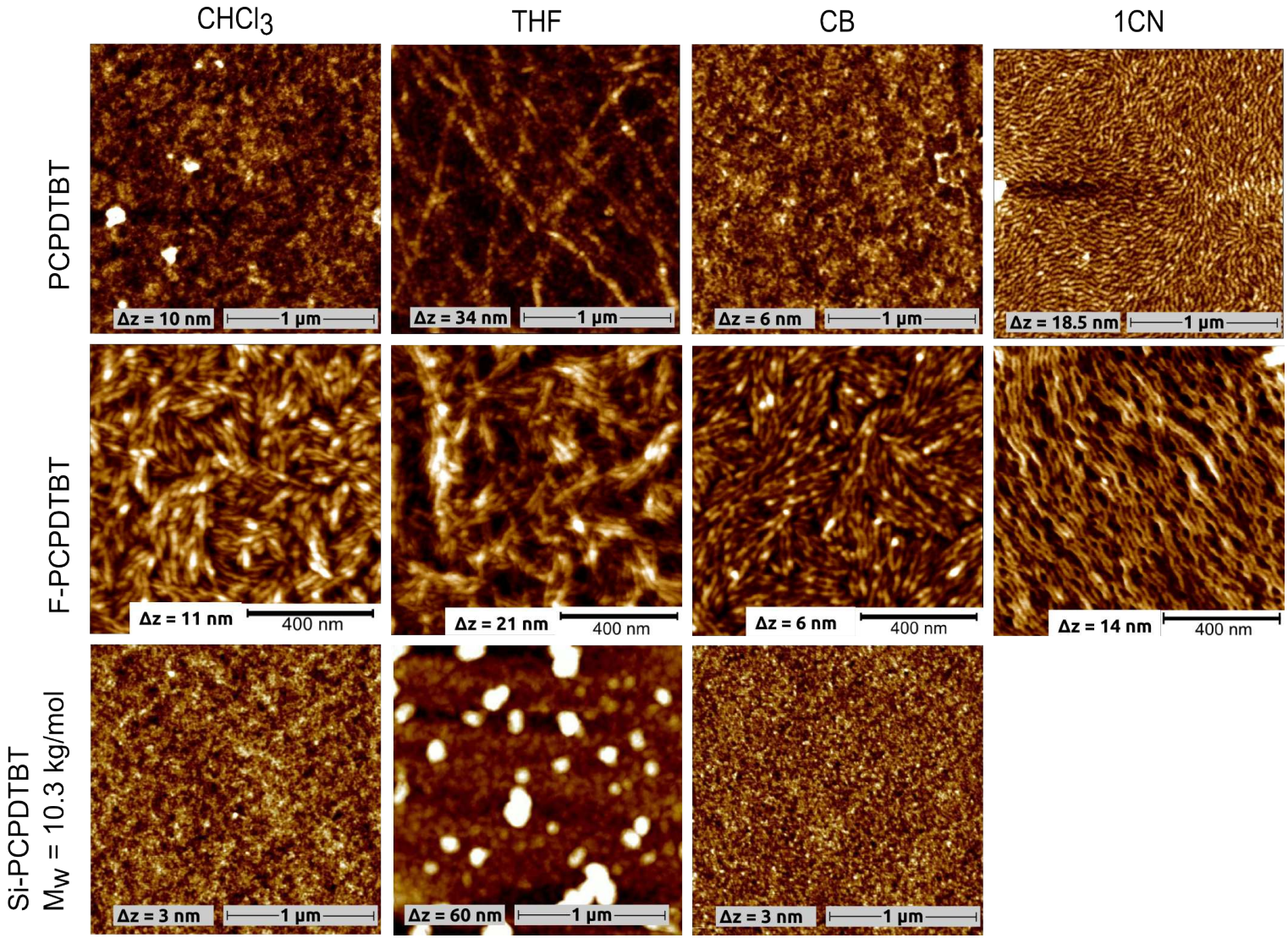

Fig. A.6: AFM height images of thin Si-/F-PCPDTBT films prepared by spin coating from different solvents.

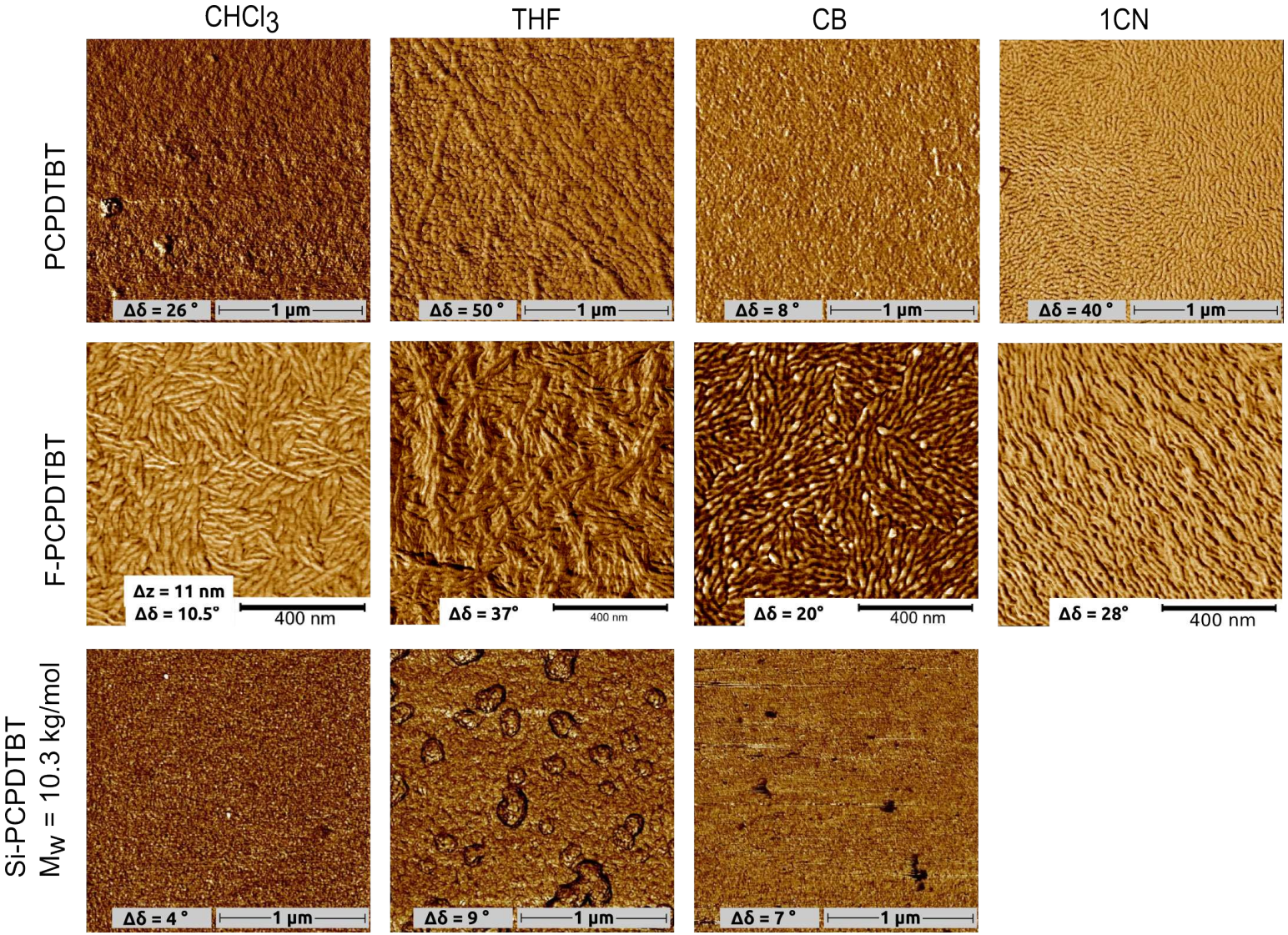

Fig. A.7: AFM phase images of thin Si-/F-PCPDTBT films prepared by spin coating from different solvents.

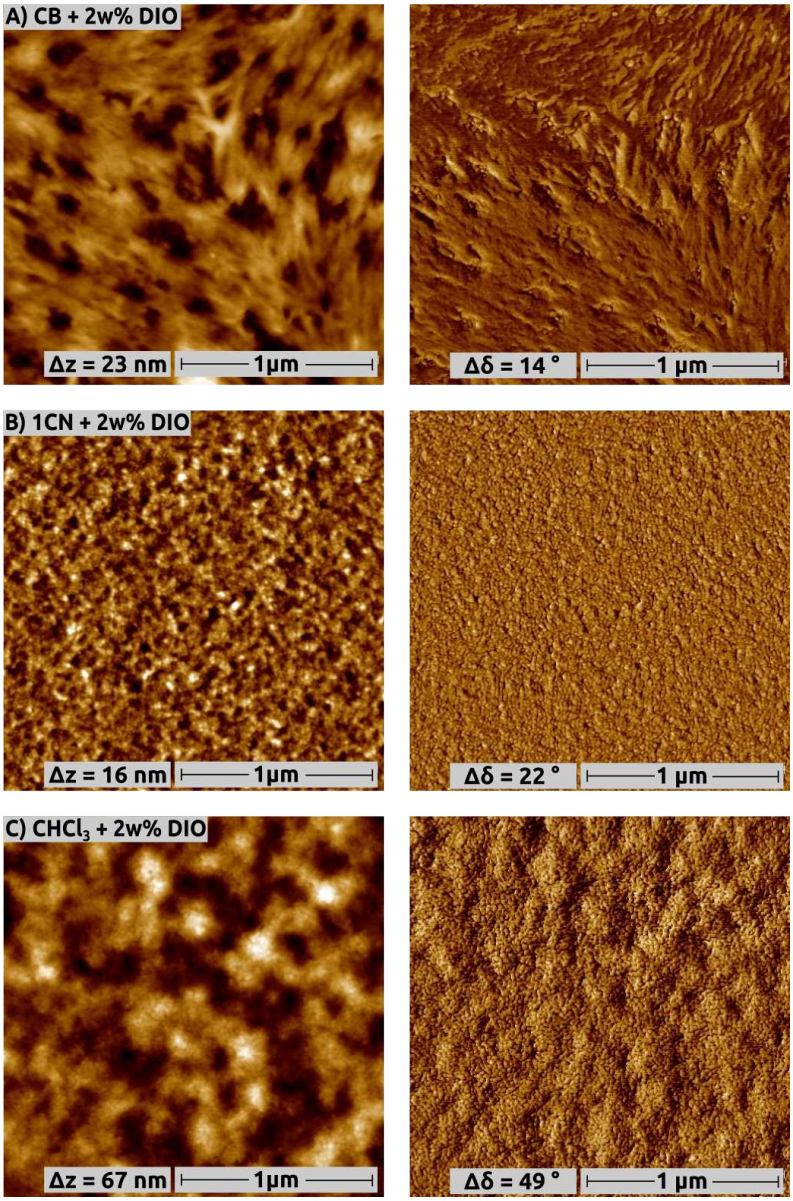

Fig. A.8: AFM height- (left) and phase- (right) images of F-PCPDTBT films on Si-wafer prepared by spin coating from $3\,\mathrm{mg/ml}$ CB (A), 1CN (B) and $CHCl_3$ (C) solutions with $2\,\mathrm{w\%}$ DIO added as solvent additive.

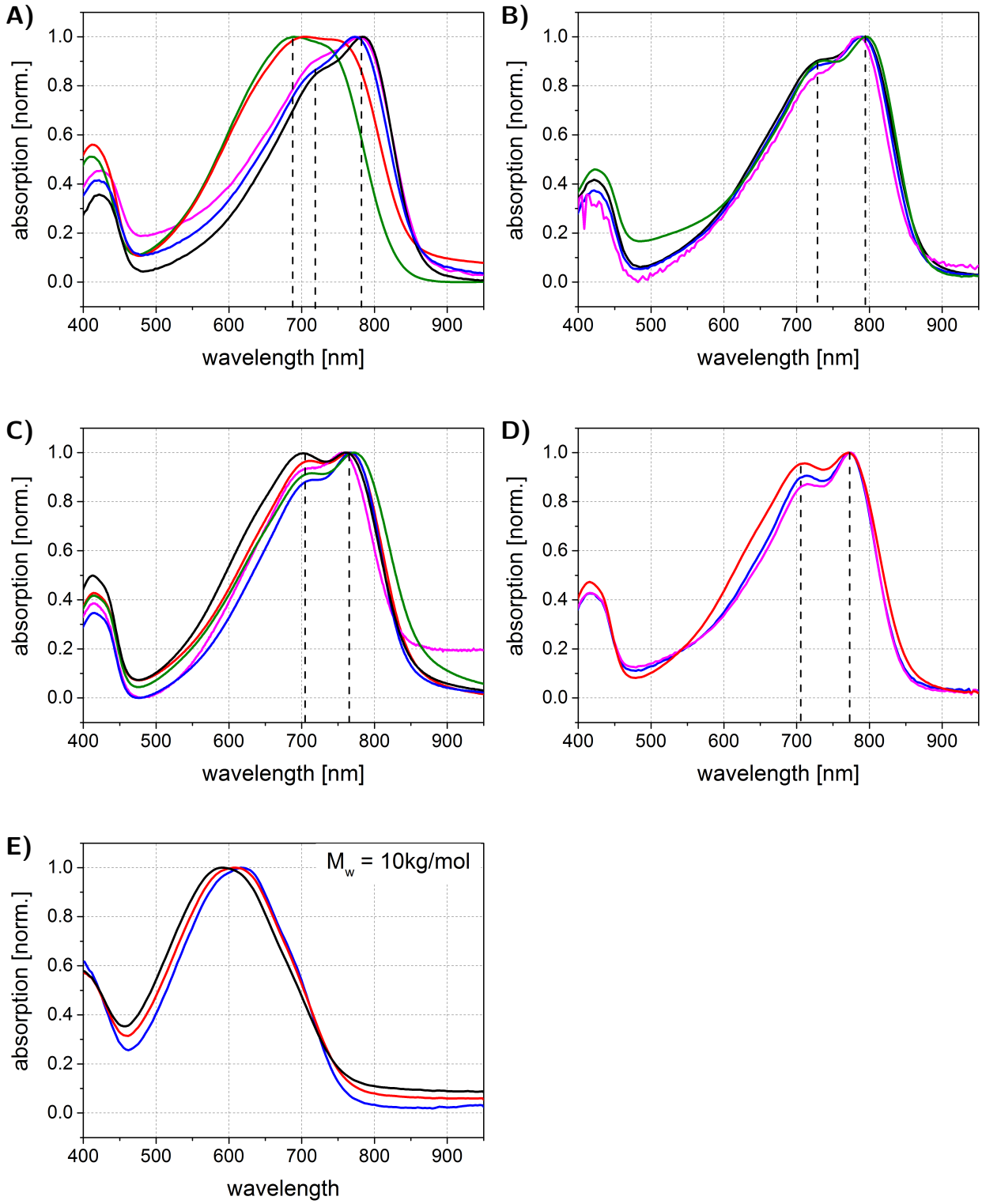

Fig. A.9: Absorption spectra of thin PCPDTBT (A, B), F-PCPDTBT (C, D) and Si-PCPDTBT (E, M_w=10 kg/mol) films prepared by spin coating from 3 mg/ml solutions of THF (black), $CHCl_3$ (red), CB (blue), 1-CN (pink) and CS_2 (green) without (A, C, E) and with (B, D) 2 w% of the solvent additive DIO.

A.5 Solvent Vapor Annealing

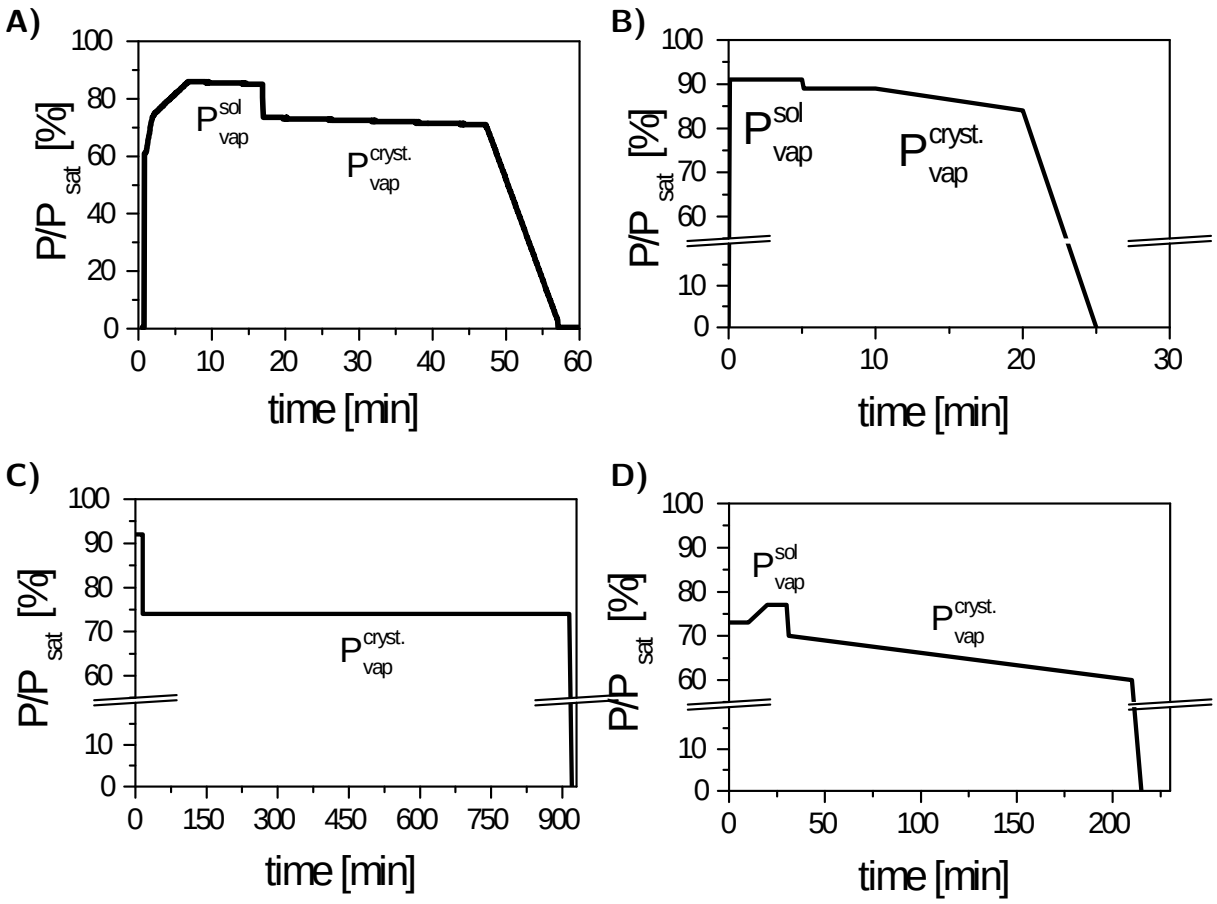

Fig. A.10: Typical solvent annealing protocols used in this study. **A)** CB-annealing protocol for PCPDTBT with vapor and substrate temperatures of $50\,^{\circ}\mathrm{C}$ and $42\,^{\circ}\mathrm{C}$, respectively. **B)** CS_2-annealing protocol with vapor and substrate temperatures of $22\,^{\circ}\mathrm{C}$ and $20\,^{\circ}\mathrm{C}$, respectively. **C)** CB-crystallization protocol for F-PCPDTBT with vapor and substrate temperatures of $50\,^{\circ}\mathrm{C}$ and $42\,^{\circ}\mathrm{C}$, respectively. **D)** CB-annealing protocol for Si-PCPDTBT with a vapor temperature of $50\,^{\circ}\mathrm{C}$ and varying substrate temperatures (stated for each sample throughout the thesis).

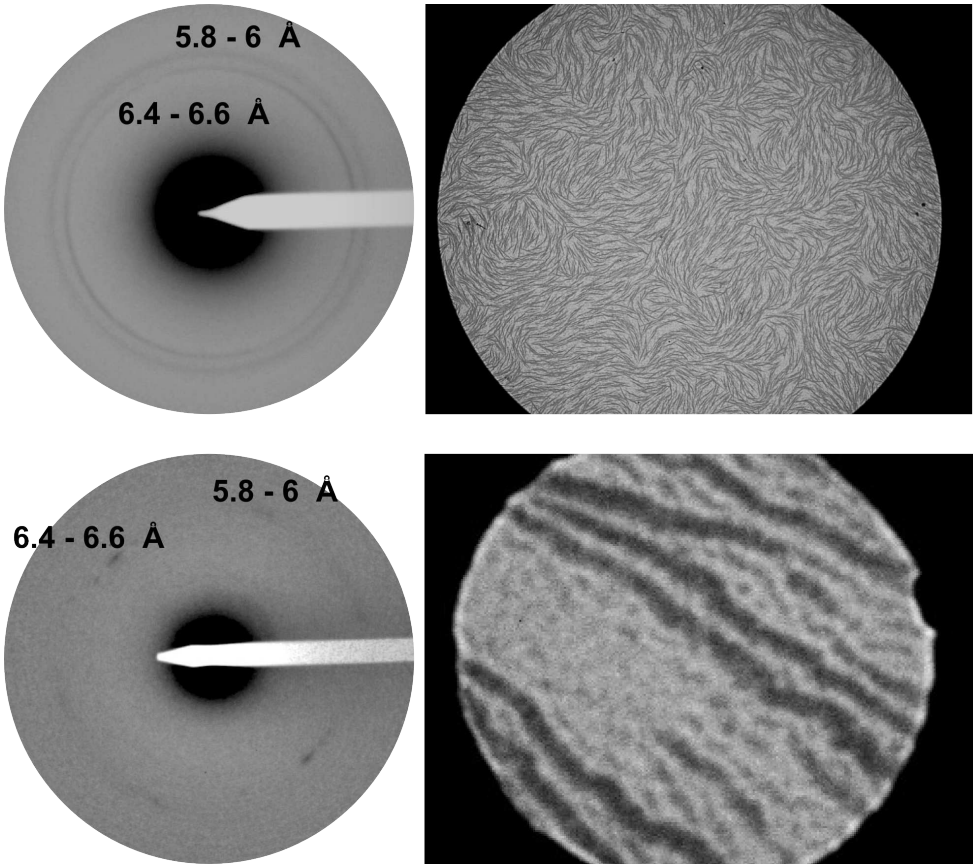

Fig. A.11: TEM/ED patterns (left) and bright field images (right) of a CS_2-annealed PCPDTBT film, with the distances of the respective reflections indicated in the images. The detailed solvent annealing protocol is given in figure A.10 (adapted from[12]).

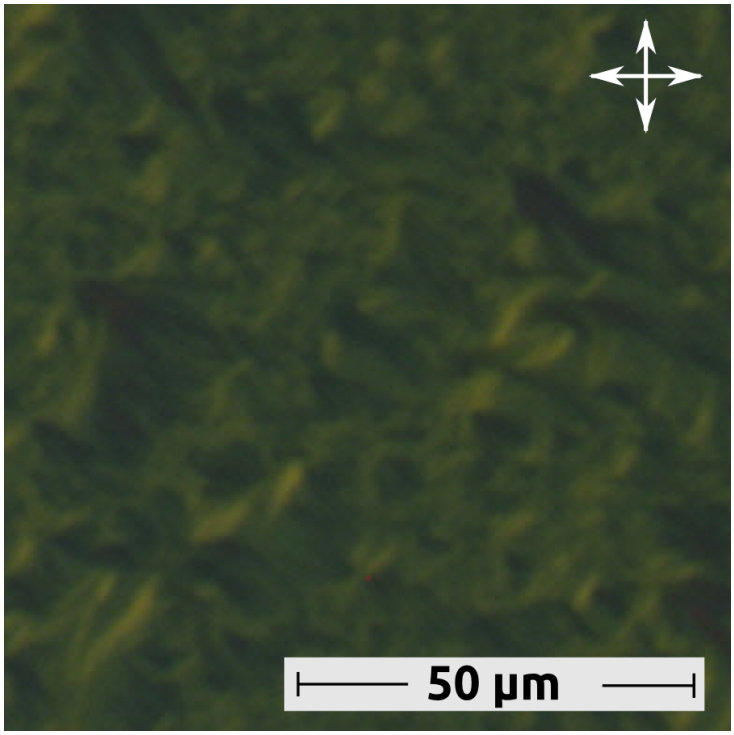

Fig. A.12: Polarized microscopy image with crossed polarizers of a F-PCPDTBT CS_2 vapor annealed film.

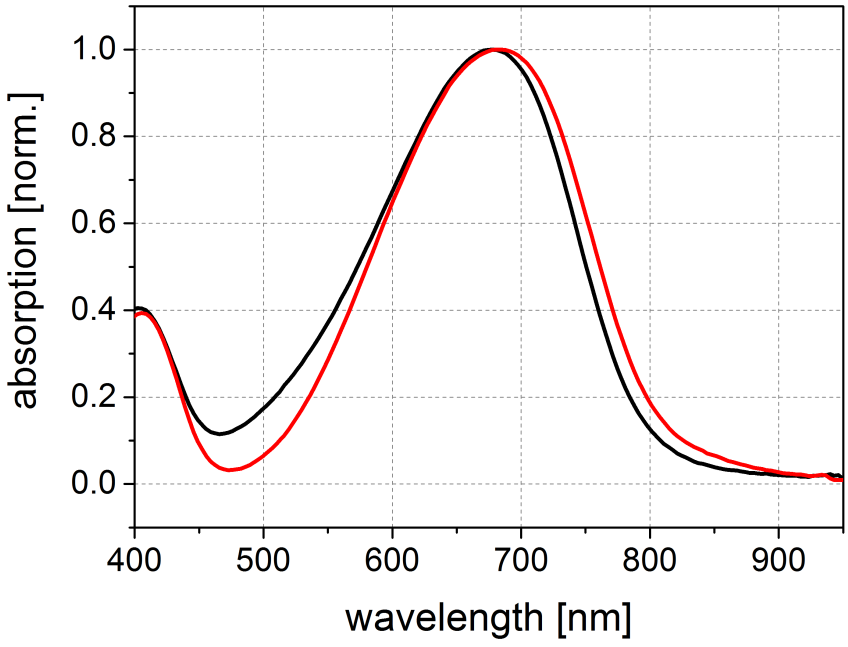

Fig. A.13: Absorption spectra of PCPDTBT films prepared by CB solvent vapor annealing (red) and spin coating from CB/DIO ($2\,\mathrm{w\%}$) at $320\,^{\circ}\mathrm{C}$ under nitrogen.

A.6 Crystal Structure

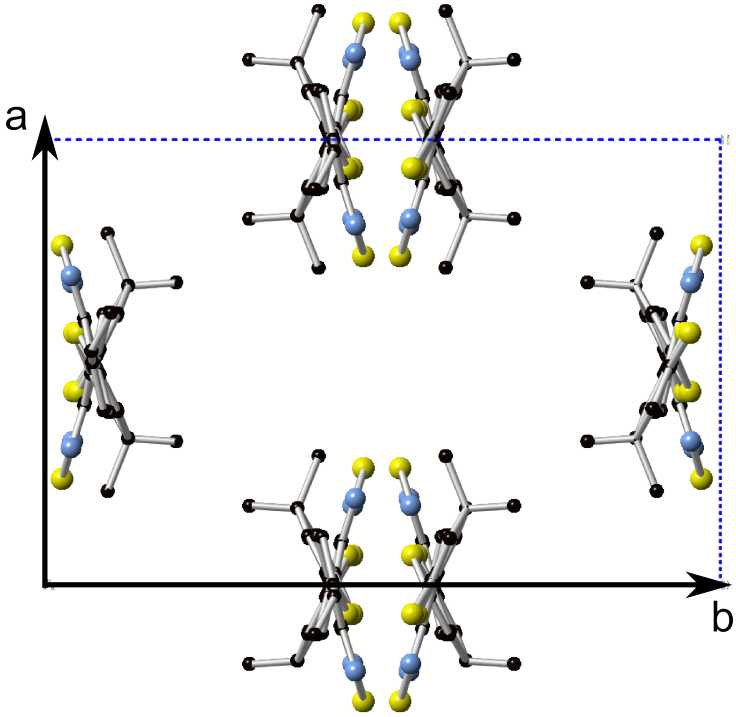

Fig. A.14: Crystal structure prepared using the P n c n space group assuming a non-planar backbone configuration. This structure was first proposed in our publication [12, Fischer et al. 2014].

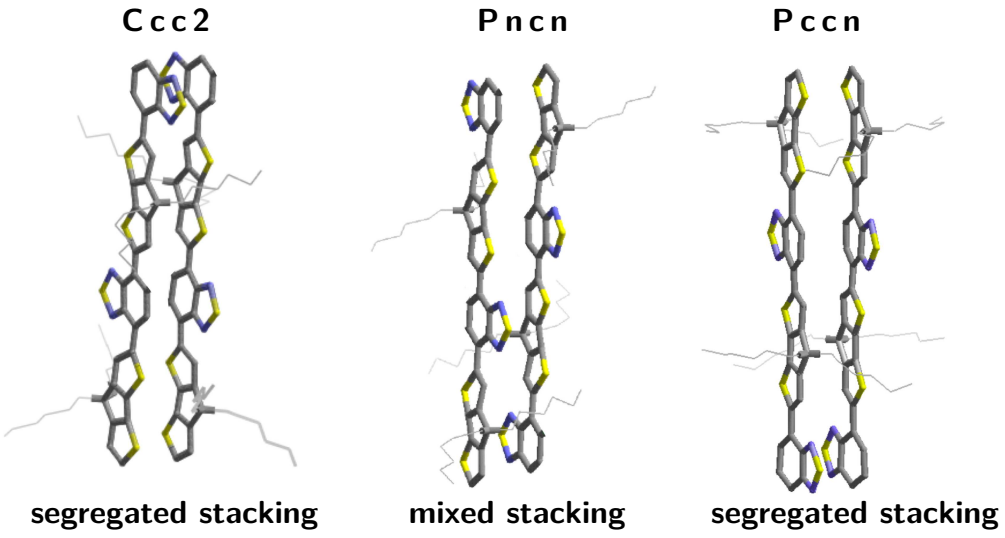

Fig. A.15: Stacking of the CPDT and BT units of PCPDTBT in the dimers of PCPDTBT depending on the space group used for form I. Image created by Dr. M. Brinkmann and published in [13, Fischer et al. 2015]

Tentative Crystal Structures

In the following the final crystal structure for PCPDTBT and F-PCPDTBT is given. The SHELX format was used following the nomenclature of a .res file.[178] The .res files are also attached to the pdf version of this thesis: PCPDTBT F-PCPDTBT

Crystal Structure of PCPDTBT

CELL 0.0000 12.4000 19.3000 24.0000 90.0000 90.0000 90.0000
LATT 1
SYMM -X+0.500,-Y+0.500,+Z
SYMM -X,+Y+0.500,-Z+0.500
SYMM +X+0.500,-Y,-Z+0.500
S1 0 0.14206 0.83832 0.54863 1.00000 0.09750 0.07200 = 0.07840 -0.01310 0.00330 -0.00860
S2 0 0.14646 0.84419 0.71798 1.00000 0.07810 0.06330 = 0.04910 0.00290 0.00110 0.00670
S3 0 0.53654 0.83379 0.88648 0.63540 0.06090 0.05610 = 0.06070 0.00090 0.00260 0.00080
N4 0 0.45524 0.83850 0.83461 0.63540 0.06120 0.05120 = 0.05670 0.00130 0.01190 0.00200
N5 0 0.45322 0.83269 0.93765 0.63540 0.06120 0.05120 = 0.05670 0.00130 0.01190 0.00200
C6 0 0.35847 0.83801 0.85750 0.63540 0.05360 0.06940 = 0.03370 0.01160 0.00050 0.00760
C7 0 0.35471 0.83501 0.91691 0.63540 0.05360 0.06940 = 0.03370 0.01160 0.00050 0.00760
C8 0 0.13868 0.85004 0.91812 0.36460 0.05360 0.06940 = 0.03370 0.01160 0.00050 0.00760
C9 0 0.14257 0.84626 0.85875 0.36460 0.05360 0.06940 = 0.03370 0.01160 0.00050 0.00760
C10 0 0.24293 0.83455 0.50128 1.00000 0.11590 0.06240 = 0.06770 -0.01730 0.02850 0.00450
C11 0 0.34251 0.83580 0.52432 1.00000 0.12700 0.05950 = 0.06510 -0.00720 0.01580 -0.00510
C12 0 0.33590 0.83851 0.58311 1.00000 0.11040 0.05000 = 0.07500 -0.00600 0.03260 0.00480
C13 0 0.23285 0.84294 0.60226 1.00000 0.08260 0.07040 = 0.03920 -0.01200 0.01450 -0.01340
C14 0 0.23392 0.84501 0.66313 1.00000 0.07820 0.05830 = 0.04170 -0.00170 0.00960 0.00320
C15 0 0.34199 0.84505 0.67984 1.00000 0.08320 0.06260 = 0.04590 -0.00670 0.01240 0.00030
C16 0 0.34825 0.84507 0.73775 1.00000 0.07830 0.06240 = 0.04170 0.00250 0.00510 0.00180
C17 0 0.25482 0.84514 0.76567 1.00000 0.07570 0.05690 = 0.03790 -0.00200 0.00640 0.00260
C18 0 0.41491 0.84134 0.62932 1.00000 0.08850 0.05910 = 0.07650 0.00850 0.01480 -0.01110
C19 0 0.39840 0.96088 0.61985 0.70200 0.10900 0.06050 = 0.23800 0.00500 0.01600 0.00100
C20 0 0.46505 0.90610 0.62996 0.29800 0.10200 0.09500 = 0.10200 -0.02100 0.01800 0.01200
C21 0 0.48903 0.78507 0.62774 1.00000 0.14100 0.04440 = 0.06610 -0.00350 -0.02410 -0.00120
C22 0 0.59900 0.80663 0.62899 1.00000 0.10550 0.05970 = 0.07540 0.00800 0.00850 -0.00460
C23 0 0.25009 0.84473 0.82699 1.00000 0.06600 0.05780 = 0.03770 0.02140 0.00560 0.00690
C24 0 0.24720 0.84174 0.94825 1.00000 0.08360 0.05890 = 0.04120 -0.00710 0.02540 -0.00820

C25 0 0.46296 1.01506 0.63061 1.00000 0.00000
C26 0 0.66057 0.76289 0.66373 1.00000 0.00000
C27 0 0.40141 1.07346 0.62102 1.00000 0.00000
C28 0 0.60502 0.69929 0.67131 1.00000 0.00000
C29 0 0.29477 1.05632 0.63245 1.00000 0.00000
C30 0 0.66383 0.65451 0.70673 1.00000 0.00000
C31 0 0.22986 1.11387 0.62247 1.00000 0.00000
C32 0 0.64992 0.58530 0.69154 1.00000 0.00000
C33 0 0.31020 0.96351 0.65371 1.00000 0.00000
C34 0 0.64359 0.79877 0.57624 1.00000 0.00000
C35 0 0.70546 0.85736 0.56534 1.00000 0.00000
C36 0 0.23321 1.01260 0.63823 1.00000 0.00000
END

Crystal Structure of F-PCPDTBT

CELL 0.0000 11.0000 20.6000 24.0000 90.0000 90.0000 90.0000
LATT 1
SYMM -X+0.500,-Y+0.500,+Z
SYMM -X,+Y+0.500,-Z+0.500
SYMM +X+0.500,-Y,-Z+0.500
S1 0 -0.09608 0.30678 -0.21974 1.00000 0.09750 0.07200 = 0.07840 0.01310 -0.00330 -0.00860
S2 0 -0.08765 0.30764 -0.05577 1.00000 0.07810 0.06330 = 0.04910 -0.00290 -0.00110 0.00670
S3 0 -0.08865 0.41768 0.11391 0.63540 0.06090 0.05610 = 0.06070 -0.00090 -0.00260 0.00080
N4 0 -0.08786 0.36927 0.05982 0.63540 0.06120 0.05120 = 0.05670 -0.00130 -0.01190 0.00200
N5 0 -0.09177 0.36582 0.16527 0.63540 0.06120 0.05120 = 0.05670 -0.00130 -0.01190 0.00200
C6 0 -0.08997 0.30841 0.08155 0.63540 0.05360 0.06940 = 0.03370 -0.01160 -0.00050 0.00760
C7 0 -0.09220 0.30666 0.14050 0.63540 0.05360 0.06940 = 0.03370 -0.01160 -0.00050 0.00760
C8 0 -0.09356 0.18989 0.13883 0.36460 0.05360 0.06940 = 0.03370 -0.01160 -0.00050 0.00760
C9 0 -0.09079 0.19135 0.08025 0.36460 0.05360 0.06940 = 0.03370 -0.01160 -0.00050 0.00760
C10 0 -0.09433 0.24687 -0.26856 1.00000 0.11590 0.06240 = 0.06770 0.01730 -0.02850 0.00450
C11 0 -0.09095 0.18489 -0.24142 1.00000 0.12700 0.05950 = 0.06510 0.00720 -0.01580 -0.00510
C12 0 -0.09179 0.19171 -0.18239 1.00000 0.11040 0.05000 = 0.07500 0.00600 -0.03260 0.00480
C13 0 -0.09423 0.25542 -0.16578 1.00000 0.08260 0.07040 = 0.03920 0.01200 -0.01450 -0.01340
C14 0 -0.08317 0.25601 -0.10993 1.00000 0.07820 0.05830 = 0.04170 0.00170 -0.00960 0.00320
C15 0 -0.08069 0.19265 -0.09290 1.00000 0.08320 0.06260 = 0.04590 0.00670 -0.01240 0.00030

C16 0 -0.08311 0.18579 -0.03472 1.00000 0.07830 0.06240 = 0.04170 -0.00250 -0.00510 0.00180
C17 0 -0.08631 0.24680 -0.00720 1.00000 0.07570 0.05690 = 0.03790 0.00200 -0.00640 0.00260
C18 0 -0.08307 0.14367 -0.13658 1.00000 0.08850 0.05910 = 0.07650 -0.00850 -0.01480 -0.01110
C19 0 -0.08920 0.25049 0.05110 1.00000 0.06600 0.05780 = 0.03770 -0.02140 -0.00560 0.00690
C20 0 -0.09424 0.24790 0.16927 1.00000 0.08360 0.05890 = 0.04120 0.00710 -0.02540 -0.00820
C21 0 0.02230 0.10453 -0.13601 1.00000 0.00000
C22 0 -0.17805 0.10099 -0.12718 1.00000 0.00000
C23 0 0.11724 0.14370 -0.11675 1.00000 0.00000
C24 0 -0.13505 0.04226 -0.14949 1.00000 0.00000
C25 0 0.22144 0.10606 -0.10754 1.00000 0.00000
C26 0 -0.21572 -0.00907 -0.13874 1.00000 0.00000
C27 0 0.31566 0.14699 -0.09170 1.00000 0.00000
C28 0 -0.16346 -0.06845 -0.15535 1.00000 0.00000
C29 0 0.42518 0.11379 -0.08710 1.00000 0.00000
C30 0 -0.24819 -0.11837 -0.14774 1.00000 0.00000
C31 0 0.41666 0.07680 -0.03868 1.00000 0.00000
C32 0 -0.20052 -0.17734 -0.16696 1.00000 0.00000
F33 0 -0.08973 0.14132 0.05454 1.00000 0.00000
C34 0 0.14103 0.19242 -0.15602 1.00000 0.00000
C35 0 -0.11256 0.05070 -0.20662 1.00000 0.00000
C36 0 0.26628 0.19865 -0.16557 1.00000 0.00000
C37 0 -0.05793 -0.00477 -0.22906 1.00000 0.00000
END

A.7 DFT Calculations

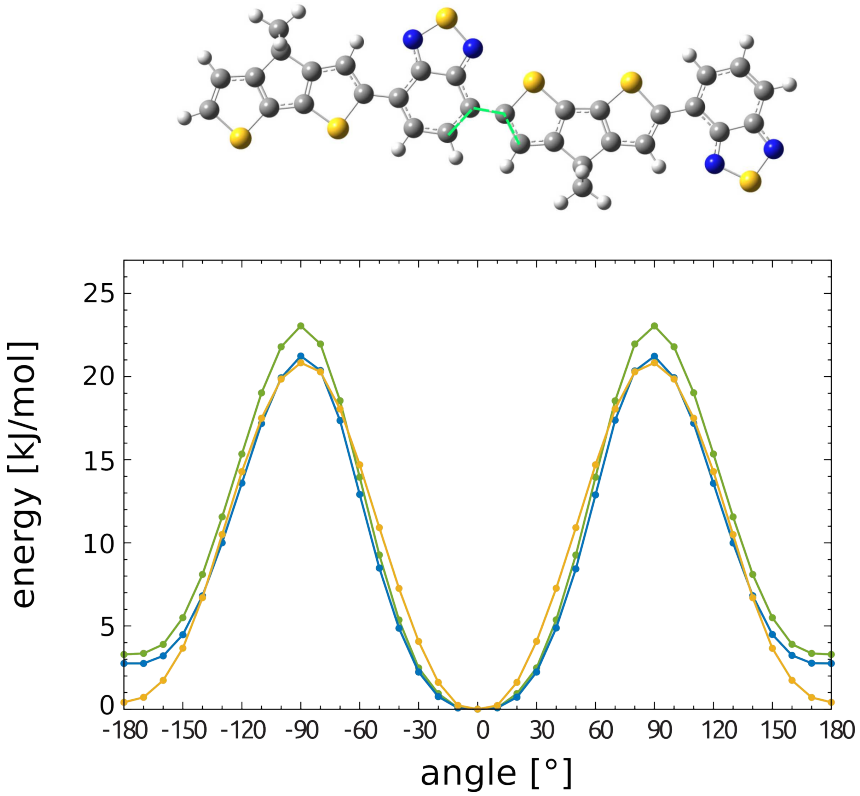

Fig. A.16: Energy of the dihedral angle between the cyclopentadithiophene and the benzothiadiazole as highlighted in green in the chemical structure calculated by DFT//B3LYP/6-311g(d,p). The calculations were performed by Anton Melnyk in the group of Dr. Denis Andrienko at the *Max Planck Institute for Polymer Research* in Mainz using a $(CPDTBT)_2$ geometry.

A.8 Electrochemistry

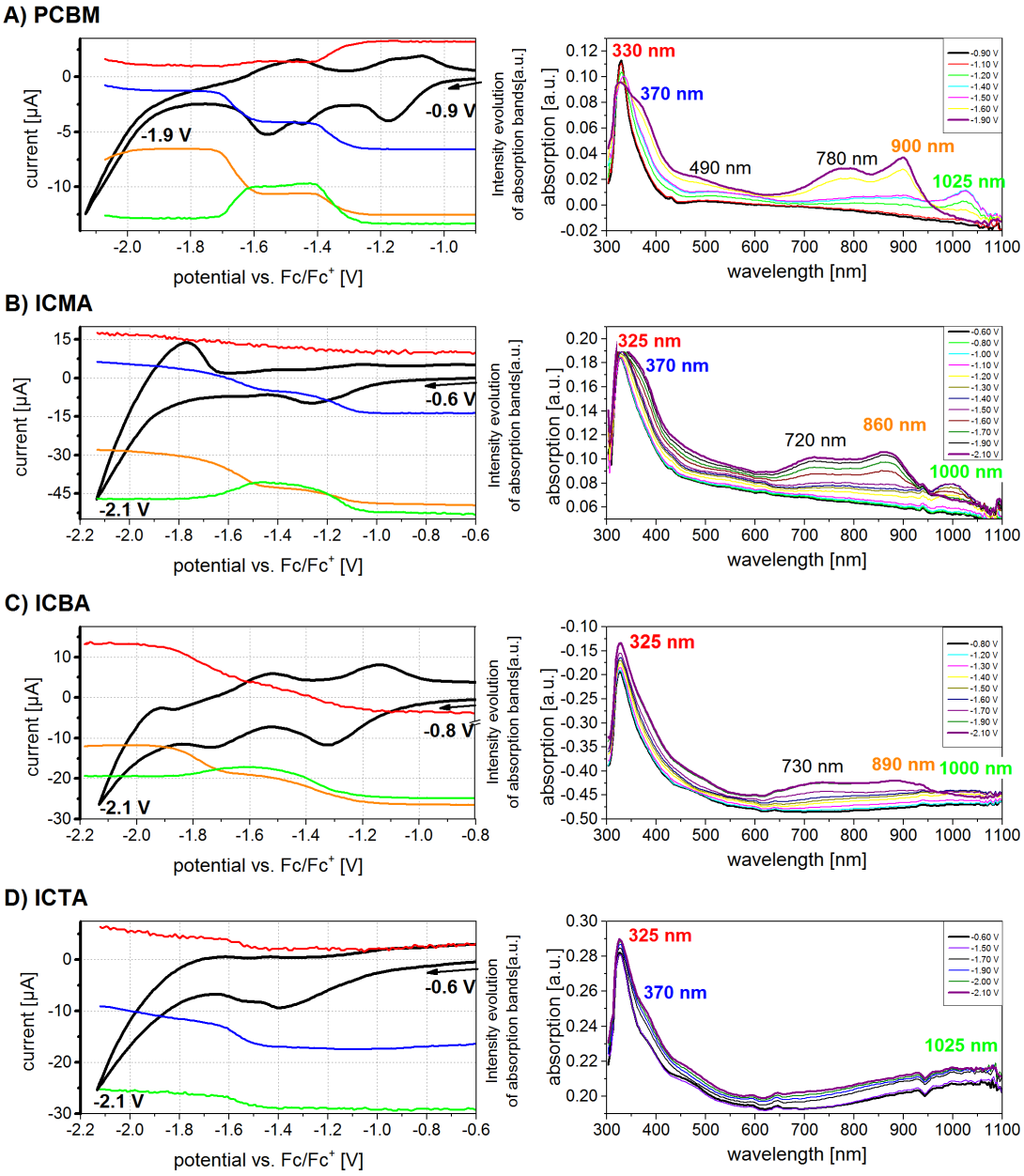

Fig. A.17: In-situ spectroelectrochemical data of **A)** PCBM, **B)** ICMA, **C)** ICBA and **D)** ICTA dissolved in methylene chloride ($3\,\mathrm{mg/ml}$ in $0.1\,\mathrm{M}$ $TBAPF_6$/methylene chloride, v=$20\,\mathrm{mV/s}$, RT, thin layer conditions). Left graphs: CVs of the first reduction cycle (left axis) and the intensity evolution of the absorption features (right axis, corresponding in color to wavelength labels of the right graphs). Right graphs: Corresponding absorption spectra during the forward scan of the reduction with all potentials indicated vs. Fc/Fc^+ (adapted from[14]).

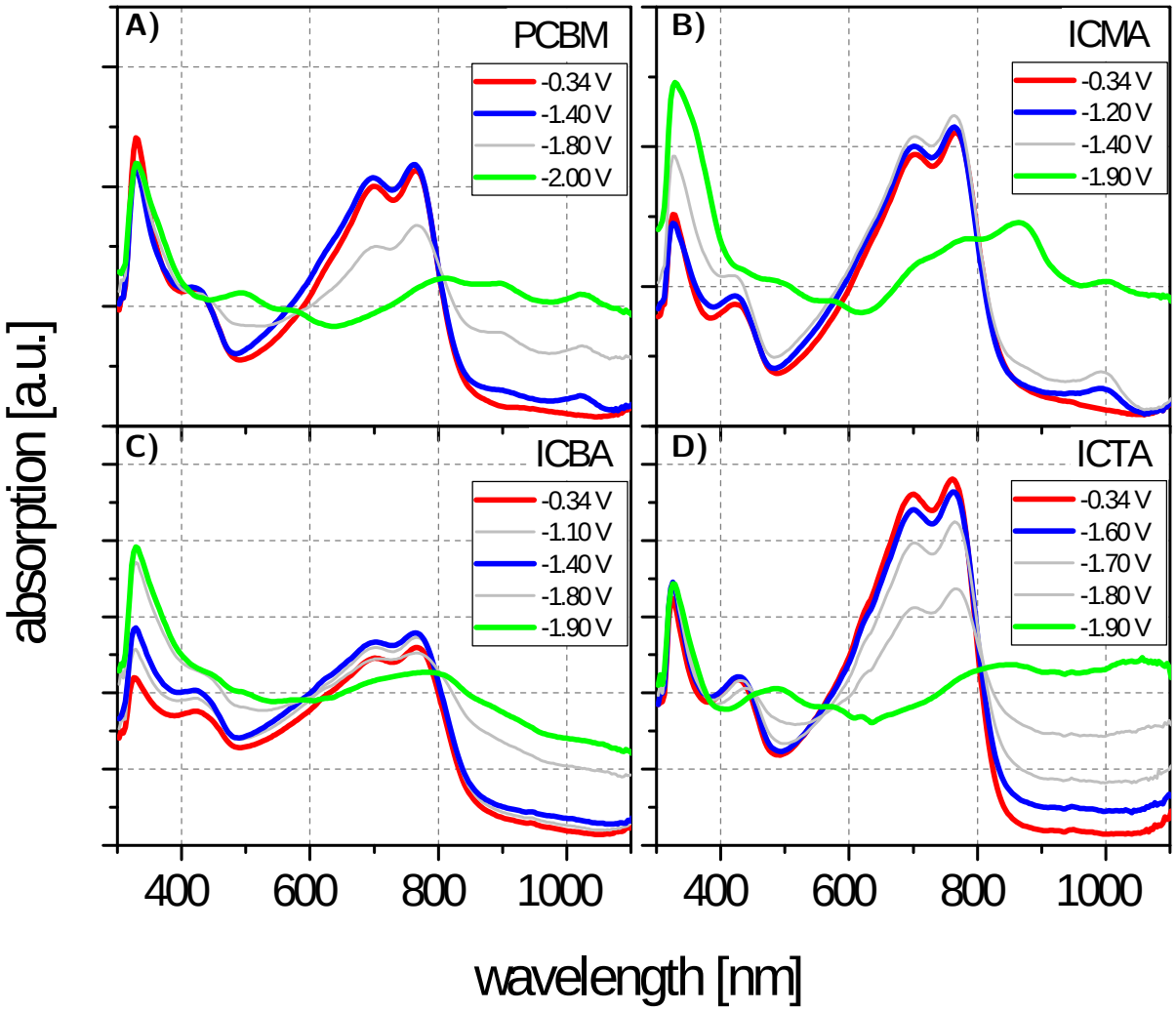

Fig. A.18: In-situ spectroelectrochemical absorption spectra of polymer/fullerene blends: **A)** PCBM, **B)** ICMA, **C)** ICBA and **D)** ICTA. Measurements were performed on pre-cast films spin coated on ITO-substrates in propylene carbonate ($0.1\,\mathrm{M}$ $TBAPF_6$/propylene carbonate, v=$20\,\mathrm{mV/s}$, RT). The corresponding cyclic voltammogramms and absorption intensity evolutions are shown in figure 5.6.

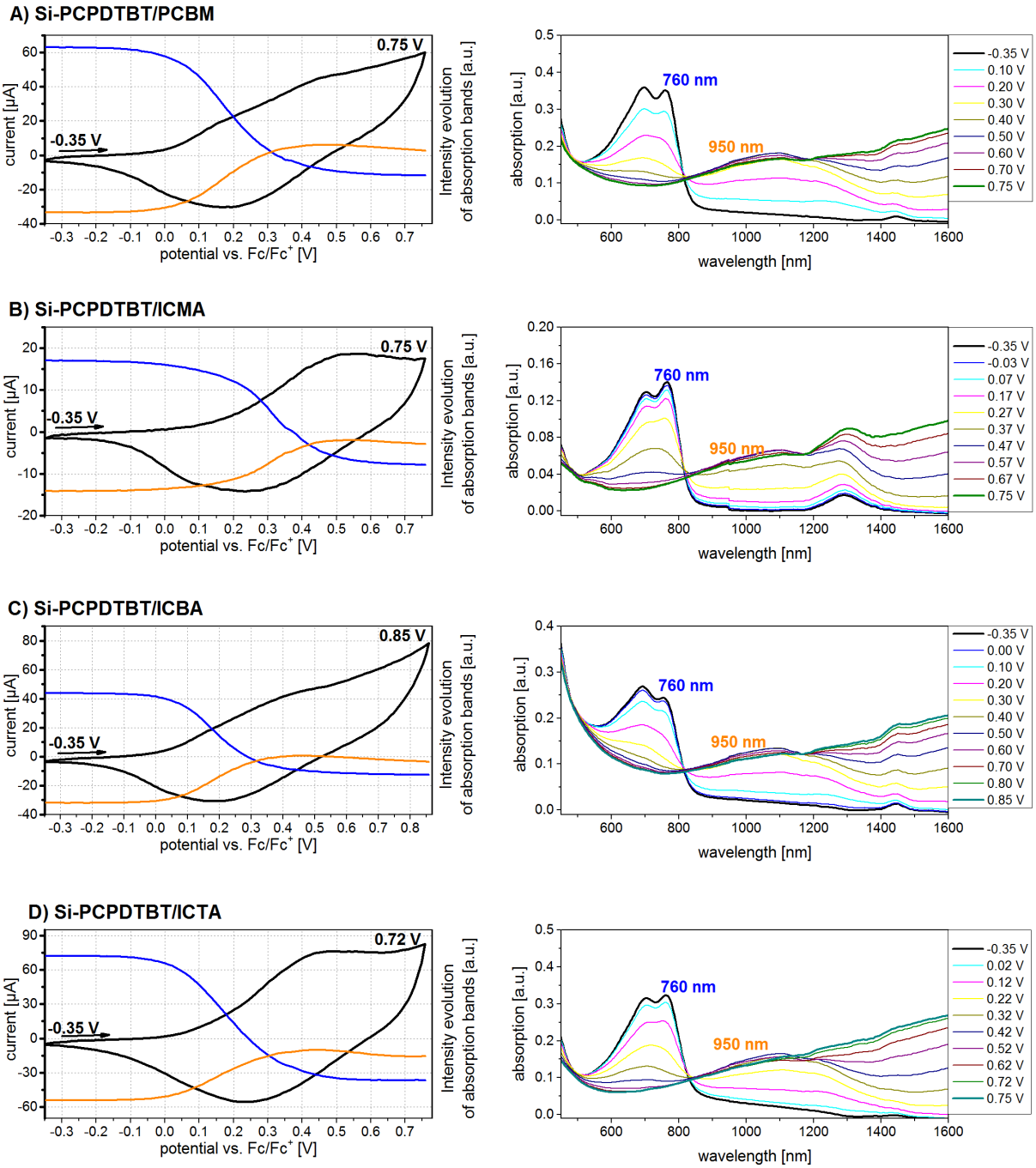

Fig. A.19: In-situ spectroelectrochemical data of Si-PCPDTBT blended with **A)** PCBM, **B)** ICMA, **C)** ICBA and **D)** ICTA. Measured as thin film on ITO in acetonitrile ($0.1\,\mathrm{M}$ $TBAPF_6$/acetonitrile, v=$20\,\mathrm{mV/s}$, RT). **Left graphs:** CVs of the first oxidation cyle (left axis) and the intensity evolution of the absorption features (right axis, corresponding in color to wavelength labels of the right graphs). **Right graphs:** Corresponding absorption spectra during the forward scan of the oxication with all potentials indicates vs. Fc/Fc^+ (adapted from[14]).

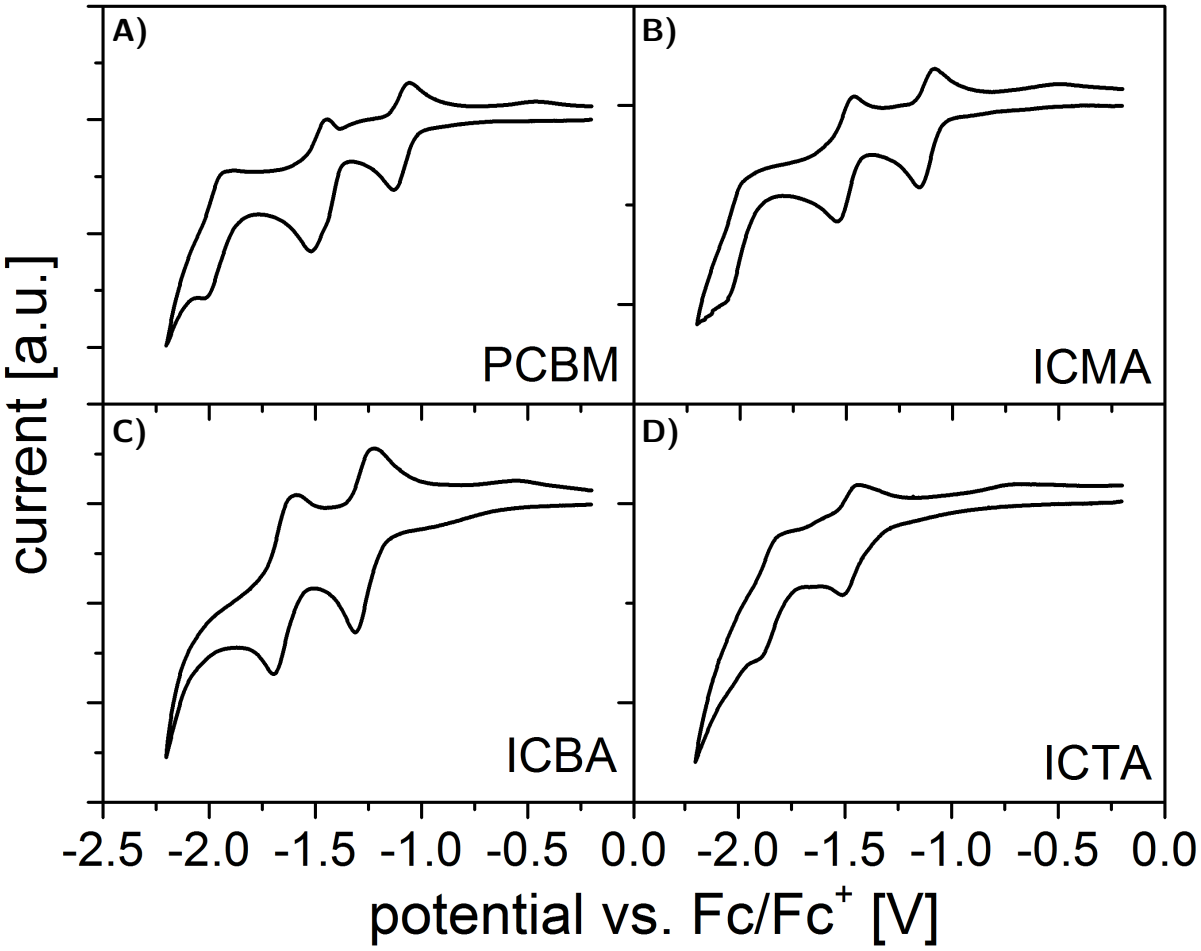

Fig. A.20: Cyclovoltammogramms of the fullerenes PCBM, ICMA, ICBA and ICTA dissolved in methylene chloride (CH_2Cl_2) with concentrations of $0.16\,\mathrm{mM}$, $0.18\,\mathrm{mM}$, $0.12\,\mathrm{mM}$ and $0.17\,\mathrm{mM}$, respectively. As supporting electrolyte $0.1\,\mathrm{M}$ tetrabutylammonium hexafluorophosphate ($TBAPF_6$)/CH_2Cl_2 was used after being deaerated by argon bubbling. Scan rates of $100\,\mathrm{mV/s}$ were used. Reference electrode: silver wire in $0.01\,\mathrm{M}$ $AgNO_3$ in $0.1\,\mathrm{M}$ $TBAPF_6$/acetonitrile, connected via a $0.1\,\mathrm{M}$ NBu_4PF_6/acetonitrile salt bridge; counter electrode: Pt wire. These measurements were performed by Dr. Adrian Ruff during his time as Post-Doc in our group.

A.9 Polymer Analysis

GPC

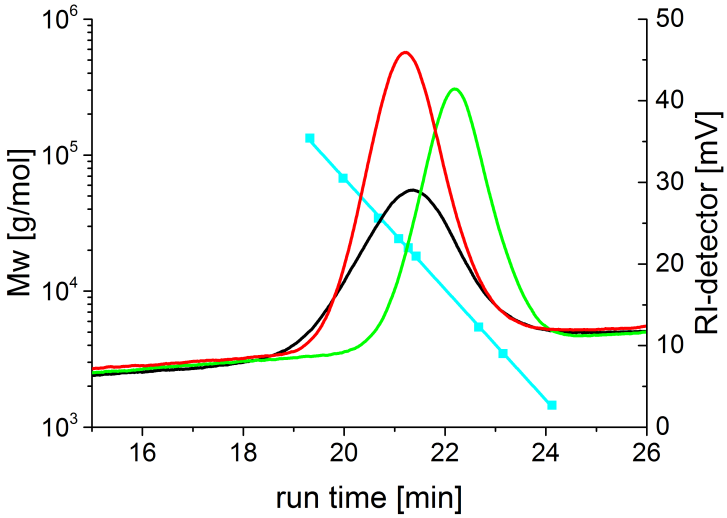

Fig. A.21: HT-GPC data of PCPDTBT (red), F-PCPDTBT (green) and Si-PCPDTBT ($32\,\mathrm{kg/mol}$, black). All polymers where measured in trichlorobenzene ($1\,\mathrm{mg/ml}$, $160\,^{\circ}\mathrm{C}$), the calibration data and a linear fit are plotted in cyan (right axis).

TGA

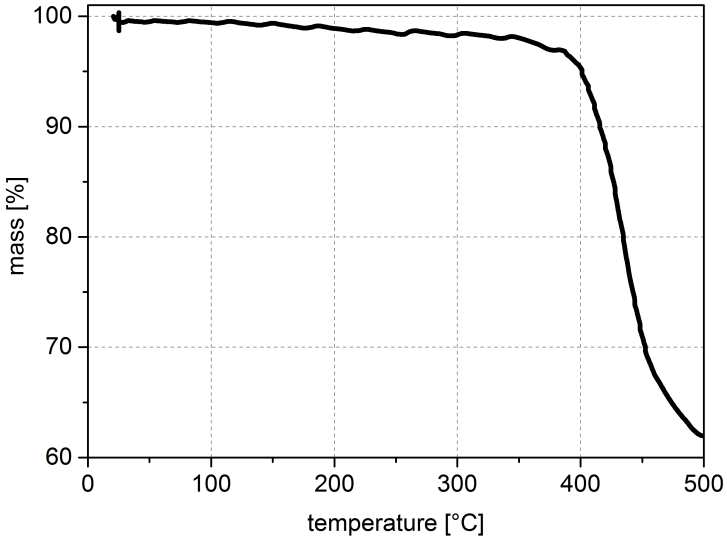

Fig. A.22: Thermogravimetric analysis (TGA) from the pure PCPDTBT in accordance to literature.[179] Measuring conditions: Al_2O_3 pan, $8.6\,\mathrm{mg}$, purging gas O_2/CO_2 (1:1 Vol.), $50\,\mathrm{ml/min}$, *NETZSCH* STA 449C, in the group of Dr. J. Kerres.